EPFL

Indoor Real-time localization system design for Internet of Things applications

Pooneh MOHAGHEGH

École
polytechnique
fédérale
de Lausanne

2023

In 958 King Harald "Bluetooth" united Denmark and Norway. His dead tooth, which was a dark blue/grey color, earned him the nickname Bluetooth.
In 1996, Intel, Ericsson, and Nokia united short-range radio technology to support connectivity and collaboration between different products and industries and they called it Bluetooth just like the Scandinavian king.
Bluetooth Special Group

جز صراحی و کتابم نه بود یار و ندیم
تا حریفان دغا را به جهان کم بینم

Acknowledgement

The present work results from many actors that played decisive roles during my journey at the integrated actuators Laboratory (LAI) of Epfl. I am deeply humbled by their inviolate involvement over the last four years.

I am grateful to Professor Yves Perrier for offering me a chance to pursue a doctoral thesis at LAI. His confidence in my colleagues and I have been invaluable for fostering knowledge generation within the laboratory.

My sincere gratitude towards my co-supervisor Dr. Alexis Boegli for his support and guidance throughout my study. His unwavering belief in me has been a constant source of motivation. I feel incredibly fortunate to have had the opportunity to learn from such an incredible mentor, not just at an academic level but also on a personal level.

Similarly, I am also grateful to Prof. Choo, Prof. Escudero, and Dr. Stadelmann for this thesis's revision and jury duty. I am also thankful to the students that contributed to my thesis and scientific publications with their projects.

I sincerely appreciate our collaborators at HE-Arc, Professor Francois Tièche, and Rabia Saeed, for their constructive input. Nicolas Sommer, Matteo Baldi, and Hakim Arfa for their enthusiasm and dedication throughout our time together. The primary stages of this thesis wouldn't be possible without the great scientific input, support, and encouragement of Denis Pravica at e-liberty SA.

I want to extend my heartfelt gratitude to Paolo Germano, and Bruno Studach, for their unwavering support and guidance. The moments of shared laughter, compassionate listening, and words of encouragement have provided much-needed strength and motivation during difficult times with all the members at LAI. Therefore, I am deeply grateful for the friendship and the enduring bond we have formed with my colleagues, Patricio Parlta, Sean Thomas, Camilo Hernandez, Adrian Thabuis, Raphael Mottet, Sofia Ntella, Marjan Ghorbani, Simon Holzer, Xiatao Ren, Ning Lui, Armando Walter. I am also grateful to Bhawnath Tiwari, Camilo Hernandez, and Marjan Ghorbani for their scientific support. Sofia Ntella, my colleague, office mate, and dear friend, has played a unique role in my Ph.D. journey. Her constant support, empathy, vast knowledge, and unwavering patience have enabled me to navigate and overcome the challenges. I am honored and privileged to have shared this journey with such outstanding individuals, and I wholeheartedly thank them for their unwavering support and guidance.

Finally, I would like to thank my family for always being there for me. My parents, Nima and Hesam, for establishing the profound value of education in me, and my sister Sahar for her

Acknowledgement

cheerful and insightful support. Without their constant support throughout my life, this Ph.D. would not have been possible. I'm grateful for all their sacrifices and encouragement, and support during my life. I also would like to send my gratitude to my friends, Fatemeh, Anahita, and Amin who supported me on various occasions during my Ph.D.

Lausanne, July 3, 2023 <div align="right">Pooneh Mohaghegh</div>

Abstract

With the prevalence of smartphones, watches, and Internet of Things (IoT) devices, the ability to track their positions is becoming increasingly important. For many indoor positioning systems (IPSs), providing an uninterrupted flow of information in real-time, effective, and low power are the main criterion. As a result, a solution is needed to withstand these conditions. This study is conducted to fill this gap and propose new solutions for an old question.

The thesis introduces three main indoor positioning systems. The first system focuses on an IPS based on 125 kHz technology. This system is a proximity-activated card with a magnetic field that is designed to communicate through a MQTT server. Through a neural network model with a sigmoid activation function, an accuracy of 20 cm was achieved in 70% of cases. The second system explores positioning in magnetic fields by incorporating a non-blocking access control scenario. It utilizes a video system to monitor a specific area. Using the Global Nearest Neighbor algorithm, a fusion algorithm is developed to assign collected data to individuals. This system demonstrated a high accuracy of 94% in various test scenarios.

While magnetic fields are not susceptible to multipath, they can be affected by large metallic objects. Positioning systems utilizing magnetic fields perform well in certain challenging environmental conditions, such as near brick walls. Despite these advantages and the achieved accuracy, smartphones have not adopted them, which is why another approach is introduced. It is based on Bluetooth Direction Finding (BLE-DF), which enables seamless integration with many IoT smart devices. This technology offers compelling performance in terms of energy consumption, speed, and positioning.

This thesis investigates two main BLE-DF architectures. Chapters 4 and 5 present the characteristics of the designed antenna arrays, a signal model for antenna arrays, and BLE-DF itself. Performance evaluations in an uncontrolled environment revealed that the proposed antenna arrays achieve up to 88% higher accuracy compared to a standard network. Various angle estimation algorithms and phase compensation processes are proposed, resulting in accuracy improvements of up to 40%. Different antenna structures and configurations are studied, and a precision of 3.7° is achieved using a Uniform Rectangular Array (URA), corresponding to an accuracy of 30 cm at a range of 5 meters. Lastly, a positioning algorithm is presented, demonstrating the achievable level of precision and paving the way for new applications.

Although the achieved accuracy is highly satisfactory, BLE-DF has its limitations. For instance, the system is susceptible to multipath effects that are inevitable in indoor spaces. To mitigate this effect, several methods are proposed. The proposed of Gaussian Mixture Models (GMM) or spatial smoothing could enhance the accuracy by approximately 85% or 40%, respectively.

Abstract

Keywords: Indoor Positioning Systems (IPS), Active RFIDs, Magnetic Positioning System, Internet of Things (IoT) Bluetooth Direction Finding, Angle Estimation Algorithms

Résumé

Avec la multiplication des Smartphones, des montres et des dispositifs de l'Internet des objets (IoT : Internet of Things), la capacité à suivre leur position devient de plus en plus importante. Pour de nombreux systèmes de positionnement en intérieur (IPS : Indoor Positioning Systems), fournir un flux d'informations ininterrompu en temps réel, efficace et à faible consommation d'énergie est le principal critère. Pour répondre à ces condition une solution est nécessaire. Cette étude vise à combler cette lacune et proposer de nouvelles solutions au problème récurrent du positionnement en intérieur.

Dans cette thèse, trois principaux systèmes de positionnement en intérieur sont proposés. Tout d'abord, l'accent est mis sur la création d'un IPS basée sur une technologie fonctionnant à 125kHz. Ce système est composé d'une carte et d'un générateur de champs magnétiques. Les champs magnétiques permettent de réveiller la carte et de la positionner. Celle-ci est conçue pour communiquer avec un serveur. Un réseau neuronal avec un sigmoïde comme fonction d'activation a permis d'atteindre dans 70% des cas une précision de 20 cm. Un second système de positionnement dans des champs magnétiques est étudié en introduisant un scénario de contrôle d'accès non bloquant. Il a recours à un système vidéo pour la surveillance d'une zone. À l'aide d'un algorithme de proximité globale (Global Nearest Neighbor algorithm), un mécanisme de fusion est développé et mis en œuvre. Il attribue les données collectées à une certaine personne. Ce système a atteint une précision de 94% dans divers scénarios de test.

Les champs magnétiques ne sont pas sujets aux trajets multiples, mais sont sensibles à de gros corps métalliques. Les systèmes de positionnement les utilisant fonctionnent bien dans certaines conditions environnementales difficiles, par exemple à proximité de murs en briques. Malgré ces avantages et la précision obtenue, les Smartphones ne les ont pas adoptés, raison pour laquelle une autre approche est introduite. Elle se base sur la localisation directionnelle Bluetooth (BLE-DF : Bluetooth Low Energy Direction Finding). Cette technologie permet une intégration transparente avec de nombreux appareils intelligents de l'IoT. Elle offre des performances intéressantes en termes de consommation, de rapidité et de positionnement. Cette thèse étudie deux architectures BLE-DF principales. Elle présente aux chapitres 4 et 5, les caractéristiques des réseaux d'antennes conçus, un modèle de signal pour les réseaux d'antennes ainsi que BLE-DF. Les performances dans un environnement non contrôlé ont révélé que les réseaux d'antennes proposés sont jusqu'à 88% plus précis qu'un réseau standard. Différents algorithmes d'estimation d'angles et un processus de modification des échantillons sont proposés. Ceux-ci permettent une augmentation de la précision qui peut atteindre 40%. Différentes structures et configurations d'antennes sont étudiées. Une précision de 3.7° est

obtenue en utilisant un réseau URA, ce qui correspond à une précision 30 *cm* à 5 *m*. Enfin, un algorithme de positionnement est présenté. Il prouve que cette précision peut être obtenue. Cela ouvre la voie à de nouvelles applications.

Bien que la précision obtenue soit très bonne, BLE-DF a ses limitations. Par exemple, le système est sujet aux trajets multiples qui sont inévitables dans les espaces intérieurs. Pour compenser cet effet, plusieurs méthodes sont proposées. Ainsi le recours aux modèles de mélange gaussien (GMM : Gaussian Mixture Models) ou au lissage spatial pourrait augmenter la précision de, respectivement 85% ou 40%. Ce travail tente également d'ouvrir la voie à de futurs chercheurs en contribuant à une meilleure compréhension des performances des systèmes proposés en tant que systèmes de positionnement intérieur à faible consommation d'énergie atteignant une précision submétrique.

Keywords : Systèmes de positionnement en intérieur, Active RFIDs, système de positionnement magnétique, Internet des Objets (IdO), Bluetooth Direction Finding, Algorithmes d'estimation d'angle

Contents

Contents

List of Figures

List of Tables

Notation

Abbreviations

2D	Two Dimensions
3D	Three Dimensions
5G	5 Generation
6DoF	6 Degree of Freedom
AGC	Automatic Gain Control
AoA	Angle of Arrival
AoD	Angle of Departure
Aox	Either AoA or AoD
API	Application Programming Interface
ASK	Amplitude Shift Keying
BLE	Bluetooth Low Energy
COF	Carrier Offset Frequency
CRC	Cyclical Redundancy Checking
CSI	Channel State Information
CTE	Constant Tone Extension
DF	Direction Finding
DFT	Discrete Fourier Transform
DK	Development Kit
DoA	Direction of Arrival
DTS	Device Tree Source
EPFL	Swiss Federal Institute of Technology in Lausanne
ESPRIT	Estimation of Signal Parameters via Rotational Invariance Techniques
FFT	Fast Fourier Transform
GFSK	Gaussian Frequency Shift Keying
GMM	Gaussian Mixture Models
GNN	Global Nearest Neighbour
GPIO	General Purpose Input / Output
HCI	Host Controller Interface
He-Arc	Haute Ecole Architecture

Abbreviations

I/O	Input/Output
ID	IDentification
IMU	Interial Measurements Unite
IoT	Internet of Things
IQ	In-Phase and Quadrature
ISM	Industrial, Scientific, and Medical
JPDA	Joint Probabilistic Data Association
JSON	JavaScript Object Notation
k-NN	k Nearest Neighbour
LF	Low Frequency
LL	linklayer
MAP	andMaximuma Posteriori
MCU	Multipoint Control Unit
MHT	Left Half-Plane
MIMO	Multiple-Input Multiple-Output
ML	MaximumLikelihood
MLP	Multiple Preceprton Model
MQTT	Message Quest Telemetry Transport
MUSIC	Multiple Signal Classification
NLOS	Non Line Of Sight
nRF	Generic name for Nordic semiconductor modules
OS	Operating System
Paas	Platform as a service
PCB	Printed-Circuit-Board
PDU	Protocol Data Unit
RF	Rafio Frequency
RFID	Radio Frequency IDentification
RPMsg	Restricted Permission Message
RSSI	Received Signal Strength Indication
RTLS	Real Time Location System
RX	Receiver
SDK	Software Development Kit
SIG	Bluetooth Special Interest Group
SMA	SubMiniature version A
SNR	Signal to Noise Ratio
SoC	Silicon on Chip
SR	Sampling Rate
SVM	Support-Vector Machine
TDoA	Time Delay of Arrival
TX	Transmitter
UCA	UniformCircular Arrays
ULA	UniformLinear Arrays

URA	UniformRectangular Arrays
VGA	Variable Gain Amplifier
Wi-Fi	Wireless Fidelity
WLAN	Wireless Local Area Network

1 Introduction

The Internet of Things (IoT) has become increasingly prevalent daily, with connected devices ranging from wearables to smart homes. However, many IoT applications require accurate indoor positioning, which poses a significant challenge due to the complexity of indoor environments. Current indoor positioning systems (IPS) lack the necessary sub-meter accuracy to provide reliable location information for many IoT applications.

1.1 Motivation

The original purpose of navigation and positioning was to guide ships on the sea [1], but in modern times, it has expanded to include various types of movement, such as humans, cars, robots, airplanes, and spaceships. The first step of navigation is positioning a target. The importance of positioning has become increasingly vital in modern applications. Accurate positioning can aid in determining the location of objects or individuals, which can improve safety, security, and efficiency [1], [2]. In addition to outdoor navigation, accurate indoor positioning has become essential in recent years.

The success of the Global Navigation Satellite Systems (GNSS) forever changed the concept of navigation, and similarly, a strong push is required to repeat that indoors as well. Locating a person inside a building or a tag in a warehouse has many advantages and the potential to enhance our lives. Unfortunately, the GNSS cannot meet the requirements of indoor positioning even with the nominal enhanced measurement accuracy down to 1 meter as receivers struggle with multipath signals and the inability to see the satellites.

Smart objects such as electronic watches, car alarms, smartphones, etc, have been used for decades. IoT brings a greater prevalence of such smart things with higher connectivity and the ability to collect data in real-time. The number of IoT devices worldwide is forecast to be close to 30 billion in 2030 [3]. IoT devices are adopted in many domains, from wearable devices to smart cars, smart homes, smart cities, to even industrial equipment. One of the main pieces of information that is required to be known for these systems is the position of such targets.

Positioning and navigation in indoor spaces are often challenging and have limitations in efficiency compared to traditional outdoor positioning methods. One of the main challenges of such systems is signal penetration through walls or bulky materials. The loss of track of the tags behind the doors, around the corners, under tables, etc., is another challenge of such systems. Multipath effect signals are reflected and attenuated by walls, furniture, and noise interference. These challenges result mainly from the influence of obstacles on the propagation of electromagnetic waves [4]. Another challenge is the Non-Line-of-Sight (NLoS) conditions and fast changes to the characteristic of the environment due to the presence of people and doors opening [5]. Short-range systems may not provide a sufficient range, requiring several beacons. This will result in several consequences, such as the extensive need for calibration, maintenance, and higher cost.

All of these challenges are the reasons for the need to explore more about creating a reliable indoor positioning system. The existing indoor environment lacks a system with high accuracy, availability, integrity, and low user costs functioning in real-time. To meet these challenges, we are studying three leading solutions in the course of this thesis. The details of each will be explored in future chapters.

1.2 Focus and Scope

After presenting the motivation behind exploring novel solutions for indoor positioning, it is essential to discuss the focus and the scope of this study. To address this issue, this thesis focuses on developing an Indoor Positioning System for IoT applications with sub-meter accuracy. Sub-meter accuracy indoor positioning systems bring about many advantages in our daily life, and deeply studying methods that can potentially become the future of indoor positioning can provide many advantages for researchers as well as the industry section. Low-power assumptions are not in the scope of this thesis.

At first glance, we briefly describe this thesis's scope and field. Chapter 3 focuses on the development of a non-blocking access control solution that is low-power and cost-effective. This will be accomplished through an RF-based solution paired with a camera, enabling the system to track and locate the target without causing any barrier disruptions.

Chapters 4 to 6 of the study will explore the use of Bluetooth Low Energy Direction Finding (BLE-DF) for indoor positioning. BLE-DF is a promising technology that can provide sub-meter accuracy in indoor environments. This study will evaluate the effectiveness of BLE-DF for indoor positioning. We will elaborate on this issue in the state-of-the-art chapter.

1.3 Relevance and Importance

Indoor Positioning Systems (IPS) are becoming increasingly important across various industries and applications, from robotics and IoT to healthcare and retail. In manufacturing and

warehousing environments, IPS can be used to track the location of inventory, tools, and equipment, which can improve efficiency, reduce errors, and optimize workflow. IPS can also be used in robotics to provide accurate location data, enabling robots to navigate and interact with their surroundings more effectively. IPS is critical in IoT applications where connected devices must be tracked and located in real-time, especially in complex indoor environments. IPSs also have surveillance applications, such as tracking the movement of personnel and assets in airports, train stations, and other crowded environments. This thesis has practical implications for the future of IoT applications, enabling more accurate and reliable location tracking in indoor environments.

1.4 Overview of the Structure

An overview of the areas this thesis covers is presented in this section. Figure 1.1 visualizes this thesis's two main focus areas. In this work, we will unfold two systems based on two different technologies for indoor positioning. First, the question of indoor positioning is studied under the common scenario of access control, and later, it is explored in the case of a real-time positioning system. The primary system was initially proposed to address the requirements of an industrial partner. In spite of the high preference and accuracy of the proposed system, the conditions were altered to fit the solution to existing infrastructures such as smartphones or watches. Introducing new infrastructures forces new challenges that were no longer in the interest of the industry partner which includes but is not limited to forcing the clients to buy new devices or big data management of the cards in the resorts. Therefore another system is proposed that is compatible with smartphone devices. This system is based on Bluetooth Low Energy (BLE) which is widely accessible and essentially low energy. It functions based on Bluetooth direction-finding (BLE-DF) protocol for positioning. BLE-DF is based on the principles of Angle of Arrival (AoA) or Angle of Departure (AoD). The data analysis process from raw BLE packets to position estimation is discussed in chapters 4 to 6. The detailed steps are presented in figure 1.2.

- *Chapter 2. State of the art*
  In this chapter, we dive into the history and the state of the art of indoor positioning and the technologies and methods currently being used. We assess the importance of such systems for industrial applications and daily life. We discuss the focus and the scope of this thesis and the problem that this thesis is trying to solve.

- *Chapter 3. Non-blocking access control*
  In the third chapter of this thesis, we focus on access control as a common application of positioning systems. We present a method based on an RF system as visualized in figure 1.1. We propose two technology based on a smart card working on the principles of active RFID systems and another solution based on a hybrid system consisting of a camera and a magnetic positioning system. Both are functioning based on received signal strength indication (RSSI) measurements. We present two methods based on
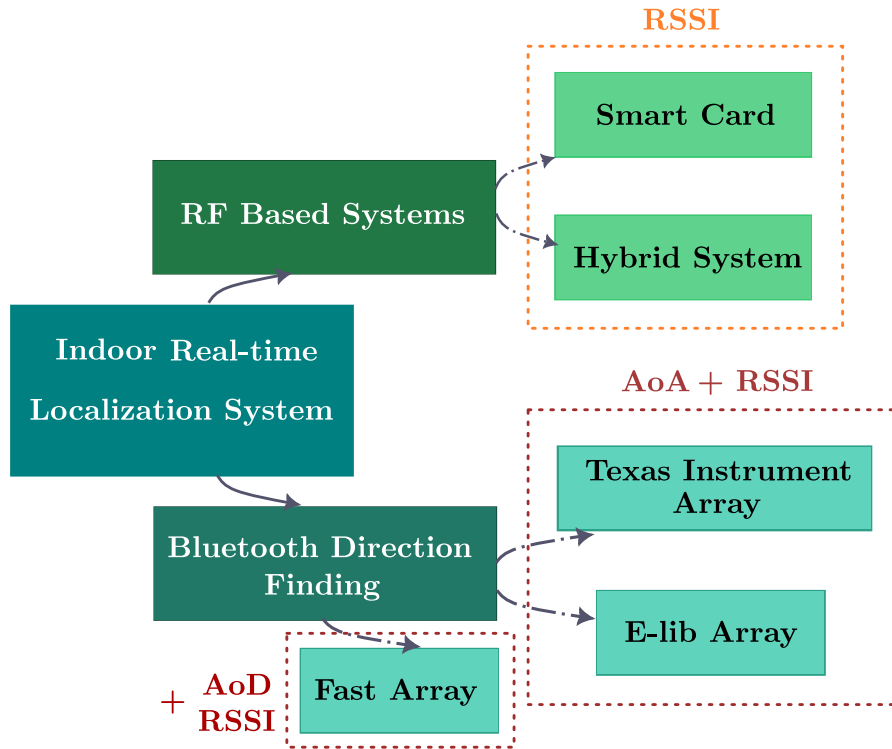
Figure 1.1: A overview of the thesis, Received Signal Strength Indication (RSSI), Angle of Arrival/Departure (AoA/AoD)

Maximum Likelihood and Neural Network to estimate the location. Moreover, we propose a merging algorithm based on the Global Nearest Neighbor (GNN) for our proposed hybrid system for access control.

- *Chapter 4. Angle Estimation and Antenna Array Design*
  In this chapter, we start to unwrap the basic principles of Bluetooth Direction Finding and the main aspects of this protocol (black box in figure 1.2). We present antenna arrays explicitly designed for direction finding presented in figure 1.1. The main characteristics of our designed antennas are presented in this chapter. As shown in figure 1.1, we initially used the Texas Instruments antenna array and then designed another antenna array called the e-lib antenna. Later, with the help of our collaborators at HE-Arc, we designed another array with a fast switch, all presented in figure 1.1. We present algorithms for angle estimation and the way we implemented these algorithms for our system (black box in figure 1.2).

- *Chapter 5. System Architecture and Sample Correction*
  This chapter presents different system architectures used throughout this thesis and magnifies their similarities and differences. It presents a data correction method and algorithm for BLE-DF data packets to estimate the Angle of Arrival or Departure (AoA/AoD). It presents a BLE AoA/AoD signal model to create the basis for implementing the discussed modifications and algorithm. This chapter includes all the steps presented
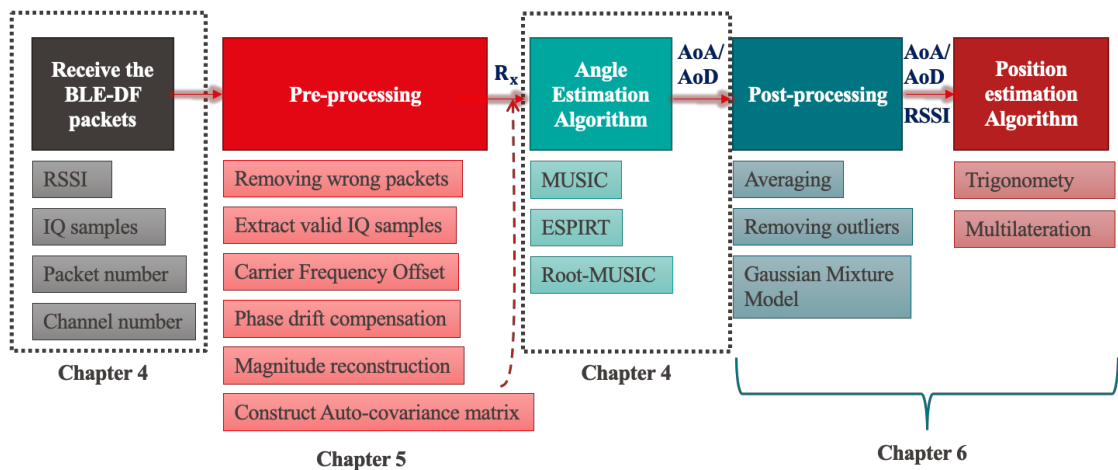
Figure 1.2: An overview of the angle estimation process presented through chapters 4 to 6. (In-phase and Quadrature (IQ), Multi Signal Classification (MUSIC), Estimation of Signal Parameters via Rotational Invariance Techniques (ESPRIT), and positioning)

in the pre-processing section of figure 1.2 to construct the input for the angle estimation algorithms.

- *Chapter 6. Angle estimation experiments and data analysis*
  This chapter presents the results of data corrections proposed in the previous chapter by testing in a controlled and uncontrolled environment. It includes the steps presented in figure 1.2. It amplifies the practical differences between the discussed antenna arrays, structures, and architectures for BLE-DF. Last but not least, this chapter presents a positioning algorithm based on collected AoA or AoD and RSSI (figure 1.1) based on the maximum likelihood method and Gaussian Mixture Model (GMM). This chapter analyzes the performance of the antenna arrays, the algorithms, and modifications and gives an overview of the process that started in Chapter 4.

- *Chapter 7. Conclusion*
  The final chapter of the thesis summarizes and concludes the scientific lessons and concrete outcomes from the present work and provides an overview of the whole dissertation. It translates and highlights the contributions of this thesis concerning the state of the art. The chapter suggests directions for future work that would be of great interest to continuing the research undertaken in this thesis

2 State of The Art

2.1 Introduction

The availability of smartphones and wearable devices with wireless communication capabilities has made it feasible to track and locate both devices and users simultaneously. This has opened up a wide range of applications and services. Precise indoor positioning has the potential to enhance indoor navigation, improve location-based services, and enable various new applications. For instance, it can facilitate indoor asset tracking and location-based advertising and aid in different areas such as health, industry, disaster management, building management, and surveillance. The Internet of Things (IoT) is playing a significant role in shaping the future of many industrial and mass-market applications, including emerging technologies like smart cities, smart buildings, and smart grids [6, 7].

IoT uses a set of diverse technologies and communication standards designed to provide end-to-end connectivity to billions of devices. Currently, research and commercial development focus on emerging technologies that enable long-range machine-to-machine communication. However, existing short- and medium-range technologies such as Bluetooth [8, 9, 10], ZigBee [11], WiFi [12, 13], and UWB [14, 15] will still be essential to the IoT network. Although long-range IoT technologies aim to provide extensive coverage and low-power communication, they cannot support the high data rates required by many local applications. Therefore, depending on the underlying application, a significant number of IoT devices will use more than one communication interface, such as one for short-range and one for long-range communication.

Many IoT applications will require seamless and ubiquitous indoor/outdoor localization and/or navigation of both static and mobile devices. Long-range IoT technologies have not been designed for indoor localization provision. Short-range communication technologies can accurately estimate the relative indoor location of an IoT device with respect to reference points, but the global location of these devices remains unknown without knowledge of the reference point locations. Emerging long-range IoT technologies can estimate the global location of a device since the locations of their access points are typically known, but their accuracy is usually low, particularly in indoor environments [7].
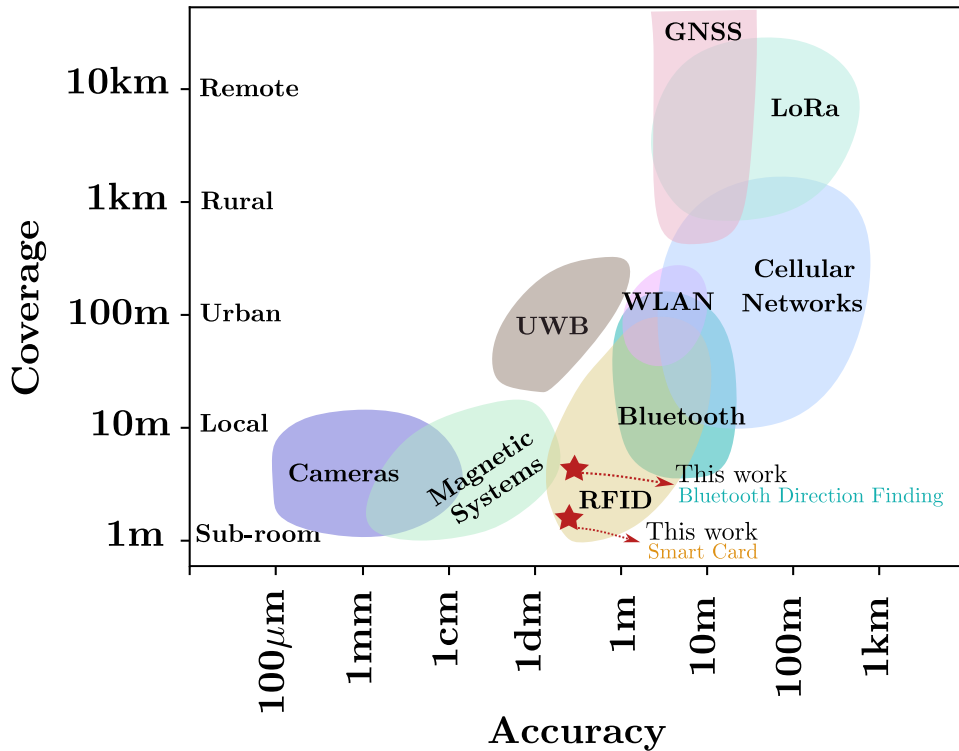
Figure 2.1: A overview of coverage and accuracy of existing indoor positioning systems [7, 5]

To meet the diverse localization requirements of future IoT networks and services, we believe that close collaboration between short and long-range IoT technologies will be necessary. Therefore, this thesis tries to fill the void of an accurate indoor positioning system that can be scaled into existing global solutions. Now that we understand the importance of creating an indoor positioning system, in this chapter, we present the latest scientific and industrial developments of indoor positioning systems with a small glaze on the history of such systems and their evolution.

2.2   A Glance at the History of Indoor Positioning

There are various technologies that can be used for positioning depending on the application, cost, and goals. These include light, sound, and magnetic waves. For example, some common tracking methods include Infrared, Ultrasound, Audible Sound, Magnetic, Optical & vision, WiFi [12, 13], and Visible light.

Figure 2.1, presents an overview of some existing technologies being used for localization purposes. This figure shows each technology's typical coverage or range of use and the typical, expected range of accuracy for each technology. Usually, indoor environments do not exceed

the urban range and start from $2-3$ m up to 50 m. Usually, this range is called an indoor environment; however, this can also be used outdoors. This term has been used in the literature for this range of applications, even though it can be used for other applications such as semi-inclosed environments [7]. Therefore, we will use the same term to describe a positioning system functioning in this range. To find the appropriate technology, we should search for some solutions, such as using a camera, a magnetic positioning system, RFIDs, UWB, or Bluetooth. All of these technologies can function in the range required for indoor positioning. However, not all might be suitable for the same application.

This thesis aims to assess the performance of three indoor positioning technologies, including a hybrid system consisting of cameras, magnetic positioning systems, active RFIDs, and Bluetooth, in both experimental and real-life scenarios. To achieve this goal, we will delve into each technology's history and current state in the upcoming sections. As mentioned, these systems have enormous applications for IoT, robotics, and day-to-day life.

Figure 2.1 presents various technologies and their typical range of applications. Some of these technologies are used for larger ranges, such as GNSS, LoRa, Cellular Networks, UWB, and WLAN. Naturally, these technologies have a larger range of accuracy as well. Among the local range technologies, in this thesis, we designed two systems based on Bluetooth Direction Finding (BLE-DF) and active RFIDs, as presented with red stars in the figure. The achieved accuracy by the active RFID system is withing still within the range of its common application. However, the BLE-DF being a novel technology, exceeds the expected ranges of accuracy and performance of traditional BLE, which enables the user to take advantage of this technology in a whole new range. We also proposed a hybrid system based on magnetic positioning and a camera, which is not presented in this figure. This is because the main criteria for exploring the performance of such an access control system is not the accuracy by cm but the precision of allocating the RF and the camera information to a person. Both individual parts of this system are functioning within the typical range presented here.

In particular, the next sections will focus on the historical development of radio frequency (RF) and magnetic field technologies for indoor Positioning Systems (PS). We also will discuss the use of Bluetooth for indoor positioning applications. These methods have evolved significantly over time, and their coverage and accuracy will be discussed in detail.

2.3   Radio Frequency (RF) Technologies

This technology utilizes RF signals and infrastructures to determine the position of a person or object for tracking and navigation purposes [16]. Inherent properties of RF enable signals to penetrate walls and obstacles, leading to a wide coverage area [4]. Attracting many researchers, the RF positioning system is categorized as a proximity detection and RSSI measurement system. Utilizing the triangulation, trilateration, or fingerprinting techniques [17].

Table 2.1 presents several study cases of different RF-based systems and their accuracy ranges.

Table 2.1: Technologies Main Characteristics Comparison [7, 18, 19, 20, 21]

Technology	Accuracy	Cost	Power	Operation Range	Limitations
UWB [22, 23, 14, 24]	Centimeter level	Medium-High	100 - 300 mW	Hundreds of meters	NoS operation
WiFi [25, 26]	Medium-High	Medium-High	10-15 dBm	Hundreds of meters	Low accuracy
Bluetooth/ZigBee [27, 28, 24]	1m - room level	Low-Medium	-25 - 10 dBm	room level	Multipath
Cellular-based	Hundreds of meters	Low-Medium	20-40 W	Order of kilometers	Require LoS
Magnetic Fields [29, 30]	Centimeter level	Low	0.1 - 100 W	5 to 6 meters	Limited time and space

This table aims to show some of the states of the art about discussed technologies during past decades and compare their performances in different categories. As per application, certain columns of this table might have more importance than others. For instance, power consumption is a critical key for a mobile IoT device. The range of power consumption for each technology varies depending on the characteristics of the devices; however, this value remains in a typical range presented in the table 2.1.

Ultra Wide Band (UWB) is a short-range, high-speed RF technology, and compared to narrowband RF signals, these signals offer superior range resolution [31]. In fact, coupled with Time of Arrival (ToA) or time-difference of arrival (TDoA) measurements, the UWB technology consents an accuracy of a few centimeters over several hundred meters of operating range in Line of Sight (LoS) conditions. However, due to the use of higher frequencies, it is affected by Non-LoS conditions and cluttered environments [32]. Practical measurements of UWB systems in NLoS environments demonstrate meter-order position errors for a system range of about 20 m [31]. Even though recent developments have decreased the system's cost [4], the complexity of the hardware and power consumption considerations are considered the main drawbacks of this technology for commercial use [4, 20, 33, 5]. For example, in [24], the average UWB transmission consumption is ≈ 280.5 mW, which is high for many IoT applications.

2.3.1 RFID

The main purpose of RFID technology is to transfer and hold data through electromagnetic transmission from a transmitter to any circuit that is compatible with Radio Frequency (RF). A typical RFID system comprises a reader that can establish communication with RFID tags. These tags emit data that can be read by the RFID reader through a predefined RF protocol, which is known beforehand to both the reader and the tags [7], [34].

RFID positioning systems are commonly implemented using ultra-high-frequency (UHF) or surface acoustic wave (SAW) systems. UHF RFID systems work by measuring either the backscatter from a passive tag or the received signal strength (RSS) of an active tag [35, 20]. These systems typically operate in the 900 MHz industrial, scientific, and medical (ISM) band, but their signals can be heavily absorbed by lossy objects in practical environments, leading to meter-level errors in range measurements [36]. In recent years, new possibilities have emerged by using lower frequency tags such as [37]. On the other hand, SAW RFID systems operate at 2.4 GHz and face similar challenges as UHF RFID systems [38, 39]. In addition, SAW systems suffer from significant errors in multipath environments due to their reliance

on the time-of-arrival (TOA) localization approach [40]. These systems are divided into two main groups active and passive RFIDs. Nowadays, RFIDs are being used in a wide range of applications.

- **Active RFID** technology typically uses Ultra High Frequency (UHF) and microwave frequency range to transmit their ID and is connected to a local power source. These RFID devices have a considerable range and can operate at distances of up to hundreds of meters from the RFID reader. They are commonly used for object tracking and localization due to their low cost and the ability to be embedded in the tracked objects. However, active RFID technology cannot achieve sub-meter accuracy and is not widely available on portable user devices [36, 38, 39, 40].

- **Passive RFID** technology operates without a battery and has a limited communication range of $1 - 2\ m$. They are smaller, lighter, and more affordable than active RFID technology and can operate in low, high, UHF, and microwave frequency ranges. While passive RFID tags can serve as an alternative to barcodes, their limited range makes them unsuitable for indoor localization. They can be used for proximity-based services using brute force methods, but this would require changes to the existing procedure of transmitting an ID to identify and track the RFID [41, 42].

These are a typical use of active and passive RFIDs. However, in recent years a new category has emerged that it's a hybrid of both active and passive systems and uses electromagnetic principles. These systems function at a low frequency of $125\ kHz - 134\ kHz$ and are based on near-field magnetic coupling as mentioned in [43]. These systems can be a solution for harsh environments also it is prone to multipath. This emerging technology is a hybrid between an electromagnetic-based system and RFIDs. Even though the concept of an electromagnetic field is not new, the possibility of using this system with smaller coils and transmitting certain information for localization is new. These systems, like RFIDs or Near-field communication (NFCs), are based on proximity. So we categorized it into the group of RFIDs. This emerging technology benefits from certain characteristics that are only feasible with low frequency and in the near-field region of the coils. These systems can be activated in the proximity of the transmitter. Therefore, it can be categorized as a semi-active RFID system. In this thesis, we are using this technology for positioning, and we categorized it into an RFID system for the two reasons mentioned above. However, one can argue that these systems can fit into a completely separate category. Whatever the category, this system's principles remain the same.

To the knowledge of the author, this method has been barely used for access control in literature. However, this solution has many uses in cases where positioning is required in harsh environmental conditions, such as a target that is buried in snow or exploring a target in the ground [44, 45]. For these applications, usually, the device is bigger in size and also costly. However, with the advent of smaller coils, the possibility of creating a new system based on this technology with lower cost and smaller size is feasible now, which is the main reason

we could take advantage of low frequency. This solution, paired with a visual aid such as a camera, can be used for surveillance or access control in many scenarios. This is one of the main causes of our study in Chapter 3.

2.3.2 Magnetic Positioning Systems

Using magnetic fields for positioning purposes dates back to ancient times when compasses were used for navigation. In 1979 a study by [46], which is still relevant, used magnetic signals for positioning within a magnetic field. Utilizing a fixed three-axis magnetic dipole source as transmitters and a three-axis magnetic sensor as receivers, the receivers receive magnetic signals from the transmitter and send the position information to a centralized location for position determination. 20 years later, [47] focused on increasing the speed of the positioning and tracking system by using two-axis generation of a quasi-static rotating magnetic dipole source and a three-axis magnetic sensor. By excitation of the source magnetic field, the sensors obtain the position and, thus, enable 5 degrees of freedom (DOF) position determination and increase in the tracking speed [48].

Later, in 2011 in [49], they categorized the magnetic PS as static and low-frequency alternating magnetic fields (dynamic). A year later, other variations of these magnetic field types, such as artificial magnetic field and electromagnetic field, were added by [33]. Also [33] mentioned are systems using antennae near the field and creating magnetic fields from currents and systems using magnetic fingerprinting. A magnetic field is generated with permanent magnets or coils using AC or DC in the static or artificial magnetic field. In the low-frequency alternating or electromagnetic magnetic field, static charges produce electric fields and currently produce magnetic fields to form the electromagnetic field.

Utilizing active magnetic coils in 2012, [50] developed a 3D indoor positioning system based on DC artificial magnetic fields to locate a mobile device. The system's accuracy depends on the signal quality of the coil's magnetic field. Also, if the range between the sensor and the mobile reference point is too large, the accuracy and performance of the position estimation are degraded [16].

Several commercial AC magnetic tracking solutions exist in the market now. For instance, Polhemus system [30], [51] and AmfiTrack [52], offer sub-millimeter accuracy in the range of centimeters. In recent years these systems have been used for many different applications depending on their precision and range. For instance, [29], used this system as a finger tracker that is being used for Augmented Reality (AR) or Virtual Reality (VR).

2.3.3 Bluetooth Low Energy

Bluetooth Low Energy (BLE) is a wireless communication technology designed for low-power consumption and short-range communication. BLE operates in the 2.4 GHz ISM band and offers a data rate of up to 24 $Mbps$, making it suitable for a wide range of applications,

including those that require high-speed data transfer. The naming conventions for Bluetooth technologies have changed over the years and still cause confusion to this day [53]. Classic Bluetooth refers to before 2010 when the Low Energy variant doesn't exist. In 2010 Bluetooth Special Interest Group (SIG) introduced Bluetooth Low Energy or Bluetooth 4.0 which includes both classic and Bluetooth LE [54]. The Bluetooth 4.1 - 5.2 released by SIG includes both Bluetooth Low Energy and classic Bluetooth. BLE has a range of up to $70 - 100$ meters, which is significantly longer than the range of classic Bluetooth. Unlike classic Bluetooth which is only used for audio streaming, BLE can be used for data transmission, location services, and device networks.

In general, BLE contributed to the creation o the Internet of Everything by having two main principles. According to the Bluetooth Specialist Interest Group, there will be a 1.62 billion annual shipment of Bluetooth devices in the next five years. 112 million asset tracking devices will be shipped by the end of 2023. This highlighters presence of Bluetooth devices in our daily lives. BLE devices can communicate with off-the-self smartphones and access points within a range of 10 m. Bluetooth Low Energy, which carries the Low Energy title, provides communication at lower budgets [55].

BLE can be used for indoor localization using various techniques such as the Received Signal Strength Indicator (RSSI), Angle of Arrival (AoA), and Time of Flight (ToF). Most of the existing BLE-based localization solutions rely on RSSI-based inputs because they are less complex. BLE devices are used for tracking livestock [56], finding lost objects [57], enabling navigation in shopping malls [58] and etc.

The power consumption of the BLE modules varies based on the used modules and the type of communication. For example, the average power consumption of BLE radios when using the minimum (7.5 ms) connection interval, was estimated in [59] to be $\approx 10mW$. In the case of a connection event as a slave, the average current draw during connection with 1000 intervals in ms is 0.010mA. Which is the case mostly being used for BLE Direction Finding.

2.3.4 RSSI-based BLE Localization Systems

It is essential to understand that Bluetooth technology and RSSI measurements have been used for indoor positioning for quite some time. For example [60] achieves 2 m with RSSI and trilateration in specific conditions, or [61, 62] used fingerprinting methods for BLE direction finding. These calculations were merely based on RSSI measurements. [63] used legacy Bluetooth devices for AoA/AoD applications, demonstrating the system's compatibility without extra hardware. All of these techniques are based on BLE technology. The limitation of RSSI-based systems is that they suffer from inaccuracies due to signal attenuation and multipath interference [64, 65]. The BLE-RSSI-based positioning method can only meet the meter level accuracy which does not offer certain satisfaction to some applications [66].

While very common, RSSI-based methods typically fail to provide sub-meter precision. Re-

Figure 2.2: Apple AirTag using UWB and BLE v5.1 for tracking and localization

cently, fingerprinting methods or neural networks are used to improve their precision, which inherently requires high computational power and prior knowledge of the environment. For instance, in 2020 [67] addressed accurate indoor localization of people visiting a museum equipped with a Bluetooth Low Energy (BLE) device, and using a feed-forward neural network trained by a measurement campaign in the considered environment and on a non-linear least square algorithm achieving $< 1\ m$ accuracy.

Top technological companies have proposed several prominent technologies based on BLE. iBeacon (by Apple Inc.) and Eddystone (by Google Inc.) have been proposed for context-aware proximity-based services for a decade now. These protocols use BLE technology to transmit location-specific information to nearby devices, enabling them to provide relevant services and information to users based on their location.

In April 2021, Apple Inc. released Apple AirTags [57]. These AirTags (figure 2.2) use a combination of Bluetooth Low Energy (BLE) version 5.1 and ultra-wideband (UWB) [22] technology to provide both connectivity and localization capabilities. Even though this technology is not using BLE RSSI, it is worth mentioning because of the effective combination of a series of RF technologies. In this technology, the BLE is mainly used to communicate with nearby devices, such as an iPhone or iPad, to determine their approximate location. Due to the ability of BLE v5.1 called BLE mesh. The UWB is used for localization. By analyzing the time difference of arrival of the signal at different points, the AirTag's location can be determined with greater accuracy. While providing accurate results, this hybrid technology is expensive and relies on the paired device GPS.

2.3.5 BLE Direction-finding-biased Localization Systems

In late 2019 Bluetooth Direction Finding was introduced as a new protocol with BLE v5.1. LE direction finding can be a key to the next generation of accurate, low-power indoor positioning solutions [68]. For decades, BLE localization systems relied on Received Signal Strength Indication (RSSI) [27], while BLE direction-finding invoked new opportunities [26], [9], [55]. Direction estimation or angle estimation generally is a more accurate positioning solution

than RSSI-based methods. Direction finding is a well-established practice that has been used since from early twentieth century, with radio direction finding supporting aviation and wildlife tracking. GNSS most promising outdoor positing system also uses the same principle for positioning.

In Angle of Arrival (AoA), the transmitting device is usually used as the asset's tag, while the locator or anchors are fixed and have multiple antennas. BLE- AoA use cases are asset tracking and ID location of people and staff. Angle of Departure (AoD), is called Indoor GPS [69]. In this scenario, the locator device can be simpler in terms of hardware design but does have software complexity for the determination and calculation of the direction-finding functionality [70]. This technology has some strong uses including in wearables and smartphones. Some scenarios where this can be used are wayfinding, Point of Interest (PoI) Information Solutions, and value asset search and find. This is why we decided to take advantage of this new technology's new possibilities.

Table 2.2: BLE-DF state of the art

Name	Antenna and Modules	Method	Precision	Time	Power
[8]	TI BOOSTXL [71], TI CC2640R2F [72], nRF52811	AoA, Calculating Phase Difference (PD) between the slots	Phase difference error of 0.19°	Needs 360ms to evaluate the Phase difference in all directions in 1° steps	PD sensitivity of the CC2640R2F under different input power levels are studied
[24]	TI BOOSTXL [71], TI CC2640R2F [72]	AoA, Outdoor environment with no obstacles	overall mean error of nearly 25°	Not mentioned	BLE radio power is ≈ 10mW
[73]	TI BOOSTXL [71], TI CC2640R2F [72]	AoA, Indoor without LOS, Using Convolutional Neural Network (CNN)	87% accuracy in a range of $5m \times 5m$	Not mentioned	Not studied
[74]	None, Simulated data	AoA, Using Deep Neural Network, 4 anchors and 3 channels	70cm precision in a room of $14m \times 7m$	Not mentioned	Not studied
[75]	None, simulated data	AoA (1μs), Using Multiple Signal Classification algorithm (MUSIC) and Neural Network and Gaussian Process	Achieving 3° with Gaussian Process in the range $(0°, 20°)$	40ms with Gaussian Process	Not studied
[76]	Software Defined Radio, customized 4-element array antenna	AoA, Multiple Signal Classification (MUSIC) algorithm	overall error exceeds 4°	Not-mentioned	Not studied

Among literature, [9] presents the advantages of direction-finding over Time of Arrival (ToA) and details about this technology. Recently, BLE-DF was utilized in [24] to achieve an accuracy of 25°. In this study, they compared the performance of UWB and BLE AoA and argued that adding more antennas to the structure could improve the accuracy. The same study [24] indicates that the average power consumption of the BLE radios is 28 times less compared to the UWB solution. This fact is a strong indicator that BLE-DF is a suitable technology for many IoT applications.

[8] introduced a method for calculating the Phase Difference (PD) between slots in received BLE data, with an error of 0.19° for all 1° steps. However, this approach requires a lengthy evaluation time of 360ms to obtain accuracy in all directions, which arguably is not in the range of a real-time system (presented in table 2.2). This work [8] also studied the PD sensitivity

(a) SiliconLab antenna array [77]   (b) BlueIot vision of AoA gateways [78]
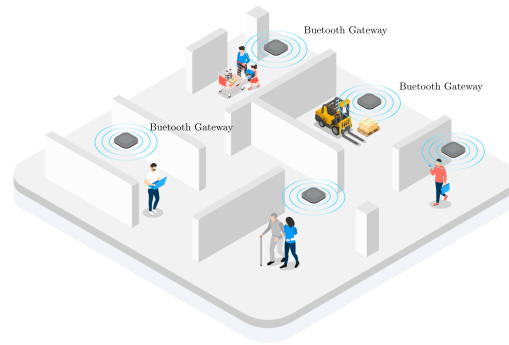
Figure 2.3

with respect to the input power of the TI CC2640R2F module. The study revealed that the PD sensitivity remains constant until approximately $-81dBm$ indicating the PD is independent of the power for higher power bonds.

Table 2.2 presents several studies about BLE-DF that have been done with different methods and their reported precision and estimated time to process the data. This table shows the state of the art of BLE-AoA. The antenna arrays and the BLE modules for each case are presented. The power consumption is studied in the first two cases however more information about the power consumption of the modules is provided in [72].

Using Neural Network models can improve the precision of estimation as presented in [74] or [73]; however, the computational power is demanding and can deteriorate the real-time functionality of the system. [75], uses several methods such as Neural Networks, Gaussian Process, and Regression Tree to process the estimated angles AoAs using Multiple Signal Classification (MUSIC) algorithms. The Gaussian Process achieves the highest accuracy, and the Regression Tree can reach slightly lower precision in 1.4ms. But this method's performance at higher elevation angles and low SNR values makes it less suitable for practical applications [75]. [76] presents a customized 4-element array antenna controlled with a software-defined radio and performs both simulations and experiments. The overall accuracy in the range of $(0°, 90°)$ exceeds $4°$. This thesis studies both AoA and AoD configurations and focuses on presenting a real-time solution.

In another recent study by [55], Channel State Information (CSI) based method is used to accurately estimate the BLE tag's location. In this study, they created stable pulses to obtain a stable frequency obtain meaningful phase and amplitude measurements and then used the Channel State Information (CSI) to estimate the location of the tags. In this study, an accuracy of 98 cm is achieved. Even though this study still does not use BLE Direction Finding, the principle of creating stable pulses is very similar to the BLE-DF protocol.

In industry, there have been several interesting progress that are worth mentioning. For

instance, Silicon Labs recently [77] claims to achieve sub-meter accuracy using BLE-AoA/AoD with an array of 16 antennas. Figure 2.3a shows this antenna array. BlueIot [78] is now producing AoA gateways with sub-meter accuracy and with software that maps the indoor space in detail and tracks the movements. Figure 2.3b shows the company's vision for using BLE gateways in an indoor space.

BLE-DF is a relatively new technology and is in its prime phase. The studies about this technology are yet to be flourished. This thesis aims to use this technology and create a basis for the future application of this technology as a real-time positioning system. The new opportunities that are brought by BLE-DF can alter the concept of indoor positioning.

After understanding the recent improvements in the technological front, it is important to address the different methods being used for localization. Therefore, in the next section 2.4, we will elaborate briefly on the existing methods and their typical use. In this thesis, depending on the technology and the measurements, we use different methods for localization. In particular, we use two different structures and angle estimation methods. This thesis does not aim to explore the power consumption of the devices. Because these assumptions have been studied for standard BLE-DF application in [59]. Yet, in Chapter 3, after explaining the basis of BLE-DF, the power consumption of the BLE modules will briefly be discussed. Implementing algorithms for the respective technology and angle estimation comprises chapters 3, 4, 5, and 6 of this thesis.

2.4 Positioning Algorithms

In general, localization techniques can be categorized into two main groups: range-based and range-free. Range-based methods utilize distance or proximity information, while range-free methods estimate location based on other factors, such as signal strength or angle of arrival of the signal. Within these categories, there are various techniques, such as RSSI, TDOA, AoA/AoD, and CSI. Machine learning-based methods like k-Nearest Neighbors (kNN) and Support Vector Machine (SVM) are usually used to improve precision. Each technique has its own advantages and disadvantages and may be more appropriate for certain applications or environments.

- *Received Signal Strength Indicator (RSSI)*: RSSI-based localization techniques use the signal strength of wireless signals (such as Wi-Fi or Bluetooth) to estimate the location of a device. RSSI values are affected by the distance between the transmitter and receiver, as well as obstacles and interference in the environment. To estimate a device's location, a database of RSSI fingerprints is created, where each fingerprint contains the RSSI values measured at different reference points in the environment [79]. The location of the device is then estimated by comparing the RSSI values measured by the device with the fingerprints in the database [80].

- *Time Difference of Arrival (TDOA)*: TDOA-based localization techniques use the time

difference between the arrival of signals at multiple receivers to estimate the location of a transmitter. TDOA requires precise timing synchronization between the receivers, and the time difference between signal arrivals is affected by the distance between the transmitter and receivers [81]. TDOA is commonly used in wireless sensor networks or cellular networks as Time of Arrival (ToA) [82].

- *Angle of Arrival (AoA) / Angle of Departure (AoD)*: AoA/AoD-based localization techniques use the angle of arrival/departure of a wireless signal to estimate the location of a device. AoA/AoD requires an antenna array at the receiver or transmitter, and the angle of arrival/departure is affected by the position of the device relative to the antenna array. AoA/AoD is commonly used in radar and wireless communication systems [83, 84].

- *Channel State Information (CSI)*: CSI-based localization techniques use the variations in the wireless channel caused by the presence of objects in the environment to estimate the location of a device. CSI requires multiple antennas at the receiver or transmitter, and the variations in the wireless channel are affected by the position of the device relative to the antennas. CSI-based localization techniques can provide high accuracy but require complex signal processing [25, 85].

- *Learning Based techniques*: Learning methods are used widely on top of localization techniques to improve the precision of localization. Neural network-based localization techniques use machine learning algorithms to estimate a device's location based on the RSSI fingerprints measured at different reference points in the environment. Neural networks can learn complex patterns in the RSSI data and can provide high accuracy but require significant training data and computational resources [86, 87, 88]. kNN-based localization techniques use the RSSI fingerprints of the k-nearest reference points to estimate a device's location. The location of the device is estimated by averaging the locations of the k-nearest reference points. kNN-based localization techniques are simple and require minimal computation but can be sensitive to outliers in the RSSI data [89, 90].

In summary, different localization techniques have their own strengths and weaknesses, and the choice of technique depends on the application's specific requirements of the technology being used. RSSI-based techniques are commonly used in indoor positioning due to their low hardware requirements, while TDOA and AoA/AoD are commonly used in cellular and wireless communication systems. CSI-based techniques can provide high accuracy but require complex signal processing, while machine learning-based techniques such as neural networks and Support Vector Machines (SVM) can learn complex patterns in the RSSI data and provide high accuracy with significant training data and computational resources. These methods require huge computational power; therefore, they might not be suitable for real-time applications as it creates latency on the estimated position. In this thesis, depending on the technology, we used different position and angle estimation methods that will be discussed thoroughly in the upcoming chapters.

2.5   Summary

This chapter establishes the history and state of the art in indoor positioning systems and their applications for IoT, industry, and daily life. Also, it highlights some of the main technologies that are the concerns of the thesis, such as using RFID, magnetic positioning, and Bluetooth systems for positioning. Later, we present different methods of positioning that will be used based on the technology in the following chapters. The details of these methods and their implementations are the subjects of this thesis.

3 Non-blocking access control

Indoor positioning has the potential to revolutionize a wide range of applications and industries, including retail, healthcare, transportation, and public safety. Some potential applications of indoor positioning include:

- Location-based services and advertising: to deliver location-specific information and advertisements to people based on their location within a building or other enclosed space ([91], [92]).

- Asset tracking: to track the location of valuable assets within a building or warehouse, helping to improve efficiency and reduce the risk of loss or theft ([93], [94]).

- Wayfinding: to help people navigate within a building or other complex environment, improving safety and convenience ([88], [95]).

- Emergency response: to help first responders locate and assist people in need during an emergency situation, improving response times and saving lives ([96], [97]).

- Access control: to provide a more secure and efficient way to manage access to a facility and prevent unauthorized access ([98], [99]).

Understanding the importance and the requirements of a well-designed indoor positioning system in our future lives motivates us to explore this topic in the Internet of Things world. In this chapter, we propose two different indoor positioning systems. First, we introduce a new active smart card. We characterize the smart cards' distance and RSSI relationship with our designed transmitter for various ranges and options. With this method, we achieve a practical formulation for our specific configuration that we later use as a reference for location estimation. In the next step, we estimate the position of the smart card in a series of defined experiments. We use an out-of-the-shelf transmitter system with known characteristics to concentrate only on the smart card's functionality. We use three transmitters and a smart card to estimate the position and gather the data in real-time for future processes. We use two different methods of location estimation, Trilateration, and a Neural Network model.

The next proposed system, which is a complex system composed of RF (EMF system) and Visual parts (depth camera), is also presented. We designed a lightweight algorithm to merge these two data sources and form a unified system. This system also is tested with the same confinement and consideration of our previous study. In conclusion, through our designed experiment condition, we compare these two proposed systems and their functionality as an indoor positioning system.

In this chapter, we use access control as an example of indoor positioning to evaluate the functionality of our systems. We verify their functionality as a non-blocking access control gate. Non-blocking access control with indoor positioning systems allows multiple people or devices to access location-based services or resources simultaneously. These systems improve the efficiency and speed of access to the resources as users do not have to wait their turn to access them, which enhances user experience and increases the pace of the process. Because of this rapid nature, the system must function in real-time, handle multiple users, and manage access to the shared resource and data structures. All of this makes it an interesting study case for evaluating the functionality of our proposed systems.

This chapter explains the process of creating the proposed indoor positioning system and several methods to evaluate its function in each step. Therefore, we explain some important information about smart card technology which starts with a general understanding of the RFID systems and then our proposed system in the next section 3.1.

3.1   Radio Frequency Identification

Radio Frequency Identification, or RFID, is an automatic identification process that uses Radio Frequency (RF) wireless communication technology based on electromagnetic transmission between RFID readers and RFID tags for tracking and/or identification purposes [100]. The tags are classified into passive and active tags [101]. An active tag powered by a source, typically a battery, will provide a more comprehensive transmission range. In contrast, the passive tag has a shorter range and responds to the reader signal after being activated by one. This system can track and determine the position and orientation of the tag via radio waves. Nowadays, passive tags are part of daily lives and are used in many bank cards, road toll tags, and portals for monitoring cargo goods.

In indoor positioning, RFID tags can be used by attaching them to people or objects and using RFID readers to determine their location [102]. However, because active RFID tags have a more extended range and lifespan, they are more suitable for extended battery life or a longer communication range, such as non-blocking access control or location-based services and asset tracking.
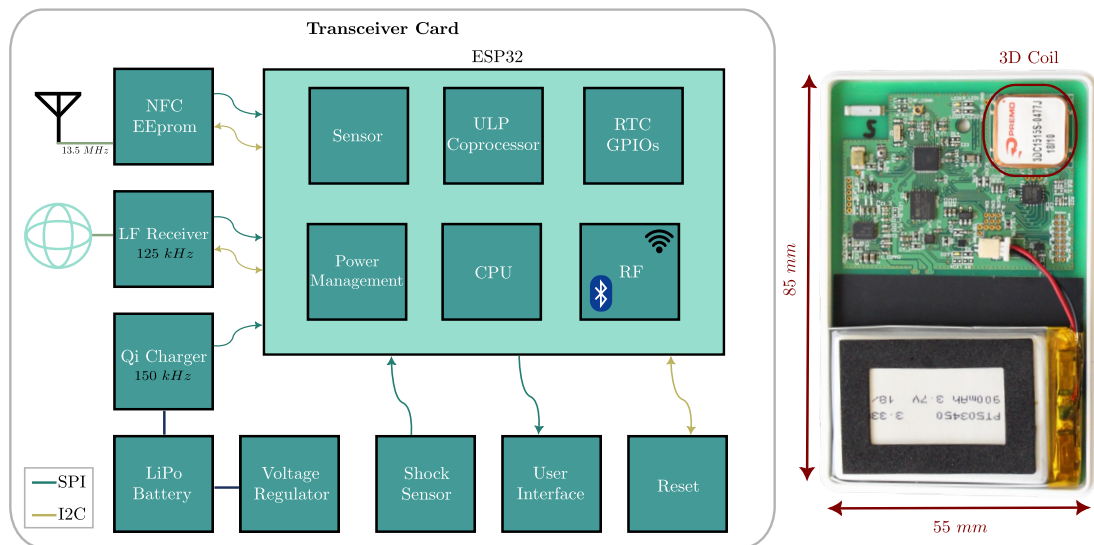
Figure 3.1: The transmitter card on the left and a block diagrams schematic of the units inside the card on the right

3.2 The Active RFID system

With technological advances, active tags are increasingly being used for various purposes ([102], [103]). The primary concern with the active tags is power consumption. As a result, the introduction of wake-up chips enables researchers to explore this concept more.

To address the discussed problem, this work presents an active RFID tag as a mobile transceiver. Three fixed coils are fed by a transmitter module to create a modulated magnetic field. The tag will be activated in this magnetic field. As mentioned in Chapter 2, this tag is categorized into active RFID systems.

The tag is used as a mobile node to communicate remotely with the reference points and the server. This module consists of three 125 kHz antennas as a receiver, an AS3933 [104] wake-up chip (the LF receiver in the figure 3.1), an ESP32 [105] microprocessor, a 2.4 GHz antenna for WiFi, a Qi charger module, a shock sensor, and a battery. The module is covered in a 3D-printed custom case (figure 3.1). The size of the tag is as big as a credit card. Conveniently, we call the module 'card' (figure 3.1). Each one of these cards is connected to the network via WiFi.

Using the 125 kHz receiver brings the possibility of sleep and wake-up mode for the system; simultaneously, a modulated magnetic field wakes up the nodes from 125 kHz transmitters dissipated in the environment. The magnetic field will wake up the AS3933 chip. The AS3933 chip is a 3D low-frequency wake-up Amplitude-Shift Keying (ASK) receiver with three channels that generates a wake-up upon receiving a signal which uses low-frequency (LF) carrier frequency between $15 - 150$ kHz using an integrated correlator. The chip detects a programmable 16-bit or 32-bit Manchester wake-up pattern (figure 3.2). We are using the
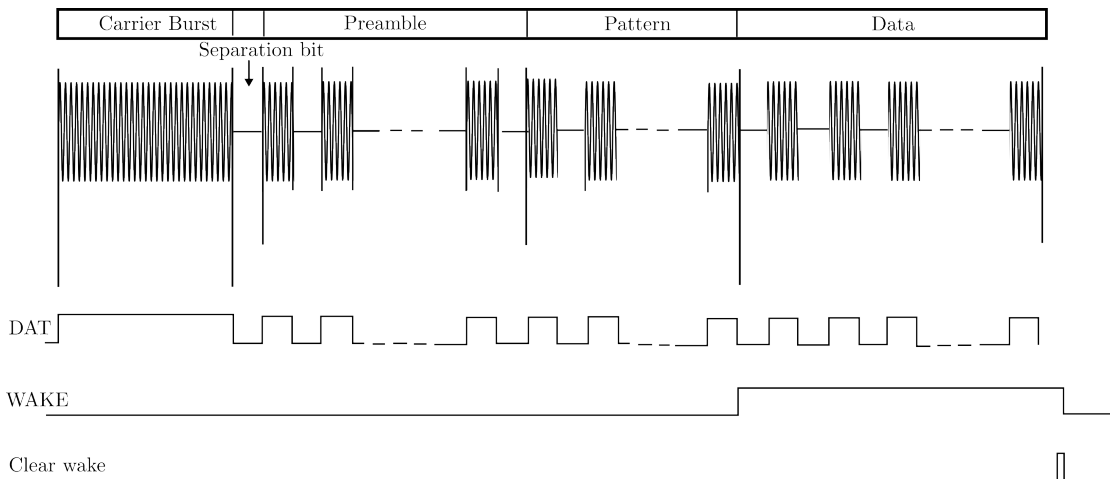
Figure 3.2: The *AS*3933 chip wake-up pattern

32-bit pattern. The device can operate using one, two, or three active channels. The *AS*3933 provides a digitized Received Signal Strength Indication (RSSI) value for each active channel. The programmable features of *AS*3933 optimize its settings for achieving a longer distance while retaining a reliable wake-up generation. The sensitivity level of *AS*3933 can be adjusted in the presence of a strong field or noisy environment.

Each of the 3 channels consists of a Variable Gain Amplifier (VGA) with Automatic Gain Control (AGC) and a frequency detector. When the *AS*3933 is in listening mode (waiting for RF signal), the gain of all channel amplifiers is set to maximum. The frequency detector counts the zero crossings of the amplified RF signal to detect the presence of the wanted carrier. As soon as the carrier is detected, the AGC is enabled, and the gain of the VGA is reduced and set to the correct value. The RSSI represents how strong the input signal is, and it is the inverse representation of the gain of the VGA.

3.3   Transmitter

In general, RFID tags function in four primary frequency ranges according to Industrial, Scientific, And Medical (ISM) radio bands: Traditionally, the LF-RFIDs are passive tags, and this frequency is readable when attached to objects containing water, human/animal tissues, metal, wood, or liquids. We are introducing an active LF-RFID. With the use of wake-up transmitter chips, we take advantage of the abilities that only LF-RFIDs can provide. This approach also adds the excess advantage of an active RFID tag, which is the higher range while taking advantage of low power consumption.

Our transmitter module consists of three 125 kHz antennas. The transmitter generates a modulated magnetic field in each antenna by recreating the wake-up pattern (figure 3.2). The LF tags have no or limited anti-collision capabilities; therefore, simultaneously reading

Frequency Bands	radiation	Range	Power	Application
Low Frequency (LF) 125 KHz - 134.2 KHz	near-field inductive coupling	short ($< 1.5\ m$)	passive	Access Control, Animal Tagging, Inventory Control, Car Immobilizer
High Frequency (HF) 13.56 MHz	near-field inductive coupling	short ($< 1\ m$)	passive	Smart Cards Item Tagging Proximity Cards
Ultra High Frequency (UHF) 433 MHz - 860-960 MHz	far-field radiative coupling backscatter coupling	Medium $4-6\ m$	passive, semi-passive	Asset Tracking Localization
Microwave 2.45 GHz - 5.8 GHz	backscatter coupling	Long $4-100\ m$	active, semi-passive, passive	Container Rail Car, Auto Toll Roads, Tracking

Table 3.1: RFID characteristic overview based on operating frequency [106]

multiple tags is impossible or very difficult [107]. With the use of a modulated magnetic field, we overcome the problem of simultaneously reading multiple tags.

The transmitter module (figure 3.3) consists of three relays [108] that each can carry up 1 A of current to drive three emitter antennas. The emitter antennas are not represented in the picture. These antennas are connected by wires to the transmitter module. We are using three KGEA-BFCR antennas [109] that are designed for the emission of an LF magnetic field. These antennas are the same as the AMS (AS3933-DK) [110] system antenna, which we later used for testing and validation. We use a $ESP32$ development kit version 4 to control the relays and generate the modulated magnetic field. The signals to derive the antenna switches are imposed by a delay of 1.2 μs for each MOSFET bridge [111] to derive antennas.

3.4   Smart card Design and Validation System

To mount several identical nodes for the designed Internet of Things (IoT) platform, it is critical to validate and test each module beforehand automatically. As mentioned, the card consists of several essential blocks which should be checked to verify its functionality. As a result, a testing module is designed. This module is designed to check specific features of the card, such as the battery state, the shaker, the antenna, and external pins to check the signals and important Input/Output (I/O) from the controller. A shaker was added to test the shocks or movement sensor. This shaker allows generating of vibrations that must be detected by the card. The shock sensor on the card also saves energy and puts the system to sleep when it is not moved. Measurements of the current and automatically flashing the cards is another
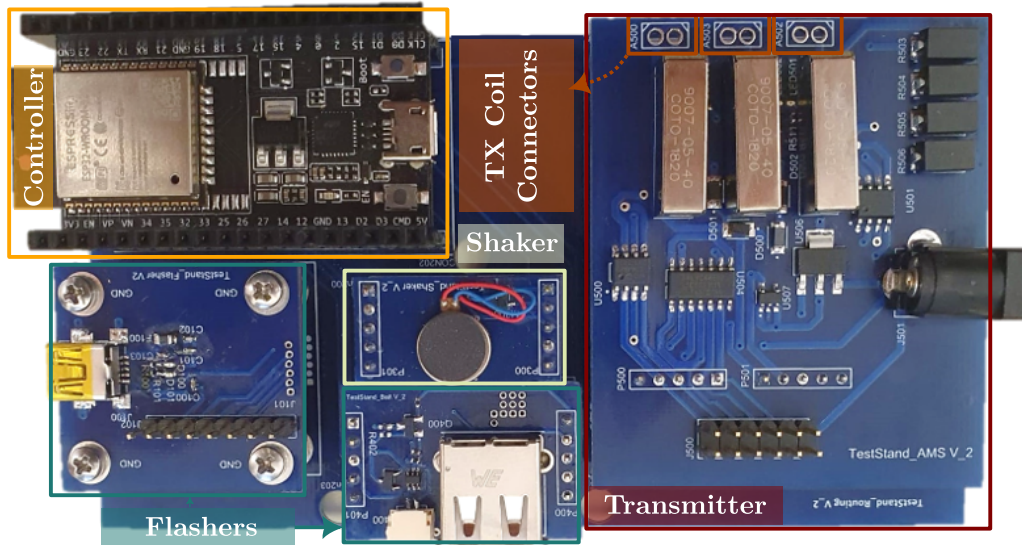
Figure 3.3: The transmitter module (red), the shaker (light green), the flasher (green), and the controller (yellow) for testing and validation. The connectors to the transmitting coils are presented by dark orange blocks

allocated task of the testing module (figure 3.3).

3.4.1 Test and Verification of the Smart card System

In the transmitter (TX), the $AS3933$ chip gives control over gain reduction and antenna damper. The gain reduction feature tightens the frequency detection tolerance, and the antenna is a set of internal resistors that can be connected to the external resistors, which allows the chip to deal with higher strength. The shunt resistors degrade the quality factor of the external resonator by reducing the signal at the input of the amplifier. In this way, the resonator sees a smaller parallel resistance (in the band of interest) which degrades its quality factor to increase the linear range of the channel amplifier (the amplifier does not saturate in the presence of larger signals).

We defined an experiment to calibrate and verify the functionality of the smart card (RX) and the transmitter. In these experiments, we defined the relationship between the Received RSSI and the distance from the transmitter for every different setting option of our transmitter. These measurements will later function as a basis for trilateration process of estimating the tag's position.

RSSI measures the strength of a wireless signal at a particular location. It is typically expressed in decibels (dB) and is used to indicate a wireless signal's power relative to a reference value.

We tried to calculate the best linear fit for different settings by changing the antenna damper

and gain reduction. In the transmitter, we get the RSSI value as a digitized value between $0-31$ for each channel. Within the near field of an electrically small antenna, the propagation relation for like antennas (electric-electric or magnetic-magnetic) antennas is given by expression [112]:

$$\frac{P_{RX}}{P_{TX}} = \frac{G_{TX}G_{RX}}{4}(\frac{1}{(kr)^6} - \frac{1}{(kr)^4} + \frac{1}{(kr)^2})$$ (3.1)

This implies that the ratio of the received power (P_{Rx}) to the transmitted power (P_{Tx}) follows from the receive antenna gain (G_{Tx}), the transmit antenna gain (G_{Tx}), the distance (r) between antennas, and the wavenumber ($k = 2\pi/\lambda$). For indoor environments, typically, the first two terms are dominant. On the other hand, a corridor can act as a waveguide, resulting in path loss with the $\frac{1}{(kr)^2}$ to be dominant [5], [113].

In the Near-Field region of the 125 kHz coils, the inductive coupling between them enables the $AS3933$ to wake up the $ESP32$ and to receive an RSSI value from each channel in the chip. The maximum available power (P_r) of the receiver in the near field depends on the transmitted power (P_t), the permeability of the air μ_0, the number of turns of TX and RX coil (N_t and N_r respectively), the radius of the two coils (R_r and R_t respectively), the frequency ω, and the distance between the two coils d [114].

$$P_r = P_t \frac{\mu_0\pi^2 N_t^2 N_r^2 r_t^4 r_r^4 \omega^2}{16R_t R_r (r_t^2 + d^2)^2}$$ (3.2)

Suppose we assume that there is no phase difference between the generated field of the source coil and the sensor coil, thus by modifications of the (3.1) so that we have $RSSI = 10lg(P_{RX})$. The measured data by the $AMS3933$ enables us to find a linear relationship between the recorded RSSI value and the position of the card. This relationship is modeled by:

$$RSSI = -10nlg(d/d_0) + A + X_\sigma$$ (3.3)

Where d is the distance between the receiver and the transmitter, n is a parameter related to the specific wireless transmission environment. A is the RSSI value in the position of d_0, and the final term (X_σ) is a Gaussian distributed random variable with the zero mean and variance of σ^2.

We tried to calculate the best linear fit for different settings by changing the antenna damper and gain reduction. In the tag, we get RSSI as a digitized value between $0-31$ for each channel. By changing the specifications of the tag, we are able to decrease or increase the operation range of the tag and its resolution. The goal is to find the optimal value for both the gain and the antenna damper so as to use the system in a range of approximately 1 m. As a result, an experiment was set to move the tag away from one antenna and then measure the RSSI value every 10 cm. This experiment provides basic information about the operation range of a single tag and an antenna.

Using linear regression and the moving average method, we tried to fit the RSSI value to the

	−4 dB		−8 dB		−12 dB	
Resistance ($k\Omega$)	3	9	3	9	3	9
R	0.04	0.00	0.09	0.41	0.65	0.095
S	-1.32	-0.26	-2.28	-2.86	-15.37	-2.60
I	-13.83	-13.48	-14.80	-14.02	-12.11	-14.42
Std	0.55	0.48	0.68	0.32	1.47	0.77

Table 3.2: The table presents the best linear fit for various antenna damper ($3 − 9\ k\Omega$) and gain reduction ($(−4, −8, −12)\ dB$ options for $RSSI_1$ vs. $20lg(d)$

	−4 dB		−8 dB		−12 dB	
Resistance ($k\Omega$)	3	9	3	9	3	9
R	0.25	0.02	0.14	0.40	0.52	0.00
S	-3.98	-1.15	-2.07	-7.49	-9.19	-0.60
I	-13.63	-11.78	-15.15	-12.46	-13.11	-12.73
Std	0.66	0.95	0.48	0.87	0.84	1.03

Table 3.3: The table presents the best linear fit for various antenna damper ($3 − 9\ k\Omega$) and gain reduction ($(−4, −8, −12)\ dB$ options for $RSSI_2$ vs. $20lg(d)$ linear fit

logarithmic value of the position. Table 3.2 demonstrates the fitted values of the $RSSI_1$ and the distance. In this fit, The R is the r-value of the fitted linear curve while S and I are the values of the slope and the intercept of the fit. Finally, the standard deviation of each group is presented by STD. As the table clarifies, using linear methods cannot lead us to the best network estimation. We performed the same measurements for the $RSSI_2$ from the second coil.

These measurements and the fitted model aid us in choosing the best configuration for the next step of our experiment. We want to choose the character which is closest to the linear fit. These tables (3.2, 3.3) reveal that using the 3 $k\Omega$ damping factor and 12 dB gain reduction is the most linear setting in the range of approximately 1 m away from the coil.

To compare the theoretical and practical results, we designed an experiment in the range of 1.5 m away from the coil. The coil was placed vertically at the Z axis, while the tag was moved horizontally along the X axis. The tag's orientation stayed the same in all measurements. The experiment was performed in an RF-friendly environment with wooden structures to hold the coil and tag. In this measurement, the calibration was done at $d_0 = 1\ m$.

In this experiment, the RSSI value of the tag was recorded and then compared to the expected value of RSSI with the theoretical formula of eq.(3.2) for near-field. Using the equation eq.(3.2) the specifications of the coils at the receiver and transmitter side, it is possible to calculate the transmitted power at each coil. The RSSI value was checked for all 3 coils on the tag. Each coil corresponds to a certain direction. The receiver's coil at X and Y direction are nearly identical (figure 3.4a, 3.4b). On the other hand, the coil in Z direction (figure 3.4c) is slightly different in

(a)

(b)

(c)
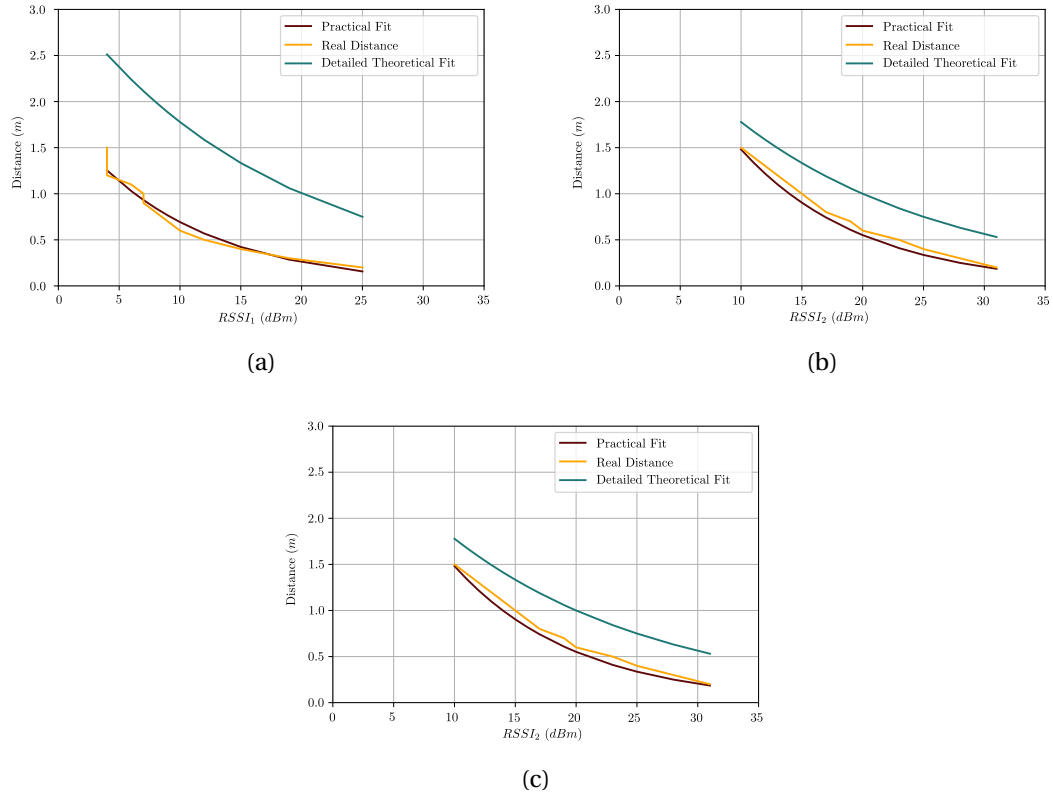
Figure 3.4: The digitized RSSI value vs. the distance from the antenna in meters from a) $coil_X$, b) $coil_Y$, and c) $coil_Z$ of the three different coils in the tag.

size; Therefore, the results are different.

The difference between the two theoretical equations and the practical measurements reveals that an empirical fitting is required in real-life experiments. The importance of this experiment lies in the fact that it proves that our designed RF system is capable of determining the location of an unknown tag position. Therefore the concept can be used for further analysis.

3.4.2 Experiment Set

We decided to design a new experiment to achieve the primary goal of designing a real-time indoor positioning system. For real-time tests and device validation, we designed a frame to accurately fix the antennas and collect data. We made a frame of 80 cm by 80 cm in width and length with a height of 2.5 m out of a metal-free composite profile of wood and plastic [115] able to move the card within the area and measure the RSSI value. We set the antennas at a fixed position as presented in figure 3.6 at the height of 1 m above the ground. We moved the tag every 8 cm along the X and Y axis, and we collected the data at a total of 100 locations within the XY plane of the gate.
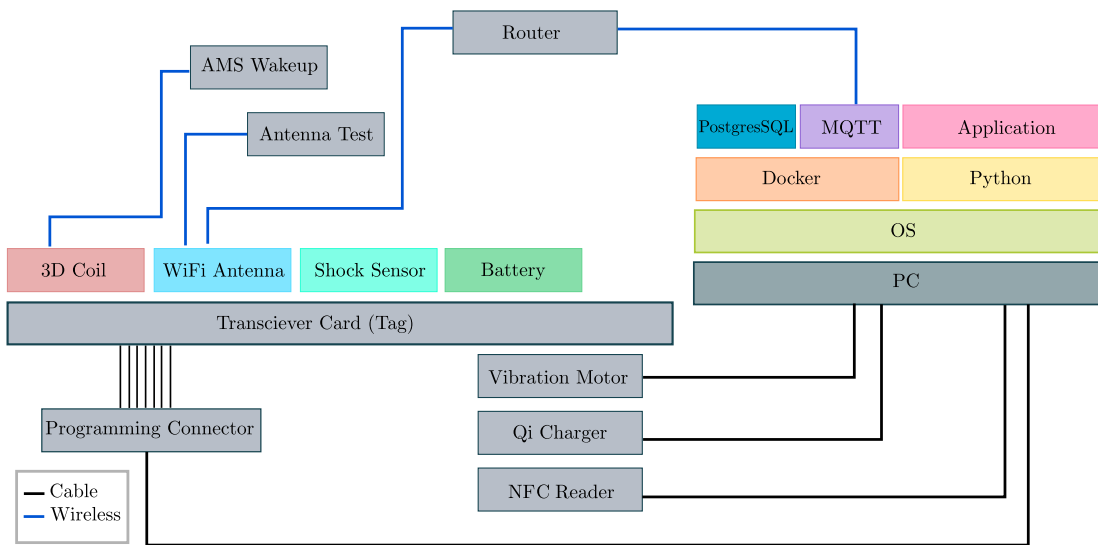
Figure 3.5: The block diagram of the system structure (test, programming, and the Card) and network architecture including the physical layer (wireless LAN, RF signals, and transceiver).

3.4.3 Database

In order to manage the data from the RF system, we collect and store the data in a structured form. First, all the information about the card position and its identity, and battery state is sent to a docker engine.

Docker is a set of Platform as a Service (PaaS) products that use Operating System (OS) level virtualization to deliver software in packages called containers. The advantage of using a docker is that the containers are isolated from one another and bundle their own software, libraries, and configuration files; they can communicate through well-defined channels. All containers are run by a single OS kernel and are thus more lightweight than virtual machines. We are using Eclipse Mosquitto [116], a lightweight open-source message broker that implements the Message Queuing Telemetry Transport (MQTT) [117] protocol versions 5.0, 3.1.1, and 3.1. Mosquitto is suitable for all devices, from low-power single-board computers to full servers. The MQTT protocol provides a lightweight method of carrying out messaging using a publish/subscribe model. This makes it suitable for IoT messaging, especially for embedded computers or microprocessors with low power consumption. Mosquitto also provides a *C* library for implementing MQTT clients (figure 3.5). Using a message broker like Mosquitto can help improve the reliability and scalability of an indoor positioning system, as it allows devices to communicate asynchronously and reduces the need for direct connections between devices.

The card (red box in figure 3.6) publishes a message to the broker, with the data to be processed consisting of the RSSI values of 3 antennas in 3 positions as described in figure 3.6. For each antenna in the receiver, we have 3 RSSI values in 3 channels. As a result, for a single position, the receiver, we have 9 values of RSSI. After receiving the data, we now proceed to estimate the
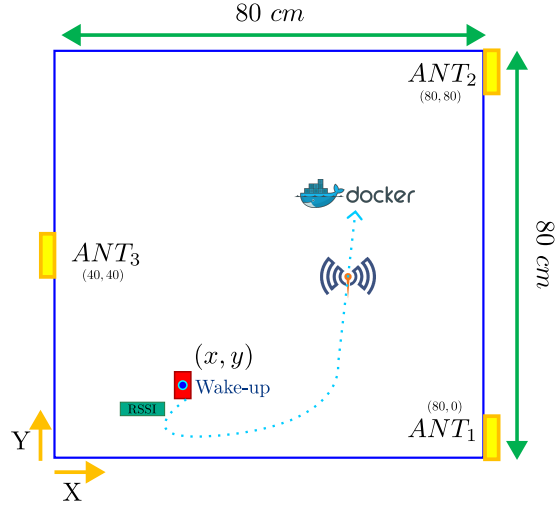
Figure 3.6: Top view of the antenna positions in a designed experiment for measurements

position of the target. In the next two sections, we are presenting two different methods that we used for position estimation. First, the Trilateration, and second, the use of a supervised artificial neural network.

3.4.4 Trilateration

Trilateration is a method to determine the position of a point based on the distances from that point to three known reference points. To find the most probable position of the tag, we used the least square as a standard approach in regression analysis to approximate the tag's position. Having at least 3 known anchor nodes with the coordinates of $(x_1, y_1), (x_2, y_2), ..., (x_m, y_m)$ and a blind node of the position (x, y). For our case with three antennas $m = 3$, and $x_i = [0, 80, 80]\ cm$ and $y_i = [40, 0, 80]\ cm$. The details of the antenna positions are presented in figure 3.6. To write the equations of the position of an unknown target in the area, we will obtain:

$$\begin{cases} (x_1 - x)^2 + (y_1 - y)^2 = d_1^2 \\ (x_2 - x)^2 + (y_2 - y)^2 = d_2^2 \\ \vdots \\ (x_m - x)^2 + (y_m - y)^2 = d_m^2 \end{cases} \tag{3.4}$$

In our problem, we would like to minimize the error in equation (3.4). Subtracting the mth equation from the first $m - 1$ equation in 3.4, the linear equation is obtained as $Ax = b$. Where A and b are:

$$A = \begin{bmatrix} 2(x_1 - x_m) & 2(y_1 - y_m) \\ 2(x_2 - x_m) & 2(y_2 - y_m) \\ \vdots & \vdots \\ 2(x_{m-1} - x_m) & 2(y_{m-1} - y_m) \end{bmatrix} \tag{3.5}$$
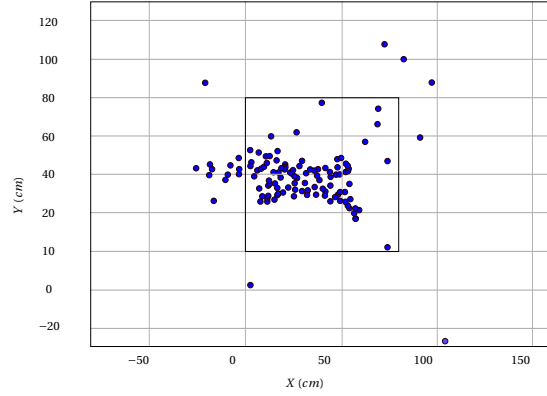
Figure 3.7: The estimated position of the card in 80 cm by 80 cm frame and at the height of 1 m from the ground of the test area by trilateration method. Each dot presents the estimated location of the tag. The tag was located at every 8 cm in the gate. The rectangle shows the boundaries of the gate area.

$$b = \begin{bmatrix} x_1^2 - x_m^2 + y_1^2 - y_m^2 + d_1^2 - d_m^2 \\ x_2^2 - x_m^2 + y_2^2 - y_m^2 + d_2^2 - d_m^2 \\ \vdots \\ x_{m-1}^2 - x_m^2 + y_{m-1}^2 - y_m^2 + d_{m-1}^2 - d_m^2 \end{bmatrix} \tag{3.6}$$

and Finally, by solving the equation due to linear algebra for X, we have:

$$X = (A^T A)^{-1} A^T b \tag{3.7}$$

As presented in figure 3.6, the card was moved point by point in a square of 80 cm by 80 cm at the height of 1 m every 8 cm. The RSSI where published and saved in a data set for further evaluation. Using the trilateration technique, by sampling a data set of 10 measurements in each position (total of 1000 measurements), we obtained an error of an average 5 cm in the X direction and 3 cm in the Y direction. However, the error sharply increases, especially on the edges. So, the standard deviation of the absolute error is approximately 34 cm for X and 20 cm for Y direction. Figure 3.7 demonstrates the estimated position of the card in a real-time experiment. As evident in the figure 3.7, by diverging from the center, the location estimation tends to be arbitrary; therefore, we decided to choose another method for localization (section 3.4.5). In fact, the RSSI vs. d relation is not linear at this range. This could also be predicted by the measurements in section 3.4.1 and figure 3.4. So, we are using a neural network to solve our non-linear problem.

3.4.5   Neural Network Model for Localization

The RSSI distance loss model is well known to be a nonlinear equation, making it challenging to map the RSSI value to the distance. Therefore, in this section, we used a Multi-Layer Perceptron (MLP) algorithm, which is the best trade-off between accuracy and memory requirements
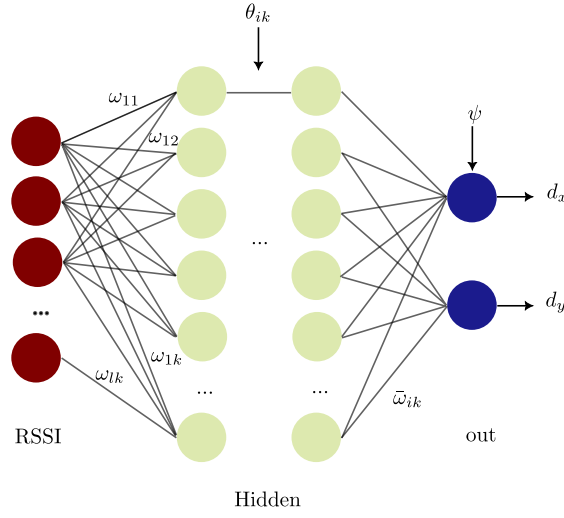
Figure 3.8: Neural network structure

among other types of neural networks [118] for localization. MLP is a supervised algorithm that learns a function by training on a dataset. The network with four-layer structure, including one input node, i hidden nodes, and $k = 2$ layer and one output node. We created the data set by collecting the RSSI data within the range of the gate, from every 100 positions by sampling twice as much as before in each position.

The training sample input value is $RSSI = \{RSSI1_{ANT1}, RSSI2_{ANT1}, ..., RSSI3_{ANT3}\}$ the training sample output is $D = \{d_x, d_y\}$. The MLP learns the function $f(x) = \omega_{lk} g(\varpi_{ik} RSSI + \theta_{lk}) + \psi$. As shown in the figure 3.8, ω_{lk} is defined as the weight from the input layer to the hidden layers. In contrast, θ_{lk} is defined as the threshold value of the hidden layer and ϖ_{ik} is the weight from the hidden layers to the output layer, and ψ is the threshold for the output. g is the activation function. We are using a linear (identity function) and a non-linear (Sigmoid) activation function that is defined as $S(x) = \frac{1}{1+e^x}$.

The MPL uses the Mean Square Error loss function and tries to minimize this function by repeatedly updating the initial random weights. Therefore, we can present the error of the jth output node in the nth data point by $e_j^2(n) = (d_j(n) - y_j(n))^2$ where d is the target value, and y is the estimated value by the network. This value is then used to adjust the node weights.

Figure 3.9 presents the results of the MLP algorithm by using a linear neural function. The red dots are the actual position of the card. Moreover, the blue dots are the estimated position by the network with an error of less than 3 cm. By using a nonlinear function, we tried to estimate the position. The exact figure presents the accuracy of this estimation.

As presented in figure 3.9a, 3.9b, the average error for Y direction is less than the same in X direction as a result of having twice as many antennas at Y direction in comparison to X.

Sometimes, the absolute or mean square error does not reflect particular conditions. In this
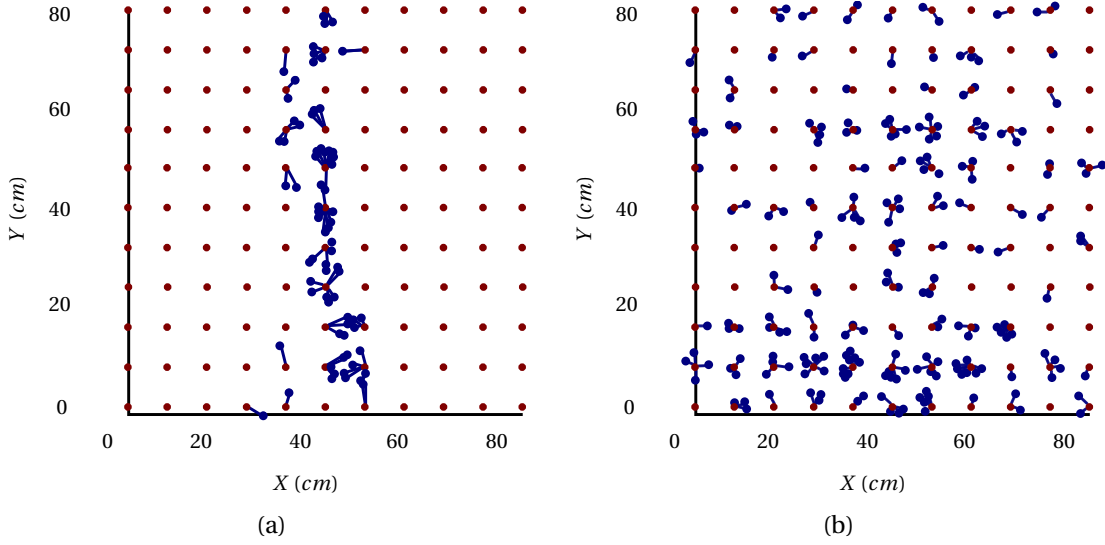
Figure 3.9: Estimated position of the tag with a) linear function and b) sigmoid function. The red points are the actual position of the card, and the blue dots are the estimated position by the network where the error is less than 3 cm.

particular case, the uncertainty is more significant where we have the reflection on the walls. This problem extends to the estimation that neural networks try to make. Therefore, we use table 3.4, to present the performance of various structures we tested.

Table 3.4 presents the percentage of estimates within each range described in the columns for some of the architectures tested. The values $\epsilon = 3, 5, 10, 15, 20$ indicate the maximum error range in cm and the values in the table are the percentage of hits within that corresponding range. In a neural network, the percentage of correct estimation within specefic range is calculated by the hit ratio. Where $H_j = \frac{1}{N}\sum_{j=1}^{n} P_j$. That P_j is the n^j estimation, and n is the number of test samples. Therefore, for each range, we have the following:

$$P_j = \left\{ \begin{array}{ll} 1, & e_j(n) > \epsilon \\ 0, & otherwise \end{array} \right\} \tag{3.8}$$

In the description of architectures, LI is the linear model, NL is the nonlinear model, LX is the number of layers, and HX is the number of neurons in each hidden layer. For example, for a maximum error range of 10 cm, with the linear model, 7 layers, and 30 hidden neurons, we reach to 18.5 hit percentage. As it is evident while considering a maximum error of 20 cm, a NL_L6_H40 network has the maximum hit. This means it is 67.7 % probability to estimate the position of the unknown target with an error of bellow 20 cm. This is a realistic estimate from the network structure.

As presented in figures 3.9a and 3.9b, using a non-linear neural network to estimate the unknown position of a tag in the area can lead us to more accurate answers. Using traditional trilateration techniques with the least square method will result in an average error of 27 cm

Table 3.4: Hit percentage in specific ranges within different architectures (XL_LX_HX)

Error Range ϵ [cm]	< 3	< 5	< 10	< 15	< 20
LI_L7_H25	2.6	4.6	17.4	29.4	42.5
LI_L7_H30	2.8	4.7	18.5	29.1	42.6
LI_L7_H35	2.7	4.7	17.6	28.8	42.7
LI_L7_H40	2.9	4.7	18.6	29.3	42.4
NL_L6_H25	4.8	10.4	27.2	42.0	56.9
NL_L6_H30	5.3	10.9	30.4	46.3	58.8
NL_L6_H35	4.4	11.3	30.3	50.0	62.0
NL_L6_H40	8.3	21.4	43.6	57.9	67.7

and 30 cm in directions y and x, respectively (section 3.4.4). Moreover, the absolute error of estimation for x and y direction for the least square method is below 5 cm, 3 cm (section 3.4.4). Note that having two antennae in the Y direction is the reason for more accuracy in the Y direction compared to X. A non-linear neural network can increase the estimation percentage for an error of 10 cm up to 60% compared to the linear network.

This study depicts the possibility of applying low-frequency active RFID systems for short-range and semi-enclosed environments. Moreover, benefiting from the magnetic coupling effect, this system can reduce power consumption because it will go to sleep mode if it is outside the transmitter's magnetic field range. This feature also creates another advantage. Because it reveals the presence of the tag, this feature can be a marker for checking the absence or the presence of tags in a defined area. This feature can be exploited for access control applications. As it is presented, this technology in this form, can not provide more accurate results. So, in the next section, we will present another system. The essence of our proposed system is similar to the electromagnetic field tracking systems in that they both use the same coil as a receiver or tag for the magnetic field.

3.5 Introducing a Hybrid Access Control Solution

The magnetic positioning system is one of the old ways of position determination that is still relevant today. In general, magnetic positioning systems involve using a magnetic signal within a magnetic field. There exist various kinds of this system, based on the ways that the magnetic field is generated [33, 119, 47]. This accurate system is applicable for short-range positioning for indoor and semi-enclosed areas. In areas with complex geometries and architecture, the multi-path fading, human body effect, penetration depth, and diffraction around the clutters are serious issues. In this regard, we are using an out-of-the-shelf system based on electromagnetic field (EMF) tracking, which is the same principle as the AMS system. This system does not suffer from Non-Line of Sight (NLOS) errors as for other technologies such as cameras, with a low frequency, the magnetic field can travel within the range of its application. There are no cameras to align, no special lighting required, and you don't need to

be in a field of view.

With the help of an electromagnetic positioning system and a stereo-based depth camera [120] in a zenithal position, we can describe an algorithm to detect the people crossing the camera's field of view and determine whether or not they have the RF tag in real-time. The whole system will complete our Real-Time Localization System (RTLS). First, we talk about each localization system individually. This includes an electromagnetic positioning system and a camera for person detection. Then the network structure is explained, followed by two merging algorithms and their performance. Later, we conclude the system as a whole and analyze it.

3.5.1 Electromagnetic Positioning Systems

Throughout time, there have been many articles in literature focusing on electromagnetic field positioning systems such as [121, 122, 123]. The studies have demonstrated that magnetic field-based localization performs better when considering the three magnetic field components. This can be crucial in scenarios with low magnetic field variability [124]. Taking advantage of several properties of the electromagnetic field positioning system, we are using a starter kit from AmfiTrack ™[52].

AmfiTrack is an embedded electromagnetic tracking system that provides $3D$ positioning with 6 Degrees of Freedom ($6DoF$). The system uses a $3D$ coil and a maximum of 3 sensors as an electromagnetic field source. Using this system benefits us with no NLOS problems, multipath effect, and deflection, which are common obstacles for indoor positioning. Moreover, the system provides movement orientation for each sensor. The system accuracy in the static condition is below 1 mm in position and less than 0.5° in orientation. The source is emitted through three different channels at different frequencies. The sensor receives the power intensity and the magnetic field phase and then converts them to digital data. The final position is then processed through a Kalman filter. The sensors benefit from a 2.4 GHz RF link to rapidly communicate the received information through WiFi [125].

3.5.2 Person Tracking with Camera

Camera-based systems are also widely used for detecting and localizing people and objects. In these systems, one or more cameras cover a respective area where people must be detected or tracked for indoor and outdoor applications. The position and type of camera play an essential role in the algorithm's robustness. For example, placing a camera overhead at a zenithal position instead of a frontal one reduces occlusion problems. Similarly, a depth camera can avoid errors due to illumination variation.

The collaboration with HE-Arc University of applied science has resulted in the design and development of a visual system using depth cameras to detect people walking in the designated area. In this system, two Realsense $D435$ [120] cameras were placed, one at 2.75 m (top camera)
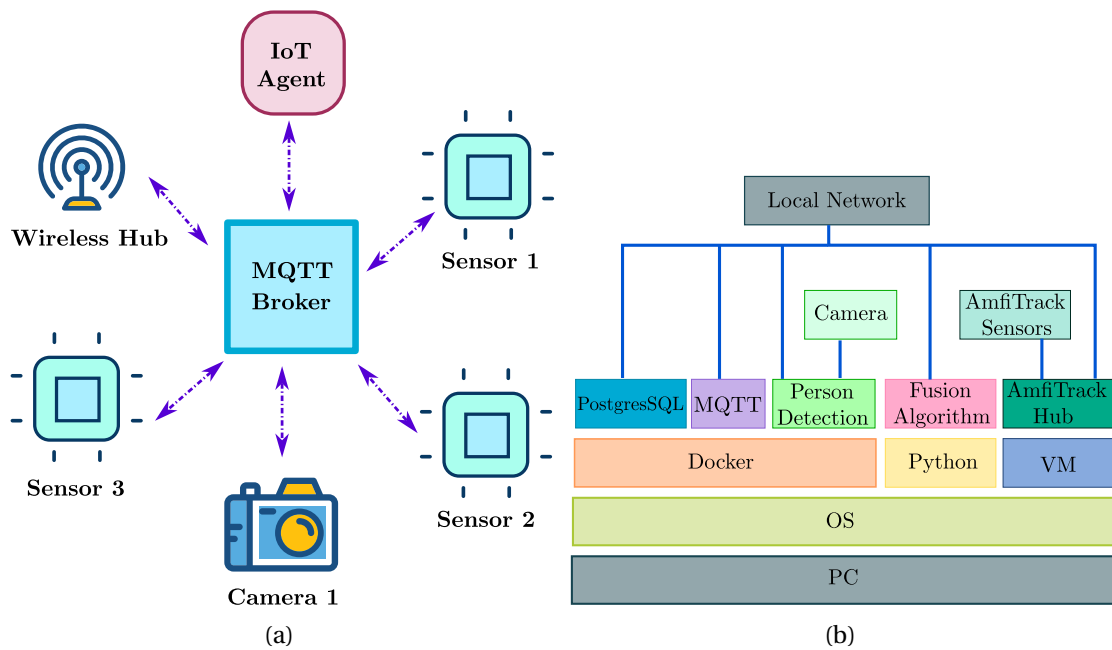
Figure 3.10: a) IoT agent communication with IoT devices via MQTT broker (sensors: Amfi-Track tags, the camera, wireless hub: AmfiTrack wireless hub). b) the system architecture. The camera algorithm is the person detection algorithm used by the camera. The fusion algorithm is the algorithm to merge the camera and the RF system data.

and another 2 m at the frontal position.

The top camera detects the people's heads. At each time instant, the results from the camera, along with a unique identification number (ID) for each person, are sent to the database using MQTT. Hence, the person's path is recorded, and the count of people passing under the camera is determined.

The frontal camera takes facial images of people passing under the camera and saves them in a local folder. The front camera is calibrated with the top camera for 3D. Hence, the person's position determined by the zenithal camera is passed to the front camera to take a picture. In the case of multiple people under the camera, it waits for the person to come in direct view of the front camera such that there is no occlusion and take a picture to store it locally.

3.5.3   Hybrid System Network Structure

As mentioned above, each sensor can send the position (6DoF) through an RF link. We use MQTT protocol standards for the Internet of Things (IoT). This extremely lightweight publish/subscribe messaging standard is designed to transport messages and connect remote devices with a small code footprint and minimal network bandwidth. We also use Eclipse Mosquitto as an open-source message broker that implements the MQTT protocol (figure 3.10).

Docker Application Programming Interface (API) is used to isolate various machines. This API is developed in collaboration with HE-Arc. The Docker runs all the services, including the database, camera, AmfiTrack firmware, and the MQTT broker. All these containers are connected through the Docker network by a bridge.

The architecture of the system is designed so that it can be run over a server in the cloud. For that reason, Docker with containers is used. Parts of the system are packaged in Docker containers. These containers can be run, stopped, and replaced on any system that has Docker capabilities. This also enables scalability and quick setup in new locations.

- There is the container with the PostgreSQL [126] database configured with tables for camera position data and AmfiTrack position data.

- The second container is the MQTT Mosquitto server. This takes care of the communication with JavaScript Object Notation (JSON) messages on the first level of the system. It relays messages from the camera, AmfiTrack, and the decision algorithm.

- The third container is running the camera image processing program.

- The fourth container is running the decision algorithm. After the decision, the algorithm takes position data from MQTT and sends a message back.

3.5.4   The Merging Algorithm

The system as a whole collects data from two parts and communicates through MQTT. Amfi-Track wireless Hub, working on a virtual machine over Windows 10, is publishing the position information of the AmfiTrack with a rate of $300 - 400$ $kbps$. On the other hand, the camera sends its information through MQTT with a maximum rate of 5 fps. These different transmission rates between the two systems impose specific constraints on our merging algorithm. In this algorithm, the AmfiTrack data is stored when the camera sensor detects a person to avoid an overload of data from the AmfiTrack every 8 timestamps. Most data association algorithms such as Global Nearest Neighbor (GNN) [127], Joint Probabilistic Data Association (JPDA) [128], and Multi Hypothesis Tracker (MHT) [129], require a fast rate of data update. Concerning the relatively low update rate of camera data in comparison to the AmfiTrack data, we are creating our own take of a classic Global Nearest Neighbor (GNN) algorithm with some twists.

Moreover, for our application, the prediction of the future state of the target has no use. For the primary phase, in an area of approximately 1 $m \times 1$ m, the physical constraints can be used in our favor. This means having more than three adult people in this area is physically impossible. As we collect the data simultaneously, the detected points from each data source are associated with their IDs.

In each timestamp, the camera will send a list of the collected observations from the surveillance area, and at the same time, the RF system will also send its collected data. Using the

merging algorithm, we associate the received data from the camera and the RF system. If a non-associated data point from the camera exists, this data is reported as an unauthorized person. Our algorithm uses the principles of a traditional Global Nearest Neighbor (GNN) problem. So, we are looking for the nearest neighbor for each observation from each data source. However, we do not intend to predict the trace of the person. We are only interested in associating the AmfiTrack data with the cameras'. Thus, a trajectory prediction is no longer required, and a simple data association is enough. There are several advantages of the link-layer fusion algorithm. For example, the modular design creates the opportunity to generate a specialized camera and RF solution. Moreover, communication is optimal by sending only the position information and the ID from each data source. Moreover, we are introducing some limitations to the algorithm in different scenarios which perfectly fit the physical constraints of our gate.

In general, accuracy is a concern for most link-layer fusion solutions. The accuracy of this method is firmly bound to the accuracy of each module. For example, if the AmfiTrack is exposed to soft or hard magnetic material, its accuracy will drop significantly. As a result, the overall accuracy of data association is affected too. This is an issue we will face in a real-life scenario very often. To solve the problem, we used the physical boundaries in each timestamp. The algorithm will check for the unauthorized person if there is a significant time difference between two sources when a person is moving outside the area to avoid the detection of false non-associated points. Regarding the gap between the update rate of the two sources, the problem does not fade completely. As a result, more considerations are required for the lower velocity of movements.

3.5.5 Application of k-nearest Neighborhood Algorithm

Primarily, we applied the k-nearest neighborhood algorithm to associate the clutters of data received by the camera and the AmfiTrack system to acquire a baseline sensation of the existing solutions. In our calculations, k changes are based on the number of detected persons by the camera system. This algorithm which is a computationally costly method creates considerable delays for non-static conditions.

Figure 3.11a presents the position of the detected person by AmfiTrack and the camera. In this figure (3.11a), each blue dot is the estimated location of the tag, and each red dot is the person's estimated position. Because the tag is usually kept in hand, a minor position difference between the camera position and the tag is inevitable.

Figure 3.11b presents each data cluster's position information of the k-Nearest Neighborhoods (k-NN). The algorithm clusters two data sets from the camera and the Amfitarck sensor. These calculations were done in a static condition where the targets were not moving. In figure 3.11b, the blue dots are the center of the clutters calculated by the k-NN algorithm. This method can associate the camera data with the RF data.
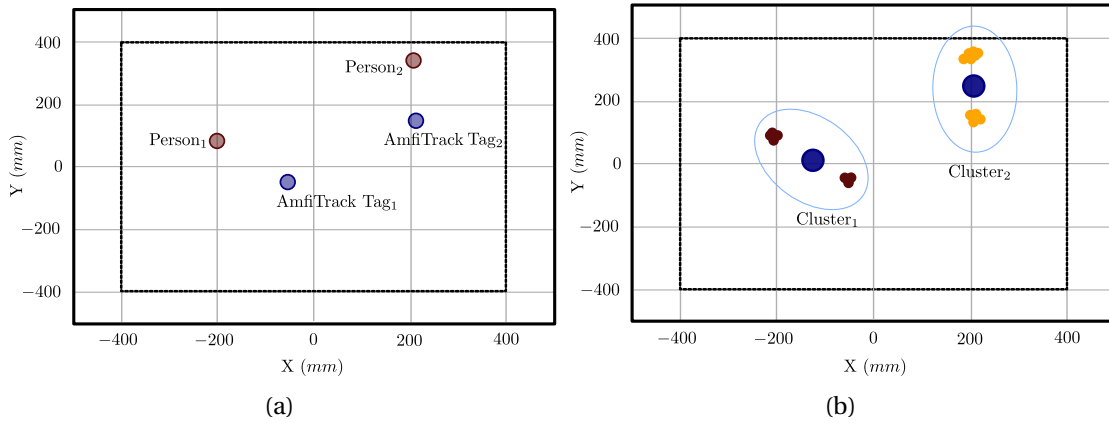
Figure 3.11: a) A snapshot of a real-time position of two people carrying AmfiTrack tags in their hands. The red dots represent the head position, and the blue dots present the AmfiTrack tag in each person's hand. b) The k-nearest neighborhood ($k = 2$) algorithm in static condition for associating the data from AmfiTrack and the Camera. The blue oval separates two clusters from one another. The inner rectangle shows the boundaries of the gate area.

The k-NN algorithm tends to show excellent accuracy in static or offline conditions. The accuracy is dependent on the number of clusters (K). However, the intrinsic behavior of predicting the future status of the input data creates considerable delays for real-time applications (in a range of > 10 ms). Therefore we observed that, for a real-time application where the tags are moving, we are unable to determine the accuracy of merging by this method. The computation cost is quite high because the algorithm needs to compute the distance of each query instance to all samples. That is why we decide to use our algorithm without a prediction step which does not require distance computation for each query. So, the calculations are not computationally expensive, and we will not face considerable delays in communication or detection.

3.5.6   Application of AmfiTrack Camera Comparison Algorithm

The following algorithm 1 tries to find each person passing through the limited test area. If a person passes without carrying the AmfiTrack sensor, the camera can detect her. As a result, the system covers all possible scenarios of various conditions when different people pass. This merging algorithm decides in real-time the status of each person passing through the test bed. The last 8 transmitted values of AmfiTrack and Camera are stored in a variable to keep track of the changes without the need to check the database. Thus, avoiding unnecessary delays the speed. Once a person without an AmfiTrack sensor passes through the test bed, her ID is sent through the MQTT to the broker. Then this ID is then used to reveal the person's face.

Assume that we have N data source with P_j observed position values from each source. Where $j = 1, 2, ..., j$ is the number of observations per timestamp. $D_{i1}, D_{i2}, ..., D_{ij}$ is defined as the hypothesis of associated formulations where observations $i1, i2, ..., ij$ come from the same

---

Algorithm 1 AmfiTrack Camera Comparison Algorithm

Ensure: MQTT Transmits data
 1: **while** Camera Data $\neq 0$ **do**
 2:     $P_{2j} \leftarrow$ Camera Position
 3:     **if** AmfiTrack = 1 **then**
 4:         $P_{11}, ..., P_{18} \leftarrow$ RF Position
 5:         $D_{ij} \leftarrow$ Euclidean distance
 6:         **if** $min(D_{ij}) < D_{lim}$ **then**
 7:             This person has AmfiTrack Tag
 8:         **else if** $(D_{2j}) < D_{lim}$ **then**
 9:             Found an Imposter
10:             Broker $\leftarrow$ Camera ID
11:             Local folder $\leftarrow$ person image
12:         **end if**
13:     **else if** AmfiTrack = 0 **then**
14:         Found an Imposter
15:         Broker $\leftarrow$ Camera ID
16:         Local folder $\leftarrow$ person image
17:     **end if**
18: **end while**

---

target source i. For our scenario, we only have two data sources, the AmfiTrack, and the Camera; therefore, $N = 2$, and we choose $j = 8$. Therefore D_{23} refers to observation 2 from source 1 (AmfiTrack), observation 3 from source 2 (Camera).

The algorithm calculates the Euclidian distance between the ith AmfiTrack sensor and the jth person detected by the camera (D_{ij}). Then the algorithm checks for the minimum distance at each interval. If this minimum is inside the area, the jth person is carrying the ith AmfiTrack sensor. If not, and this person is inside the area, this person is passing without the AmfiTrack sensor. As a result, the algorithm can distinguish several people in the area and their respective AmfiTrack sensors.

Since in each data set, we receive the ID information from the person and the AmfiTrack sensors; it is easy to distinguish between each point in a given timestamp. However, the classic issue of any GNN-based algorithm appears when two or more AmfiTrack sensors and a person are too close. In this case, associating each AmfiTrack sensor with a specific person is impossible. For example, 3 person and 2 AmfiTrack sensors exist, and one person is too close to another. Because in every interval, one of these distances will be the minimum. Since this algorithm is designed to function in real-time and static scenarios to solve the problem, we can not simply rule out one of the people once the first decision is made. So, we decided to introduce new limitations to the algorithm. Thus, once the minimum of D_{ij} is more than the threshold and this person is moving outside the surveillance area, the algorithm decides and picks the first person who leaves as an unauthorized person as we are using this system within certain physical boundaries the solution functions accurately enough. We also have time
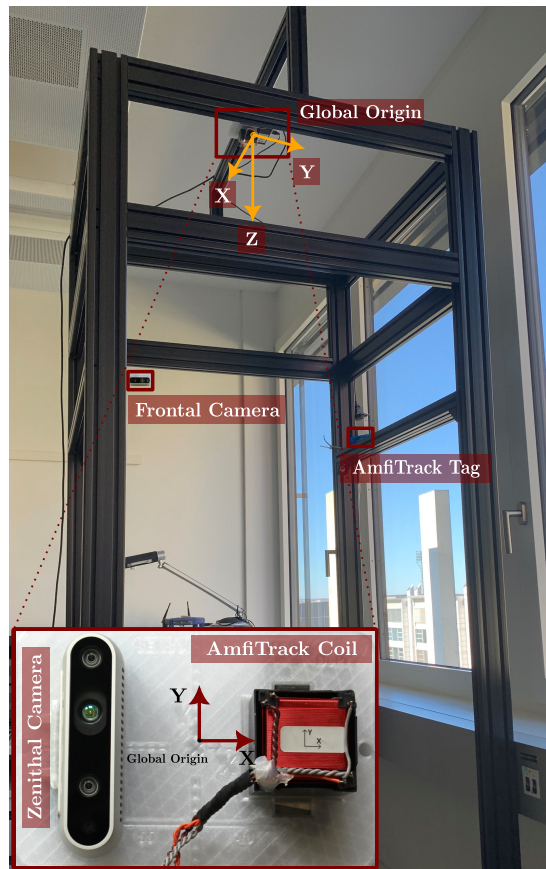
Figure 3.12: The area of interest for the localization test. The location of both cameras and the AmfiTrack source is marked. A zoomed picture of the global origin and the 3D printed stand for the zenithal camera and the AmfiTrack coil is also added.

limitations for our algorithm. It means that if the second person is detected after 8 intervals ($t_0 = t_0 + 8$), the sensor belongs to the previous person. The time confinement aligns with the number of data points we save in the initial step.

3.5.7 The test setup

We devised a setup to test the whole localization system, as shown in figure 3.12. In an area of 80 $cm \times$ 80 cm and a height of 2.75 m, the camera and the AmfiTrack source are installed. The camera's origins and the AmfiTrack system are calibrated concerning a global origin figure 3.12. AmfiTrack source is placed at a 1.1 m from the ground, and both cameras and the global origin are at the same height. The structure is designed so more than one person can pass through or stand inside the area. Another critical aspect of the structure to consider is that the whole structure is made from an RF transparent material [115].

The goal is to determine anybody within the area. As a result, the camera plays as a complementary rule even when a person without an electromagnetic field sensor passes through the
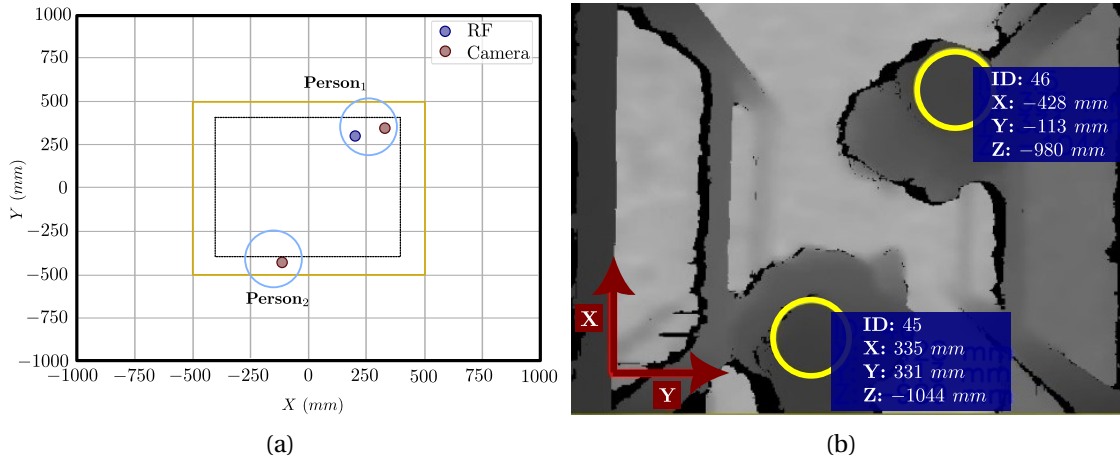
Figure 3.13: a) showing the detected people with the camera (red points) and the AmfiTrack system (blue points), and b) the top view of the camera, which detects human heads. The second person moving through the area does not carry any AmfiTrack sensor with her. The yellow rectangle presents the area of interest for the camera.

area. In the first step, we tried to minimize the error between the calculated position from the camera and the AmfiTrack system. As we are using a virtual global origin, most of the calibration between these two systems could be solved by addressing the difference between the local origin of both cameras and the AmfiTrack with the Global origin.

Finally, the camera can detect people with an accuracy of less than 5 cm. In comparison, the accuracy of the AmfiTrack system is less for static conditions. The distance between the source and sensor is from 10 cm to 3 m, which provides a wide range of applications.

3.5.8 Results

As depicted in figure 3.13b, the people's head are shown by red dots. The blue dot is the position of the AmfiTrack sensor. A black rectangle limits the area of interest. The yellow area is the barrier defined as a threshold transient area. As shown in the scenario, the first person with a camera ID of 41 is walking with the AmfiTrack sensor in her hand. While at the same time, the second person with a camera ID of 42 enters the area, having no AmfiTrack sensor. In both cases, the camera detects the person and sends this information to the database.

The face of each person passing under the camera is saved locally. The person's face is revealed if the person is not carrying an AmfiTrack sensor. It is essential to remember that the AmfiTrack position may be the hand position of a moving person or the sensor's position when placed inside someone's pocket. As a result, we defined a margin of $D_{ij} = 20$ cm for the difference between the estimated position by the camera and the AmfiTrack system. This means that if the Euclidean distance of the camera position and the AmfiTrack position is less than 20 cm, we are assuming that these two measurements are pointing at the same person.

Table 3.5: Confusion Matrix

		Actual	
		Non- Associated	Associated
Predicted	Non- Associated	42	2
	Associated	4	52

Table 3.5 presents the results of 100 cases of people passing through the surveillance area. The AmfiTrack sensors were all placed close to the chest of these people being held in their hands. The tests were done in real-time conditions, and the values were recorded each time people passed through. We checked various scenarios. This confusion table gives us very important information about these 100 cases where we deliberately tried some marginal conditions. For example, if two people with one sensor were passing or a case where two people were passing too closely at the same time through the area (For example, an adult holding a baby). The accuracy of the test is 94%, and we had a 4% error. Moreover, the sensitivity of the test is 91.3%.

The system differentiates people from moving or static objects. Moreover, the merging algorithm is just as accurate as its constitutive, i.e., the camera and the AmfiTrack system. We tried two different methods to merge the data. Using a K-NN algorithm and our lightweight GNN algorithm. This algorithm can provide accurate and fast results (section 3.5.6).

However, the whole system requires further examination and experiments for more complex scenarios with more people and sensors. Such as increasing the surveillance coverage area of the camera and the number of sensors simultaneously. For example, in a case where an adult person is holding a pet or a baby, the surveillance system is not capable of distinguishing the difference as well as the fact that because of the proximity of these two targets, the algorithm may not be able to allocate a tag to the right person. Therefore, the algorithm also requires some modifications. For example, we can propose an adaptive method that the D_{ij} that can vary based on certain variables such as the size of a human body detected by the camera.

3.6   Summary

Initially, this chapter explored the possibility of using a new smart card system based on a modulated magnetic field transmitter and a 3D coil receiver. We performed some initial tests and validation to evaluate our designed smart card and gather proof of concept for using it as a positioning system. To validate the functionality of the smart card, we also designed a test system. We tested the system with two methods of trilateration and a neural network. The system's overall performance is within the range of a positioning system with an accuracy of below 0.5 m. This range is the desired range for most access control or location-based systems.

Nowadays, RFID systems for access control are very common. Since most of these systems are based on passive RFID tags, a blocking gate is required. However, with the smart card, the

concept of a blocking gate no longer exists, which provides freedom of mobility for the targets. The targets now can be mobile robots moving in a warehouse or even people trying to enter different facilities. This system is also low energy because, unlike traditional active RFIDs, it only functions once in the magnetic field's proximity. It is also possible to recharge the battery with a wireless charger, which makes the whole system durable. The smart card remains an outstanding concept for location-based systems because it will only activate where it receives the wakeup pattern.

The smart card can correctly estimate around 70% of the received signal with an accuracy of 20 cm. Yet, it requires several modifications for more accurate results. Such as improvement in the transmitter and the receiver coils to create a more linear range for the system. Another factor that can be improved is using more transmitters in a wider area so as to have at least two transmitters in the linear range of the RSSI vs. d relation at all times. As it is clear, using bigger receiver coils with more power is unsuitable for a portable IoT device, but for other applications, it might be interesting. Moreover, the improvement in the usage of various localization algorithms can also be a determinant factor in the calculation process. For example, creating a bigger dataset of a larger area or using other neural network structures can possibly improve the performance of the smart card system. With this technology's limitations, our proposed method is in the expected accuracy range (< 50 cm) and provides additional value, such as being low-power, chargeable, and durable. However, the system fails to function in specific conditions. For example, the smart card is linear in a limited range, affecting its performance out of this range. The smart card system uses low frequency, which allows sending signals through dense materials such as water, ice, or walls without propagation of deflection. Still, it is not prone to huge metallic bodies, which will create limitations for some indoor applications.

Due to the above-mentioned, we decided to explore the possibility of creating another positioning system based on an EMF tracking system (AmfiTrack) combined with a visual system. The tag's coil in this system is the same as the smart card; however, one uses 3 transmitter coils (AMS system), and the other uses a 3D coil source (AmfiTrack source). This fundamental difference between these two systems creates a difference in the accuracy of the whole system. The AmfiTrack system constantly sends information, while the smart card only activates in special conditions. On the other hand, the AmfiTrack system, being a development kit for positioning systems, provides interesting features such as 6DoF and very high accuracy 3.6 at static conditions. It also takes advantage of an Interial Measuring Unit (IMU), which can enhance the system's performance. With the aid of a depth camera, we created a new positioning system.

With the same limitations as our previous experiments, we tested our hybrid system in a non-blocking gate. As mentioned before, this real-time system is capable of detecting people's heads and their tags crossing along the surveillance area. The electromagnetic positioning system utilizing very low frequency does not suffer from multipath fading effects, which are very common for indoor and complex areas. On the other hand, this system is inherently

Transmitter	Receiver	Accuracy	Considerations	Range (m)
AMS system	Smart Card	2D 67.7% at $\epsilon < 20\ cm$	sensitive to bulk metallic structures	up to 2.5 m
Electromagnetic Field	AmfiTrack	6DoF static $< 1\ mm$	sensitive to bulk metallic structures and body	up to $2.5 - 3\ m$

Table 3.6: Summary of main characteristics of two positioning systems

vulnerable to solid metallic bodies because they affect the area's magnetic field. One of the ways to overcome this vulnerability is to fingerprint a map of the area of interest and use this map to position the sensors (tags) accurately. However, this method is robust only for a static environment where the interested area's topology is not constantly changing. We plan to use other techniques to improve positioning accuracy for more dynamic situations.

Regarding the inherent distortion of the magnetic field in close proximity to substantial solid metallic bodies, we considered essential modifications for the RF system. The tags are sensitive to the human body, which has a huge impact on the accuracy of the received signal. This fundamental limitation adds up to the fact that this system requires extra infrastructure for its users (humans or robotic) to function. Moreover, since this system is based on 3D coils, it is physically impossible to decrease the size of the tags, which can be an issue in special mobile scenarios. Therefore, in the next steps of our research, we explore another technology. We decided to use a technology that is more accessible and compatible with most IoT devices. Where the user won't need an extra device for localization and the locating anchors (transmitters in this case), uses some of the more common existing technologies such as WiFi or BLE.

4 Angle Estimation and Antenna Array Design

The aim of this chapter is to answer the following questions: what is a direction finding and why are we using it for indoor positioning? What are the various methods of direction finding and which one suits the best, especially for access control and tracking solutions? What are the hardware requirements to perform direction finding and how do we deliver this requirement?

As mentioned in chapter 1, we plan to explore the principles of direction-finding methods. Therefore, first, we explain different direction-finding methods and their advantages and disadvantages. Second, we explain the principles of the new protocol of Bluetooth Direction Finding (BLE-DF) and this technology's important and deterministic aspects. Third, we explain the physical principles of angle estimation and the signal model of three different shapes of antenna arrays we used during our study. We explore different angle estimation algorithms and their signal model in the next section. Later, we present the requirements to design a specific antenna array for the BLE-DF protocol. Finally, we present an antenna array that we used and two arrays that we designed specifically for direction finding via BLE-DF.

4.1 Introduction to Direction Finding

Direction finding (DF) is one of the methods used in indoor positioning systems to determine the direction of arrival (DoA) of a signal from a known source, such as a wireless access point or a beacon. Direction finding (DF) techniques have a wide range of applications, including indoor positioning, navigation, target localization, hospital and emergency services, asset tracking, surveillance, etc. This can be used to triangulate the position of a device, such as a smartphone or a tablet, within a building. Some indoor positioning systems use a combination of techniques to improve accuracy such as Received Signal Strength Indicator (RSSI) and Angle of Arrival (AoA) or Time Difference of Arrival (TDoA).

The choice of technique will depend on the specific application and factors such as the environment, the type of signal, and the required accuracy. Generally, solutions to the direction-finding problems can be divided into two categories: 1) spectral-based methods, which include

Bartlett, Multiple Signal Classification (MUSIC), and Capon, ESPRIT, and root-MUSIC, and 2) parametric-based methods, which include algorithms such as maximum likelihood [130, 75]. Some of these methods include but are not limited to the following:

- Time Difference of Arrival estimation: This method uses the time difference of arrival of a signal at two or more receivers to estimate the AoA. This method can be quite accurate, but it requires a synchronized time reference between the receivers and can be sensitive to clock drift and multipath propagation [83, 20].

- Beamforming: This method uses an array of antennas to form a directional beam in the direction of the signal. By measuring the phase difference between the signals received at different antennas, the AoA of the signal can be estimated. Beamforming approaches [131] include the Bartlett method, Minimum Variance Distortion less Response (MVDR) [132], and Linear prediction [133].

- MUSIC (MUltiple SIgnal Classification): This method uses an array of antennas to estimate the AoA of the signal. It assumes that the signals are composed of a few distinct sources, and it estimates the AoA by creating a pseudo-spectrum and finding its peaks. This method can provide high resolution and accurate results when the signal-to-noise ratio (SNR) is high, and the number of sources is less than the number of antennas. However, it can be sensitive to errors in the signal model and may not work well when there are multiple signals in the environment [134, 135, 131, 136].

- ESPRIT (Estimation of Signal Parameters via Rotational Invariance Techniques): This method uses an array of antennas and a rotational invariance property of the received signals to estimate the AoA. This method can provide accurate results with high resolution when the signals have certain rotational invariance properties. It can also perform well in a noisy environment. ESPRIT gets smaller computing while constraint to larger asymptotic variance and apply for coherent signals [60, 137].

- Maximum Likelihood (ML) and maximum a posteriori probability (MAP): These methods use an array of antenna, the signal model, and the noise model to find the maximum likely or maximum a posteriori AoA value. These methods are optimal under certain assumptions on the signal and noise models and can provide accurate results when these assumptions hold [60, 130, 138, 139].

- Machine Learning based: These methods use a dataset of previously estimated AoAs and RF signals to train a neural network for AoA estimation. These methods can provide accurate results when the dataset used to train the neural network is diverse and include all possible scenarios [135, 55, 75, 140].

The decision to utilize any discussed methods is closely related to the application. Energy consumption, device complexity, and processing capability limitations for IoT applications are complex schemes that should be considered. For many indoor positioning systems, such

as asset tracking and access control, an accuracy below 1 *m* is required, which is also our goal. Therefore, we decided to use BLE-direction finding for this purpose. To our point of interest, the sub-space-based solutions are quite interesting because of their high resolution and low sensitivity to SNR. Synchronized time references add up to the complexity of the system and usually require high power consumption, which is not desirable for a mobile IoT device. Also, the algorithm's computation requirements are important for real-time applications, so computationally expensive solutions such as machine learning or MAP cannot be the solution. However, machine learning methods or maximum likelihood solutions can improve the data processing after angle estimation. We explain the data processing thoroughly in Chapter 5.

4.2 Bluetooth Low Energy Direction Finding

After understanding the different methods of DF and their role in the localization systems, we would like to explain in more detail about BLE Direction Finding and why we decided to use Bluetooth direction finding for our indoor positioning system.

In the past few decades, Bluetooth has become an inevitable part of many connected devices such as smartphones, smart watches, TV, speakers, and even home and kitchen utilities such as light bulbs or a scale. Nowadays, Bluetooth-equipped devices are very accessible. Moreover, the technology consumes very low energy and is compatible with other wireless solutions. Most connected devices use Bluetooth for data transfer, communication, or tracking. The Bluetooth SIG has anticipated that the annual shipment of location service devices will reach 568 million by 2026. Despite the mythical understanding of Bluetooth, this technology is essentially capable of reaching high-accuracy positioning. Bluetooth has been a tracking device in many applications for over a decade. However, these devices mainly function based on the Received Signal Strength Indication or RSSI. With the slight changes in the modulation of the packets, it is possible to achieve positioning accuracy between $2-5$ *m*, depending on the technology and the data progress.

Recently, the introduction of Direction Finding revolutionized the application of BLE for tracking and localization purpose. BLE Direction Finding can redefine indoor positioning for customers. BLE-DF enables the BLE device to determine the AoA of signals by exploiting the phase differences in the received signal across different antenna elements. This technology can be used in crowded malls, stadiums, hospitals, or even train stations to guide customers to their desired destination, which is the ultimate goal of a functioning indoor positioning system. Moreover, it can provide bellow meter accuracy and improve navigation experience [9].

4.2.1 BLE Direction Finding Protocol

Bluetooth direction-finding feature uses In-Phase and Quadrature (IQ) sampling to measure the phase of radio waves on an antenna at a specific time. In the AoA approach, the sampling

process is applied to each antenna in the array, one at a time and in some suitable sequence depending on the design of the array [68].

Sampled data is passed up the stack via the Host Controller Interface (HCI). It will then be possible to apply a suitable algorithm to the sampled data to calculate the direction of one device from the other. This core specification release does not define algorithms for calculating angles from IQ samples [68]. As a result, one of our main goals is to define a suitable algorithm.

To support IQ sampling and the use of IQ samples by higher layers in the stack, the link layer (LL) and HCI have each changed. A new field called the Constant Tone Extension (CTE) has been defined at the link layer. BLE 5.1 introduced Constant Tone Extension (CTE) as an optional bit sequence contained in the BLE packet. The purpose of the CTE field is to provide constant frequency and wavelength signal material against which IQ sampling can be performed [68]. This field contains a sequence of 1s, is not subject to the usual whitening process, and is not included in the CRC calculation [68].

CTE can be used in both connection-less and connection-oriented scenarios. For connection-less use, the regular advertising feature is required [68]. In either case, new HCI PDUs allow the configuration of various aspects of CTE PDUs, such as the CTE length, length of the antenna switching pattern, and antenna IDs [68]. The CTE has two types, namely AoA and AoD CTE,

CTE Type Value	Description
0	AoA Constant Tone Extension
1	AoD Constant Tone Extension with $1\mu s$ slots
2	AoD Constant Tone Extension with $2\mu s$ slots
3	Reserved for future use

Table 4.1: CTE Type field defines the type of the CTE and the duration of the switching slots

whose structures are shown in table 4.1. Except AoA transmits CTE, the other CTEs follow the same structure.

- The Guard period: No operations are performed ($4\mu s$)

- The reference Period: Acquiring the reference measurements ($8\mu s$)

- Switching Slots & Sampling Slots: Where the switching and sampling occur, respectively, for either $1\mu s$ or $2\mu s$.

The switch slots in the CTE structure define the periods when the switching of the antenna array element will take place. Its time duration is between $1\mu s$ and $2\mu s$, so as for the IQ sampling time slot duration (figures 4.2, and 4.1).

The maximum number of available switch and sampling slots differs due to configuring the slot duration. Recall that the entire maximum CTE time length is $160\mu s$; after the first $12\mu s$

AoA transmitter: No switching (CTE)

AoA receiver: 1us switching and sampling slots

AoA receiver: 2us switching and sampling slots
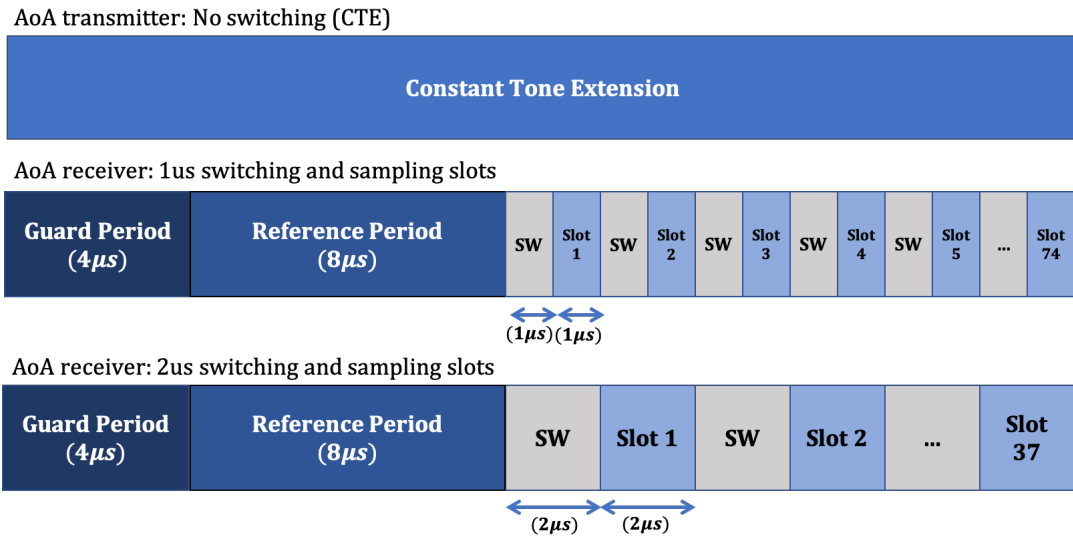
Figure 4.1: The packet configuration for AoA. When AoA CTE is transmitted, it is transmitted in a continuous way without having the antenna switched. Upon receiving AoA CTE, the receiver shall perform antenna switching at the rate and pattern defined by the host, either with $1\mu s$ or $2\mu s$ switch and sampling slot duration. *SW is Switching slot.)

($4\mu s$ guard period + $8\mu s$ reference period) is deducted, the CTE time length, which is allowed for switch and sampling remains $148\mu s$. Thus, 74 switch and sampling slot pairs can be utilized in case $1\mu s$ switch and sampling slot are configured. Correspondingly, 37 switch and sampling slot pairs in case of $2\mu s$ configuration (figures 4.2, and 4.1). In case AoD CTE is transmitted, the transmitter shall perform antenna switching in contrast to the AoA case, followed by AoD beacon sending in the TX slot. While receiving AoD CTE, the receiver does not need to switch antennas; only RF sampling is required. The maximum number of the switch and sampling slots has the same definition as for AoA. In both AoA and AoD cases, the receiver shall take an RF sample each microsecond during the $8\mu s$ (shown in figures 4.2, and 4.1) reference period and one sample pair from each sample slot.

4.2.2 Power Consumption

The power consumption BLE transmitter depending on the modules will be slightly different. For example, [141] presents the actual measurements that the average transmitted power for BLE AoA is below $-2dBm$ for each packet. The same studies with the Texas Instrument modules [59] reveal interesting information about the current and power consumption of the modules. This thorough study shows two important cases of a connection event, standby and not standby conditions for the BLE packets. For connection direction finding while sending the BLE-DF packets, these two events are the building blocks of a packet.

AoD transmitter: Switching (CTE)

Constant Tone Extension	

AoD Transmit: 1us switching and sampling slots

Guard Period (4μs)	Reference Period (8μs)	SW	Slot 1	SW	Slot 2	SW	Slot 3	SW	Slot 4	SW	Slot 5	...	Slot 74

(1μs)(1μs)

AoD receiver: 1us switching and sampling slots

Guard Period (4μs)	Reference Period (8μs)	Slot 1	Slot 2	Slot 3	Slot 4	Slot 5	...	Slot 74
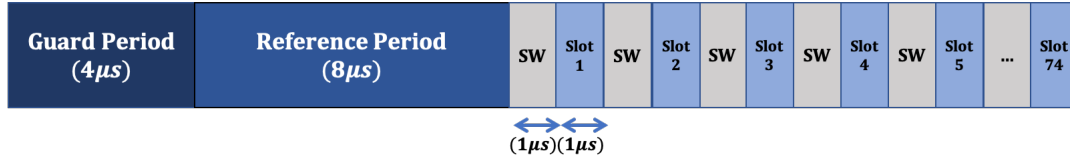
(1μs) (1μs)
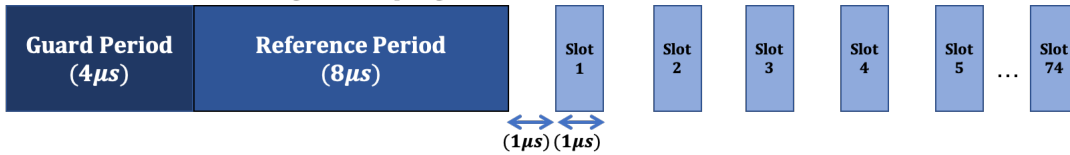
AoD Transmit: 2us switching and sampling slots

Guard Period (4μs)	Reference Period (8μs)	SW	Slot 1	SW	Slot 2	...	Slot 37

(2μs) (2μs)

AoD receiver: 2us switching and sampling slots

Guard Period (4μs)	Reference Period (8μs)	Slot 1	Slot 2	...	Slot 37
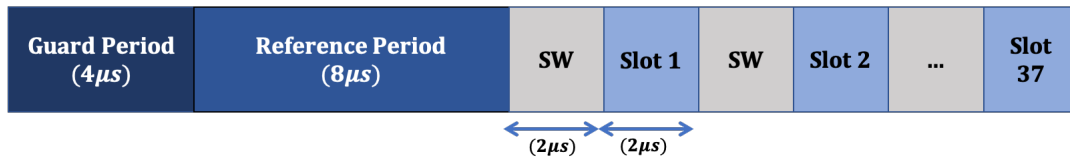
(2μs) (2μs)
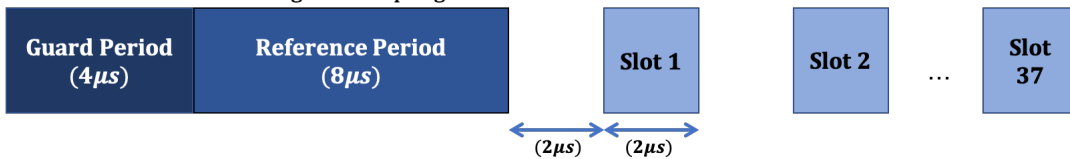
Figure 4.2: AoD CTE Structure, illustrates the AoD CTE structure.

Table 4.2: Average power and current consumption of a packet of data during a connection direction finding event

Condition	Average Current Consumption (mA)	Average Power Consumption (mW)
When Device Enters Standby	0.1026	0.3384
Device Does not Enter Standby	1.1251	3.7128

The average current during the entire connection interval, which considers the time the device is sleeping, is $9.74\mu s$ for a packet of data [59]. During a connection event with $95\mu s$ of transmission time, the average current is $7.1mA$. The average current during the connection event is $3.619mA$ [59]. While transmitting, the duration of BLE-DF packets is $20\mu s < CTE < 160\mu s$. Therefore, the range for the average current is $3.507mA < I_{ave} < 3.709mA$. The working voltage is 3.3V. Table 4.2 shows the average power and current consumption of data packet with the interval of $500ms$ in a duration of $5s$ [59].
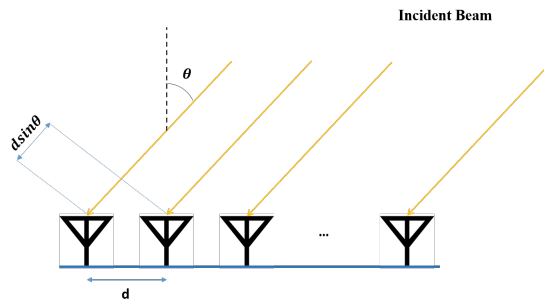
Figure 4.3: Uniform antenna array and the incident angles, the blue dots are the position of the antennas.

With this Knowledge of the power consumption of the modules, while transmitting BLE-DF packets, this thesis does not intend to explore the power consumption of the devices further as we are following the Bluetooth standard events for transmitting data.

4.3   Physical Principals of Angle Estimation

The angle of Arrival (AoA), also called the direction of arrival (DoA), is defined as the elevation and azimuth angle of incoming signals. Antenna arrays are the key element for AoA /AoD estimation. The design of these antennas is a deterministic aspect of angle estimation. The linear or 1D antenna arrays will only provide us with one angle, while the 2D antenna arrays (antennas distributed in a plane), can provide both angles at the same time. Therefore, it is important to design an antenna array specifically for the BLE-AoA application to enhance an effective and high-resolution angle estimation. In the next section, we explain in detail why and how the antenna array design imposes a direct effect on the angle estimation procedure. We start from a simple case of 1D estimation with a uniform linear array.

For AoA estimation methods, the basic idea is that different propagation paths have different AoAs. When the signal from a propagation path is received across an array of antennas, then the AoA will introduce a corresponding phase shift across the antennas in the array. The introduced phase shift is a function of both the distance between antennas and the AoA. The direction of arrival or departure can be calculated based on the propagation delays of a signal between the transmitter and the receiver. In the primary steps, we present the principles of angle estimation using a linear antenna array. Therefore, these arrays are only capable of measuring one angle. In the next steps, we will expand the same logic to other antenna array structures and will drive the formula for them.

The angle can be defined using a linear Uniform Antenna Array (ULA) with a known separation distance of d (Figure 4.3). Figure 4.3 depicts the incident wave that reaches the antenna array (receivers). If the distance between the transmitter and the receiver array is much larger than d, we can approximate the incoming wave to a plane wave [142]. Using the geometrical properties of a triangle makes it possible to estimate the desired angle. The

maximum distance between two adjacent antenna elements shouldn't exceed $\lambda/2$. if we assume the time difference between each pair of neighbor antennas is equal τ, we can write: [143].

$$\tau = d \sin(\theta)/c$$
$$\phi = 2\pi \sin(\theta)/\lambda$$

(4.1)

Where c is the free space velocity of the propagated signal, θ is the angle of arrival, ϕ is the phase difference of antennas, and λ is the signal's wavelength. Switching time, channel isolation, and the number of channels are the essential characteristics of the RX switch that can affect the sampling and estimation process. DoA estimation accuracy can be affected by many factors, such as Signal to Noise Ratio (SNR), sampling period, and physical phenomena like reflection, refraction, and diffraction among many others.

The estimated angle is calculated due to the measured phase difference. Since multiple positions might have the same phase difference, the target is equally likely to be present in a set of locations. For example, in a 2D plane, the target can be in either two positions of θ or $-\theta$. Using this principle, it is possible to estimate a signal's arrival angle in a controlled environment.

Understanding this principle provides the backbone for the theory of angle estimation methods. The next section presents a signal model for angle estimation for each array geometry.

4.3.1 Antenna Array Signal Model

Antenna arrays are ordinarily classified into three types: Uniform Linear Arrays (ULA), Uniform Circular Arrays (UCA), and Uniform Rectangular Arrays (URA). More in detail, the rectangular and circular ones are two-dimensional, while the linear array is one-dimensional. The ULA is the simplest to sketch and actualize; however, it has the disadvantage of determining the azimuth angle, considering that the traced device continuously passes on the equivalent flat. On the contrary, accuracy would be compromised if this situation did not occur. UCAs and URAs allow reliable estimating of both elevation angles and azimuth.

4.3.2 The Signal Model of Linear Arrays

Far-field or plane wave assumption is commonly used in our problem, which refers to wavelength much smaller than the source to antenna distance. Figure 4.4 presents the angle of arrival (θ) of a uniform linear array. We assume to have K number of sources, $\boldsymbol{s}_k(t) \in \mathbb{C}$ is a narrow band incident signal from the kth source, and $\boldsymbol{x}_m(t)$ is the received signal at the mth element of our M element uniformly spaced antenna array with spacing equal to d. Also, $\boldsymbol{n}_m(t)$ the additive white gaussian noise (AWGN) at the mth element, then we have:

$$\boldsymbol{x}_m(t) = \sum_{k=1}^{K} \boldsymbol{s}_k(t) e^{2\pi j \tau_k (m-1)} + \boldsymbol{n}_m(t)$$

(4.2)
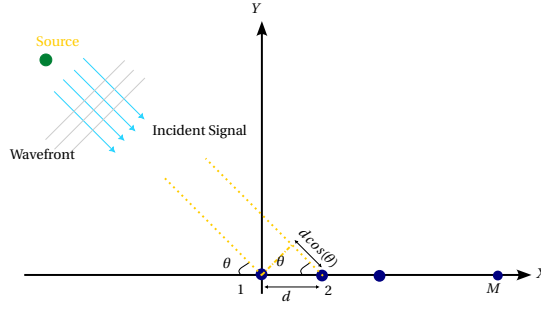
Figure 4.4: Uniform antenna array and the incident angles, the blue dots are the position of the antennas. ϕ is the angle of arrival (AoA)

Where $\tau_k = sin(\theta_k)\frac{d}{\lambda}$ and is the phase shift per antenna in the array. All variables labeled m belong to the mth array element, and all of k belong to the signal source k. $\boldsymbol{n}_m(t)$ is a zero-mean temporarily white additive Gaussian noise with a mean of zero and variance of σ^2. Let $\boldsymbol{a}_m(\theta) \in \mathbb{C}^M$ be the response function of array element m to signal source k. Hence,

$$\boldsymbol{a}_m(\theta) = [1, e^{2\pi j \tau(\theta)}, e^{2\pi j 2\tau(\theta)}, ..., e^{2\pi j (m-1)\tau(\theta)}]^T \tag{4.3}$$

Therefore, we have:

$$X = AS + N \tag{4.4}$$

Where,

$$X = [\boldsymbol{x}_1(t), \boldsymbol{x}_2(t), ..., \boldsymbol{x}_M(t)]^T, S = [\boldsymbol{s}_1(t), \boldsymbol{s}_2(t), ..., \boldsymbol{s}_K(t)]^T, A = [\boldsymbol{a}(\theta_1), \boldsymbol{a}(\theta_2), ..., \boldsymbol{a}(\theta_K)]^T \tag{4.5}$$

and as well the noise matrix will be $N = [\boldsymbol{n}_1(t), \boldsymbol{n}_2(t), ..., \boldsymbol{n}_M(t)]^T$. T is the transpose operator. If having N_s sampling points to construct $\boldsymbol{x}_m(t)$, the issue becomes to sample the output signal ($\boldsymbol{x}_m(t)$) and the estimate the angle of signal source from $\boldsymbol{x}_m(i), \ i = 1, 2, ..., M$. Thus it can take the array signal as a superimposed spatial harmonic noise. According to 4.3, we can define the steering vector in its general form. The closed form of the signal model stays intact for other geometries of antenna arrays. The only changing part will be the steering vector.

4.3.3 Signal Model of Rectangular Arrays

In its simple form, we can view the rectangular arrays as multiple rows of linear arrays with vertical and horizontal spacing. Figure 4.5 shows a $M \times N$ array placed on the horizontal xy plane to measure the angles on the superior plane. The element separation is denoted by d_x and d_y, respectively. A Uniform rectangular Array is when having $d_x = d_y$. knowing the position of the elements, we can construct the steering vector. Therefore for the nth and m^{th} element in the array we have:

$$\boldsymbol{a}_{mn}(\theta, \phi) = \exp\left(j2\pi(md_y sin(\phi)sin(\theta) + nd_z cos(\phi))\right) \tag{4.6}$$
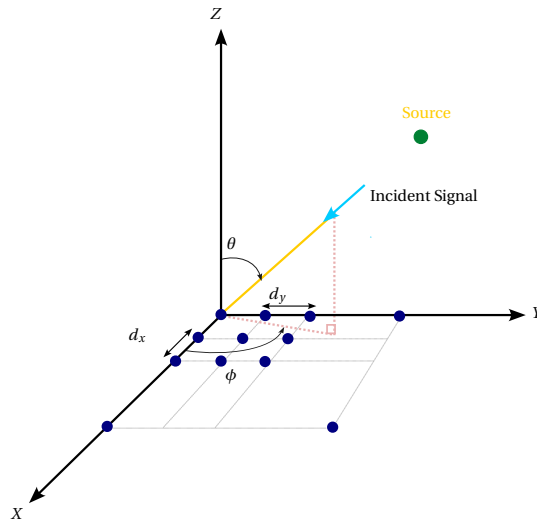
Figure 4.5: Uniform rectangular array and the incident angles, the blue dots are the position of the antennas. ϕ is the azimuth angle and θ is the elevation angle.

Depending on the URA configuration, the Azimuth and the Elevation angle will be influenced. We assume that the elements consist of patches; thus, they can only receive energy from the frontal plane. The angular distribution with this orientation is $-\pi/2 < \phi < pi/2$ and $0 < \theta < pi$.

4.3.4 Signal Model of Circular Arrays

On a similar note, the signal model for the circular arrays stays the same. However, the steering vector will be different based on the position of the antennas in the array. To generate the steering vector for a UCA with a radius equal to d and $\theta = 2\pi/M$, we can have:

$$\boldsymbol{a}_m(\theta, \phi) = \exp\left(j2\pi(cos((m-1)\phi) + sin((m-1)\phi))sin(\theta)\right) \tag{4.7}$$

4.4 Direction of Arrival Estimation Algorithms

As mentioned, a variety of methods have been proposed in the literature on DoA estimations. These estimations refer to the process of retrieving the direction information from the output of the receiving antenna array. These estimations are based on the signal angular spectrum since the signal is distributed in every direction of the space. The array structure of the receiver provides a spatial sampling of this waveform.

In this section, we will present and compare three high-resolution methods based on the subspace concept to estimate the arrival directions of RF signals. The principle difference is in fact the decomposition of this autocorrelation matrix of observation vectors into orthogonal subspaces. For the search of DoA, they use the search for an extremum in a pseudo-spectrum, finding zeros of a polynomial and eigenvalues of a matrix, respectively. We will primarily
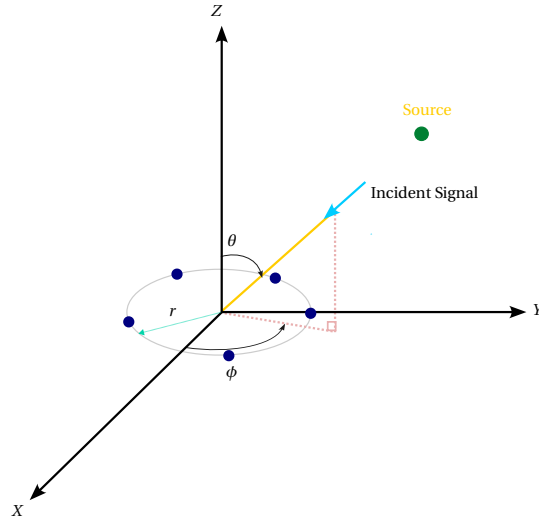
Figure 4.6: Uniform circular array and the incident angles, the blue dots are the position of the antennas. ϕ is the azimuth angle and θ is the elevation angle.

explain the principles of Eigenvalue decomposition for the MUSIC algorithm.

4.4.1 Multiple Signal Classification Algorithm

The main principles of the Multiple Signal Classification Algorithm or MUSIC algorithm is presented here. In equation 4.4, since the signal and noise are uncorrelated (as shown in figure 4.7), using the array output, the auto-covariance matrix of all received signals from all the antennas can be written as:

$$\boldsymbol{R_x} = \mathbb{E}[\boldsymbol{X}\boldsymbol{X}^H]$$
$$= \mathbb{E}[(\boldsymbol{A}\boldsymbol{S} + \boldsymbol{N})(\boldsymbol{S}^*\boldsymbol{A}^* + \boldsymbol{N}^*)]$$
$$= \boldsymbol{A}\mathbb{E}[\boldsymbol{S}\boldsymbol{S}^*]\boldsymbol{A}^* + \mathbb{E}[\boldsymbol{N}\boldsymbol{N}^*]$$

$$\boldsymbol{R_x} = \boldsymbol{A}\boldsymbol{R_s}\boldsymbol{A}^H + \sigma^2\boldsymbol{I} \tag{4.8}$$

$\mathbb{E}[.]$ denotes the expectation operation, $\{.\}^H$ is the hermitian operation. Where $\boldsymbol{A}$ is the array steering matrix $\boldsymbol{A} \in \mathbb{C}^{M \times K}$ and $\boldsymbol{R_s} = \mathbb{E}[\boldsymbol{s}\boldsymbol{s}^*]$ is the source correlation matrix. $\boldsymbol{I}$ is a unity matrix of size M. We have as many steering vectors as propagation paths; therefore the overall matrix is $\boldsymbol{A} = [\boldsymbol{a}(\theta_1), \boldsymbol{a}(\theta_2), ..., \boldsymbol{a}(\theta_k)]$ and $\boldsymbol{R_s} = diag[\sigma_1^2, \sigma_2^2, ..., \sigma_k^2]$ is a $K \times K$ matrix whose diagonal entries are signal variance. Using the Singular Value Decomposition (SVD) method, we can estimate $\boldsymbol{R_x}$ by:

$$\boldsymbol{R_x} = \boldsymbol{U}\boldsymbol{\Sigma}\boldsymbol{U}^H \tag{4.9}$$

Where $\boldsymbol{U} = [\boldsymbol{U_s}, \boldsymbol{U_n}]$. $\boldsymbol{U_n} \in \mathbb{C}^{M \times M-K}$ represents an orthogonal basis of the estimated noise subspace, and $\boldsymbol{U_s}$ is the eigenvalue matrix corresponding to the signal subspace (i.e. $\boldsymbol{U_s} \perp \boldsymbol{U_n}$). As these orthogonal bases are shown in a hypothetical condition in figure 4.7. Finally, the pa-
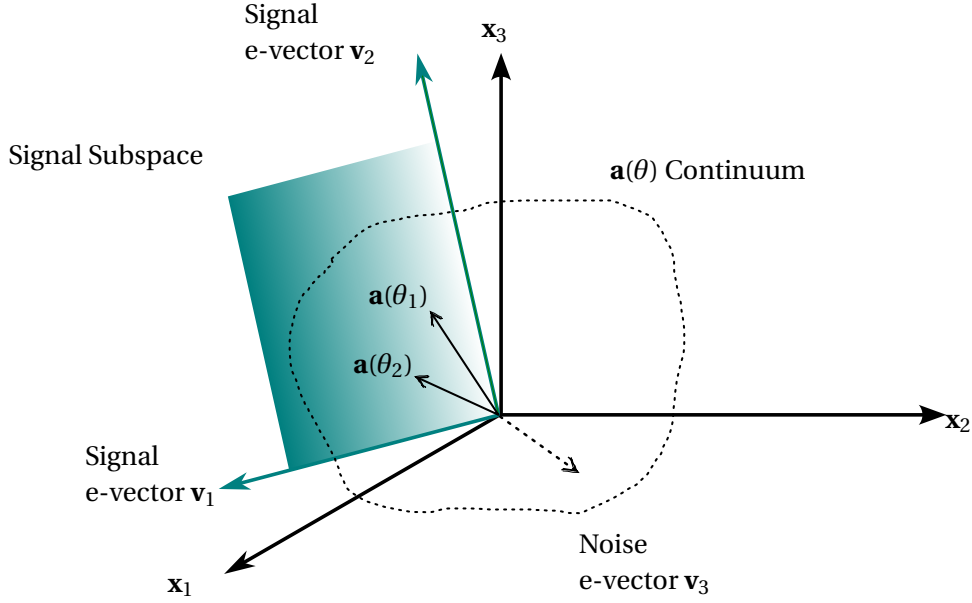
Figure 4.7: In this three-antenna example, the two incoming signals (at θ_1 and θ_2 respectively) lie in a three-dimensional space. Eigenvector analysis identifies the two-dimensional signal subspace shown, and MUSIC traces along the array steering vector continuum measuring the distance to the signal subspace. Figure adapted from [144]

rameters of the sources are obtained by maximizing the following criterion using characteristic noise value of $(M - K)$ column vectors:

$$\boldsymbol{U_n} = [\boldsymbol{v}_{K+1}, \boldsymbol{v}_{K+2}, ..., \boldsymbol{v}_M], \tag{4.10}$$

Where spatial spectrum is:

$$P_{mu}(\theta) = f(\frac{1}{||\boldsymbol{U}_n \boldsymbol{a}(\theta)||^2}) = f(\frac{1}{\boldsymbol{a}(\theta)^H \boldsymbol{U}_n \boldsymbol{U}_n^H \boldsymbol{a}(\theta)}) \tag{4.11}$$

Where f is a function that indicates the maximum of the spectrum above, after obtaining the spectrum, the question is to find the maximum of the spectrum above for each data packet or AoA/AoD. Generally, the MUSIC algorithm is sensitive to noise. When having a low Signal-to-Noise Ratio (SNR), the estimation performance decreases or even results in singularity problems. If the noise is weaker than the incoming signal, then when the eigenvalues are sorted in non-decreasing order, the smallest $M - D$ corresponds to the noise while the next D corresponds to the D incoming signals.

Algorithm 2 Music Algorithm

 1: **Input** Received signal X, Antenna number M, Sources K, Snapshots N_s, Angle range
 2: **Output** Computes the DoAs
 3: $\boldsymbol{R_x} \leftarrow \mathbb{E}[\boldsymbol{XX^H}]$;
 4: $\boldsymbol{U} \leftarrow eig(\boldsymbol{R_x})$;
 5: $\boldsymbol{U_n} \leftarrow \boldsymbol{U}[:, D:M]$;
 6: **for** each angle θ **do**
 7:     compute $\boldsymbol{a}(\theta)$
 8:     $P_{mu}(\theta) \leftarrow 1/|\boldsymbol{a}(\theta)^H \boldsymbol{U_n U_n^H} \boldsymbol{a}(\theta)|$
 9: **end for**
10: $psindB \leftarrow \log(\frac{10 P_{mu}(\theta)}{max(P_{mu}(\theta))})$
11: $DoA \leftarrow peak(psindB)$

4.4.2 Estimation of Signal Parameters via Rotational Invariance Techniques

The estimation of Signal Parameters via Rotational Invariance Techniques (ESPRIT) is based on the rotational invariance property of the signal space and not the noise subspace. This method neither requires the calculation of pseudo-spectrum on the extent of space nor the search for roots of a polynomial.

This method exploits the property of translational invariance of the antenna array by decomposing the main network into two sub-networks of identical antennas; one can be obtained by a translation of the other. ESPRIT imposes a particular geometric constraint on the array, but it has a tremendous computational advantage over MUSIC, and further, it eliminates the required array calibration.

The main advantage of this method is that it avoids the heavy research of maxima of a pseudo-spectrum or a cost function (therefore a gain calculation) and the simplicity of its implementation. In addition, this technique is less noise-sensitive than MUSIC and root-MUSIC.

Consider K sources by designating $\boldsymbol{x}_1(t)$ and $\boldsymbol{x}_2(t)$ as observation vectors at the outputs of sub-networks 1 and 2, the received signal vector in the baseband of the complete network is written as the following:

$$\boldsymbol{x}(t) = \begin{bmatrix} \boldsymbol{x}_1(t) \\ \boldsymbol{x}_2(t) \end{bmatrix} = \begin{bmatrix} \boldsymbol{A} \\ \boldsymbol{A}\Phi \end{bmatrix} . \boldsymbol{S}_k(t) + \begin{bmatrix} \boldsymbol{n}_1(t) \\ \boldsymbol{n}_2(t) \end{bmatrix} \tag{4.12}$$

with rotation matrix of:

$$\Phi = diag[e^{-j\frac{2\pi d}{\lambda}sin\theta_1}, e^{-j\frac{2\pi d}{\lambda}sin\theta_2}, ..., e^{-j\frac{2\pi d}{\lambda}sin\theta_k}] \tag{4.13}$$

This relation will allow estimating the angles of arrival without knowing the expression of the matrix **A** of source vectors. It so allows the use of the ESPRIT algorithm to antennas of badly

known or unknown geometry. The correlation matrix of the complete network is given by:

$$R_x = \begin{bmatrix} A \\ A.\Phi \end{bmatrix} . R_s . \begin{bmatrix} A^H \\ \Phi^H . A^H \end{bmatrix} + \sigma^2 . I \tag{4.14}$$

where $A = [a(\theta_1), a(\theta_2), ..., a(\theta_k)]$ is a $M \times K$ matrix of source vectors defined in a sub-network and R_x is the spatial matrix of sources. With the antenna configuration, the matrix A is the same as for the MUSIC algorithm. As described before, this matrix is Hermitian and with real eigenvalues of:

$$\lambda_1 \geq \lambda_2 \geq, ..., \geq \lambda_k \geq \lambda_{k+1} = ... = \sigma^2 \tag{4.15}$$

The largest K eigenvalues correspond to the space signal generated by the K sources. The signal subspace E_s is a $M \times K$ matrix composed of K eigenvectors associated with the signal subspace. The signal subspace E_s of the whole network can be decomposed into two subspaces E_1 and E_2 which are the $(M-1) \times K$ matrices whose columns are composed of K eigenvectors corresponding to eigenvalues of the covariance matrices of the sub-networks 1 and 2. These two matrices E_1 and E_2 are related by the following relation of the invertible linear transformation:

$$E_s = \begin{bmatrix} E_1 \\ E_2 \end{bmatrix} = \begin{bmatrix} AT \\ A\Phi T \end{bmatrix} \tag{4.16}$$

with $T = R_{11}^{-1}.R_{12}$ and $R_{11} = \frac{1}{N}X_1 X_1^H$ and $R_{22} = \frac{1}{N}X_2 X_2^H$ are the covariance matrixs between the two sub-networks of the antenna array. and we have:

$$E_2 = ATT^{-1}\Phi T = E_1 \Psi \tag{4.17}$$

where $\Psi = T^{-1}\Phi T$ is a $K \times K$ matrix. The eigenvalues of Φ and Ψ are common and are expressed by $\lambda_i = e^{jkdsin(\theta)}$ with $i = 1, 2, ..., K$. The angle of arrival is given by $\lambda_i = |\lambda_i|e^{jarg(\lambda_i)}$. Therefore we have:

$$\theta_i = sin^{-1}(\frac{arg(\lambda_i)}{kd}) \quad i = 1, 2, ..., K \tag{4.18}$$

Knowing the principles of the ESPRIT algorithm, we used it for different configurations of our designed antenna array. The rotational nature of this technique enabled us to use it even for cases where the antenna configuration does not fall into the common categories. The algorithm 3, presents the ESPRIT algorithm in summary.

4.4.3   root-MUSIC

The advantage of this method lies in the direct calculation of the DoA by the search for zeros of a polynomial, which so replaces the search for maxima, necessary in the case of MUSIC. This method is limited to networks of linear antennas uniformly spaced out. In addition, it allows

---

Algorithm 3 ESPRIT Algorithm

1: **Input** Received signal $\boldsymbol{X}$, Antenna number M, Sources K, Snapshots N_s, Angle range
2: **Output** Computes the DoAs
3: $\boldsymbol{R_x} \leftarrow \mathbb{E}[\boldsymbol{X}\boldsymbol{X}^{\boldsymbol{H}}]$;
4: Compute $\boldsymbol{E_s}$
5: Compute $\boldsymbol{\Psi}$
6: Compute $\lambda_i = eig(\boldsymbol{\Psi})$
7: $DoA \leftarrow \theta_i = sin^{-1}(\frac{arg(\lambda_i)}{kd})$

---

a reduction in computing time and so an increase in the angular resolution by exploiting certain properties of the received signals. The principle of the Root-MUSIC algorithm is to form a polynomial of degree $2(M-1)$ and extract the roots [19]-[20]. For a linear antenna array uniformly spaced out, the projection of the steering vector on the noise subspace can be expressed according to 4.11 by the following relation:

$$P_{MUSIC}^{-1}(\theta) = \boldsymbol{a}(\theta)^H \hat{\boldsymbol{U}}_{\boldsymbol{n}} \boldsymbol{U}_{\boldsymbol{n}}^H \boldsymbol{a}(\theta) \tag{4.19}$$

Let $\boldsymbol{C}$ be $\hat{\boldsymbol{U}}_{\boldsymbol{n}} \boldsymbol{U}_{\boldsymbol{n}}^H$ therefore the equation becomes as:

$$P_{MUSIC}^{-1}(\theta) = \boldsymbol{a}^H(\theta).\boldsymbol{C}.\boldsymbol{a}(\theta) \tag{4.20}$$

Using the analytical representation and the expression of the steering vector $e^{-j(m-1)\frac{2\pi d}{\lambda}sin\theta}$ of the mth element of the linear network ($m = 1, 2, ..., M$) we can write:

$$P_{MUSIC}^{-1}(\theta) = \Sigma_{m=1}^{M}\Sigma_{n=1}^{M} e^{-j(m-1)\frac{2\pi d}{\lambda}sin\theta}.\boldsymbol{C}.e^{-j(n-1)\frac{2\pi d}{\lambda}sin\theta} \tag{4.21}$$

where is the element of the the mth line and the the nth column of $\boldsymbol{C}$ By combining the two sums in 4.21 we obtain the following expression:

$$P_{MUSIC}^{-1}(\theta) = \Sigma_{-M+1}^{M+1}\boldsymbol{C_l}e^{-jl\frac{2\pi d}{\lambda}sin\theta} \tag{4.22}$$

Where $\boldsymbol{C_l} = \Sigma_{m-n=l}\boldsymbol{C}_{mn}$. Equation 4.22 can be transformed to Root-MUSIC polynomial, which is a function of z defined by:

$$D(z) = \Sigma_{-M+1}^{M+1}\boldsymbol{C_l}\boldsymbol{l}^l \tag{4.23}$$

Where $z = e^{-j\frac{2\pi d}{\lambda}sin\theta}$.

Directions-of-arrival of signals being functions of z, the problem is therefore, to calculate the $(M-1)$ double roots of the polynomial whose useful zeros are thus on the unit circle. The phases of these complex roots correspond to the desired electric phase shifts. The angles of

arrival of signals can then be deducted from the following equation:

$$\theta_m = -sin^{-1}(\frac{\lambda}{2\pi d} arg(z_m)) \tag{4.24}$$

Where z_m is the mth closest roots to the unit circle. Studies have shown that the root-MUSIC

Algorithm 4 root-MUSIC Algorithm

1: **Input** Received signal X, Antenna number M, Sources K, Snapshots N_s, Angle range
2: **Output** Computes the DoAs
3: $R_x \leftarrow \mathbb{E}[XX^H]$;
4: Compute C
5: Compute $D(z)$
6: Compute roots of $D(z)$
7: $\theta_m \leftarrow -sin^{-1}(\frac{\lambda}{2\pi d} arg(z_m))$

---

algorithm 4 has better resolution than the spectral-MUSIC algorithm. However, this method only gives us the roots and never the spectral density.

4.5 AoA Antenna Design Considerations

After exploring various signal processing solutions to the AoA/AoD problem, one other important aspect should also be discussed. No algorithm can function adequately unless the hardware is also well structured. Therefore, we have to understand the basics of designing an antenna array for BLE Direction Finding. As a result, we need a solid understanding of the protocol and specifically the antenna switching. Therefore, in this section, we explain the details of BLE AoA/AoD antenna switch.

BLE Direction finding protocol sends packets of information through narrow band channels speared from $2.4GHz$ to $2.85GHz$ [145]. Moreover, switching at $1us$ time slots requires fast switching between the antennas in the array. To calculate the AoA, the incoming RF carrier phase must be measured with minimal impact on the signal phase of the carrier itself using two or more co-located antennas. Therefore, there are several considerations to understand when designing a Bluetooth Low Energy antenna array.

First, to determine which antenna is closest to the transmitted signal, the antenna phase centers must be within $\lambda/2$ of each other (will be discussed in section 4.5.1). Consequently, antenna spacing becomes a concern as undesired coupling can occur reducing the efficiency of the antenna array.

Furthermore, to avoid additional phase measurement errors and any added calibration requirements, the phase centers of the antenna should be constant. If the phase center shifts due to the direction of the incoming signal, the phase center change must be accounted for in the AoA calculation.
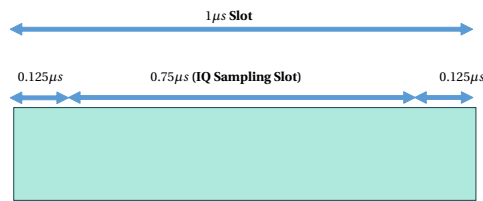
Figure 4.8: IQ Sampling Window for $1\mu s$ Sample Slots

Finally, with any antenna design, other antenna basics such as grounding and efficiency should be understood to improve the overall effectiveness of the receiver and ensure minimal interference from reflections.

Another aspect of the AoA hardware design is the RF switch required to switch between two or more antennas. It is important to understand the RF switching times to calculate the AoA measurement and meet the Bluetooth 5.1 specification as well as understand the RF switch specifications to ensure good performance.

4.5.1   Antenna Spacing

One of the important factors is the antenna spacing in an array of antenna. For example, in a two-element antenna system, the receiving antenna phase centers must be within $\lambda/2$ (maximum phase difference of 180°) to determine which antenna is closer to the transmitter easily. So, each antenna will take a turn to measure the phase. Finally, the phase difference between these two antennas is used to calculate the AoA/AoD. Therefore, if the difference is greater than 180°, the true phase difference could be incorrectly interpreted. For an antenna array to function correctly for the Bluetooth spectrum ($2.44GHz$), the antenna spacing must be less than or equal to $61.5mm$. Therefore, antenna coupling can affect the antenna arrays' efficiency.

4.5.2   Antenna Switching

RF switch characteristics that matter the most in an AoA/AoD application are the switching time, channel isolation, and the number of channels. Switching time is important because the Bluetooth 5.1 specification requires $2\mu s$ or switch slots with the option of supporting quicker $1\mu s$ switch slots 4.8, 4.9.

Therefore, the RF switch must be able to switch and settle within the specified switch slot time (whether $2\mu s$ or $1\mu s$). It is important to note that IQ sampling begins $0.125\mu s$ into a $1\mu s$ slot and $1.125\mu s$ into a $2\mu s$ slot and ends $0.875\mu s$ into a $1\mu s$ slot and $1.875\mu s$ into a $2\mu s$ slot.

Channel isolation is also an important specification because it directly affects the efficiency of the system. The better the isolation between the RF channels, the better the overall efficiency of the RF system. Lastly, the number of channels is important as it plays a large factor in the
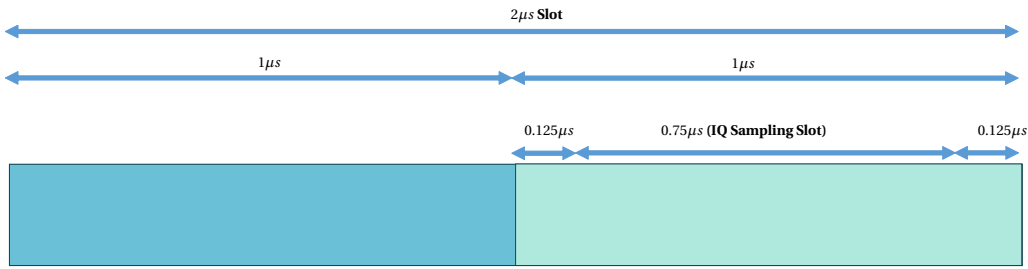
Figure 4.9: IQ Sampling Window for $2\mu s$ Sample Slots
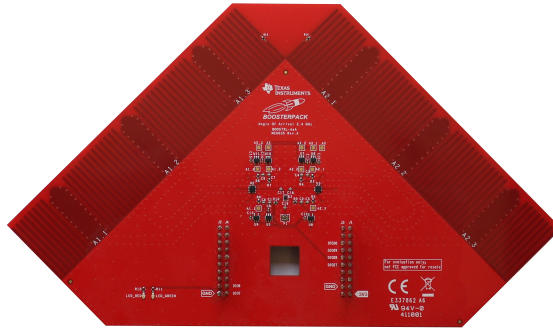
Figure 4.10: Texas Instrument antenna array structure with the switches

switching cost.

4.6 Antenna Array Design

4.6.1 Texas Instrument Antenna Array

To evaluate the BLE-direction finding protocol, we used an out-the-shelf antenna array from Texas Instrument called TI BOOSTXL as an antenna array [146]. With its unique shape, this antenna array allows $2\mu s$ switching between each antenna. With two rows of 3 antenna elements and the spacing equal to 3.5 cm for each pair of antennas in each row (figure 4.10). Both rows can not be used simultaneously; however, it is possible to switch between each row. The choice of this antenna array enables us to explore the BLE-DF protocol freely with an existing dedicated antenna array for this purpose.

This antenna array consists of two rows of uniformly spread dipole antennas. The choice of dipole antenna provides two main advantages. One, the phase center is at the feeding point and is constant. Which will not introduce phase error to the array due to the shifting phase center. Second, the dipole antenna does not receive or transmit RF power in the direction of its own axis. As a result, antenna coupling will be minimized, especially when phase centers are bellow $\lambda/2$.

Despite these advantages, the dipole antenna requires isolation from the ground. Which
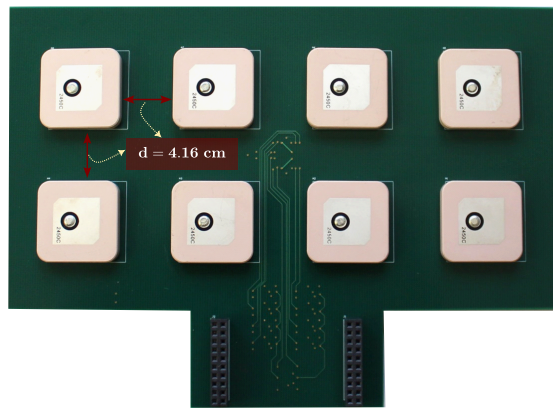
Figure 4.11: E-lib antenna array structure with the switches at the back of the PCB

directly conflicts with the BLE receiver's ground plane. If the ground plane is too close to the antenna, the antenna is effectively shorted because the ground plane reflects the inverse of the incoming wave. However, if the ground plane is further away, it will still reflect RF power back to the antenna and reduce its efficiency [147].

To resolve the ground plane issue, a corrugated ground plane is implemented. The corrugated ground plane removes the boundary current by shifting the reflected phase $180°$ per finger by taking the boundary current on a $\lambda/2$. detour. Therefore, each segment cancels the effect of the neighboring segments, and the net effect is zero current and an in-phase reflection [147].

4.6.2 E-lib Antenna Array

As mentioned in section 4.5.2, the switching sample plays an important role in the BLE-direction finding protocol. Moreover, the antenna spacing and the number of antennas are also deterministic. Therefore, we decided to create a new antenna array that enables new features for us. This new antenna array (E-lib Antenna) consists of two rows of four uniformly spaced patch antennas (figure 4.11). In this design, we replaced the dipole antennas with patch antennas for several reasons. Unlike dipole antennas, patch antennas only receive energy from the frontal plane. This simplifies the ground plane consideration because they have a ground plane on one side and a radiating patch on the other. These antennas are lightly weighted, small in size, and have good mechanical strength, wide frequency band, and high gain.

Moreover, in this design, we use three ultra-fast switches that can be controlled separately. In our design, we use two SP4T (SKY13322-375LF) switches with very high isolation of 28 dB at $1 GHz$ and bandwidth of 20 MHz to 6 GHz. RF Channel isolation is a deterministic factor that directly affects the efficiency of the antenna array. We are also using an SPDT switch (SKY13323-378LF) to control the rows of the antennas in the array. For the antennas, we are using eight out-of-the-shelf antennas (Taoglas WLP.2450.25.4.A.02) with a $5dBi$ peak gain.

The antenna has a center frequency of 2.4 GHz and a bandwidth of 85 MHz. The spacing between each antenna in the array is $\lambda/3 = 4.16$ cm given that the central frequency of the BLE spectrum is 2.4 GHz. A key characteristic of such an antenna array is the delay imposed on the signal due to the slight variances between the antenna characteristics and routing. In our design, we matched routing to the 50 Ω impedance transmission line of the RF switch. To check the switching, we measured the delay of the switches at 2.4GHz.

We measured the propagation time (the delay) of a signal at 2.4 GHz between the Bluetooth radio output and the antennas to ensure the array's uniformity. Ideally, these delays should be the same with the same frequency. Due to the slight variation between each switch in the array or the routing, the delay will not be constant for each antenna. Table 4.3 shows the network

Table 4.3: Delays of antennas

Antenna	Magnitude(dB)	Phase(deg)	Delay(ns)
1	-4.0194	67.921	2.4443
2	-4.0963	65.167	2.3633
3	-3.977	65.432	2.7573
4	-4.0566	64.897	2.4857

analyzer output of the antenna array at 2.4 GHz. We measured the phase, magnitude, and delays of the scattering parameter of S12 through the circuit. The table shows that the delay of a maximum of 0.394 ns will lead to a maximum of 0.4° degrees of error which is negligible. On the other hand, we can see a slightly smaller magnitude received by the third antenna in the array, which results in higher delays eventually.

4.6.3 Antenna Array Panel and the Switch

The antenna array configuration is the key component for an accurate AoA/AoD estimation. With the BLE-DF protocol, it is possible to switch between 74 antennas. Also, the protocol allows a 1μs or 2μs sampling rate. Plus, different antenna configurations have an impact on the angle estimation accuracy. As a result, we decided to design an antenna array and a switch that is capable of switching up to 64 antennas. With the collaboration of our scientific partners at HE-Arc, we designed an antenna array, and its special switch for this purpose [148]. In this design, the antenna array and the switch are physically separated and connected with RF cables.

This antenna array is a metallic panel made from aluminum with several slots for patch antennas in the array. The panel consists of several linear, circular, and rectangular arrays with different geometries. The spacing for each antenna element in an array is $d = \lambda/3.5$. The special design of this array, with predefined antenna slots, enables various scenarios for real-time testing. The plane also has two large arrays of 64 slots with two different spacing,
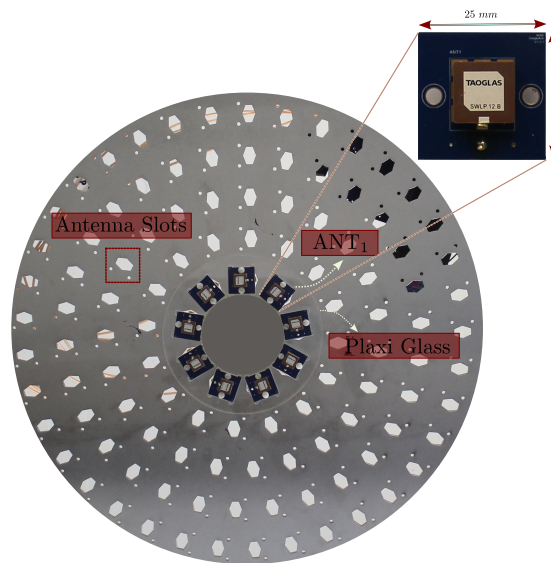
Figure 4.12: A section of the antenna array panel with a circular structure. The panel consists of two circular structures and 4 rectangular arrays, and two linear arrays with 64 antennas in each array.

enabling testing to the BLE-DF protocol's limit. This design separates each antenna from another.

We created a duplicate panel made of plexiglass to fit the antennas in each slot with a laser cutter. Once placed in the slot, each patch antenna will be in direct contact with the metallic panel, and the plastic panel secures the antenna from additional movement or misalignment. This configuration enables a quick and easy possibility of changing the antenna array's geometry while providing more than one antenna array for testing at the time.

We also designed a specially fast switch for 64 antennas, enabling $1\mu s$ sampling and controlling all the elements simultaneously. This antenna array consists of two main groups of switches. We used an SP5T RF [149] switch with 5 symmetric ports and Fast switching time of $265ns$. This switch has an integrated CMOS decoder that facilitates a three-pin low-voltage CMOS control interface. This switch is the main switch presented in figure 4.13.

We also used 5 CHW-SP16TS switches from the CoreHW ™. These switches are specifically designed for BLE-AoA antenna switches. We have 5 sections in the switchboard that each controls 16 antennas. TAB 1 is shown in figure 4.13. The device comprises of very low phase mismatch antenna switch array. This enables real high-accuracy positioning with single or multiple locators. It is a single Chip Antenna Switch with 16 single-ended antenna ports. Theses Antenna switches have a fast start-up time, and very low external component is required. The chip operates on a single positive supply. Thus, an external negative supply is not needed.

Each antenna is separately soldered to a PCB board with an SMA connector at the back.
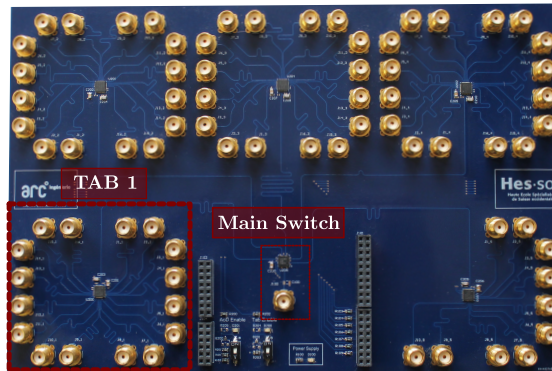
Figure 4.13: A section of the antenna array panel with a circular structure. The panel consists of two circular structures and 4 rectangular arrays, and two linear arrays with 64 antennas in each array.

This design enables the connection and production of an unlimited number of antennas for any desired antenna array geometry. For this purpose, we used SWLP.2450.12.4.B.02 from Taoglas™, which is a $2.4-2.5\ GHz$ WiFi Patch Antenna with a high gain of $2\ dBi$. Table 4.4 shows an example of phase delay for 8 sample antennas in the array when testing from the range of $2.402-2.480\ GHz$ with a spectrum analyzer. The average phase delay is $5.68\ ns$ for the antenna array. These delays are calculated with the connecting cables intact; therefore, it will also show the effects of cables, with an average of $5.67\ ns$ delay.

Table 4.4: Delays of antennas in the panel

Antenna	Delay(ns ±0.01 ns)	Antenna	Delay(ns ±0.01 ns)
1	5.68	5	5.68
2	5.65	6	5.70
3	5.65	7	5.65
4	5.71	8	5.70

4.7   Summary

As mentioned before, this chapter provides the basis for understanding the process of angle estimation for BLE-DF application, from the physical principals to the signal models and estimation algorithms to the antenna array design. As mentioned in section 4.1, different AoA/AoD estimation methods exist; however, the choice is truly bound to the application. The chosen angle estimation method plays an important role in achieving a real-time indoor positioning system. For real-time applications, we need a lightweight algorithm. Moreover, this algorithm should provide high resolution so as to determine the final position of the target accurately. Therefore, we decided to implement all three mentioned algorithms in section 4.4

for real-time angle estimation. We will present a complete comparison between all these three algorithms implemented into our system in Chapter 6.

In the first section of this chapter, we explain the principles of BLE-DF protocol and the details about AoA/AoD packets. One of the important aspects of these packets is the antenna pattern that can be chosen. In the upcoming chapters (chapter 6), we will study the effect of antenna patterns on the whole system's performance. The chapter also outlines the varying data packets depending on the selected system architecture and switching rate. Both AoA and AoD architectures are studied, and their respective results will be compared in chapters 5 and 6. This chapter serves as a foundation for comprehending the differences between each architecture.

An additional crucial aspect explored in this chapter is the comprehension of the physics underlying the use of antenna arrays for angle estimation purposes. Section 4.3 presents a signal model to formulate antenna arrays based on their shape for angle estimation algorithms. Three main shapes of antenna arrays, namely ULA, URA, and UCA, are utilized, with each shape possessing unique performance characteristics. The latter two shapes can provide both azimuth and elevation angle, making the understanding of the physics behind these antenna arrays essential for angle estimation algorithms.

Section 4.4 introduces the fundamental concepts of the three main algorithms that will be utilized for angle estimation. A pseudocode is provided for each algorithm to compute the angle. In the next chapter, the received packets from the BLE receiver will be formulated to construct the auto-covariance matrix. This process involves the conversion of the received signal and its formulation for the algorithm, which is a crucial step that will be covered in the following chapter. The main contribution of this section is the implementation of this lightweight algorithm for three different antenna array structures.

In section 4.6, the focus was on the design criteria for antenna arrays used in BLE-DF applications. The switching of antennas in the transmitter and the spacing between the antennas are two deterministic aspects that were identified as important. The TI BOOSTXL antenna array was initially explored to understand the abilities and limitations of the new protocol, and this was followed by a progressive approach to designing new antenna arrays, with each step addressing possible problems. Two antenna arrays, each with its own advantages and disadvantages, were designed and presented in section 4.6.2 and section 4.6.3. The antenna array in section 4.6.2 is suitable for AoA applications due to its faster switches, more antennas, and low delay. In contrast, the modular design presented in section 4.6.3 can control more antennas of different shapes and can be used with several transmitters to create multiple anchors simultaneously, making it highly flexible for testing and evaluating other desired antenna configurations. The sections also contribute to the thesis by highlighting the important characteristics of these antenna arrays for BLE-DF applications. The design of the antenna array presented in 4.6.2 is another contribution of this thesis. To improve this design, we collaborated with HE-Arc to design another array using fast switches, which is another

contribution of this work.

5 System Architecture and Sample Correction

In Chapter 4 the development and implementation of two specific antenna arrays and switches were presented. This section will detail the system structure and data processing steps. Firstly, we will discuss the key differences between the two system architectures, highlighting the main characteristics of the AoA or AoD architecture and their respective benefits. We will then provide a detailed explanation of the architecture of the different systems used for angle estimation, as well as the distinctions between the two development kits utilized for generating and transmitting signals. Following this, we will explain the main concept behind gathering IQ samples and the subsequent steps for processing these data for further analysis. Lastly, we will guide the readers through the data preparation process for AoA algorithms.

5.1   AoA/ AoD Device Roles and Responsibilities

Bluetooth Core specifications v5.1 enable the BLE controller to use both the Angle of Arrival (AoA) and the Angle of Departure (AoD). This section explains the technical differences between these two configurations and the decision to choose between these two options. In each case, special signals are transmitted. In AoA, the receiver consists of multiple antennas, and in AoD, it's the transmitting device (figure 5.1).

The antenna switching in each device is according to the specified pattern in HCI configuration commands which follows strict timing (figure 4.1). When performing IQ sampling, similarly strict timing rules apply but with some variation possible according to configuration. How these rules are applied and which device is subject to which rules depends on whether AoA or AoD is being used and whether the device is transmitting or receiving. This will change the transmitted signal in two configurations. In section 4.2.1, we explain the differences between these timings.

Antenna switching applies to devices that contain an antenna array. This is the transmitting device when utilizing the AoD method or the receiving device performing AoA. Conversely, a device that does not contain an antenna array will continuously transmit the Constant Tone
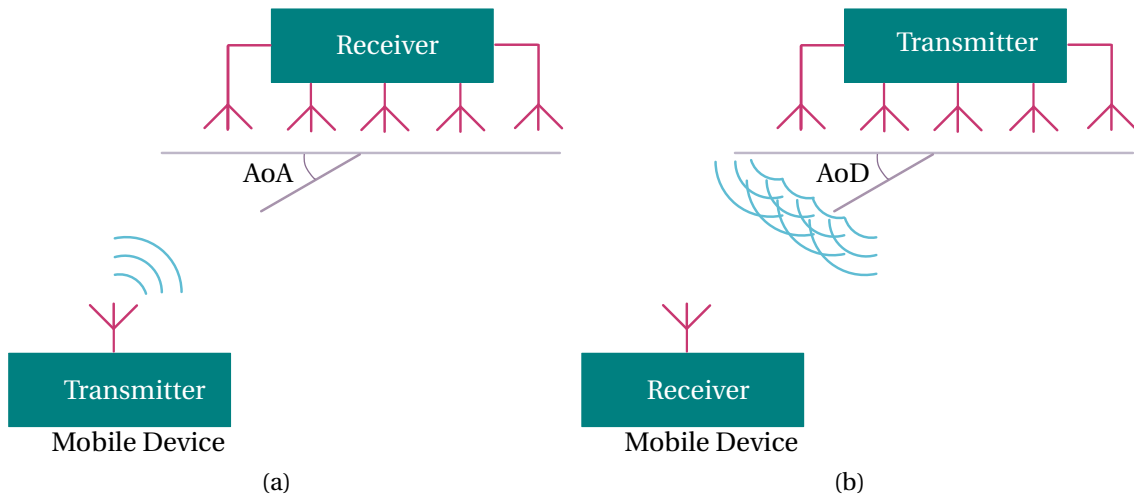
Figure 5.1: The AoA and AoA configuration of the mobile tag and the antenna array. a) In AoA, the antenna array receives the signal, while the transmitter acts as a Beacon with a single antenna. b) In AoD, the transmitter is a Beacon with multiple antennas and does not perform IQ sampling, while the receiver can be a mobile device or an observer with a single antenna, and it performs the sampling.

Extension without any antenna switching. IQ sampling is always performed by the receiving device, irrespective of the number of antennae it contains.

	AoA		AoD	
	Switching	Sampling	Switching	Sampling
Transmitter	-	-	X	-
Receiver	X	X	-	X

Table 5.1: Switching and sampling roles and responsibilities [68]

Table 5.1 provides a simple summary of the roles and responsibilities of devices with respect to both antenna switching and IQ sampling. When using AoA and receiving a CTE, antenna switching takes place according to the configuration provided by the host via HCI commands. When transmitting, no antenna switching is required. In this case, the mobile device or the tag, is sending a beacon using a single antenna (figure 5.1a). This method has many applications, such as asset tracking or point of interest (PoI).

In the case of AoD (figure 5.1b), antenna switching is required when transmitting a CTE but not when receiving. In this case, where the transmitter contains the antenna array, the receiver performs IQ sampling and takes measurements from its single antenna. Then it uses the details of the design of the remote antenna array, to attribute the measurements to a particular antenna in the transmitter's array. This method has many applications such as way-finding and tracking.

These are important differences between the two cases of AoD and AoA. Based on the application, both solutions can be appropriate. Bluetooth Core Specification v5.1 allows either connection-oriented or connectionless communication. In our work, we are using connection-oriented AoA and AoD applications.

	AoA	**AoD**
Conection-less	Controller support is optional	Controller support is optional. AoD will tend to use connection-less communication
Connection-Oriented	Controller support is optional. AoA will tend to use connection-oriented communication.	Controller support is optional

Table 5.2: AoA and AoD communication options

Table 5.2 shows the four possible permutations of AoA/AoD and connectionless/connection-oriented communication. All are valid and in all cases, support in the Bluetooth LE controller is optional [68]. As explained in section 5.1, two different configurations of AoA and AoD are used for the antenna arrays. We use two different modules to generate the AoA/AoD signals. Consequently, it is necessary to verify the validity of the received signal in each structure. To achieve this, the Texas Instruments TI BOOSTXL antenna array [71] is used as a reference. Later, we use nRF [150] modules because they provide the ability to use more switches and faster-switching slots, enabling us to create an antenna array that supports up to 74 antennas and a switch capable of handling all with a switching slot of $1\mu s$.

5.2 Architecture of the System

To test the performance of the antenna arrays that have been designed, we conducted a series of experiments. We tested them in an indoor environment and an anechoic chamber. In all these experiments, the receiver and the transmitter were 2.5 m far apart and about 1 m above the ground. Figure 5.2 shows a case where a TI BOOSTXL antenna array is used with a mobile tag. As presented, there is a 45° shift between the array position and the tag's position, which should be compensated in the calculations.

In these experiments, we test an AoA configuration, where the antenna array takes the role of the receiver, and a mobile tag transmits the AoA beacons. Figure 5.1 illustrates the two different architectures of BLE-DF including AoD or AoA. Based on the antenna array, we use two different chips that create the BLE AoA/AoD packets. In the next subsections, we explain these two systems and the advantage and disadvantages of both systems. The general architecture of both systems remains the same in the case of AoA, but the software application is different.
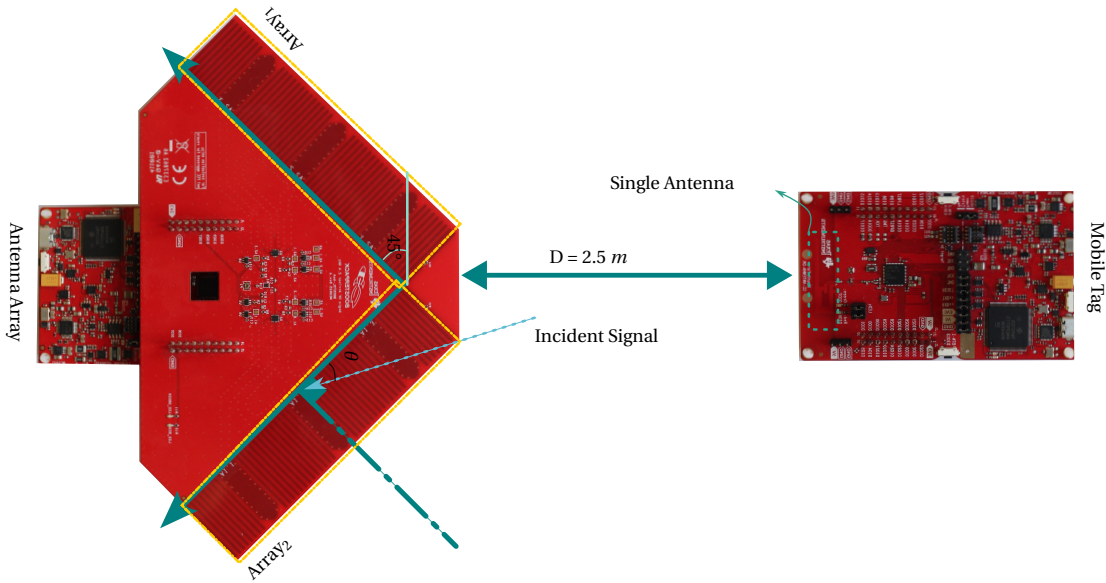
Figure 5.2: The TI modules and their relative position for testing. In this configuration, there is a 45° angle between each array and the tag

5.2.1 Texas Instrument System

In our experiments, we use the LAUNCHXL_CC26XR1 Evaluation board from Texas Instrument [151], a development kit consisting of a wireless MCU and support for Bluetooth, Zigbee, and Thread. The Bluetooth Low Energy device has an extremely low standby current (0.94 μA) with an excellent sensitivity of -97 dBm enabling a longer range with a max +5 dBm output power. The module has a 48 MHz Arm®Cortex®-M4F processor. This module has a total of 5 GPIOS for switching the antennas in the array. Also, it uses the SimpleLink™ CC13x2 and CC26x2 Software Development Kit (SDK). We used this module to control the TI BOOSTXL and e-lib antenna array with AoA configuration. We also used another chip to act as the tag. Then we collected the data for further analysis. To collect the data, we used the SDK and saved the IQ samples in real-time for further analysis.

The TX and RX microcontrollers require modifications on the antenna array arrangement while using the TI LAUNCHXL modules for the e-lib antenna array. We defined the specific pattern to control four antennas in the array. These modifications with this system are not changeable after flashing the chip; therefore, we need a new build with a new antenna arrangement. Moreover, the TI LAUNCHXL has only five active GPIOs for controlling the antenna patterns; therefore, we decided to use another system that will provide more options for various configurations of the antenna array.
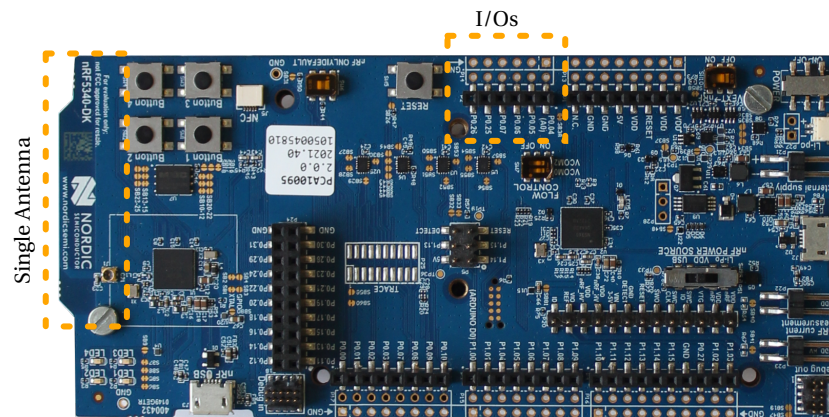
Figure 5.3: A nRF5340 Development Kit and its I/Os for antenna control

5.2.2   nRF System

For the reasons mentioned above, we use the Nordic nRF5340 Development Kit [150] with two Arm®Cortex®M33 processors (figure 5.3). The nRF5340 SoC supports an extensive range of wireless protocols [150]. It supports Bluetooth Low Energy and is capable of all AoA and AoD roles in Bluetooth Direction Finding. It provides us with 7 GPIOs to control antennas in an array. Therefore, we can control 74 antennas in the antenna panel with this module. nRF52 series use special development software called nRF Connect SDK. The nRF Connect SDK is the software development kit for the nRF5340 SoC, offering a complete solution that integrates the Zephyr RTOS, protocol stacks, application samples, and hardware drivers.

Zephyr is a Real-Time Operating System (RTOS) optimized for resource-constrained devices, across multiple architectures [152]. Zephyr is an open-source project that supports new hardware, developer tools, sensors, and device drivers. It also frequently incorporates enhancements in security, device management capabilities, connectivity stacks, and file systems. Zephyr is a full-featured OS with an architecture that allows developers to focus on applications such as Bluetooth. Zephyr uses a Device Tree Source (DTS) and is highly configurable and modular, these features simplify the transformation of one application from one module to another. As a result, using the nRF system provides more freedom to create our new application for BLE AoA/AoD. So, we are using this module to control our fast switch with both AoA and AoD configurations.

The collaboration with HE-Arc, university of applied science has resulted in the design and development of a program that consists of two cores; the application and the network [148]. The network executes the Bluetooth controller and the application lies on top of the Bluetooth host (figure 5.4). In the network core, the application is similar for both the transmitter and the receiver. It initializes the Bluetooth controller and then waits in an infinite loop for a message from the application core or the Bluetooth controller. The application core can send data to two Remote Processor Messaging (RPMsg) endpoints, primarily for Bluetooth communication and then for custom information communication.
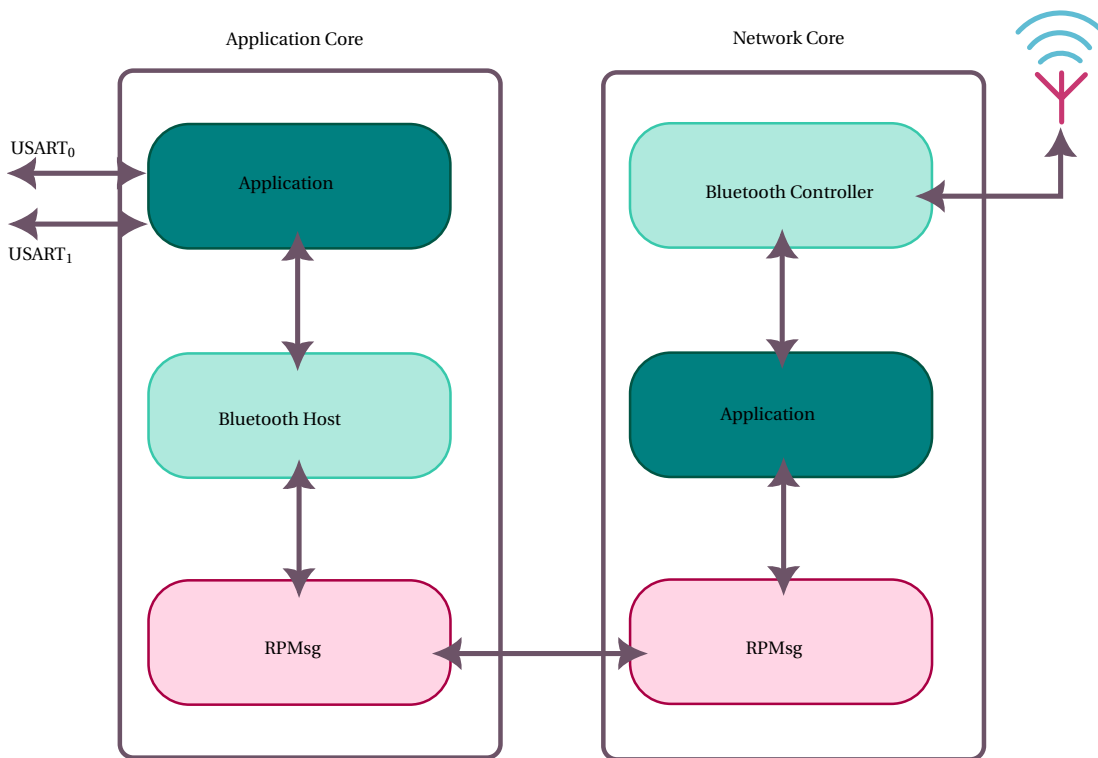
Figure 5.4: nRF5340 core representation. The module consists of two main cores, the application and the network. [148]

In the application core (figure 5.4), the software is divided into three sections Interface, Modules, and Management. The Interface handles the direct communications with the chips. The Modules handle the information about the component logic and the chip. Finally, the management handles the behavior of the whole system.

The Interface layer is controlled by Zephyr. The Modules layer is identical for both the transmitter and receiver. The code executed in the Manager layer differs, as it represents the general behavior of the program. With this configuration, we are now able to control the antenna pattern and the switches after the code is executed and we can easily change this pattern while testing without reconfiguration the chip. For more information, please check [148]. With this system, we are able to choose between AoA/AoD and 1 μs or 2 μs sampling slots as well as change the sampling rate and the CTE time. CTE-Time defines the length of the CTE in 8 μs units between 2 and 20 units, reflecting the 16 μs and 160 μs CTE duration.

After understanding the fundamental differences between these two BLE modules, it is essential to understand the data structure and important processing steps before being able to correctly analyze the raw IQ samples we receive from the BLE modules. In each interval of receiving data, we store several important values in a data frame. These values are sample index, I and Q, channel number, RSSI, and packet number.
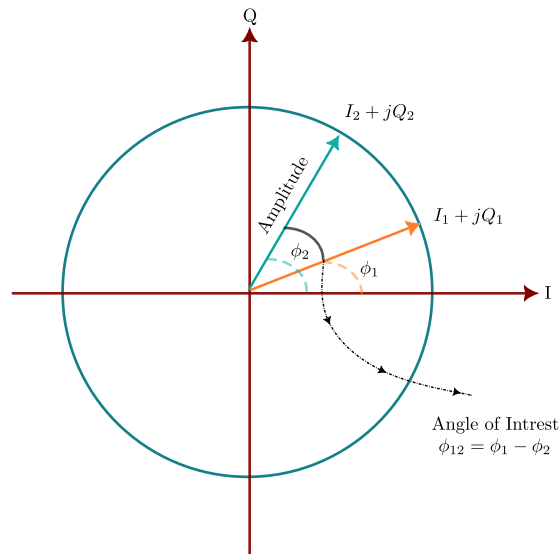
Figure 5.5: The IQ samples in the cartesian coordinates, the phase of each sample is shown in the graph. Each IQ sample forms an angle with the vertical axis which is called the phase ϕ_i. The phase difference between these two samples represent the AoA

5.3 Data Preparation

This section focuses on the preparation of data for further analysis. Raw IQ samples are received from BLE modules, which require modifications for accurate analysis. Firstly, IQ sampling is introduced, and the received data of the TI system is presented. The method of pre-processing is then explored, which includes several steps such as reference frequency evaluation, extraction of valid IQ samples based on the configuration, phase modification process, and correlation matrix configuration. We explained this method in our published papers such as [153, 154]. The following sections will be dedicated to presenting the pre-processing of the data before applying the angle estimation method, which is one of the main contributions of this thesis.

5.3.1 IQ Sampling

BLE-DF uses In-phase and Quadrature (IQ) Sampling. The receiver proceeds with the signal by taking a number of phase and amplitude measurements at precise intervals. In IQ sampling, the receiver mixes the incoming signal with a local oscillator at 0° (I) and 90° (Q) offsets, which creates two orthogonal components known as In-phase (I) and Quadrature (Q) samples. A single IQ sample consists of the wave's amplitude and phase angle represented as a set of cartesian coordinates [145]. The IQ samples can be converted to Cartesian in the form of an imaginary number. Therefore we can calculate the phase of each sample as $\phi = arctan(Q/I)$ and the magnitude as $\sqrt{I^2 + Q^2}$.

Figure 5.6 presents the raw IQ samples transmitted by the TI LAUNCHXL module and received
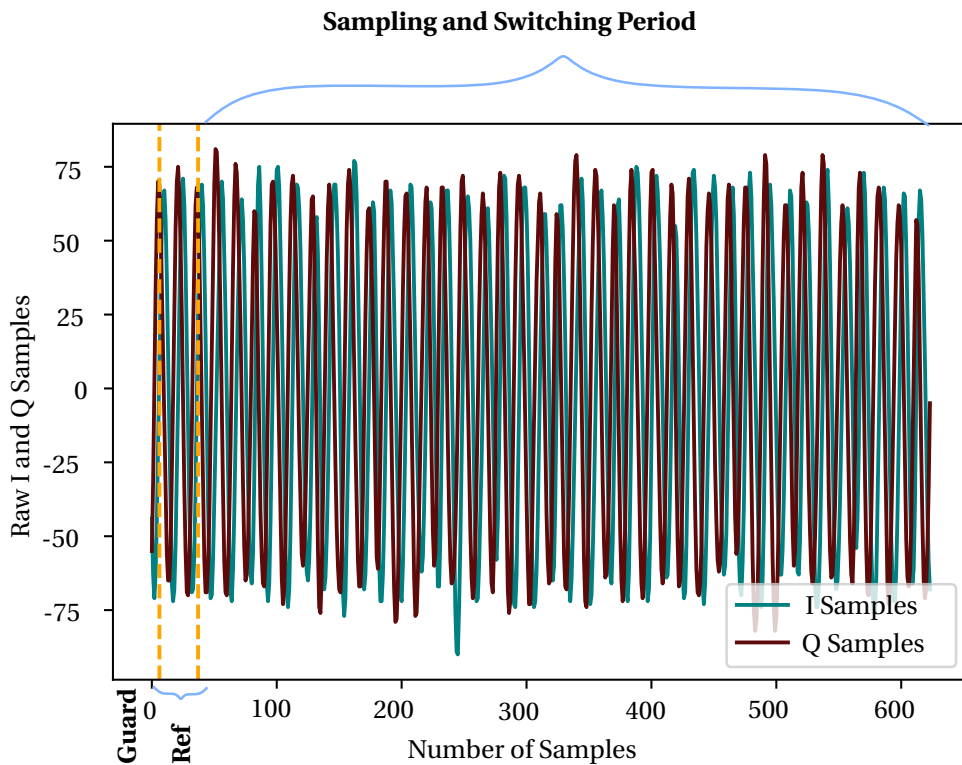
Figure 5.6: The received I and Q samples from one packet of data with a sampling rate of 4 MHz and the sampling slots of 2 μs and a CTE with the length of 160 μs. The presented samples are raw data from an indoor environment.

by the TI BOOSTXL module. This figure perfectly shows that there is a small phase difference between these signals which is the essential basis for the phase calculation. In this figure, we presented all three different parts of the received signal, including the guard, reference, and sampling period. This is the received IQ samples for a sampling rate of 4 MHz and the sampling slots of 2 μs and a CTE with the length of 160 μs. Therefore, with this configuration, the total number of samples is 624.

Figure 5.7 presents three randomly picked packets of raw data collected from TI BOOSTXL module. In these figures, we can see that at certain points, some of the data is missed, and the raw data is not complete. Some of these points are shown by yellow circles. Not all the collected data follows the perfect sequence. What we cannot see, is the data duplicates. Data duplicates are when we have exactly the same data including, packet number, channel, and sample index. Before, any data analytics, these data points should be removed from the data. Otherwise, the packets may look very distorted. Therefore, in figure 5.7, we first removed data duplicates before presenting the data. So, we might have some missing data points. These figures were sampled at three different channels (2, 30, 21). As a result, we don't keep these packets as valid packets when the missed data is within the sampling slots. Even though this behavior is not very repetitive (around 5 every 800 packets), it indicates a problem in the sampling sequence. Therefore, we exclude these packets to remove errors.
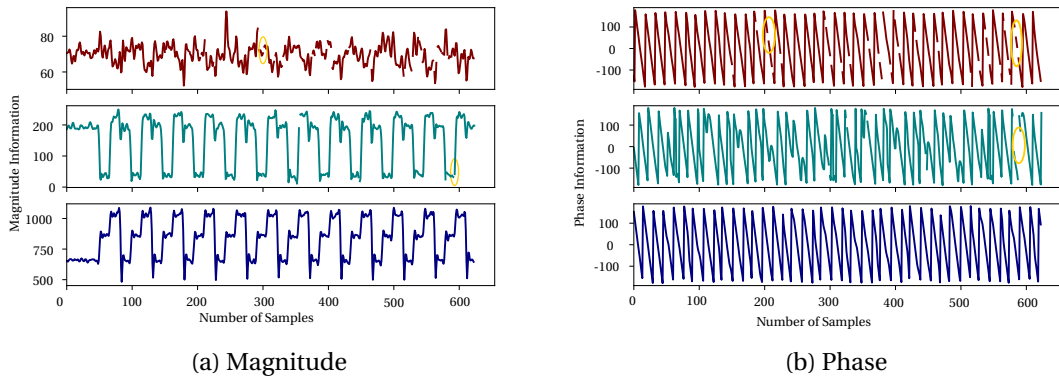
(a) Magnitude   (b) Phase

Figure 5.7: The a) magnitude and b) phase of three random packets of raw IQ data collected with a sampling rate of 4 MHz and the sampling slots of 2 μs and a CTE with the length of 160 μs. These data were collected at channel numbers 2, 30, and 14, respectively

We can see a repetitive behavior of the sampling, which indicates the switching between each antenna. In general, we expect to have approximately a constant value for the magnitude per antenna and during the reference period (Ant_{ref}). However, the red plot is very noisy in figure 5.7a and we cannot see any repetitive pattern on the received signal anymore as well as having a lot of missed samples. Therefore, we are using these properties as a method to validate the received signal. In the next section, we explain different methods we used to eliminate the occurring errors or compensate for inevitable ones.

The phase of the samples is between $-90°$ to $90°$ for all the samples. We expect to see repetitive behavior from the phase as well. During all the sampling and switching slots, we can see phase jumps between the samples. In addition to the missing IQ samples, the phase requires some modifications to compensate for the phase shifts during the sampling period.

5.3.2 Carrier Offset Frequency

The received AoA data packet contains a reference frequency period that we use to determine the validity of the received packet. The reference period has a fixed length of 8 μs in time. However, the number of samples depends on the sampling rate. For BLE-DF, four different sampling rates of $SR = [1, 2, 3, 4]$ MHz exist. Therefore, the number of reference samples is $SR \times 8$. BLE-DF adopts two of the three physical layers of the BLE (LE 1M and LE 2M [66]).

BLE is operated in 2.4 GHz ISM Band (2400 $MHz - 2483.5$ MHz), where the whole range is divided into 40 channels with 2 MHz channel bandwidth each. BLE applies Gaussian Frequency Shift Key (GFSK) modulation scheme with 0.5 standard modulation index to minimize the transceiver complexity. The frequency deviation for LE 1M and ± 250 kHz, while ± 500 kHz for LE 2M.

The CTE is an unmodulated carrier consisting of unwhitened, modulated "1"s where the

receiver samples a waveform offset of 250 kHz from the channel center in 1 $Mbps$ mode, and in 2 $Mbps$ mode samples a waveform offset of 500 kHz from the channel center [66]. The first antenna that is sampled is the reference antenna and during the reference period.

There is generally a frequency offset between the transmitter and receiver which is called Carrier Offset Frequency (COF). This frequency offset can be calculated from the IQ samples in the reference period. We use this frequency offset to compensate for all IQ samples. The frequency offset estimate can be defined by switching back to the reference antenna in one or several later switch slots [155].

We expect this frequency offset to be in the defined range per each data packet. In the initial step, we calculate the frequency of the reference period IQ samples. This frequency should stay in the range, therefore, if the calculated frequency (f_d) is larger than the absolute value of the frequency deviation in each case, we eliminate that specific packet. For 1 μs sampling we have $f_d < 250\ KHz$ and $f_d < 500\ KHz$ for 2 μs. This process makes our calculation more accurate. In 30 batches of data containing 30 data packets, 4-5 packets were outside the discussed bounds. We decided to exclude these packets from our calculations.

To estimate the frequency, we are using a function based on a one-dimensional Discrete Fourier Transform (DFT) with the efficient Fast Fourier Transform (FFT). Since we are analyzing a signal during a very short time of 8 μs, the FFT is not time-consuming. In the case where we have the most number of samples, i.e., with $f_s = 4\ MHz$ sampling, the maximum number of collected IQ samples is $8 \times SR = 32$. (SR being the Sampling Rate and is equal to 4 samples per $\mu\ s$.)

Due to the nature of BLE channel hopping, the Central frequency (f_c) of the signal alters with each channel. Each packet is only sampled through one channel. Therefore, understating these frequency changes and creating a method to compensate for the changes is the key to an accurate angle estimation. We have to make sure that the antenna distancing (d) is less than, $\frac{\lambda}{2} = \frac{c}{2(f_c + f_d)}$ (c being the free space velocity, and λ, is the signal's wavelength). As a result, in the case where the channel number is at its highest (40), we have $\frac{\lambda}{2} = 30000/2(2480 - 0.5) = 6.04\ cm$, which is still within the limits of our design ($d < \frac{\lambda}{2}$). This is the main principle for designing our antenna arrays. Any frequency drift larger than the defined value creates an uncompensated error in the process of AoA estimation. We can use this value to compensate for the frequency drift. Therefore, in every packet, we use the $f_c + f_d$ in our calculation.

Another importance of analyzing the reference period is to calculate the phase and the magnitude of the reference antenna. Therefore, in our process, we also calculate each sample's phase and magnitude for the next step of AoA estimation. We normalize the magnitude per packet 5.3.4.
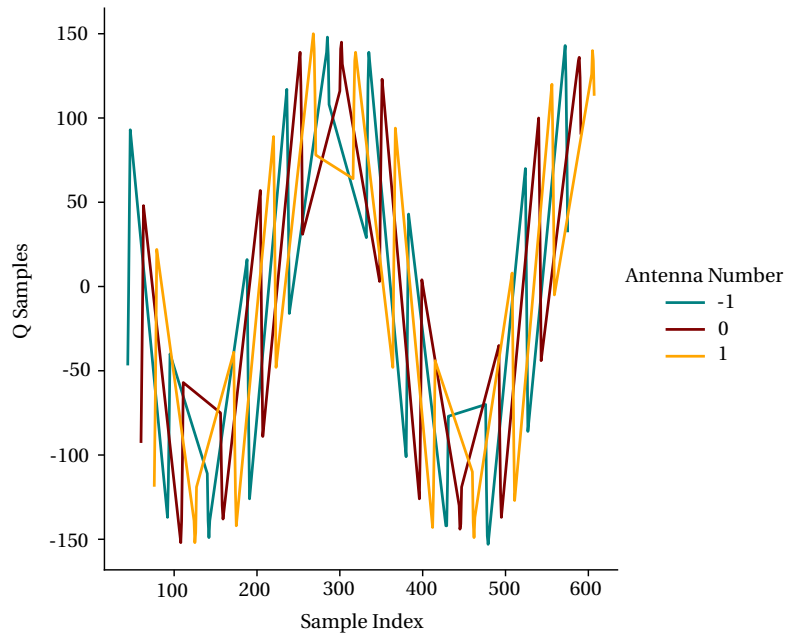
Figure 5.8: Shows the separated Q samples and their respective antenna number in a sample packet of data. Here, $SR = 4$, and the number of antennas is 3. The Q samples are the raw values received in a packet of data.

5.3.3 Extracting valid IQ samples

As mentioned before, in the BLE direction-finding protocol, we will receive all the data from the guard period to the end of one switching period, which can last up to $160\mu s$. Therefore, this data should be refined to access the IQ samples during the sampling slot. While receiving the data in one packet, the antenna sequence is not given. Also, depending on the sampling rate and the switching duration, the starting sample index will differ. Moreover, the guard and the reference period should also be omitted from the beginning of the sample series.

Therefore, knowing the switching sequence, we can arrange the samples in the correct order for each antenna in the array. To illustrate, figure 5.8 shows the valid IQs per packet. For the case of 3 antennas using the Texas Instrument BOOSTXL module. Every four consecutive samples in the packet are from one antenna. The horizontal axis is the sample index of the received IQ sample. This figure shows how each antenna's sample index changes.

The Q vs. I plot of each antenna shows the phase diagram of that antenna per packet (figure 5.9). This figure shows the Q_i vs. I_j for each antenna in the array. This figure 5.9 gives us more information about imperfections that happen during IQ sampling. The I_i (the I samples from i^{th} antenna in the array) and Q_j (the Q samples from j^{th} antenna in the array) create an oval shape in an imaginary plane. We expect the Q vs. I plot to form a circular graph for each antenna. The sub-figures on the right diagonal of figure 5.9 the phase of each antenna. In this figure, the Q vs. Is are normalized for demonstration purposes. The measured phase
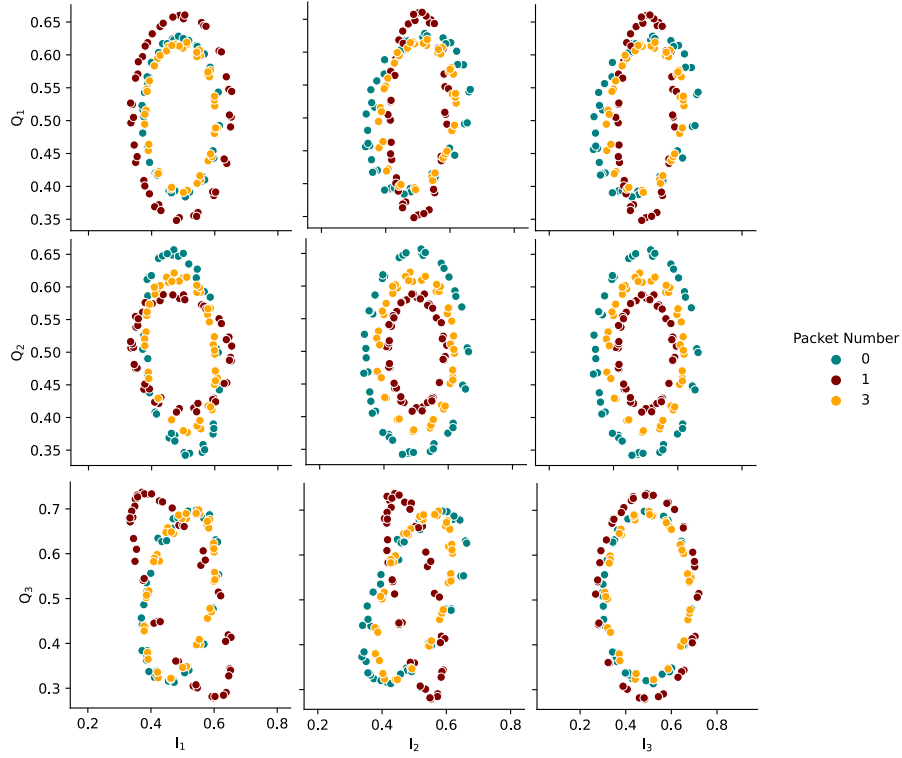
Figure 5.9: Presents the Q vs. I for each antenna in 3 consecutive packets. Here, we separated the IQ samples of each packet to present the imaginary vs real part for each antenna. I and Q are normalized values.

per antenna (ϕ_{ii}) changes during this period. We expect (ϕ_{ii}) to remain linear in a switching period, meaning the Q vs. I should be a circle.

This oval shape in figure 5.9 perfectly shows the effect of phase drift while sampling through the antennas. We can say that the circle is projected along an imaginary vector, where the phase of this vector is ϕ_{ik} and between each pair of adjacent antenna it should be:

$$\phi_{ij} = \phi_{jk} + 2\pi l \tag{5.1}$$

l being a natural number, Ant_{ij} and Ant_{jk} are two pairs of adjacent antennas, meaning that only a phase shift is acceptable in each period. We can see this effect by comparing each antenna's Q vs. I graph with the other pair. We have repeating circles in the map plot, considering that Ant_1 is the reference antenna.

Figure 5.10 also shows the imperfections of phase difference between i^{th} and the jth antenna (ϕ_{ij}) in another way. In figure 5.10, we are presenting the phase of two adjacent antennas with the same spacing. The yellow oval shows the shift in the ϕ_{23} phase in the figure. Even in a valid packet, we can see that the phase plot of two adjacent antennas, can have a huge jump. These jumps can be the result of several things, such as reflections, path loss, multipath, and shift in
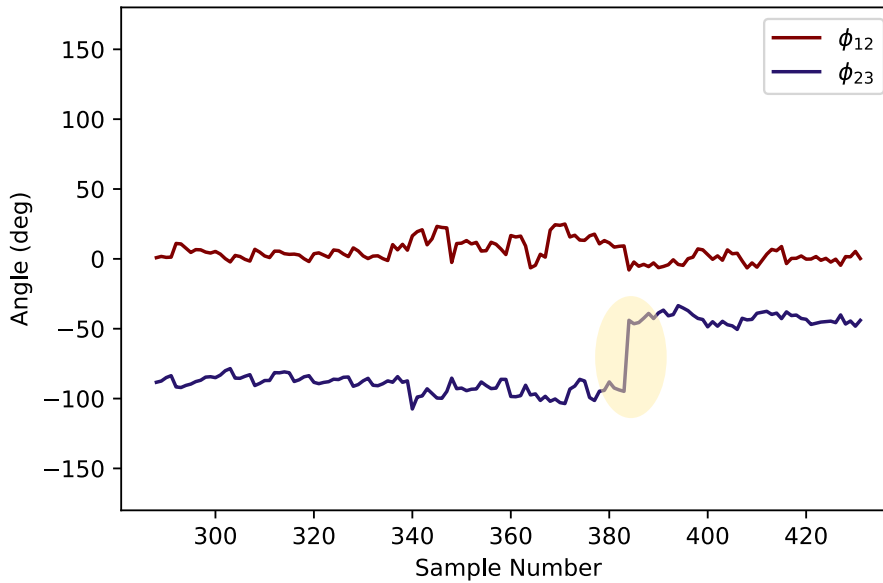
Figure 5.10: Presents the ϕ_{ij} for an array of 3 antennae consisting of two adjacent antennas with the same spacing of $d = 3.5\ cm$

the phase center of the antennas ϕ.

Extracting valid IQ samples is dependent on the sampling rate and the slot duration. Therefore, for each AoA or AoD configuration, we created a method to extract and group all the samples based on their antenna number. We follow the rules, as it is presented in section 4.5.2. For instance, when switching with $SR = 4$, antenna number (M) is 3, and the CTE length is $160\mu\ s$, we have a total of 624 samples. But among all of these samples, only 144 samples are valid IQ samples. We are not using the last 4 samples in each packet to avoid an unequal number of samples per antenna. In reality, these samples actually have the maximum value of phase drift (ϕ_{ii}) because they are the furthest from the reference and the errors accumulate.

5.3.4   Phase Drift Compensation

We expect the phase to be continues among each antenna. There are several reasons for the phase of the received signal to change. One of the main reasons for this change is the multipath effect. Multipath is the propagation phenomenon that results in radio signals' reaching the receiving antenna by two or more paths.

As mentioned above, there are several external reasons for the distortion of the signal. The switches and the whole sampling sequence can also affect the phase. Channel isolation and switching times can create inaccuracies in the received signal phase [66]. Also, the asynchronicity of the transmitter's carrier frequency plays an important role in the frequency
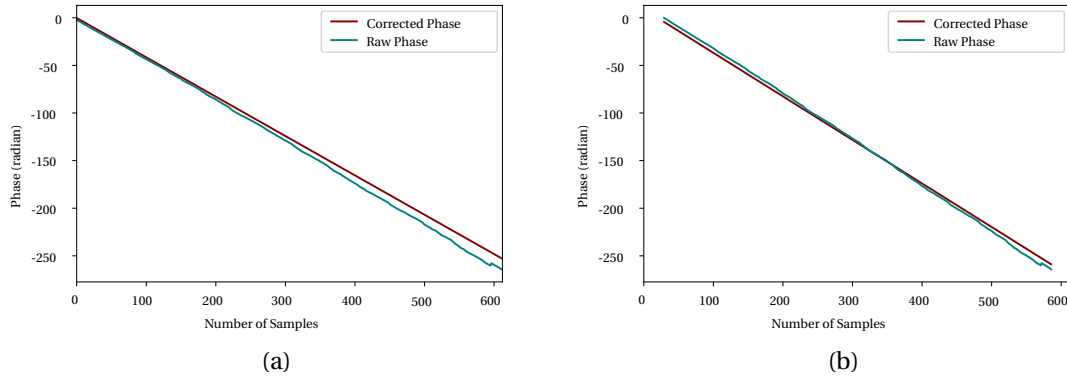
Figure 5.11: The corrected phase (red) and the raw phase (green) of two sample packets, including all IQ samples after the unwrapping function.

shift [156, 73]. All of which will affect the accuracy of the received phase. Figure 5.7b shows these imperfections for some of the samples. In this section, we are proposing a method to correct these phase imperfections for each channel.

Phase correction of IQ samples involves adjusting the phase angle of each sample by a certain amount to compensate for any phase offset that may have occurred during transmission. The phase and magnitude of the reference period serve as a primary guide to predict and correct the phase of the rest of the data packet after confirming the reference period's validity. By using this process, the accuracy of angle estimation can be improved. This process helps improve the accuracy of angle estimation. This will be thoroughly explained in the next chapter. During the reference period, we collect $8 \times SR$ samples. Based on phase evolution, we build a linear model. The switching that happens during the switching slots does not contain valid IQ samples. In the next slot, we collect the IQ samples from the next antenna (for example, antenna 2). In this instance, we compare the phase of antenna 2 with the phase of the signal during the reference period. There is a phase difference between these two samples. This value is, in fact, the phase difference between the two adjacent antennas of i and j, and we call it ϕ_{ij}. In an ideal condition where no multipath exists, and the switching is perfect, this value should be constant for all the adjacent antennas (with the same distance) and should be in a valid range of $[-\pi, \pi]$.

However, in reality, this value changes for each instance. The difference between the anticipated value for the next sample and the actual sample determines the ϕ_{ij}. This value is later used for AoA estimation. However, we look for abnormalities in the primary steps in this phase difference. If $|\phi_{ij}| > \pi$, this indicates an error in the received signal, which can be due to several reasons. As a result, we try to compensate for this error by replacing this value with the previously predicted value in case this happens. This method will decrease the error due to the fact that the time bases in the receiver and the transmitter are different, especially when the phase changes are not major, or such samples are not frequently occurring.
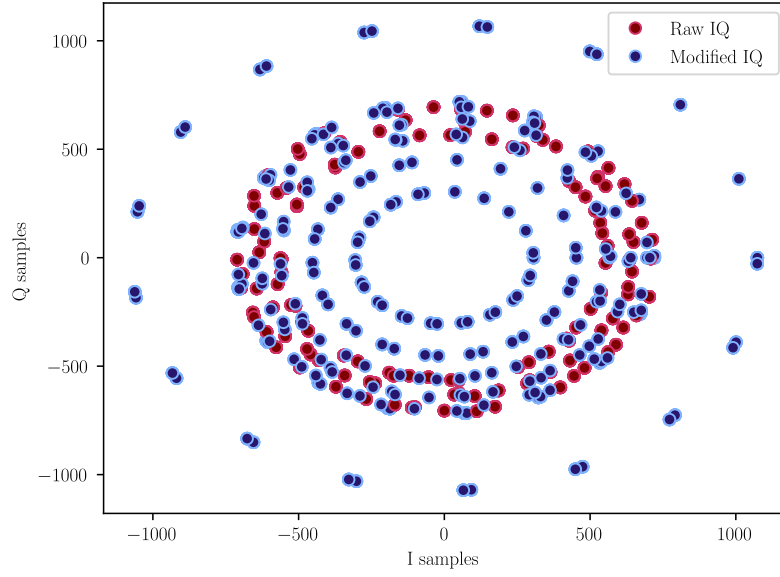
Figure 5.12: Presents the Q vs. I samples of a selected packet. The raw IQ samples (blue), the modified samples (red)

To correctly fit the linear correction, we first unwrap the phase of all the samples. Whenever the jump between two consecutive angles is greater than or equal to π radians, the unwrap function shifts the angles by adding multiples of $\pm 2\pi$ until the jump is less than π. Then, we fit a linear line based on the reference period for the rest of the samples. Figures 5.11a and 5.11b show the fitted line (red) and the unwrapped raw phase of the samples in two different sample packets. The figure shows all the samples in consecutive order. As time passes, the accumulation of switching errors builds up. Therefore, we can see a distinguishable difference between the estimated phase (linear fit) and the recorded value, especially in figure 5.11a. Figure 5.11b also shows another case where the phase changes are more frequent. Therefore, a method to compensate for these ripples is essential to the validity of the angle estimation.

Let I_k and Q_k be the kth sample of the in-phase and quadrature components, respectively, and let ϕ_k be the phase offset associated with that sample. Then the phase-corrected samples, denoted by $\hat{I}_k$ and $\hat{Q}_k$, can be obtained as:

$$\hat{I}_k = |A_{Magnetidue}| \sin(\phi_k) \tag{5.2}$$

$$\hat{Q}_k = |A_{Magnetidue}| \cos(\phi_k) \tag{5.3}$$

The values of ϕ_k are the anticipated values by the linearization method. Therefore, we have:

$$\hat{I}_k^2 + \hat{Q}_k^2 = I_k^2 + Q_k^2 = A_{Magnetidue}^2 \tag{5.4}$$

85

As a result, the new IQ samples $(\hat{I}_k, \hat{Q}_k)$ are generated by this method. Figure 5.12 presents a selected package's IQ samples after applying the phase and magnitude modifications. This specific figure does not include any normalization step. But for visualization purposes, we scaled the samples by order of 2/3 for modified data. The red dots are the raw IQ samples. By modifying the phase and the magnitude of the samples, we are creating a new set of data based on our anticipation of a perfect packet sample $(\hat{I}_k, \hat{Q}_k)$, which are the blue dots. This figure shows that the blue dots are placed in a hypothetical circle while the red dots are not. This means that the modification process corrected the samples. When performing normalization, we normalized the IQ samples in each packet based on the maximum magnitude of the sampled IQ of the respective antenna. In fact, we have $\bar{A}_{Magnetidue} = A_{Mag_i} / A_{Max_i}$. Where the A_{Mag_i} is the magnitude of a sample corresponding to antenna number i and A_{Max_i} is the maximum magnitude of collected IQ corresponding to antenna number i. $\bar{A}_{Magnetidue}$ is the normalized magnitude. Normalizing helps us unify all the collected packets. Also, it avoids generating wrong data for each antenna. Even though the magnitude of the samples is important in the overall localization process (see section 4.4.1), as far as the phase estimation is concerned, it does not play a role.

Figure 5.13 presents the result of a linearization process when using the TI BOOSTXL antenna
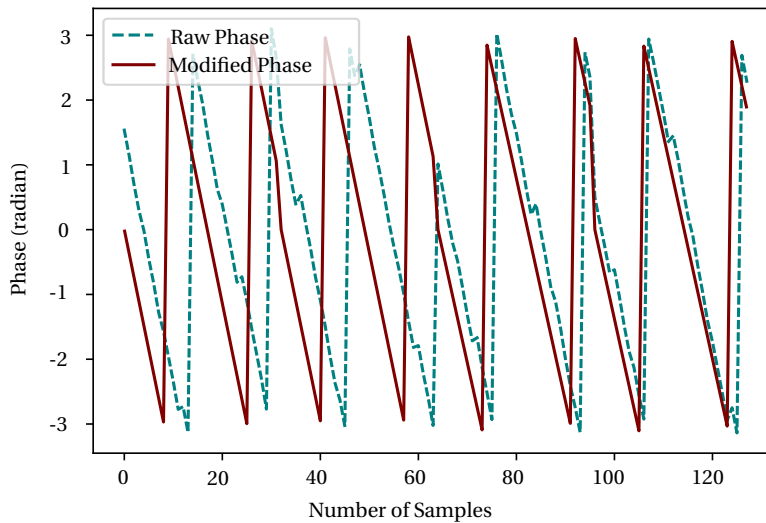
Figure 5.13: The modified phase of a data packet after the phase linearization process

array. This figure only shows the phase of valid IQ samples. The signal is switching between 3 antennas. The raw phase has some ripples during the process. The modified version of the samples tries to compensate for that. The modified version starts from another phase, which is the expected phase of the samples if there were no switching slots. As the phase cannot exceed $\pm\pi/2$, the figure oscillates between these two values. Since the switching slots are omitted from the samples, a jump in the phases is inevitable. This is why a compensation method can improve the accuracy of the estimated angle.

5.4   Bluetooth signal model

As mentioned in the previous sections, there are several steps of pre-processing the IQ data before actually performing the AoA algorithm estimation. Validating the reference period and the size of each packet to eliminate the non-correct packets is the first step. After ensuring, the phase linearization as presented in section 5.3.4, is another important step. Whether we are using the MUSIC algorithm or the ESPRIT, another step is to create the Auto-covariance matrix as an input to the algorithm. After presenting the basics of the BLE signal, we propose a signal model for the received samples that can be used as an input for the angle estimation algorithm.

5.4.1   Transmitter Signal

BLE transmits at 37 channels of the ISM band (3 are reserved for advertisement), where each channel is sent through a pseudo-random channel selection order. Figure 5.14 shows a blog diagram of the generated signal by the BLE transmitter as well as the BLE channel. If we assume the baseband transmitted signal is $s_b(t)$, therefore, we have:

$$s_b(t) = s_i(t) + js_q(t) = \sqrt{\frac{2E}{T}}(cos(\phi(t) + \phi_0) + jsin(\phi(t) + \phi_0)) \tag{5.5}$$

This equation is the basis of having the I and Q samples. Regarding the fact that GFSK modulation only affects the phase of the signal, the E and T are the energy and the period of the transmitted signal and are constant. ϕ_0 is the initial phase of the transmitted signal and $\phi(t)$ is:

$$\phi(t) = \frac{\pi\iota}{T} \int_{\infty}^{t} \sum_{\infty}^{\infty} s[n]g(\tau - n\tau)d\tau \tag{5.6}$$

 Where ι is the modulation index ($0.45 < \iota < 0.55$) in the BLE standard. $s[n] = \pm 1$ is the baseband pulse sequence, and $g[k]$ is the Gaussian Filter in discrete time with a sampling period of T_g with the mean of zero and variance of σ. Then, the transmitted signal is $s(t) = $ Re($s_b(t)e^{2\pi f_c t}$) and we have:

$$s(t) = \sqrt{\frac{\pi\iota}{T}}cos(2\pi f_c t + \phi(t) + \phi_0) \tag{5.7}$$

Where $2.4 \leq f_c \leq 2.48$ is the carrier frequency.

5.4.2   Channel Model

At any given time, N signal ($s(t)$) is transmitted through the channel. In each path the signal passes through, the transmitted signal becomes weaker, and finally, an attenuated version of

BLE Wireless Channel
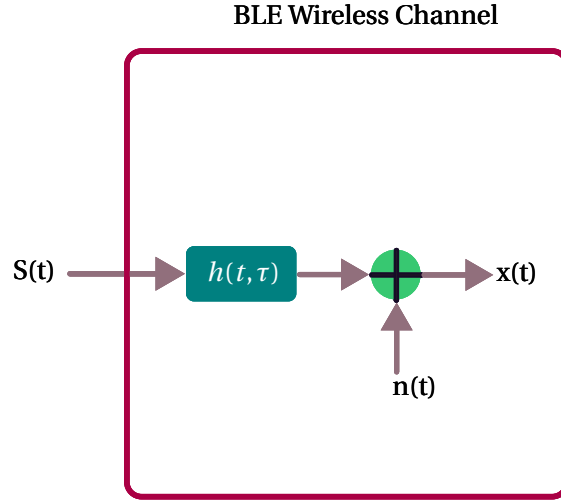
Figure 5.14: The block diagram of the BLE wireless channel model. The diagram shows how does the noise is introduced to the system through the channel model.

the signal reaches the receiver. The baseband channel response of the transmitted response is $h_b(t, \tau)$, which is a Complex Finite Impulse Response (FIR) that illustrates both the multipath and path loss on the transmitted signal as follows:

$$h_b(t, \tau) = \sum_{k=1}^{N} \gamma_k(t, \tau) e^{-j\theta_k(t)} \sigma(t - \tau_k(t)) \tag{5.8}$$

Where $\tau_k(t)$, $\theta_k(t) = 2\pi f_c \tau_k(t)$, and $\gamma_k(t, \tau)$ denotes the kth path delay, phase shift, and path attenuation, respectively. In an RSSI-based localization, the system measures the wireless channel's $|\gamma_k(t, \tau)|$ absolute value.

let γ denote the attenuation experienced at the first antenna by the signal traveling along the k_{th} path. As a result, the attenuation at the second antenna in the array is the same except for an additional phase shift due to the additional distance traveled by the signal, which depends on d and θ_k. For a single path $\gamma(t)$, it is directly dependent on the path as $\frac{\alpha}{d} e^{j2\pi d/\lambda}$ [26, 55]. Where α, d, λ are the signal's attenuation factor, path distance, and wavelength, respectively. But when there are multiple paths, the absolute value of the channel is determined by how the channels along different paths combine. Therefore, we now have the following:

$$\gamma_k(t) = \sum_{k=1}^{K} \frac{\alpha_k}{d_k} e^{j2\pi d_k/\lambda} \tag{5.9}$$

assuming K is the number of paths, and d_k is the length of the kth path, and α_k is attenuation of the signal in the respective path. In this equation, α_k is the attenuation of the received packet in *dBm* and is the collected *RSSI - RF_ Noise*. Where in different conditions, this background noise differs based on the environment.

5.4.3 The Receiver

On the receiver side, we receive a continuous-time signal denoted as $x_b(t)$, which is the distorted version of the transmitted signal. Each antenna in the array receives it by a phase difference. In addition to the wireless multipath fading channels, noise has a destructive impact on the transmitted signal. Therefore, we can write for the received signal:

$$x_b(t) = \frac{1}{2}(s_b(t) * h_b(t, \tau))e^{j2\pi f_d(t)t + \phi_d(t)} + n(t) \tag{5.10}$$

Where $\phi_d(t)$ is the phase shift and $f_d(t)$ is the frequency shift of the signal at the receiver side. As mentioned before in section 5.3.2, the frequency shift is due to the transmitter's carrier frequency asynchronicity. Therefore we have: $s(t - \tau_k(t)) \approx s(t)$ [73, 157]. Therefore, the received signal is [157]:

$$x_b(t) = a(t)s(t) + n(t) = s'(t) + n(t) \tag{5.11}$$

Where $n(t) \sim N(0, \sigma^2)$ is a zero-mean temporarily Additive White Gaussian Noise (AWGN) with the mean of zero and variance of σ^2. Also, we can write the $a(t)$ as the channel model like:

$$a(t) = \sum_{k=1}^{N(t)} \frac{\alpha_k}{d_k} e^{-j\theta_k(t) + j2\pi f_c t + \phi_c(t)} \tag{5.12}$$

5.4.4 Generating the Auto-covariance Matrix

In general, we are solving the question for a 3D environment where K incident signal with azimuth and elevation angles of θ, ϕ respectively reach an array of antenna with $M \times N$ element, where $M \times N > K$. The steering vector of the received signal can be represented for each antenna in the array (chapter 4).

We change the notation of $x_b(t)$ to $x_{mn}(t)$, similarly the attenuation of the received signal at the $(m, n)^{th}$ antenna can be formulated with an extra phase term of $a_{mn}(\theta_k, \phi_k)$. Therefore we can re-write the signal received at the $(m, n)^{th}$ antenna at time t as:

$$x_{mn}(t) = \sum_{k=1}^{K} s_k(t) a_{mn}(\theta_k, \phi_k) + n(t) \tag{5.13}$$

Where $a_{mn}(\theta_k, \phi_k)$ describes the interactions of the incoming signals with the $(n, m)^{th}$ element in the antenna array. Here we are presenting an example based on a URA topology. This vector is also known as the steering vector.

$$a_{mn}(\theta_k, \phi_k) = \sum_{m=1}^{M} \sum_{n=1}^{N} exp(-j\frac{2\pi d}{\lambda} sin(\theta_k)[(m-1)cos(\phi_k) + (n-1)sin(\phi_k)]) \tag{5.14}$$

In equation 5.14, the $\frac{d}{\lambda}$ is dependent on the carrier frequency and shift, meaning the $f_c + f_d$. When $f_d \ll f_c$, the difference is negligible. Also, $s_k(t)$ is a matrix of received signals. We have

as many steering vectors as the propagation paths, and the overall steering matrix A is defined as $A = [a(\theta_1, \phi_1), ..., a(\theta_L, \phi_L)]$ and has the dimension of $(MN) \times L$.

Each propagation path has two parameters associated with the model, attenuation and AoA. The received signal at the antenna array is obtained by the superposition of the signals due to all the paths. Therefore, we can create a vector of complex attenuation $\Gamma = [\gamma_1, ..., \gamma_L]^T$ along L paths where γ is presented in equation 5.9. If we sample the signals at a certain sampling rate and denote n_s^{th} sampled data vector $x_{mn}(t)$ as a snapshot $x[N_s]$, we stack N_s snapshots into a data matrix X. Now we can construct X by using the received signal $x_{mn}(t)$ for each of K sources. Without losing the generality of our assumption, we can write the X for all T collected data as $X = A\Gamma$, where Γ is the complex attenuation/gains matrix and A is the steering matrix. The data we receive from the BLE device provides us with the matrix X, and the goal is to

---

Algorithm 5 Data Extraction and Preparation Algorithm

 1: **Data:** the IQ samples and RSSI from each target to each of the R Anchors and P packets
 2: **Results:** the AoA of the received signal and RSSI of the right packet
 3: **for** each **Anchor** $\in 1, 2, ..., R$ **do**
 4:     Remove the duplicate data
 5:     **for** each packet $p \in 1, 2, ..., P$ **do**
 6:         Remove the Gaurd Period;
 7:         **if** Sample Index missed **then**
 8:             Wrong Packet order;
 9:             $p = +1$;
10:         **else**
11:             Calculate f_d from Reference Period;
12:             **if** $f_d > |250|kHz$ **then**
13:                 Wrong Frequency
14:                 $p = +1$
15:             **else**
16:                 Remove the Reference Period;
17:                 Phase & Magnitude Modification;
18:                 Re-arrange Samples based on Antenna Pattern;
19:                 Construct Matrix X;
20:                 Construct $R_x = XX^H$;
21:                 Compute Eigen Matrix of Noise Subspace $\mathbf{U_n}$;
22:                 Obtain AoA based on Algorithm;
23:             **end if**
24:         **end if**
25:         Append AoA and RSSI from Multiple Packets;
26:     **end for**
27: **end for**

---

estimate the matrix A, from which it's easy to deduct AoA. The rest of the calculations remain the same for different algorithms. The main idea behind the MUSIC algorithm is that the eigenvectors of $R_x = XX^H$ corresponding to the eigenvalue zero if they exist, are orthogonal

to the steering vector. This assumption only applies if the steering matrix A is skinny and full rank. In other words, the number of rows of the steering matrix should be greater than the number of columns in Γ. Physically this translates to having a larger number of sensors than the propagation paths. For instance, this algorithm doesn't function well when having only three antennas in an environment with multiple significant propagation paths (which is quite likely). This is the main reason why we introduce more antennas to the array.

Now that we explained in depth the generation of the auto-covariance matrix of XX^H as an input to the MUSIC algorithm, in the next chapter, we present the performance of the algorithm and the antenna array in various conditions (indoor and controlled environment). The rest of the formulation for angle estimation is covered in the previous chapter. Moreover, we will compare the raw data results with modified IQ samples to present the effect of these modifications on angle estimation.

5.4.5 Data modification and angle estimation algorithm

Now that we explained in detail the process of preparing data for angle estimation, in this section, we present the algorithm we use to summarize the processes. Algorithm 5 presents the steps for preparing the IQ samples for further analysis. This algorithm summarizes all the processes that the raw IQ sample undergoes until the AoA/AoD is estimated. Depending on the chosen algorithm, different methods of calculation are used for AoA estimation. For example, MUSIC (algorithm 2), rootMUSIC (algorithm 4), and ESPRIT (algorithm 3). The initial process of generating valid input for all these algorithms remains the same. As mentioned before, checking the number of samples in a packet and looking for missed points is an initial step for the validity of each packet. Therefore, we exclude those packets where the number of samples is not right. Depending on the CTE and the sampling period, this value varies. Also, the f_d varies depending on the sampling rate as mentioned in section 5.3.2.

In the algorithm 5, steps 1 to 16 creates the raw data and step 17 creates the modified data which includes the phase drift compensation and magnitude reconstruction presented in section 5.3.4. For ease of use, the term "modified data" is used throughout the thesis for this process.

5.5 Summary

To conclude this chapter, we have discussed various stages involved in preparing the received signal for AoA estimation. We began by examining different system architectures and highlighting their differences. We then delved into the BLE modules we used and the reasoning behind their selection. Finally, we presented one of the main contributions of this thesis data preparation outlined in algorithm 5, which included phase drift compensation and generating modified IQ samples to remove multipath errors.

We have discussed the differences between the AoD and AoA architectures in section 5.1. Depending on the needs and requirements of a specific application, one architecture may be more suitable than the other. For example, when dealing with a large number of mobile tags, AoD may be the preferred option for direction finding as it can support a higher number of tags than AoA. However, this requires the calculations and estimation to be performed on the mobile tags, necessitating the use of a lightweight algorithm that can operate in real-time. Choosing an appropriate AoA algorithm compatible with mobile devices consumes minimal energy and can perform calculations quickly without any time delays, which poses a significant challenge. Therefore, we decided to use the three discussed algorithms (chapter 4) to ensure the real-time application of the whole system.

During the initial stages of our research, we utilized the AoA configuration to understand better the limitations of the new BLE protocol. AoA provides the advantage of sampling and switching occurring at the same location, allowing us to eliminate potential errors and focus solely on algorithm development. Therefore, we utilized the AoA structure to validate the performance of our algorithm in eliminating errors that may arise due to differences in location for sampling and switching. For this purpose, we used the TI BOOSTXL antenna array and TI LAUNCHXL module. Even though this module is very practical, it also has several limitations (section 5.2.1). As a result of these limitations, we decided to design our own antenna array called e-lib array in section 4.6.2.

As the progress evolved, we utilized the AoD configuration as a more generic solution to the localization problem. To estimate the direction of multiple mobile tags in an indoor environment, several transmitters are required to switch antennas while all other receivers perform their own sampling based on the received signal, making the AoD configuration more practical. However, the lack of information on the antenna array in the BLE standard means that this information must be provided to the receiver side. This is one of the reasons why we chose to design our own antenna array and switch for transmitting AoD signals. In addition, the use of Nordic modules (nRF53xx) (section 5.2.2) enabled us to develop and design our own firmware to implement the knowledge of the antenna array on the receiver side. With the aid of our collaborators at HE-Arc, we were able to develop an application specifically for this use. After, we changed the application in several aspects to fit our requirements. We changed the data acquisition for the BLE-AoD application and used our own data extraction method. Also, we adjusted the application and the Graphic User Interface (GUI) for 2D antenna arrays and presented the location in real-time in the GUI application. last but not least, we changed certain specifications to allow more than 8 antenna switching by the nRF5340.

Efficiency is a key requirement for our algorithm, which necessitates the creation of corrected input for the calculations. Here lies one of the important contributions of this thesis. In section 5.3, we detail the various refinement and correction processes required for these inputs (IQ samples). After explaining the details of IQ sampling, we identify several reasons for sample distortion in an indoor environment and provide solutions to overcome these challenges. Additionally, we present a method for compensating for inevitable phase ripple and carrier

frequency offset by studying the reference period of the received signal.

After detailing a method for compensating for various errors, we present the Bluetooth signal model for the IQ samples received from the modules. This is another contribution to the process. In this model, we provide a detailed analogy for generating the input matrix for different proposed algorithms in the previous chapter, enabling us to rewrite and adjust these formulations to the BLE IQ samples and create the auto-covariance matrix. Algorithm 5 summarizes all the preprocessing steps required for the received data to prepare it for AoA estimation.

To conclude, the main original contributions of this chapter are two folds. First, the data preparation and modification step enables accurate estimation. Second, modifications to the auto-covariance matrix are being used for angle estimation. This process is explained by presenting the signal model of the Bluetooth Direction Finding.

Another aspect that is worth mentioning is the implementation of three presented algorithms for real-time application. We will elaborate on this matter in the next Chapter. In the next chapter, we will explore the practical effects of these modifications on data collected from different antenna array structures and in two distinct environments. In addition, we will also examine the impact of the antenna pattern, which has been an overlooked factor until now.

6 Angle estimation experiments and data analysis

This chapter focuses on analyzing the received IQ samples from the designed BLE-DF systems. In the previous chapters, we began by introducing the fundamentals of BLE-DF technology and the signal-processing techniques used in the system. We then discussed the process of obtaining the IQ samples from the received signal and the techniques used to extract the AoD/AoA information from the IQ samples. Chapter 5 also covers the challenges associated with analyzing IQ samples, such as noise and interference, and the techniques used to mitigate these challenges.

Antenna arrays, as essential components of BLE-DF systems, provide the necessary spatial diversity to estimate the BLE signal's direction of arrival (DOA). Designing an antenna array for BLE-DF requires a deep understanding of the system's requirements and the antenna array's characteristics, which have been covered in Chapter 3. The DOA resolution is determined by the number of antennas in the array and the spacing between them. Therefore we present three antenna arrays. This chapter investigates the performance of these three antenna arrays for BLE-DF applications in two environments: indoor and an anechoic chamber. The following sections present the experimental setup used to evaluate the performance of the antenna arrays. The setup includes the BLE-DF system, the antenna arrays, and the measurement procedures. The chapter then presents the results of the experiments, showing the DOA estimation for each antenna array in the two different environments. The performance of the three antenna arrays is compared in terms of their accuracy in DOA estimation, and their suitability for specific environments and applications is discussed. The factors contributing to the performance differences among the three antenna arrays in the two environments are also analyzed.

6.1   Antenna Array Performance

Testing the performance of an antenna array in an anechoic chamber is important for several reasons. In an anechoic chamber, there is no external interference, reflections, or multipath propagation. This enables accurate testing of the antenna array's performance, as the signals

(a) TI BOOSTXL

(b) e-lib

(c) Fast Switch
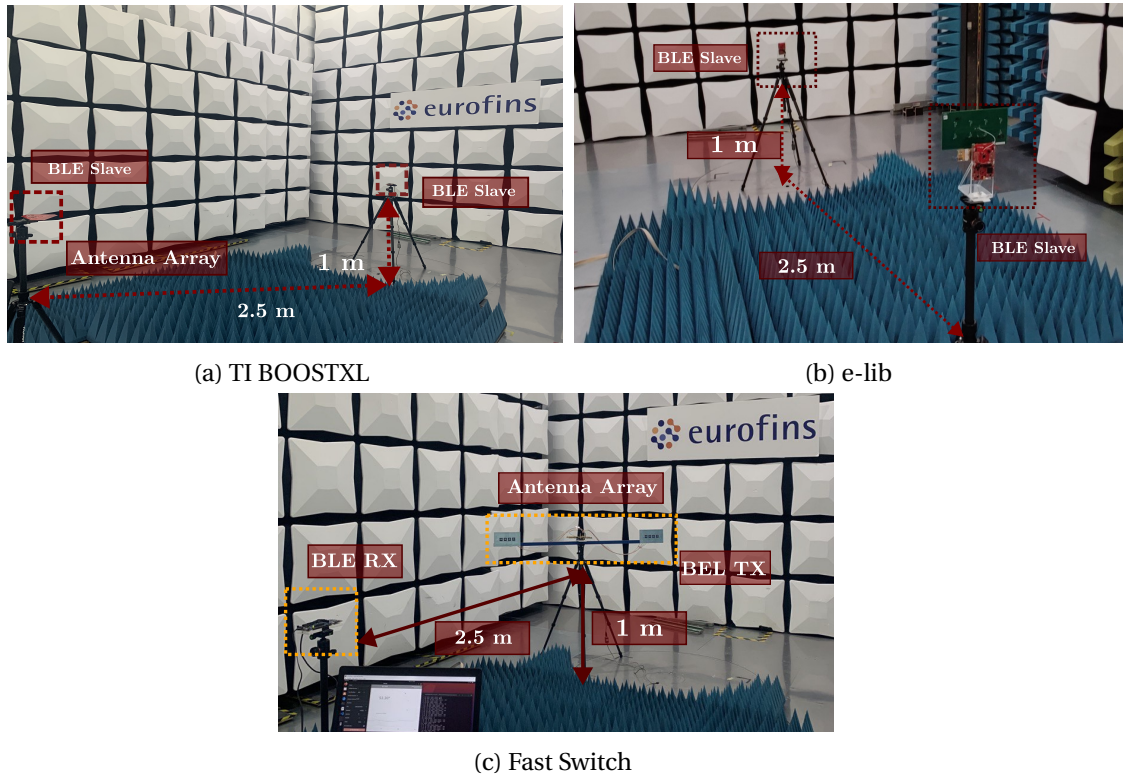
Figure 6.1: Three different antenna arrays being tested in the anechoic chamber.

received are solely from the source being tested. Therefore, we performed experiments in this condition using all three antenna arrays.

6.1.1 Anechoich Chamber Experiments

Testing the performance of an antenna array in an anechoic chamber provides an opportunity to conduct experiments with known propagation paths. Our experiment aimed to evaluate the performance of the antenna array in an environment without multipath interference. The results obtained in the anechoic chamber can serve as a reference point to compare the performance of the antenna array in other environments, such as indoor settings like an office. Therefore, these tests can serve as a benchmark for future experiments. This section presents the results of testing three different antenna arrays the TI BOOSTXL 4.10, the e-lib 4.11 antenna array, and the fast switch module 4.13. We designed a smaller array with four elements compatible with the nRF module [150] to test the fast switch module. The identical antennas were used for all arrays tested in the anechoic chamber. Visuals of the antennas being tested in the anechoic chamber are presented in figure 6.1.

In Figure 6.1, we showcase the three configurations of our antenna arrays tested in an anechoic chamber. Our experiments were conducted at Eurofins Scientific AG to evaluate the performance of the antenna array and the algorithm in a controlled environment. The receiver and

(a) TI BOOSTXL

(b) e-lib

(c) Fast Switch
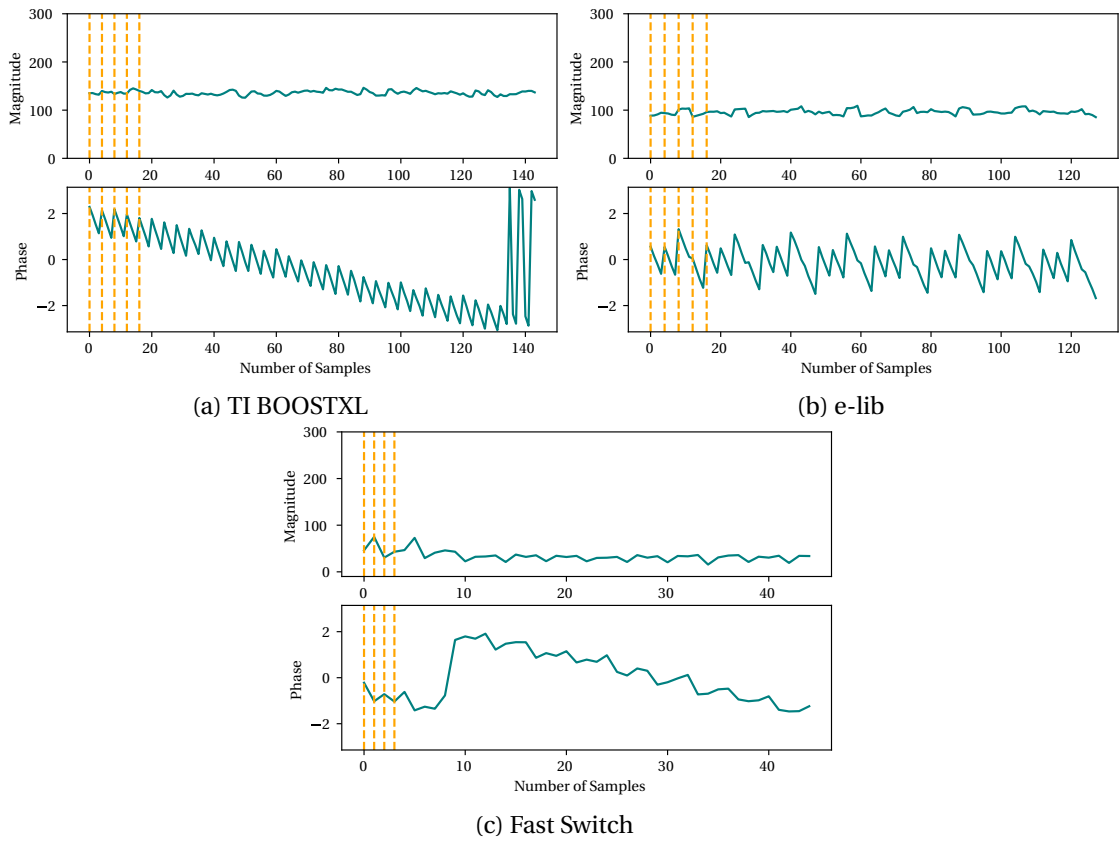
Figure 6.2: The phase and the magnitude of three different antenna arrays being tested in the anechoic chamber.

transmitter were positioned $2.5m$ apart and about $1m$ above the ground, as shown in Figure 6.1. To ensure that phase modification would have an actual impact on angle estimation, we performed a test at known angles.

$2\ \mu s$ sampling slots test all the antenna arrays in these experiments. For the fast switch (figure 6.1c), we are using the AoD architecture, while for the e-lib (figure 6.1b) and the TI's antenna array (figure 6.1a), we are using the AoA configuration.

Phase and Magnitude Analysis in Anechoic Chamber

As mentioned, we decided to test our antenna arrays in an ideal condition, such as an anechoic chamber. In this way, we can ensure the algorithm's performance and gain a reference point to compare the results of the anechoic chamber with the indoor environment tests. In our experiment, we placed the antenna array and the BLE module as depicted in figure 6.1. Figure 6.2, depicts the amplitude and the phase of the raw and valid IQ samples collected from the e-lib antenna array in the anechoic chamber. The magnitude of the samples stays approximately at the same level during the sampling time, which indicates the most important properties of

the anechoic chamber, controlled multipath. The TI module tested the TI and the e-lib array, while the nRF module tested the Fast switch. Therefore, these two modules have different ranges of IQ samples. The magnitude depends on the antennas' power and IQ samples' range by each module. In figure 6.2, We can see the same behavior through all three antenna arrays. The yellow lines separate the samples of each antenna in the array.

As well, in the exact figure 6.2a, the phase of samples changes through each antenna change. We can see the phase ripples here due to the antenna switch. Nevertheless, what is interesting is that the changes through each antenna throughout the sampling time stay approximately constant. In the same figure 6.2b, we can see the phase of each antenna after extracting the switching samples. Each yellow line separates the duration of sampling by an antenna. This figure shows that after the first period of four antennas is passed, the phase has a repetitive pattern through the sampling period. This is a strong indicator that multipath does not affect the phase measurements in an anechoic chamber. In figure 6.2c, we are testing the AoD configuration with a sampling rate of $1\ MHz$. Therefore, each sample represents the phase of one antenna. As a result, in this antenna array, we can see a less repetitive behavior of the phase. However, the phase changes among each antenna generally stay approximately the same through the sampling duration. The difference between each figure is due to the properties of each antenna array.

No phase ripple during the switching is witnessed while using the fast switch 6.2c. In AoD protocol, the receiver only receives the samples; therefore, no data is omitted in switching samples. The yellow lines separate each sampling slot. For figure 6.2a and 6.2b, there are four samples collected during this time, while in 6.2c, only one sample is collected. Switching speed is also doubled in 6.2c, which is another reason for fewer ripples for this antenna array.

Angle Estimation in Anechoic Chamber

Figure 6.3 presents the ESPRIT and MUSIC algorithm results of a sample packet at zero degrees using three different antenna arrays in the anechoic chamber. Here we performed the algorithm on the raw data without any phase modification. Because in this environment, the multipath does not create an error in the signal phase. Also, here the MUSIC spectrum did not undergo any spatial smoothing or processing step.

In general, concluding the performance of the antenna arrays based on only one packet of data is not accurate; therefore, we decided to perform the test with more data packets. For example, figure 6.4 presents the estimated DoAs of more than 30 data packets at zero degrees for each antenna array. The yellow line presents the expected estimated angle, and each green dot represents the peak of the MUSIC spectrum for that respective packet. The red dots presents the estimated angle by the ESPRIT algorithm. We can see that both algorithms at these lower angles are performing close to each other For instance, the estimated angle with these three antenna arrays is respectively $(-1.75°, -2.2°, 0.57°)$ with MUSIC algorithm and $(1.75°, -4.5°, 2.7°)$ with ESPRIT algorithm. So, it is difficult to differentiate the performance of

(a) TI BOOSTXL

(b) e-lib

(c) Fast Switch
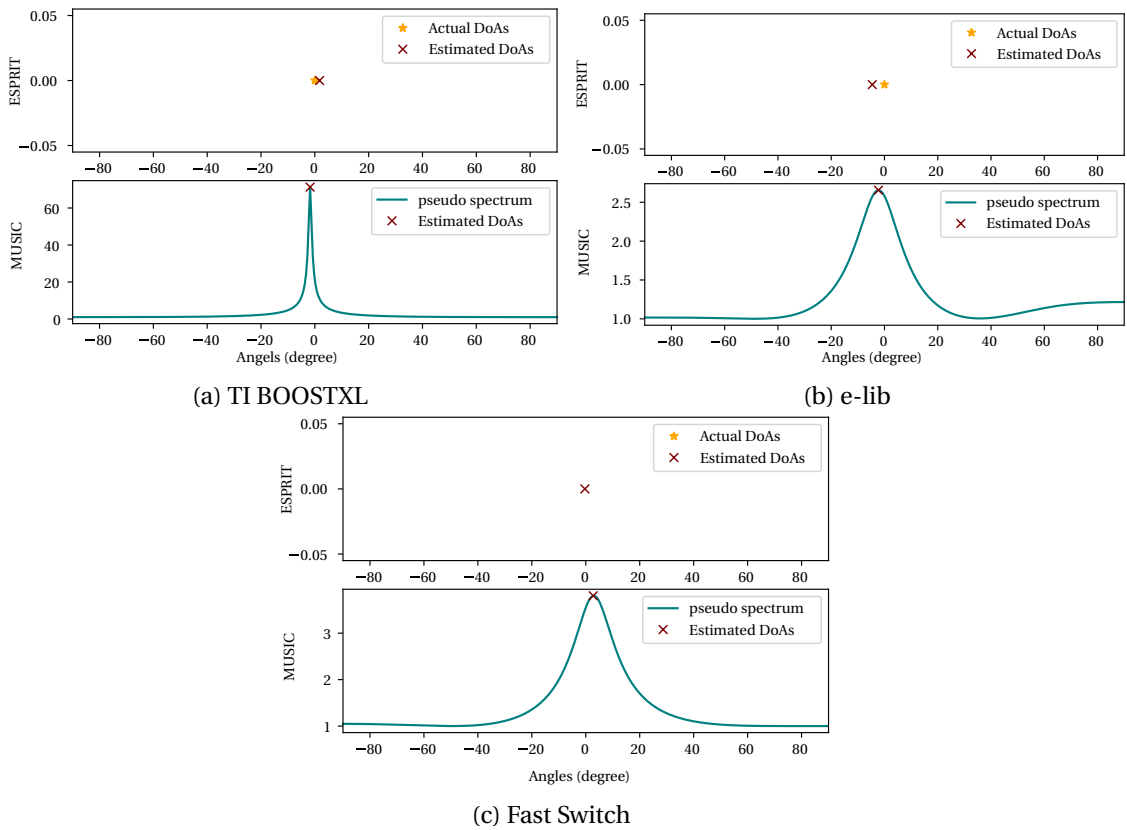
Figure 6.3: The MUSIC and ESPRIT spectrum of a sample data packet in the anechoic chamber using three antenna arrays at zero degrees. The estimated angle with these three antenna arrays is respectively $(-1.75°, -2.2°, 0.57°)$ with MUSIC algorithm and $(1.75°, -4.5°, 2.7°)$ with ESPRIT algorithm.

these two algorithms merely by comparing these results.

We performed a test collecting data at different angles to compare these three antenna arrays at different angles. We collected more than 300 packets at each angle position. With a rotating tripod, we measured the respective angle of the BLE receiver and the transmitter. In our experiment, for the cases of AoA, using Texas Instruments and the e-lib antenna array, we sampled at a 4 MHz sampling rate. For the case of AoD, we sampled at 1 MHz and 2 MHz sampling. Since our final goal is to develop a fast algorithm for AoD detection, we decided to increase the number of data points. As a result, the calculations will take less time to compute.

In figure 6.5a, we collected more than 30 packets and calculated the AoDs with two algorithms. The green line is the estimated AoD by the MUSIC algorithm, and the red line is from the ESPRIT algorithm. The yellow line is the excepted or real angle. As we can see, all three antenna arrays are performing with minimal errors, especially within the range of $\theta < 30°$. The average absolute error for this array is $(7.8°, 8.4°)$ for ESPRIT and MUSIC algorithms,

(a) TI BOOSTXL

(b) e-lib

(c) Fast Switch
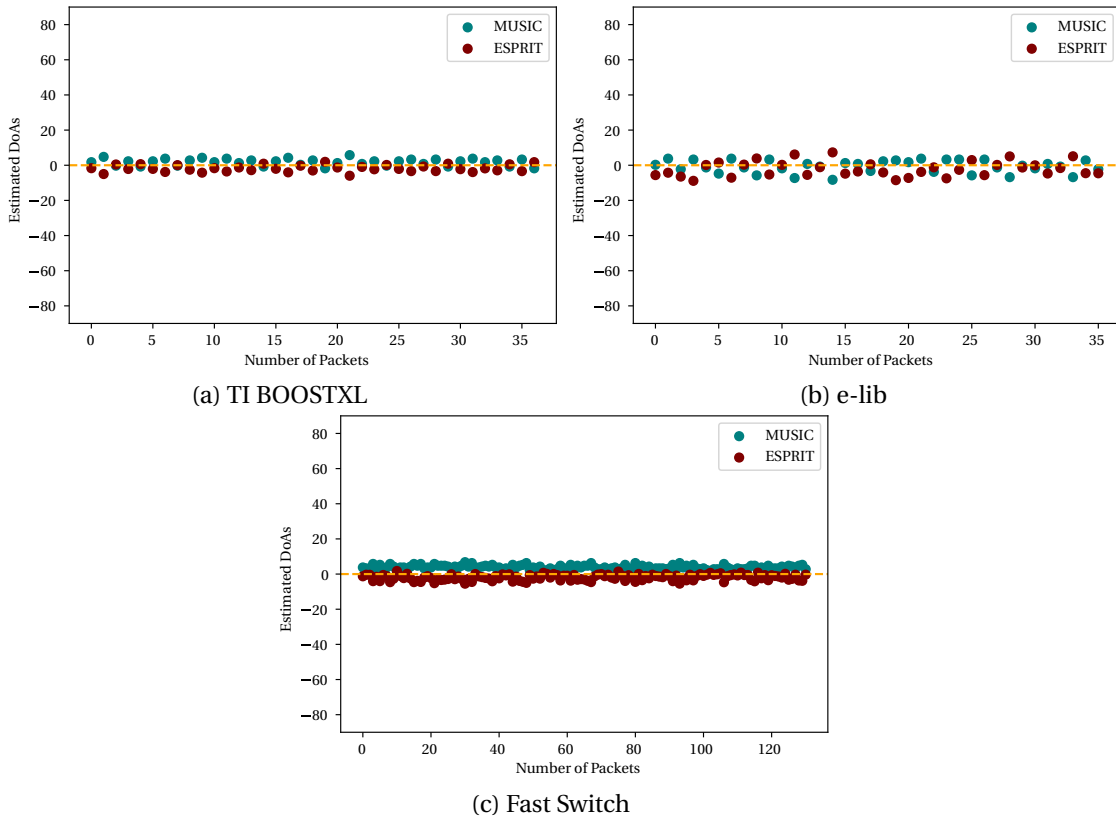
Figure 6.4: The estimated angles by MUSIC and ESPRIT algorithm with three different antenna arrays at zero degrees. The estimated angle with these three antenna arrays is respectively $(0.5°, 2.1°, 4.3°)$ with MUSIC algorithm and $(0.95°, −2.4°, −3.2°)$ with ESPRIT algorithm.

respectively. For the TI array 6.5a, as we diverge from $60°$, the estimated angle is less accurate. The TI antenna array, because of its unique shape, has a minimal error at around $45°$, but at larger angles, $θ > 60°$, its performance declines. For this antenna array, the relative angle between the antenna array and the BLE tag should be $θ' = θ + 45°$. This is because of the shape of the antenna array (figure 5.2).

The e-lib antenna array has more linear behavior (figure 6.5b) in comparison to the TI antenna array and has less error at $θ = 90°$. Each dot in this figure is the average of all collected AoDs at that specific angle. This antenna array's average estimation absolute error is $(5.9°, 3.9°)$ for ESPRIT and MUSIC algorithms, respectively. One factor that is not very visible here is that using the ESPRIT algorithm, it is possible that in equation 4.18, the argument of the sinus function is bigger than 1. Therefore, the algorithm cannot estimate the angle for this case. This happens especially for $θ > 60°$ where it is more probable for the argument in equation 4.18 to exceed the 1. For example, after collecting 52 data packets at $θ = 90°$, the ESPRIT can only estimate 33 packets of data, and the equation 4.18 cannot converge to a meaningful value for the rest of the packets. This is why the MUSIC algorithm is superior to the ESPRIT in larger angles. The same behavior will happen in smaller angles when multipath creates a significant

(a) TI BOOSTXL

(b) e-lib
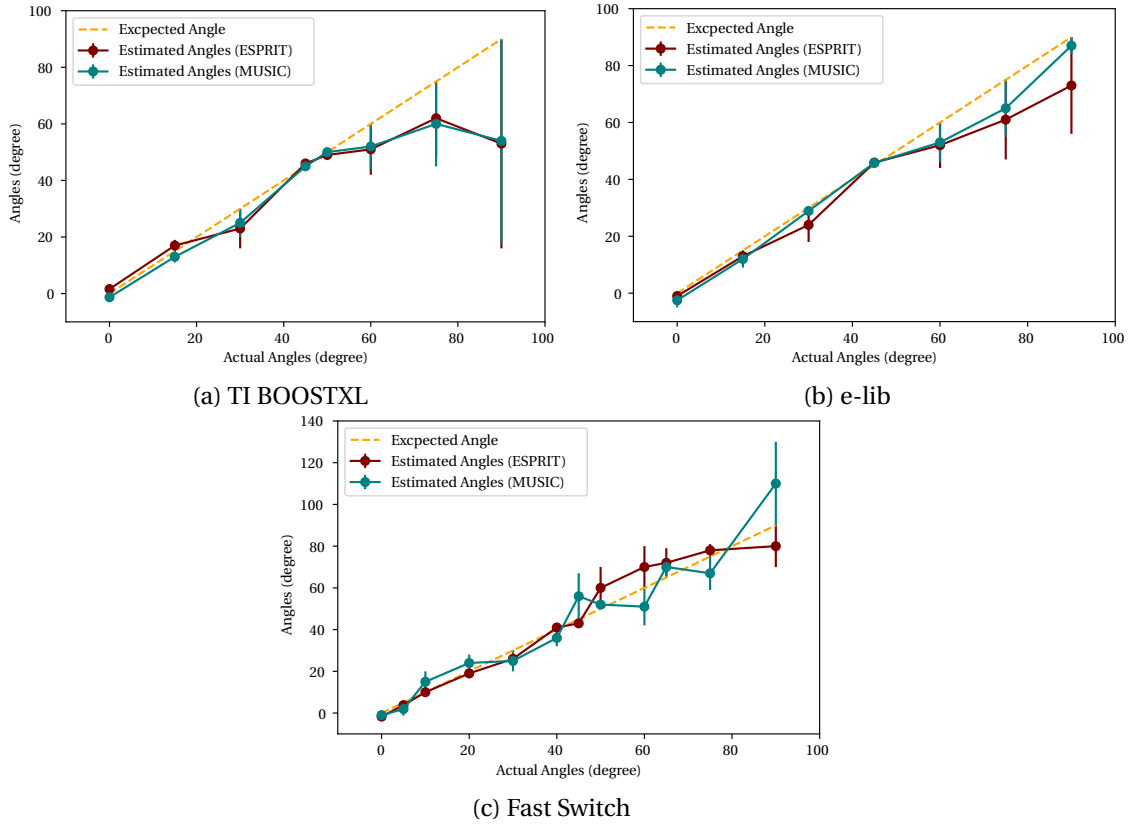
(c) Fast Switch

Figure 6.5: The average estimated angles by MUSIC and ESPRIT algorithm with three different antenna arrays in the range of $(0°, 90°)$.

phase shift in the collected data.

Figure 6.5c show the AoDs of the BLE tags using the nRF module and the fast switch. The average absolute error for this array is $(-0.92°, -1.4°)$ for ESPRIT and MUSIC algorithms, respectively. This antenna array collects the data at the sampling rate of $1\ MHz$. The total behavior of the array is linear and has minimal errors at lower angles [158]. At $\theta = 90°$, this error increases. This is common among all antenna arrays due to the array's nature at this angle. In fact, in this angle, since the $tan(90°) = \infty$, the error rises, and we can have a wide range of changes in the estimated angle value. One of the methods to overcome this problem is designing 2D arrays or non-linear arrays. This problem is especially dominant in beamforming scenarios [159, 160, 158] and refers to Cramér–Rao Lower Bound considerations for the antenna array. Collecting a lot of data points and averaging can dilute this error, as shown in figure 6.5b.

Study the Channel Effect in Angle Estimation in Anechoic Chamber

Another interesting aspect of comparing and studying in the anechoic chamber is the effect of the carrier frequency or the channel on the final result. In the ideal condition, the difference

(a) TI BOOSTXL

(b) e-lib

(c) Fast Switch
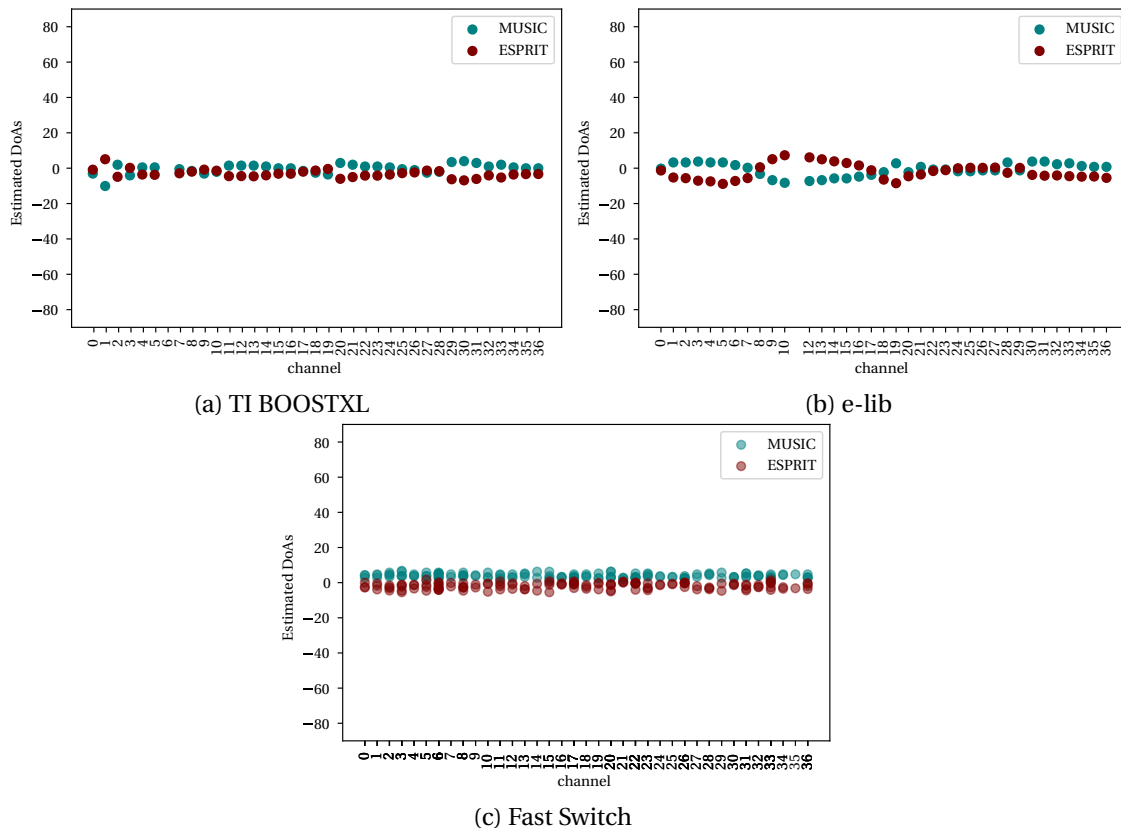
Figure 6.6: The average estimated angles by MUSIC and ESPRIT algorithm with three different antenna arrays at different angles with respect to the channel. a) testing angle zero, estimated $(1.8°, -1.8°)$, b) testing angle zero, estimated value $(0.7°, -2.1°)$, c) testing angle $5°$, estimated value $(3.8°, -1.8°)$, with MUSIC and ESPRIT algorithms respectively

between these frequencies should not be considered, as we can also see in figure 6.6. In this figure, we are presenting the estimated angles at each channel. For figures 6.6a and 6.6b, there exists one channel that has never been used during the duration of our sampling (in this specific batch of data). In general, we can not see a distinctive difference between the channels in the anechoic chamber. For example, in figure 6.6c, we present estimated AoAs of 120 packets at five degrees; but the higher frequency channels and the lower frequency ones behave the same. Figure 6.6b that is presenting the results at zero degrees seems to have slightly more error in the lower frequency channels, but when comparing the results on a larger scale and with more data packets, the difference in the estimated value is at low-frequency channels and higher frequency channels are smaller than 1%. This is true for all antenna arrays we tested in the anechoic chamber. This observation is predictable because, in the anechoic, we expect all the channels to have the same behavior.

Summary

These experiments in the anechoic chamber provide an understanding of each antenna array's performance and the angle estimation algorithm that we can use later as a reference to compare. Also, we can correct the collected data in the indoor environment based on these measurements. Therefore, these measurements act like ground truth for later calculations. For instance, we can anticipate the behavior of the antenna arrays in the indoor environment and compensate for the error with the knowledge we gain from this measurement. For instance, we collected the RSSIs from each antenna array and used them to calculate the average path loss in the anechoic chamber.

The root-MUSIC algorithm only looks for the roots of the auto-correlation matrix. Therefore, this method is more practical for real-time applications. Since the spectrum does not need to be calculated, this method is faster than the MUSIC algorithm. However, we will not get an estimate of the density of the peak (AoA) with this method.

6.2 Experimenting in Indoor Environments

After experimenting in the anechoic chamber, another critical step is to test and validate our antenna arrays in the indoor or office environment. The indoor environment is where the antenna arrays are supposed to function. Therefore, we designed several scenarios to evaluate the antenna arrays and the angle estimation algorithm. In this section, we mainly focus on the methods and process of estimating the angle in an indoor environment. Therefore, in the next step, we will present some sample data to show the results of the process without further correction or processing. Later, we explain the different methods we applied to improve the angle estimation process. Also, as mentioned before, the final aim, which is location estimation, will be explained.

6.2.1 AoA Estimation with TI Antenna Array

In this section, we present the performance of the Texas Instruments antenna array in the test environment, which is an office. The office is an example of an indoor environment. The multipath is not controlled and can dramatically change angle estimation accuracy if a correction method is not used. Figure 6.7 presents the experimental setup for the angle of arrival estimation with TI's antenna array. During all our experiments, the distance between the tag and the transmitter stays the same, and we change the relative angle between them with every $5° \pm 0.2°$. We use BOSCH GLM 500 PROFESSIONAL laser measuring device [161].

As presented in the previous chapter, the in-phase and quadrature data, especially indoor, require modification due to the multipath error. We performed all the discussed steps in Chapter 5. In this process, we estimated the angle by three main algorithms, as discussed in Chapter 4. This section compares each method and its performance in an indoor environment.
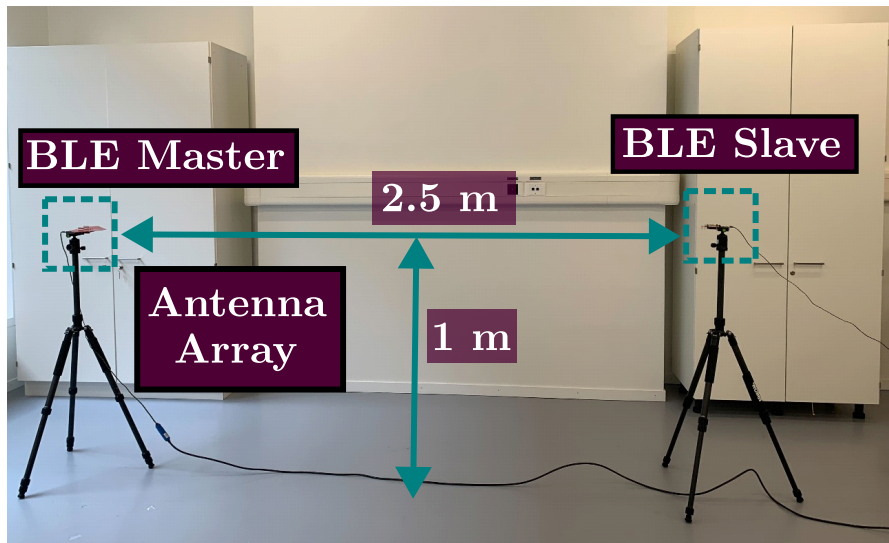
Figure 6.7: The physical test setup using TI antenna array

Figure 6.8 presents the MUSIC spectrum of a sample packet after applying the modification process over the IQ samples. In this figure, the dark blue line is the MUSIC spectrum of the raw data without any phase or amplitude modification. It is essential to understand that the raw data only includes the valid IQ samples and not the data collected during the switching slots. The green line shows the MUSIC spectrum of the same packet when the samples are modified by the method explained in Chapter 4. Zero degrees is the relative orientation of the tag and the antenna array in our calculation. In this figure, we can only see one spike in both the raw and modified data. More peaks might appear due to the multipath effect when diverging from zero degrees. We will discuss this issue later in the next section.

Figure 6.9 presents the estimated AoA of 34 data packets at 45°. The red line is the AoA of the modified data, and the green line is the AoA of the raw data. We can see a massive difference in the estimated angles with and without modifications. The yellow dashed lines are the average of AoAs for each group. It is essential to know that, in general, if we are measuring at angle θ, through the estimation process, we can have both the θ and $-\theta$ as the estimated angle.

Study the Effect of Channels on the Estimated AoA

The total average of 34 data packets collected at 45° is presented in the third row of table 6.1. Table 6.1 shows the numerical average of the estimated AoAs presented in figure 6.9 separated by the low and high-frequency channels. The low frequency has a channel number below 17, and the high frequency has a channel number above and including 17. In this table, we are using the average as a method to compare these three algorithms. By considering the average of estimated angles, we can see that the modified IQ samples will dramatically increase the accuracy of the estimated angle. In our modification, we also had to add a bias value to the estimated value by the algorithm based on the measurements in the anechoic chamber. The
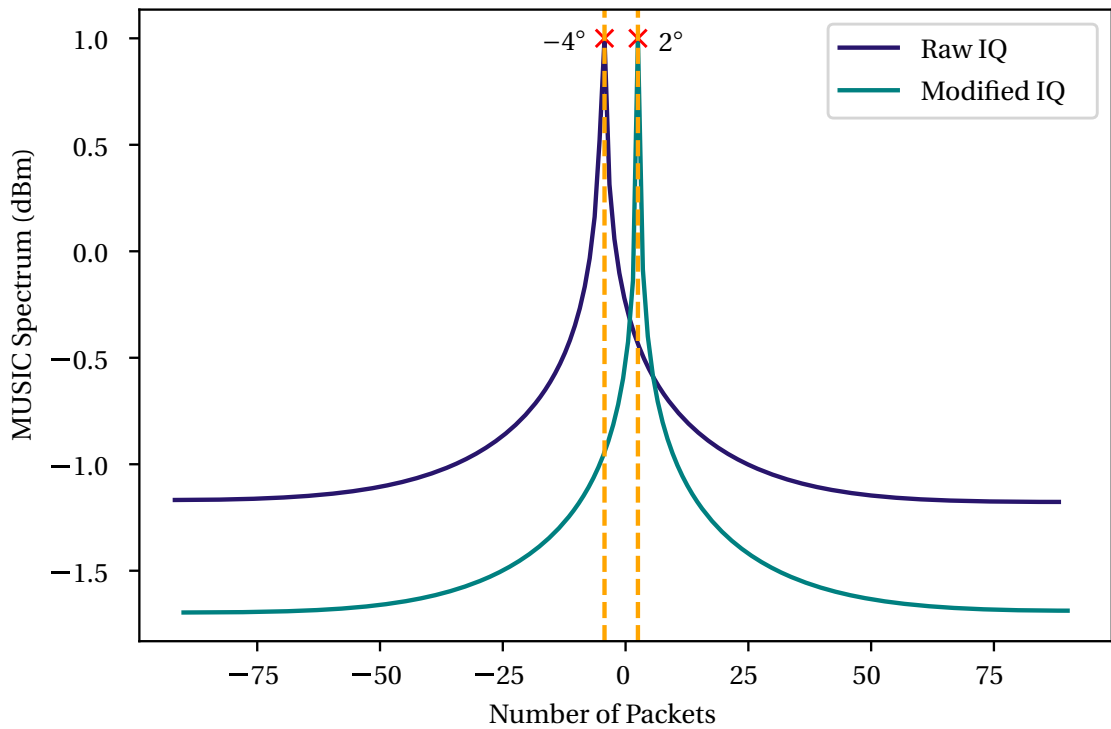
Figure 6.8: The MUSIC spectrum of the estimated angle at zero degrees in the indoor environment. A comparison between the raw and the modified data

estimation accuracy without any phase modification is below 50%, whereas by correcting the phase, the accuracy jumps to above 90% for some instances. This table and its visual representation perfectly highlight the phase correction effect on the estimated angle. A small important thing to note is that using average as an estimate for the final angle estimation is not always the best method. In the following sections, we will expand on this matter.

In figure 6.10, we present the estimated AoA by each method for better visualization. The color intensity and the colors of the dots increase as the channel number increases. In this batch of samples, we generally have 34 data packets sampled in 22 unique channels. We can see that the calculations overestimate the value for the MUSIC and the ESPRIT algorithm at lower frequencies. At higher frequencies, the AoAs are closer to the expected value. Finally, using the full range of channels can enhance the estimation process, which is one of the methods for eliminating the multipath effect. The ESPRIT method is significantly efficient when we do not diverge drastically from zero degrees. However, sometimes this algorithm fails to converge, especially when the argument in equation 4.18 is bigger than 1. The root music algorithm is considerably fast and can provide very accurate results. MUSIC algorithm is the best method for visualization, even though spectrum calculation and plotting in real-time applications can be computationally costly and time-consuming, respectively.

These values result from only a few batches of data, each containing about 35 packets, and are only used to visualize the different effects we are presenting here. Several important aspects

(a) MUSIC Algorithm

(b) ESPRIT Algorithm

(c) root-MUSIC Algorithm

Figure 6.9: The estimated angles by MUSIC and ESPRIT and root-MUSIC algorithm with TI antenna arrays at 45°

should be studied to reach a more general conclusion, such as testing the system in a broader range and with more data. The following section addresses this concern.

General Presentation of AoA Estimation with TI Antenna Array

In this section, we present the result of massive data analytics that we collected at several angle orientations using the TI antenna array and the TI modules for AoA estimation. We collected more than 300 packet at every interval of 5° in a wide range of (0°, 90°) as presented in figure 6.7. We collected over 300 data packets at every interval of 5° in the anechoic chamber and 900 data packets for the indoor environment. Since we are eliminating the corrupted data packets, not all 900 measurements can be used for analysis. For instance, after extracting the wrong data packets at 40°, we were left with 611 data packets out of 714.

We collected the IQ samples from all packets to estimate the angle. Then we averaged over all the packets to compare the accuracy of angle estimation for packets of valid data (figure 6.11) Each dot represents the average AoA value for over 300 data packets at the respecting angle. The trend looks linear primarily in the test range; however, the accuracy decreases as we

Channel	MUSIC	MUSIC Modified	ESPRIT	ESPRIT Modified	root-MUSIC	root-MUSIC Modified
Low	22.5	48.0	22.0	47.6	39.0	43.6
High	18.1	42.7	17.7	42.6	32.7	35.7
All	19.7	44.6	19.5	44.3	34.6	38.5

Table 6.1: The absolute value of the average of estimated angles separated based on the low and high channel frequency as well as the average through all the channels in 45°

diverge from the center (45°). Vertical lines in Figure 6.11 show the average standard deviation of over 300 data packets for each angle. In this figure, we eliminate the data outliers. We also present the results after data correction and the phase linearization process. The quantity of the packets changes because of the elimination process of the packets. Nevertheless, we tried to obtain a minimum of 300 packets for each angle to stay statistically correct.

In figure 6.11, each point is an average through a set of more than 300 data packets. We extract the data outliers by evaluating the standard score of each data group. Assuming μ_a is the mean of these n_a ($n_a = 300$) sets of data, and σ_a is the standard deviation of the samples, then the Z_a of the standard score is $Z_a = (x_a - \mu_a)/\sigma_a$ where x_a is the observed value from angle estimation. So this brings an extra level of accuracy to the calculations. We are using this method to enhance the unwanted effects of the multi-path by adding more data from different channels to the calculations.

In figure 6.11, the difference between each AoA with different algorithms is difficult to distinguish. This has several reasons. First, since the data undergoes a modification process, it aids in unifying the results using all three algorithms. Second, the difference is small when only measuring the average to distinguish between these algorithms. However, as mentioned before, these algorithms act differently in real-time applications. Also, the required computational power varies for each method. For instance, in this figure (6.11), the average error for ESPRIT, MUSIC, and root-MUSIC algorithm is 3.3°, 4.0°, and 4.0° respectively. However, the MUSIC spectrum is very costly for computational power in real time. Although the ESPRIT method has a slightly smaller error, it is less likely to estimate the results at higher angles. For instance, after performing the algorithm estimation with ESPRIT, only eight packets could converge to an answer in a batch of 34 data packets at 60°. Therefore, we decided to use the root-MUSIC algorithm for real-time application because it has the same accuracy as the MUSIC algorithm but is less time-consuming. In comparison to MUSIC, root-MUSIC takes 30% less time.

The estimated angle at specific ranges has better accuracy rather than the rest. This is because the ULA is tilted for 45°. As a result, the estimated angle is accurate at around 45°. As we diverge from this angle, especially at higher angles, the standard deviation of the acquired angle increases. The antenna array arrangement can be used to the users' advantage concerning the area of interest for testing. The achieved accuracy using the MUSIC algorithm will result

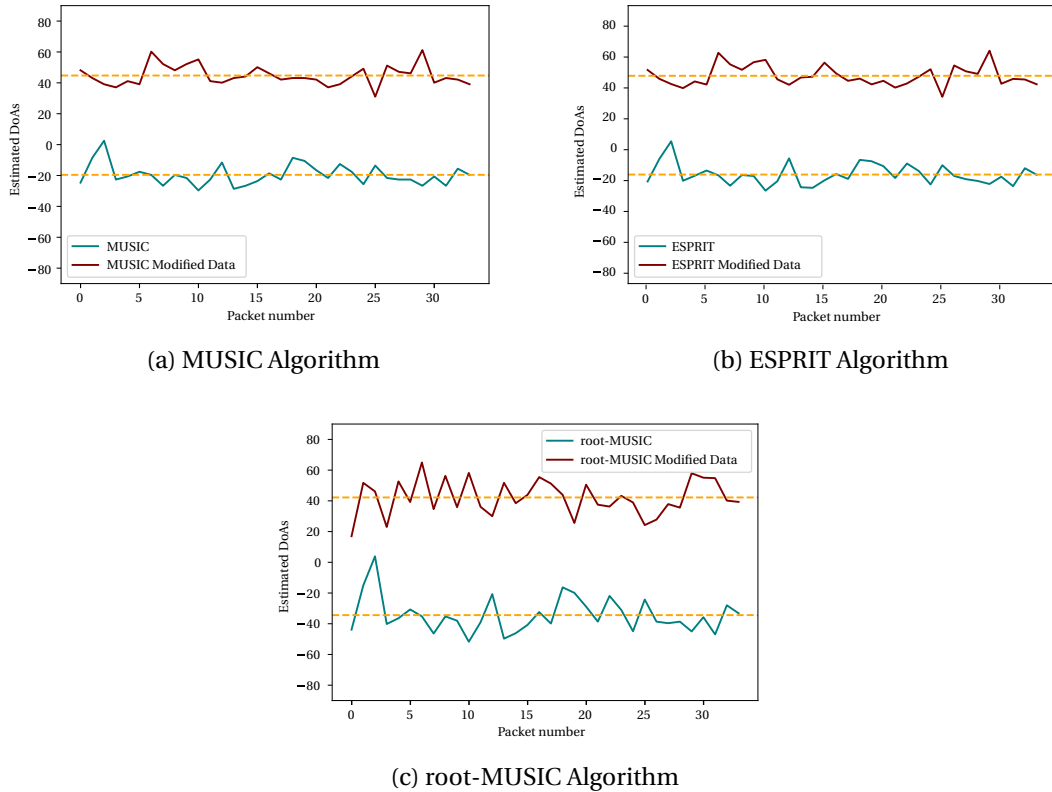(a) MUSIC Algorithm

(b) ESPRIT Algorithm

(c) root-MUSIC Algorithm

Figure 6.10: The estimated angles by MUSIC and ESPRIT and root-MUSIC algorithm with TI antenna arrays at 45° with respect to the channel

in approximately $\frac{\pi \theta r}{180} = 31.5 \ cm$ accuracy of position estimation in a radius of $r = 5 \ m$, which makes it 93.8% of accuracy. This is an 80% improvement compared to the state-of-the-art [24].

6.2.2 AoA Estimation with e-lib Antenna Array

As mentioned before, to have more antennas in the array, we designed our "e-lib" antenna array. The details about this antenna array as well as its advantages, are presented in the previous chapters. Nevertheless, we also have to investigate the performance in the indoor environment. So, in this section, we are presenting these results. Having more antennas in the array increases the accuracy of the estimation process [162, 163, 164].

In figure 6.12, three different spectrums at 15° are presented. The dark blue curve is the spectrum from valid IQ samples (raw data) without any modification. The term raw data refers to the valid IQ samples collected in each packet. In algorithm 5, the raw data is the data in line 16. So, line 17 in this algorithm (5) generates the modified data. The rest of the process remains unchanged unless it is indicated. The green curve is the spectrum after the phase modification process. We can see that the modification process not only shifted the biggest
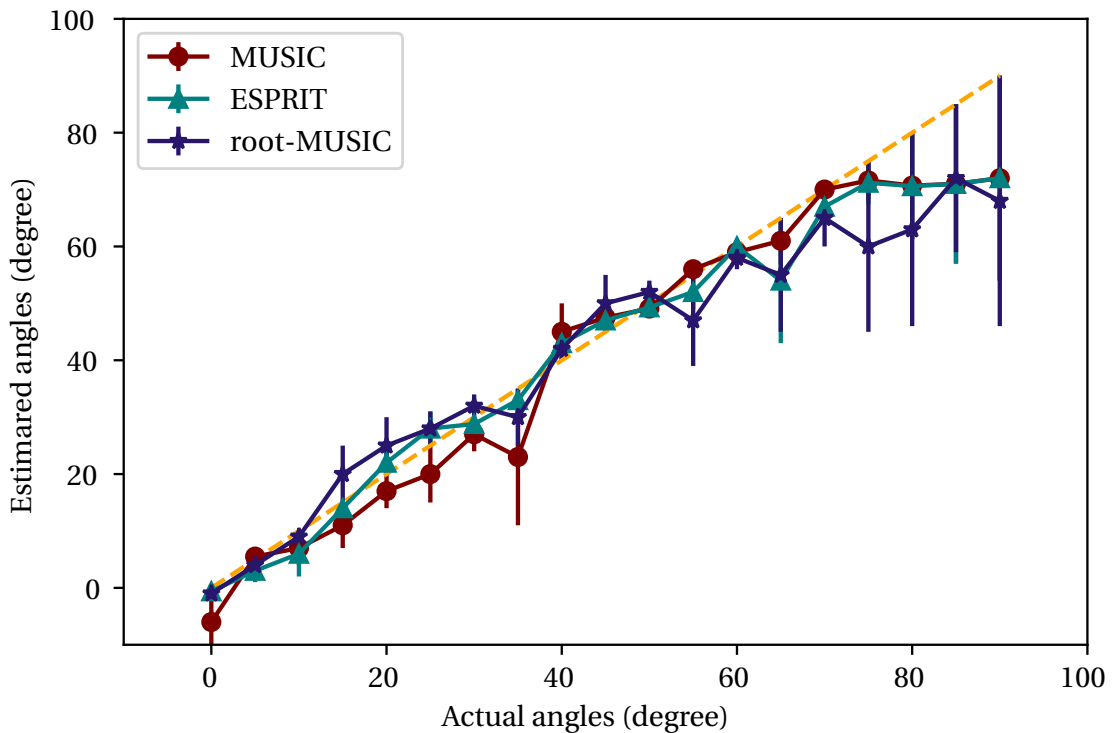
Figure 6.11: A comparison of the estimated angle vs the real angle in a range of $[0°, 90°]$ in an indoor environment for different algorithms

peak of the curve but also introduced a new peak to the cure at the left wing of the spectrum. At first sight, one might assume that the biggest curve is the AoA. However, other peaks can be the correct value due to the severe multipath effect in this environment and the noise. Two angles are the candidate for AoA for these packets, as presented by the red and yellow crosses on the corresponding spectrum.

To eliminate the possibility of wrong estimation, we performed a spatial smoothing step on the calculated spectrum of modified data. The process is described below. In figure 6.12, the light blue curve is the spectrum after spatial smoothing. As it is presented, we no longer have the peak at the tail of the spectrum as one of the estimated angles. Moreover, this curve shows a more significant peak around $11°$. While the peaks for the raw data are $-4.5°$ and $73°$ and for the modified data are $-62°$ and $11°$.

Spatial smoothing is a process in which the data are averaged with their neighbors, which acts as a low pass filter that enhances the low frequencies while filtering the high-frequency data. This process is especially effective when calculating in a noise environment where SNR is high. Spatial smoothing creates a smaller averaged covariance matrix over L maximum overlapped subarrays.

This preprocessing spatial smoothing scheme starts by dividing a uniform linear array with M_0 sensors into uniformly overlapping subarrays of size M [165]. $L = M_0 - M + 1$. L is the over-
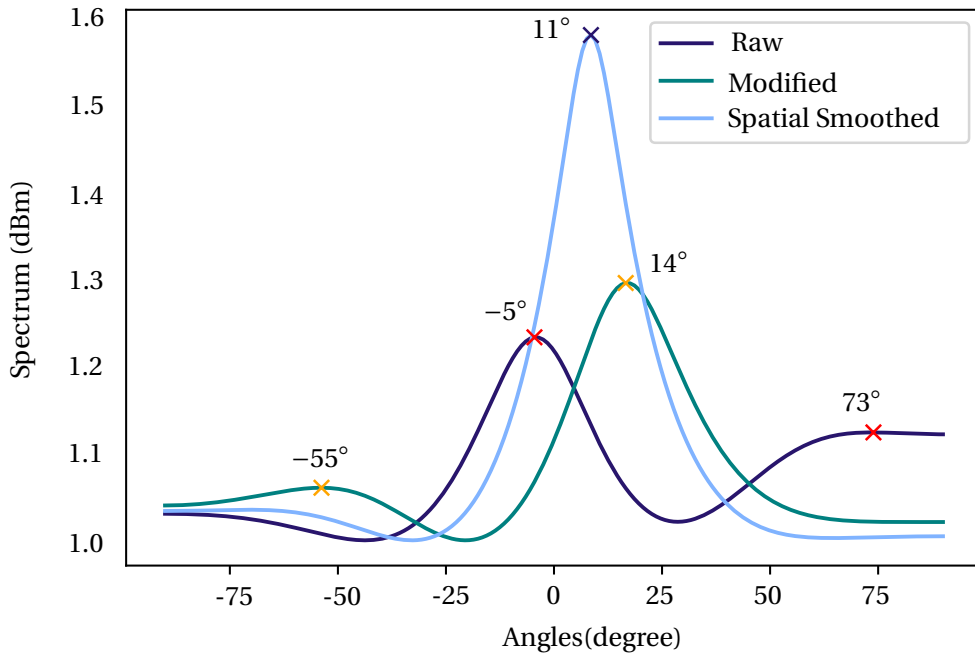
Figure 6.12: The MUSIC spectrum of the estimated angle at zero degrees in the indoor environment. A comparison between the raw and the modified data using the e-lib antenna array

lapping subarrays of a uniform array with M identical elements [165]. For more information about the details of this process, please refer to [165, 166].

We used the forward-backward spatial smoothing method to filter high noise. Therefore, we can eliminate the errors and increase the sensitivity of the estimation.

Figure 6.13 presents the estimated angles by three different algorithms at $15°$ degrees using the e-lib antenna array in an indoor environment. In these figures, the green points are the DoAs of the raw data, the red dots are from the modified data, and the yellow dots are from the spatially smoothed data. As mentioned before, we might sometimes see more than one peak in the MUSIC spectrum, as in figure 6.13a through the first few packets. Even after the modification process, two peaks might still exist. This can be due to the multipath effect. Even though these peaks might not be as high as the main peak as presented in figure 6.12; they create ambiguities during the angle estimation process. Using the spatial smoothing method, we smoothed the spectrum and eliminated some parts of the error in the spectrum. As a result, the yellow dots are the presenters of this modification. We no longer have two peaks per packet; only the dominant one is presented here. The purpose of this figure is to demonstrate the effect of spatial smoothing on the modified data points.

Using the ESPRITalgorithm and the root-MUSIC algorithm, we can see that the spatial smoothing does not significantly change the estimated AoA for each packet. The average estimated
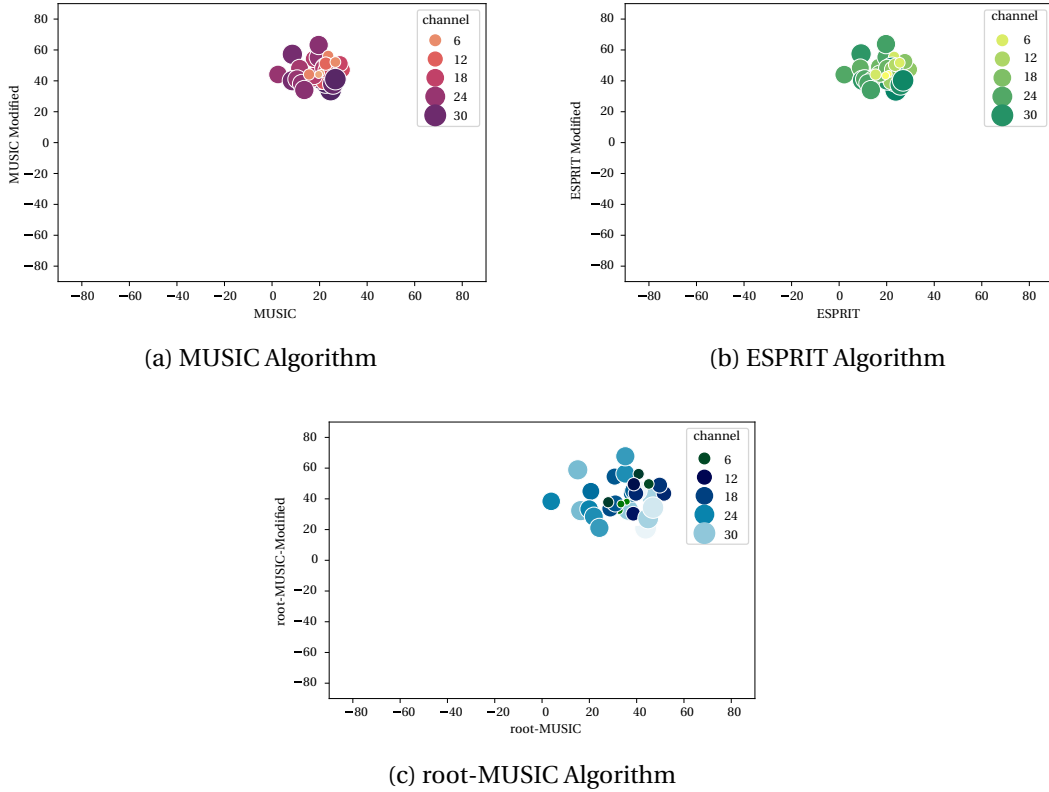
(a) MUSIC Algorithm

(b) ESPRIT Algorithm

(c) root-MUSIC Algorithm
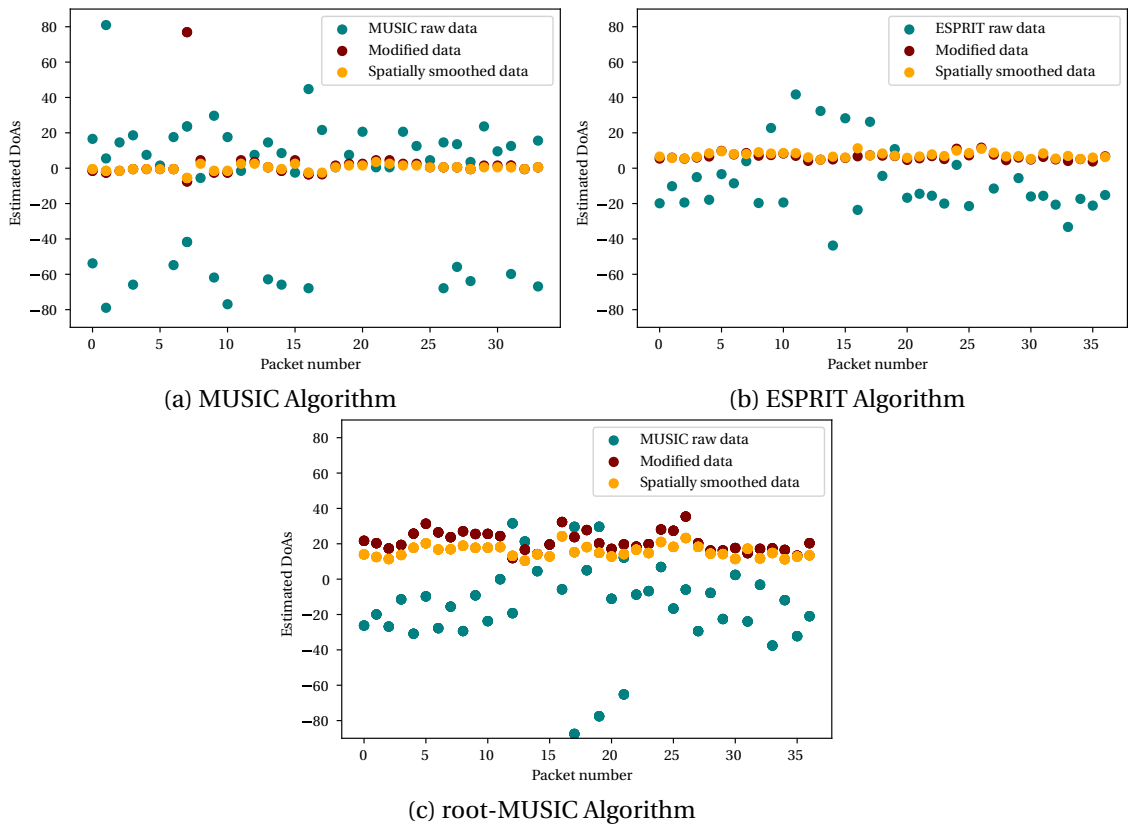
Figure 6.13: The estimated angles by MUSIC and ESPRIT and root-MUSIC algorithm with e-lib antenna arrays at 15° with respect to the packets

AoA using the ESPRIT algorithm is around 6°, and using the spatial smoothing could only improve the accuracy by 1°, which is equal to a 16% improvement. Still, the spatial smoothing changed the average of the root-MUSIC algorithm from 21.3° to 15.6°, which is an improvement of approximately 35%. The most significant improvement, as it is perfectly presented, is while using the MUSIC algorithm, this method highlights the most critical peak. The estimated AoA after spatial smoothing of the modified data is around 13°.

Study the effect of channels on estimated AoA

Figure 6.14 presents the estimated AoAs at different channels of a packet bundle of size 36. Each dot in this figure presents the estimated angle of the raw and the modified data. As the channel number increases, the size of the dots also increases. The larger the dots, the larger the frequency of the channel. As mentioned before, we have several peaks for each packet in certain cases. For example, in figure 6.14a, we can see that the estimated angles are less likely to be correct as the channel number increases (bigger dots). The central cluster in the figure is in the range of expected value for the angle of 15°. However, in the figure, we can see other clusters in the range of (60°, 80°) as well as (−60°, −80°). These points mostly happened

at higher frequencies considering the raw data. The modified data, being the closest to the expected value, is more diverse and is less dependent on the channel number. This figure also perfectly depicts the importance of introducing a new method to eliminate the non-valid spectrum peaks at each data packet.

(a) MUSIC Algorithm

(b) ESPRITAlgorithm

(c) root-MUSIC Algorithm
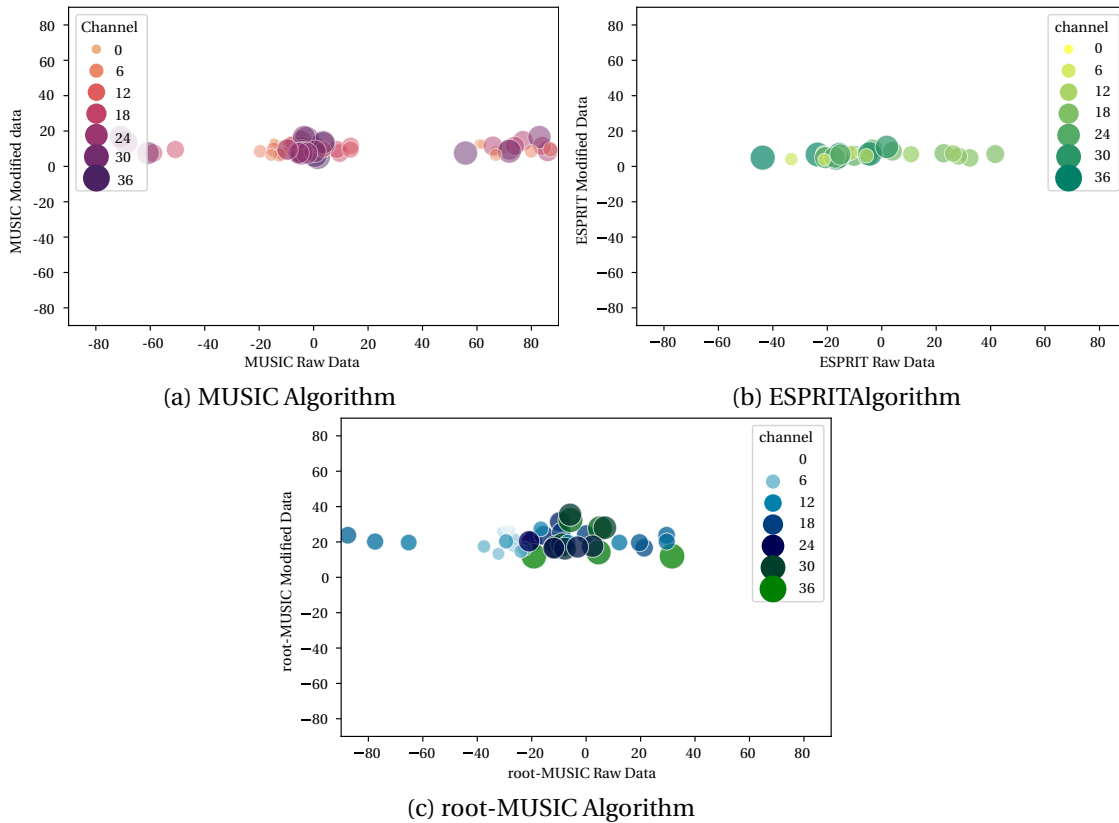
Figure 6.14: The estimated angles by MUSIC and ESPRIT and root-MUSIC algorithm with e-lib antenna arrays at $15°$ with respect to the channel. A comparison between the raw data and the modified data.

Figure 6.14b shows the estimated AoAs of raw and modified data using the ESPRIT algorithm. The estimated AoA has a small dependency on the channel number for the modified data. We can see that the AoAs of the modified data is not changing concerning the channel number; however, this value changes more when using the raw data. This can also be the effect of uncorrected noise of the raw data.

Figure 6.14c presents the same result from the root-MUSIC spectrum. We are not presenting the roots that are outside the bounds of $(-90°, 90°)$ as they are not valid results. However, we can see that both the modified and the raw data created a data cluster in the middle of the figure. Nevertheless, we can also see three outliers on the left. The raw data for these packets creates a misleading value between $(-80°, -60°)$ at a low frequency. The same behavior is present here too. The modified data is less dependent on the channel number than the raw

data.

(a) MUSIC Algorithm

(b) ESPRIT Algorithm

(c) root-MUSIC Algorithm
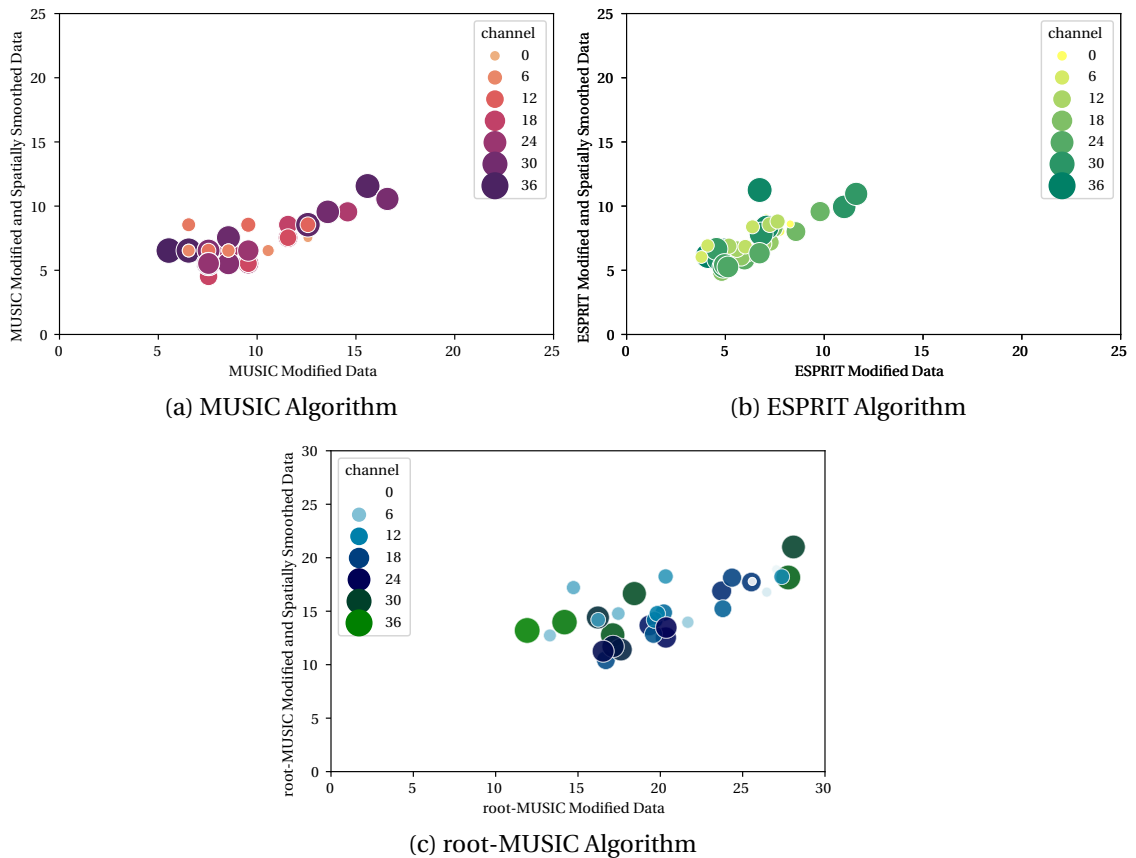
Figure 6.15: The estimated angles by MUSIC and ESPRIT and root-MUSIC algorithm with e-lib antenna arrays at 15° with respect to the channel. A comparison between the modified data and the spatially smoothed data.

In this section, we study the spatially smoothed and modified data in different channels. This process is done to the autocovariance matrix of the modified data and acts as a low-pass filter. If we convert the spectrum to a Fourier form, the spatial smoothing step filters out the high frequencies of the spectrum. As shown in the three plots of figure 6.15, both methods have a diverse range of AoAs values with respect to the channel number. An important factor that is worth mentioning here is that the figures only present the AoAs in the expected range of (0°, 20°) because outside these bounds, the estimated AoA of the modified spatially smoothed does not exist. Therefore, the comparison is redundant and inexplicable.

General presentation of AoA estimation with e-lib Antenna Array

We performed another set of experiments with the "e-lib" antenna array in an indoor environment using three different algorithms. In these sets of experiments, we collected more than 200 data packets at an interval of 10° with the e-lib antenna array. In figure 6.16 each dot
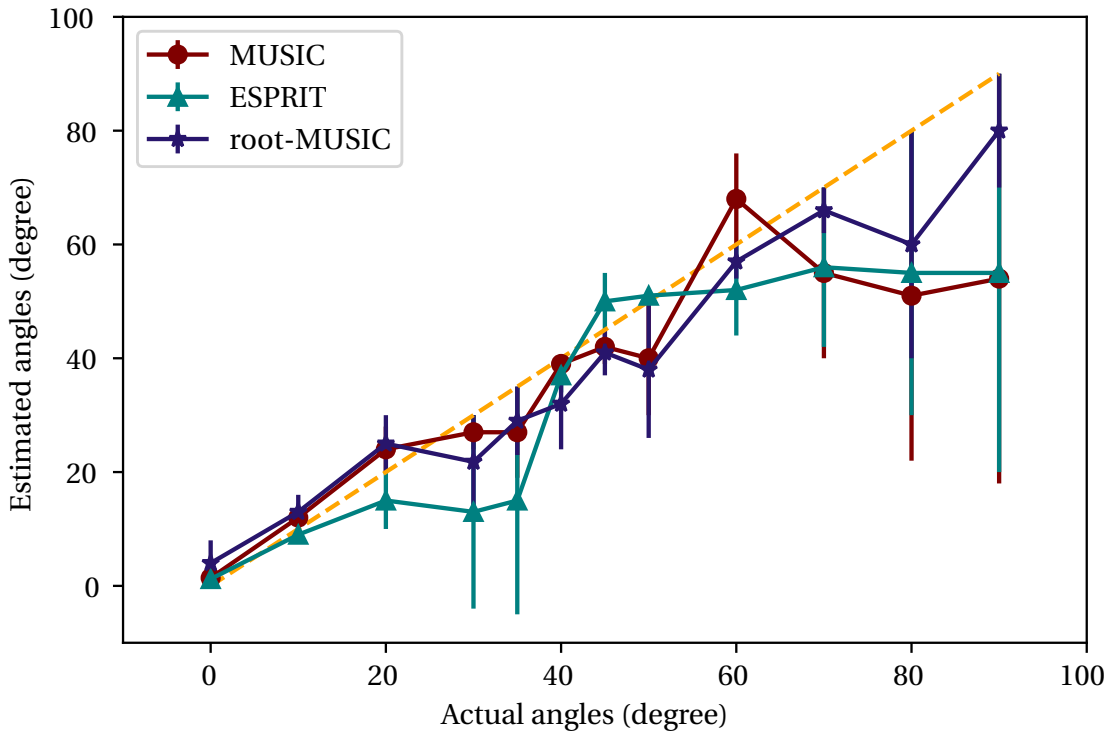
Figure 6.16: A comparison of the estimated angle vs the real angle in a range of $[0°, 90°]$ in an indoor environment for different algorithms using e-lib

presents the estimated AoA at several tested packets. We excluded the data outliers to obtain more accurate results. This figure shows that different algorithms are performing differently, especially at both tails of the spectrum. The ESPRIT algorithm here is less accurate than the MUSIC and root-MUSIC algorithms. The total error for ESPRIT is around 10°. Here, we calculate the error by subtracting the actual angle from the average estimated angle. Using the MUSIC algorithm and after data modification, we achieved an accuracy of about 5.3° and 5.2° for the root-MUSIC algorithm. We can see that the absolute errors tend to increase dramatically in the non-linear ranges of *arctan*.

The inaccuracies tend to be more evident as we diverge from 50°, and the variance of data increases for higher angles. The estimated angle at 90° is changing in a wide range. The error is inevitable due to the nature of this angle where $arctan(\pi/2) = \infty$. This is why we have a vast range of errors, especially in the case of indoor environments. We did the test at 89° degrees to avoid the problem. The antenna array had an average of $-2.2°$ degrees at zero degrees. Therefore, we used this value in the indoor test to calibrate the antenna array at zero degrees. As a result, a bias is added to all the data we recorded.

E-lib array has an average error of 3° degrees in the semi-linear range of $[0°, 60°]$. In fact, by placing the arrays in the correct orientation, a smaller range with more accurate results can improve the position estimation of the whole system.

Using root-MUSIc or MUSIC algorithm and e-lib antenna array, one anchor can achieve below 0.5 m accuracy for position estimation using $\frac{\pi \theta r}{180} = 45\ cm$ in a range of 5 m in diameter. This accuracy is enough for most direction-finding purposes. Even though the e-lib antenna array uses more antenna, the TI antenna array is approximately 20% more accurate in the overall range. This is the reason we designed another antenna array with a faster switch to improve the performance of the e-lib antenna array. Therefore, the next section is devoted to the antenna panel (a section of the panel is presented in figure 4.12) and its performance during different scenarios.

6.2.3 AoD Estimation with Fast Switch and Antenna Panel

As mentioned before, our goal is to create a system that can perform as an indoor positioning system; therefore, in theory, this system requires handling more than ten tags. Therefore, using the AoD paradigm is the answer. As discussed before, the packet structure in AoD differs from the AoA structure. As a result, in this configuration, the receiver only receives the IQ samples. Therefore, there are no steps for extracting non-valid IQ samples from the data. This also increases the processing speed. But because the switching is happening only on the transmitter side in this architecture, it increases the possibility of more errors in the whole system because of the possible unsynchronization between the transmitter and the receiver in connection-less AoD. Using the nRF modules, in our configuration, the sampling slots are 1 μs. In this section, we first study the performance of a ULA array with four antennas, and then we study the effect of the antenna pattern on the received data.

ULA Structure

ULA is considered the primary form of an antenna structure for study. Therefore, we use an antenna array of 4 elements with 3.5 cm spacing to create an analogy for AoD architecture. We are using 1 μs sampling slots and 1 MHz sampling rate to increase the speed of estimation. In general, in this configuration, the mobile tag should perform the angle estimation. As a result, creating the fastest solution with the minimum of calculations is crucial to maintain the energy of the device and having a lightweight calculation. To compensate, we are adding more antennas to the pattern to increase the estimation accuracy. In this method, the preparation of the auto-covariance matrix contains fewer steps. But without the data modification process and phase compensation, the estimated AoD is far from reality. So, the modification process stays intact. The following algorithm 6 presents AoD estimation's real-time data preparation process with nRF modules. Because the sampling is happening on a mobile device, every collected index is considered to have the correct sample index. So, the duplicates and wrong sample numbers aren't required to be distinguished. Also, the step of sample re-arrangement based on the antenna pattern is merely re-constructing the matrix based on the antenna pattern. As a result, this method inherently requires less computational power for estimation. For instance, for a packet of data, this algorithm requires less than 1 ms to run and calculates the AoD with three algorithms of MUSIC, ESPRIT , and root-MUSIC simultaneously. In this

---

Algorithm 6 Data Preparation Algorithm for AoD

Data: the IQ samples and RSSI from each target to each of the R Anchors and P packets
Results: the AoA of the received signal and RSSI of the right packet
for each **Anchor** $\in 1, 2, ..., R$ **do**
    for each packet $p \in 1, 2, ..., P$ **do**
        Remove the Gaurd Period;
        Calculate f_d from Reference Period;
        if $f_d > |250| kHz$ **then**
            Wrong Frequency
            $p = +1$
        else
            Remove the Reference Period;
            Phase & Magnitude Modification;
            Re-construct Matrix X based on antenna pattern;
            Construct $R_x = X X^H$;
            Compute Eigen Matrix of Noise Subspace $\mathbf{U_n}$;
            Obtain AoD based on Algorithm;
        end if
        Append AoD and RSSI from Multiple Packets;
    end for
end for

---

study, the calculations were performed on a virtual Linux Ubuntu 14 OS over Python 3.7. This is the reason why this method can be used for real-time applications. However, as mentioned before, the modification step plays an essential role in the accuracy of the estimated AoD.

In figure 6.17, we can see three different algorithms being used and the comparison between the raw data, modified data, and spatially smoothed data. In real-time applications, we only use the modified data to achieve a result as fast as possible. Using the MUSIC algorithm with raw data gives two sets of AoDs, making it challenging to comprehend the actual angle. Therefore, the modified data can improve the result. Using the average as an indicator of the estimated angle within these packets may give us a result that is very close to the desired value. For instance, in this figure, the average of the estimated angles for raw, modified, and spatially modified data is 23°, 17.8°, and 17.3°. The last two values are very close to the expected value. However, the majority of estimated angles are around 10° using the modified data (figure 6.17a).

The majority of the estimated AoD with the ESPRIT algorithm also had the same issue (figure 6.17b). The average estimated AoD is 14° using the spatially modified or the modified data, but the majority of data is around 10° if only checking data with the $|Z_a| < 0.5$. For this condition, the average of estimated AoD with the raw data is around 25°. Both result in accuracy above 5°.

On the other hand, the root-MUSIC algorithm is more accurate, especially with the modified

(a) MUSIC Algorithm

(b) ESPRIT Algorithm

(c) root-MUSIC Algorithm
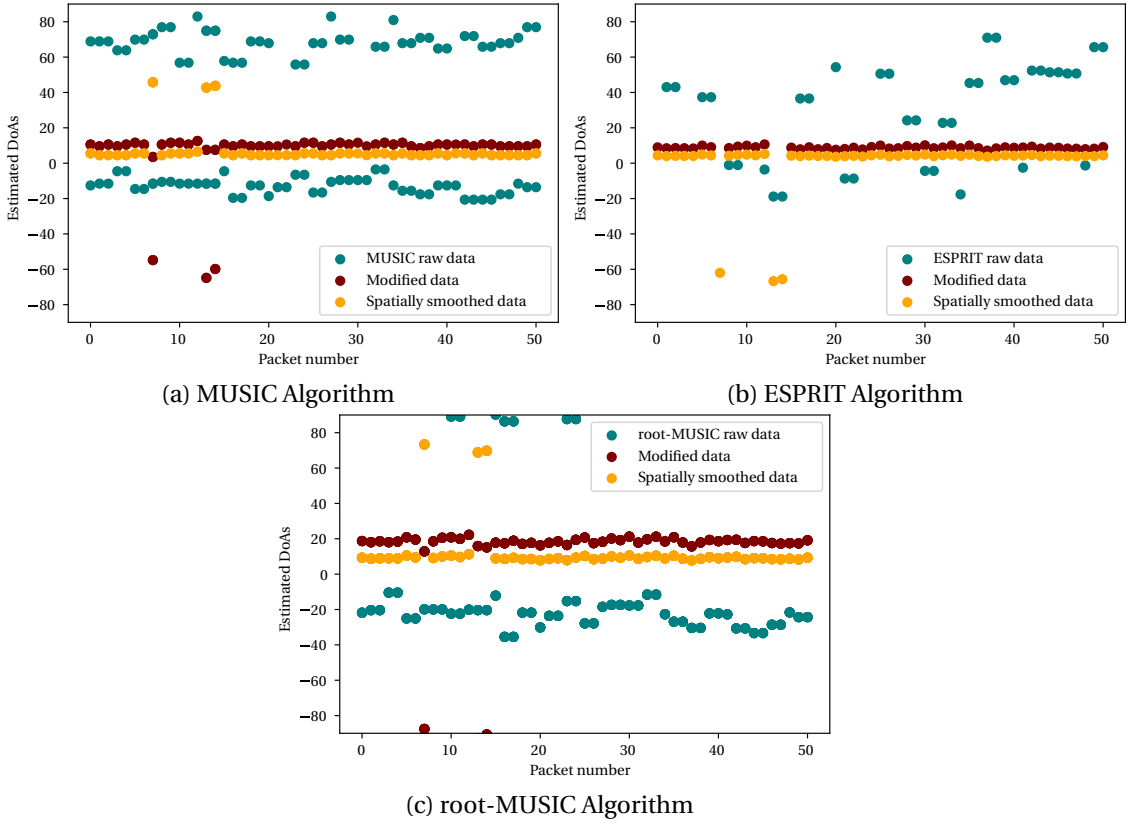
Figure 6.17: The estimated angles by MUSIC and ESPRIT and root-MUSIC algorithm with nRF modules and ULA antenna array at 20°. A comparison between the raw data and the modified data and spatially smoothed data.

data. In figure 6.17c, most red dots resenting the estimated AoDs of the modified data are very close to the expected angle of 20°. Only considering the roots in the range of $(-90°, 90°)$, the average AoD is 17°. This method's absolute raw data average is also very close to 20°. We used the root-MUSIC algorithm with the modified data for real-time applications to acquire the AoDs.

In figure 6.18, each dot is the average estimated AoD of more than 100 correct packets at each orientation. This figure presents the estimated AoDs of modified data with the $|Z_a| < 1$. The overall accuracy is very high if averaging the data. If removing the outliers from the data, the overall accuracy of the MUSIC, ESPRIT , and root-MUSIC algorithm is 2.6°, 4.0°, and 2.0° respectively. This accuracy will lead to the position accuracy of about 22 cm, 34 cm, and 17 cm, respectively, in a radius of 5 m. With this accuracy, the position estimation with an accuracy of < 50 cm is possible. Besides adding a new antenna to the array, using the fast switch and sampling at 1 μs slots is a reason for this accuracy. We also used the $|Z_a| < 1$ to remove the outliers. This criterion is very strict because, statistically, outliers are the data points where the Z-score is over 3. A Z-score of 1.0 would indicate a value of one standard deviation from the mean. However, we must collect more than 30 packets for the $|Z_a|$ to achieve this real-
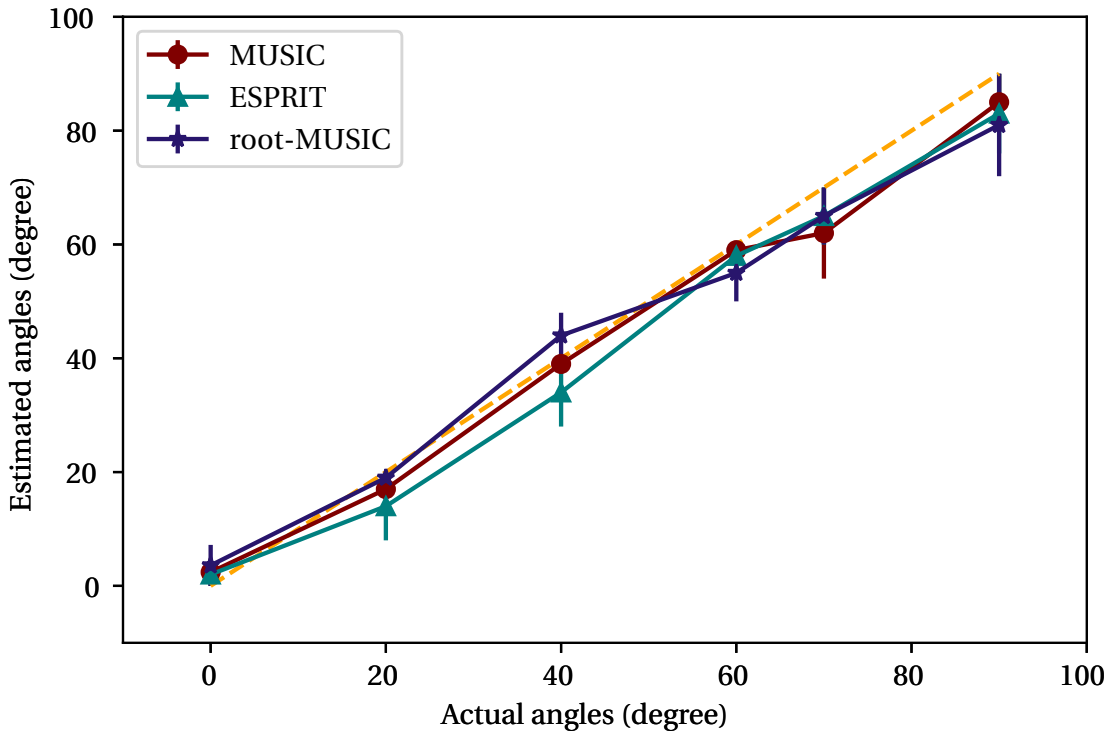
Figure 6.18: The average estimated angles by MUSIC and ESPRIT and root-MUSIC algorithm with nRF modules and ULA antenna array at the range of $(0°, 90°)$

time accuracy. Therefore, we decided to improve the process of AoD estimation by different methods. The following sections will elaborate on the effect of the antenna pattern and the structure on the estimated AoDs.

The effect of antenna pattern

As explained previously, the antenna pattern can play an important role in the angle estimation process. Until now, all of our patterns started from the reference antenna and then continued to the remaining antennas in the pattern. For example, for an array with four elements, the pattern is A_{ref}, A_1, A_2, A_3, where the A_{ref} is the first antenna in the array. Let us call it A_0. Therefore, during the reference and switching time, the antenna A_0 acts as the reference antenna. It references antenna is the antenna used to compare the phase of the rest of the antennas with respect to it. Therefore, we decided to study the influence of the antenna pattern on the estimated AoD.

Figure 6.19, presents the estimated AoD with three different algorithms when the antenna pattern is $A_{ref}, A_1, A_{ref}, A_2, A_{ref}, A_3, A_{ref}$ at zero degrees. Using this antenna pattern, we can always compare the phase with the reference antenna. In figure 6.19, after data modification, all the packets have approximately the same AoDs and are very close to zero degrees. In fact, during the phase linearization step, since we have the data of the reference antenna in the
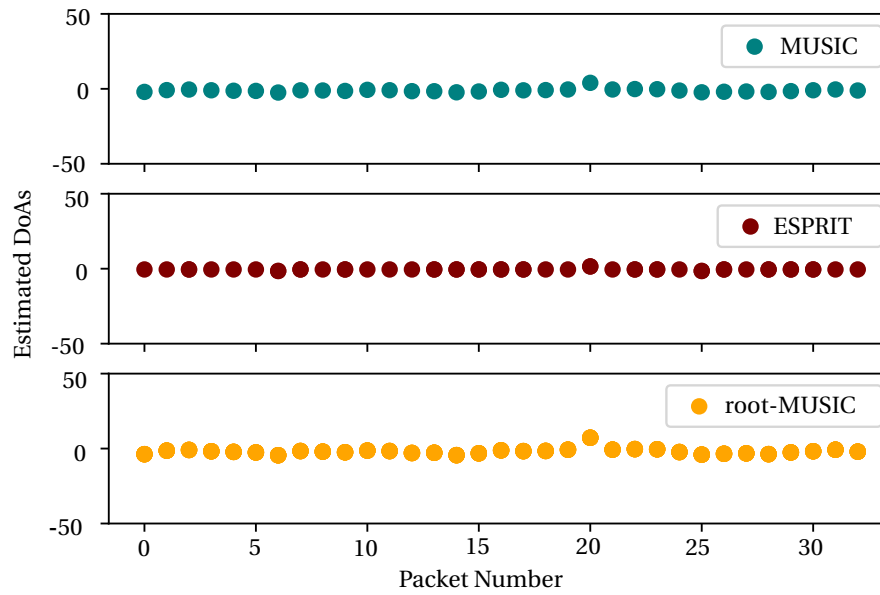
Figure 6.19: The estimated angles of modified data by MUSIC and ESPRIT and root-MUSIC algorithm with nRF modules and a 4-element ULA antenna array at zero degrees with antenna pattern $A_{ref}, A_1, A_{ref}, A_2, A_{ref}, A_3, A_{ref}$

process, every other sample is the value we expect the phase to be. The estimated AoDs for MUSIC, ESPRIT , and the root-MUSIC algorithm are $0.6°$, $1.3°$, and $-1.9°$ respectively.

A different antenna pattern can impact the angle estimation accuracy by 40%. However, the phase linearization process still plays an important role in the estimation. In general, the antenna pattern and the array steering vector will change accordingly in the algorithm, but using the same antenna has the greatest impact on the phase linearization process. When wanting to use only four antennas, this process can improve the estimation accuracy without adding more antennas to the mix or changing the physical configuration of the array. Another antenna pattern that can truly impact the performance of the estimation is using a 2D antenna array. In the next section, we will elaborate on this matter.

6.2.4 UCA with nRF Modules

Adding another dimension to the angle estimation process has several benefits. First, we can have both the azimuth and the elevation angles. As a result, we can obtain the position of an unknown target in a room in 3D space by using the RSSI from the BLE modules. Another important aspect is that it can increase the accuracy of estimation simply because of having more antenna elements, therefore, more samples. However, there lie some drawbacks too. For example, introducing a new dimension increases the complexity of the calculations and the antenna array design.

BLE-DF supports up to 74 sampling slots when having 1 μs sampling slots. An important

(a) Elevation angle

(b) Azimuth angle
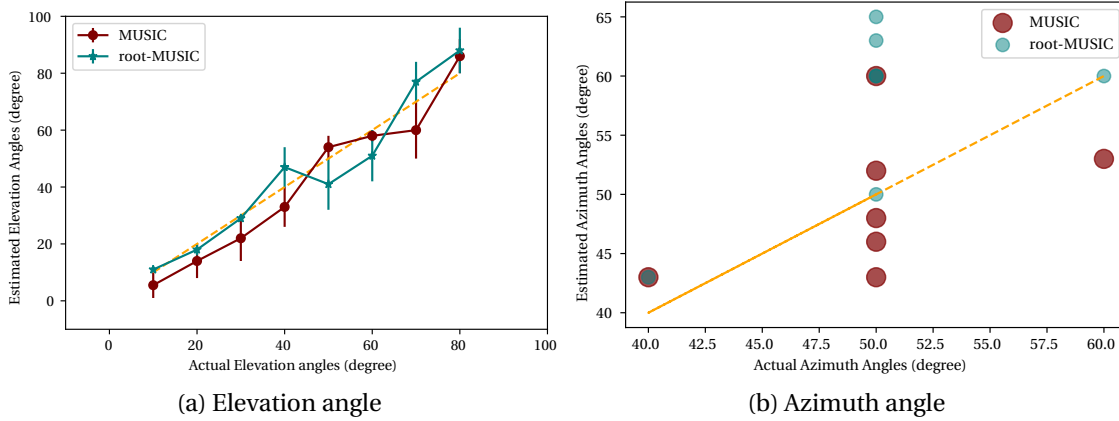
Figure 6.20: The estimated angles by MUSIC and root-MUSIC algorithm with nRF modules using an 8-element circular array

aspect of having 74 sampling slots is the possibility of increasing the snapshots when collecting data. We can see this effect when using the TI or the e-lib antenna array in our study. It can mean that it supports up to 74 antennas. However, increasing the number of antennas to 74 is not necessarily the solution to a more accurate estimation. The most straightforward reason for it is that maintaining the critical low of $\phi < \pi/M$ becomes practically very difficult when $M = 74$ (ϕ is the max phase difference allowed between two adjacent antennas and M is the number of antennas). The maximum allowed phase difference between the reference and last antenna should not exceed the π/M, allowing a phase difference that we can no longer measure. In theory, after a certain number of antennas, the effect of antenna number is not significant [162, 163] after around 10 to 16 antennas.

In the case of AoD and $1\mu s$ sampling rate, having 16 antennas means each antenna in the pattern is used four times (snapshot = 4). This snapshot is too small for the auto-covariance matrix to converge to the theoretical value. In practice, we cannot access the $\boldsymbol{R_x}$. Therefore the covariance matrix $\hat{\boldsymbol{R}}_{\boldsymbol{x}} = \frac{1}{N_s}\Sigma_{i=1}^{N_s}\boldsymbol{X}(t_i)\boldsymbol{X}(t_i)^H$ is sampled and the aim is to maximize the likelihood of $\boldsymbol{R_x}$ estimation. N_s is the number of samples, and this equation is only possible if $N_s > M$ for the MUSIC algorithm. Of course, we can still measure the AoD with other methods, such as looking for the phase differences of the elements or increasing the sampling rate to increase the number of samples.

We used a UCA of 9 elements with a spacing of 3.5 cm presented in figure 4.12. Figure 6.21 presents the setup of our experiments. The antenna array is placed on top of the gate, and the tag is placed on a tripod. We collected the data at different elevation angles, and the azimuth angle remained within a specific range as we mainly focused on measuring the elevation angle. We measured the relative angle between the center of the antenna array and the tag with a BOSCH GLM500 laser telemeter. The relative orientation of the tag and the antenna array is what we call elevation and azimuth angle. The antenna pattern is pattern is $A_{ref}, A_1, A_2, A_3, A_4, A_5, A_6, A_7, A_8$ ant it repeats until the end of the CTE.
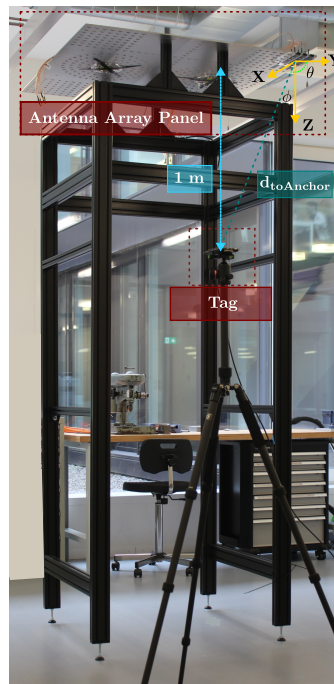
Figure 6.21: The antenna panel setup and the tag being tested in a laboratory environment

Figure 6.20 depicts the estimated AoDs of this array. In our experiment, we placed a tag on a tripod and moved it along a line to achieve different elevation angles. We measured the relative angle between the circle's center (antenna array) and the tag with a BOSCH GLM500 laser telemeter. The average error is 5.5° and 5.2° for the MUSIC and root-MUSIC algorithms. Which translates to a 45 cm accuracy in the location estimation. The main focus of these experiment sets is the elevation angle, even though the structure enables the possibility of measuring the azimuth angle simultaneously.

Figure 6.20 presents the average of estimated AoDs while measuring the elevation angles in figure 6.20a. Each dot in this figure is the average of the estimated azimuth angle at the respective angle. As we can see, the range of change in the azimuth angle is not wide because of the nature of the experiment. We moved the tag in a line. We just changed fewer times to measure the azimuth angle. We should remember that the previously measured AoDs show the azimuth angle estimations. The estimation accuracy for this small range is below 0.5°, which is irrelevant because of the high number of samples (using approximately 300 packets for each angle).

6.2.5 URA with nRF Modules

We are using an 8-element URA to test the performances of the array for an indoor environment. The antenna elements in this array are placed 3.5 cm apart vertically and horizontally ($d_x = d_y = 3.5\ cm$). The antenna array consists of two rows of 4 element antennas, and we

(a) Elevation angle   (b) Azimuth angle
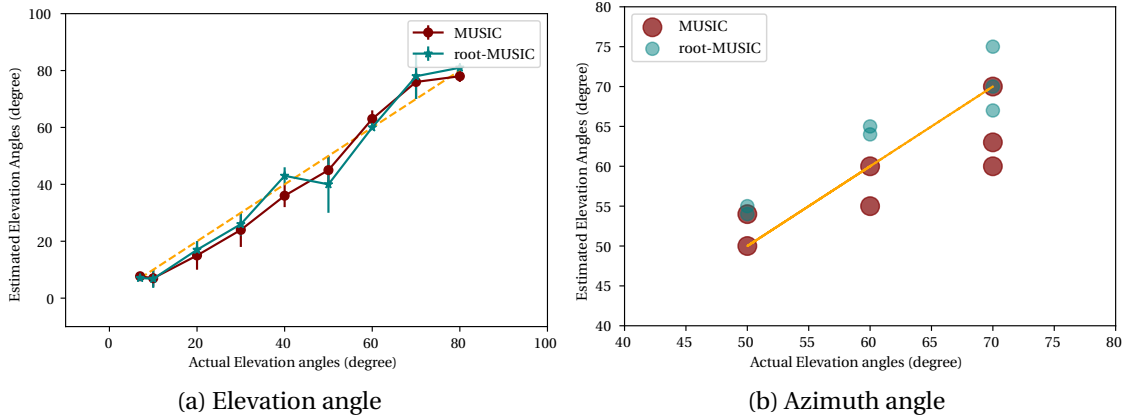
Figure 6.22: The estimated angles by MUSIC and root-MUSIC algorithm with nRF modules using a 2 × 4 rectangular array

are using the antenna pattern is $A_{ref}, A_1, A_2, A_3, A_4, A_5, A_6, A_7$ where the reference antenna is the first antenna in the first row of the array or A_0. This structure enables the possibility of measuring both azimuth and elevation angles.

Figure 6.22 presents the estimated AoDs measured by the 2 × 4 rectangular array for azimuth and elevation angles. In figure 6.22a, each point is the estimated AoD of a packet of data collected in real-time where the Z-score is $|Z_a| < 1$. This is the average of at least 100 data packets for each point. We changed the elevation angle by changing the tag's position along a line approximately every 10°. The absolute error of estimated angles by MUSIC and root-MUSIC is 3.8° and 3.5°. The absolute error is measured as the average absolute difference between the expected value and the estimated AoD. Therefore, by this method, we can reach an accuracy of about 33 cm and 31 cm in a radius of 5 m.

As we are testing on a relatively straight line on the X-Y plane, the azimuth angle does not change in a broader range. Measuring the elevation angle is the primary focus of these sets of experiments. For the azimuth angle, figure 6.22b presents several points for each angle. These points are the respective AoDs measured during the elevation experiment. The absolute error of the azimuth angle for this range of angles 3.7° for both algorithms leads to a 32 cm accuracy with a radius of 5 m.

6.2.6 Gaussian Mixture Models

As is presented in figure 6.17a, the estimated AoDs with the raw data can be divided into two clusters of data, and one of them is very close to the expected value. Even though averaging through the samples and data modification could take the estimations to the expected values, in some cases, it requires the elimination of up to 40% of the collected data. We decided to estimate the values with another method known as Gaussian Mixture Models or GMM [167, 168]. This method can be used for clustering data. Since we are already calculating

the collected data's means and variances, this method can be used later to cluster datasets. GMM is an unsupervised learning method. Therefore, it does not require predefined labels and ground truth, unlike supervised learning methods. As a result, it is a suitable method for clustering the collected data and understanding its nature without prior knowledge.

Essentially, GMM is a type of probabilistic model representing complex probability distributions. GMM represents the distributions as a mixture of multiple Gaussian distributions, each with its own mean and variance. In other words, a GMM assumes that the observed data is generated by a mixture of several Gaussian distributions with unknown parameters. These unknown parameters include the means, variances, and mixing proportions of the individual Gaussians.

As a result, we used a GMM model to cluster these data points and evaluate the model's performance on our data set. Here we explain the four steps to create the algorithm.

Step1. Initialization: First, we set the initial values of the means u_k, covariances Σ_k, and mixing coefficients π_k by simply using our estimated value from the averaging step.

The mixing coefficients refer to the weights assigned to each component Gaussian distribution in the mixture model. Each Gaussian component represents a cluster of data points, and the mixing coefficient specifies the probability that a randomly selected data point belongs to that cluster. If we assume K Gaussian components in the mixture model, the mixing coefficients are denoted as $\pi_1, \pi_2, ..., \pi_K$, where π_k is the weight assigned to the k_{th} Gaussian component. These coefficients must satisfy the following properties:

$$\pi_k \geq 0 \forall k \tag{6.1}$$

$$\sum_{k=1}^{K} \pi_k = 1 \tag{6.2}$$

Step2. Expectation(E): In this step, we compute the responsibilities γ_{nk} using the current parameter values:

$$\gamma_{nk} = \frac{\pi_k \mathcal{N}(\mathbf{x}_n | \mu_k, \Sigma_k)}{\sum_{j=1}^{K} \pi_j \mathcal{N}(\mathbf{x}_n | \mu_j, \Sigma_j)} \tag{6.3}$$

The notation $\mathcal{N}(\mathbf{x}_n | \mu_k, \Sigma_k)$ represents the Gaussian probability density function for the kth Gaussian with mean μ_k and covariance matrix Σ_k. Note that $\mathbf{x}_n$ represents the nth data point. This should not be confused by the X used for calculations of the MUSIC algorithm. Here, the $\mathbf{x}_n$ simply is the estimated AoDs by the algorithm.

Step3. Maximization (M): This step is to re-compute the parameters using the current responsibilities as:

$$\mu_k^{\text{new}} = \frac{1}{N_k} \sum_{n=1}^{N} \gamma_{nk} \mathbf{x}_n \tag{6.4}$$

and also we have:

$$\Sigma_k^{\text{new}} = \frac{1}{N_k} \sum_{n=1}^{N} \gamma_{nk}(\mathbf{x}_n - \mu_k^{\text{new}})(\mathbf{x}_n - \mu_k^{\text{new}})^\top \tag{6.5}$$

$$\pi_k^{\text{new}} = \frac{N_k}{N} \tag{6.6}$$

Where $N_k = \sum_{n=1}^{N} \gamma_{nk}$, also N is the total number of data points.

Step4. Evaluation: Finally, the evaluation step computes the log-likelihood function as:

$$\ln p(\mathbf{X}|\mu, \Sigma, \pi) = \sum_{n=1}^{N} \ln \left\{ \sum_{k=1}^{K} \pi_k \mathcal{N}(\mathbf{x}_n|\mu_k, \Sigma_k) \right\} \tag{6.7}$$

and check for convergence (i.e., of either the parameters or the log-likelihood). If the convergence criterion is not satisfied, return to E-step. The EM algorithm alternates between computing the responsibilities and updating the parameters until convergence is reached. The responsibilities determine the likelihood that a data point belongs to each Gaussian, while the parameter updates adjust the Gaussian means, covariances, and mixing coefficients to fit the observed data better.

Algorithm 7 EM algorithm for GMM

Require: Observed data $\mathbf{X}$

Ensure: GMM parameters μ, Σ, π

1: **Initialize** the means u_k, covariances Σ_k, and mixing coefficients π_k

2: **while** not converged **do**

3:     **E Step**: Compute the responsibilities γ_{nk} using the current parameter values:
    $\gamma_{nk} = \frac{\pi_k \mathcal{N}(\mathbf{x}n|\mu_k, \Sigma_k)}{\sum_{j=1}^{K} \pi_j \mathcal{N}(\mathbf{x}_n|\mu_j, \Sigma_j)}$

4:     **M Step**: Re-compute the parameters using the current responsibilities:
    $\mu_k^{\text{new}} = \frac{1}{N_k} \sum_{n=1}^{N} \gamma_{nk} \mathbf{x}_n$
    $\Sigma_k^{\text{new}} = \frac{1}{N_k} \sum_{n=1}^{N} \gamma_{nk}(\mathbf{x}_n - \mu_k^{\text{new}})(\mathbf{x}_n - \mu_k^{\text{new}})^\top$
    $\pi_k^{\text{new}} = \frac{N_k}{N}$ where $N_k = \sum_{n=1}^{N} \gamma_{nk}$

5:     **Evaluation**: Compute the log-likelihood:
    $\ln p(\mathbf{X}|\mu, \Sigma, \pi)$

6:     Check for convergence (e.g., of the parameters or the log-likelihood).

7: **end while**

This algorithm 7 presents all the steps to cluster the collected data after performing the AoD estimation. It is beneficial for cases where we witness recurrent peaks in the data, as we can see in figure 6.17a or when estimating both azimuth and elevation angles simultaneously. For instance, figure 6.23, presents the performance of the GMM algorithm on a set of data collected at 20° elevation and 75° azimuth angle.

In figure 6.23a, the red rectangle is the center of the estimated Gaussian or the μ_k values for azimuth and elevation angles, respectively. Each dot in the plot shows a packet's estimated

(a) Step 1   (b) Step 19
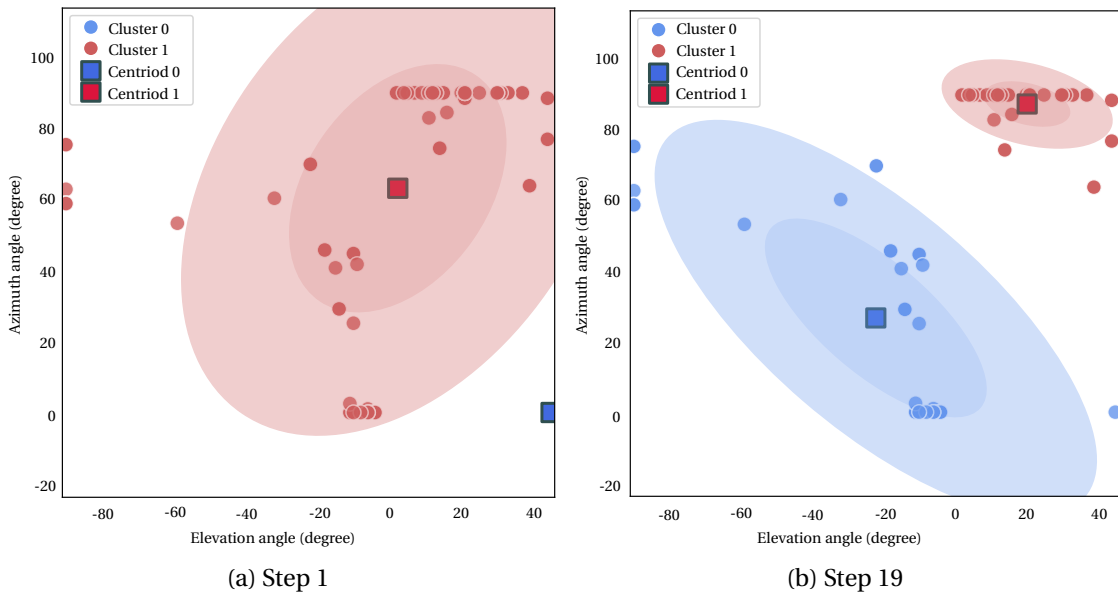
Figure 6.23: The M-step of the GMM algorithm over a set of data at 20° elevation and 75° azimuth

azimuth and elevation angle. The eclipse radius, width, and angle are proportional to Σ. We assumed to have two clusters of data (another one presented in blue). This is because, during the AoA estimation, two AoDs are found. The process starts with an initial random guess. Later, after several iterations, the algorithm should be able to allocate two regions for two categories. Therefore, we see in figure 6.23b that this already happens, and the two clusters are already created.

In the first step (figure 6.23a), the clusters are not yet formed; by several steps of iteration (figure 6.23b), these clusters form. A smart initial guess, such as the average of the estimated values, can decrease the iteration process. In figure 6.23 deliberately, a random value is chosen to present the process of the cluster allocation better.

For this specific data set, the estimated $\pi_k = (0.41, 0.58)$ for cluster numbers zero and one, respectively. This means it is more probable for a random data point to be classified in cluster zero than one. The center of this cluster indicates the estimated angle that should be around 20° for elevation and 80° for azimuth angle approximately.

As we can see, using the mean of the collected data as the initial guess for this case could classify the points into two separate groups after a few steps of iterations. Also, it could give the probability of a given data being in a certain class. Nevertheless, GMM has two important drawbacks.
This method is very dependent on the initial guess. A small change in the initial guess will greatly affect the classes. This method can drastically decrease the error when the estimations are close to the expected value. However, choosing the wrong initial guess can introduce huge

errors.

Another drawback of this method is that it cannot be implemented in real-time applications as it requires a learning step consisting of multiple iterations of the E-step and the M-step. Using a smart initial guess can decrease the number of iterations and increase the chance of convergence. On the other hand, this method can be used on the server side to track and locate the tag when collecting data sets. Moreover, it can be used for different tags in the area to distinguish the tags from each other. Therefore, this method is a great tool for analyzing the collected data.

6.2.7 Summary

By using the URA antenna array and collecting enough data packets, we can reach an accuracy below 50 *cm*. Using a URA as a new antenna structure has the benefit of providing both azimuth and elevation angles. However, it will decrease the speed of estimation. As an effort to improve the execution time of the code, we modified the algorithm to perform fewer searches as well as fewer loops by using double nested comprehension lists. These processes decrease the execution time by approximately 60%. Even this value can be decreased if searching within a specific range of angles (for example, the range of $(0° - 45°)$) for the azimuth or the elevation angle based on the relative position of each anchor in the room. For example, having several anchors in a room, we can anticipate the possible range angles that the tags might exist in that area depending on the room architecture. Therefore, we can limit the angle search loop to a smaller range to decrease the calculation speed.

These measurements are the recorded values from a real-time experiment. Recording and presenting the pseudo spectrum of the packets require extra time and processing. Therefore, we are only recording the peaks of the spectrum or using the root-MUSIC algorithm to speed up the process. In fact, using only the root-MUSIC is the answer for increasing the seed. We are only presenting the MUSIC spectrum here for comparison. As these two algorithms are essentially the same (one calculates the peak of the spectrum, and the other looks for the roots of the same spectrum), the accuracy of these two algorithms is also very similar in most cases, as we already witness. When using the ULAs, since the system is only searching for one angle (either azimuth or elevation, depending on the application), the spectrum can be drawn with and presented in real-time application. However, as the complexity arises with the 2D angle estimation, presenting the spectrum in 3D or two 2D spectra is time-consuming and eventually unnecessary. As a result, we modified our Graphic User Interface (GUI) to present both estimated angles in the shape of a gauge. We will elaborate on this matter in the next section. All and all, for this application, using the root-MUSIC algorithm for 2D estimation can drastically increase the estimation speed without decreasing the accuracy. So, to estimate the position of the tags, we are using this algorithm. Unlike MUSIC which involves plotting pseudo spectrum versus angles and searching the peak, root-MUSIC involves finding the roots of a polynomial [169].

A fundamental problem with using the ESPRIT algorithm is that having an estimation is not always guaranteed. The ESPRIT is only accurate if it can converge to a value. It is also limited to linear arrays. For a real-time application of indoor environments where the multipath is inevitable and the range of angles can be wide, the choice of ESPRIT might result in ambiguity when the algorithm fails to estimate the angle. Therefore, it cannot even provide the initial guess. When the sampling is happening in real-time, we need to have a result from each received packet unless the tag moves away, and this results in a loss of data. Therefore, we need to guarantee to have an estimation rather than having no estimation at all. This is the reason we decided to exclude ESPRIT from our real-time 2D estimations. We should remember that for 1D estimation, since the calculations are not as heavy, these issues are not problematic, and we will not require these considerations. The ESPRIT algorithm is easier to implement on an embedded system for real-time application because it does not require the spectrum computing step of the MUSIC algorithm. For instance, TI implemented a method based on the ESPRIT algorithm on their TI LAUNCHXL [151] modules with three antennas [146]. Therefore, it is recommended especially for 1D estimation when the algorithm should run locally on the device.

We need to collect more than 20 or 25 data packets to achieve such high accuracy. In general, the performance of the ULA array without modifications or using the data from the anechoic chamber as a reference is poor, around zero because the correlation across the array is high, and there is little diversity advantage [164]. Since the peaks at the URA are sharper and do not have peaks at the end of the spectrum, therefor this configuration is the best for AoD measurements.

As mentioned before, a single packet may not be accurate enough. What is important is that this initial estimation can be a good starting point for the system to build up the position estimation process using the received RSSI and estimated angles. As the results of the URA are more promising than the rest of the configurations we studied for the AoD architecture, we are using this configuration for positioning. In our journey, using the AoA architecture had two main benefits. First, it enables evaluating the algorithm's performance with an existing antenna array. Second, we could test the theory with another faster array with more antennas and different spacing. These two steps help us understand and polish the data extraction and modification process. The final aim of this system is to create a positioning system for real-time application. After a comprehensive study of AoD and AoA estimation with BLE-DF in the previous sections, in the next section, we will elaborate on the problem of positioning using other features of BLE-DF, such as RSSI.

6.3   Position Estimation

The final aim of this system is to design a real-time positioning system for indoor applications and below-meter accuracy. BLE-DF packets provide two pieces of information that can be used for positioning: the IQ samples that will result in direction estimation and the RSSI.
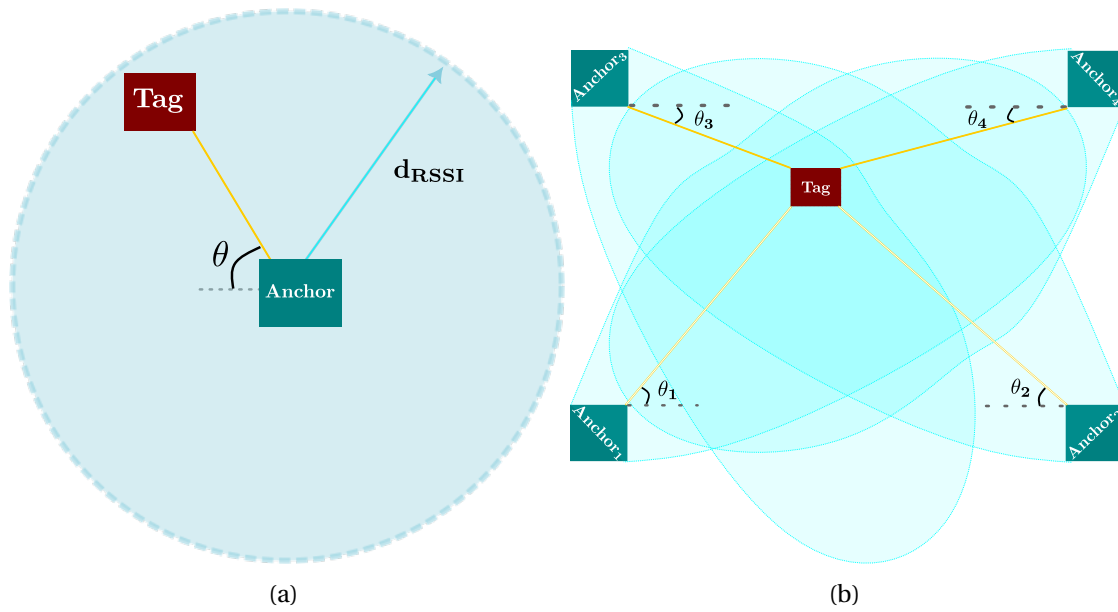
Figure 6.24: Presenting two different methods to estimate location having a) an angle and RSSI or b) only using angles

Each channel gives the RSSI and is constant during the IQ sampling period. Therefore, after processing each AoA/AoD (or Aox) packet, we will have two pieces of information: Aox and the RSSI. To estimate the location of the tags, we have two solutions. First, use the angle and the RSSI of one anchor simultaneously and estimate a range for the tag's location. This method is presented in figure 6.24a. The first method is less complex because it does not require more than one anchor to function at a time, but it fails to provide a very accurate result for the same reason. Also, it only gives the 2D estimation. So, during our measurements, the height of the tag remains constant and equal to the $1\ m$ from the origin presented in figure 6.21.

Second, use several anchors in a room to estimate the location of the tags by the triangulation method (figure 6.24b). The second solution is complex because it requires controlling several arrays simultaneously. With our designed antenna switch, this control is possible. So that we can use control two or more arrays as long as we can separate the reference antennas of two arrays; this means that in each array, the first antenna is the reference. For instance, if having two 4-element ULA arrays, the fifth antenna of the pattern will act as the reference for the second array. Regarding the influence of the reference period on the phase modification process, this method might not be very accurate. With the antenna pattern and the structure of the Aox packets, not using separate controllers can introduce errors in the estimation.
In fact, there are several other methods of calculating the tag position, such as using the geometric properties of the azimuth and elevation angle and having at least two anchors. We
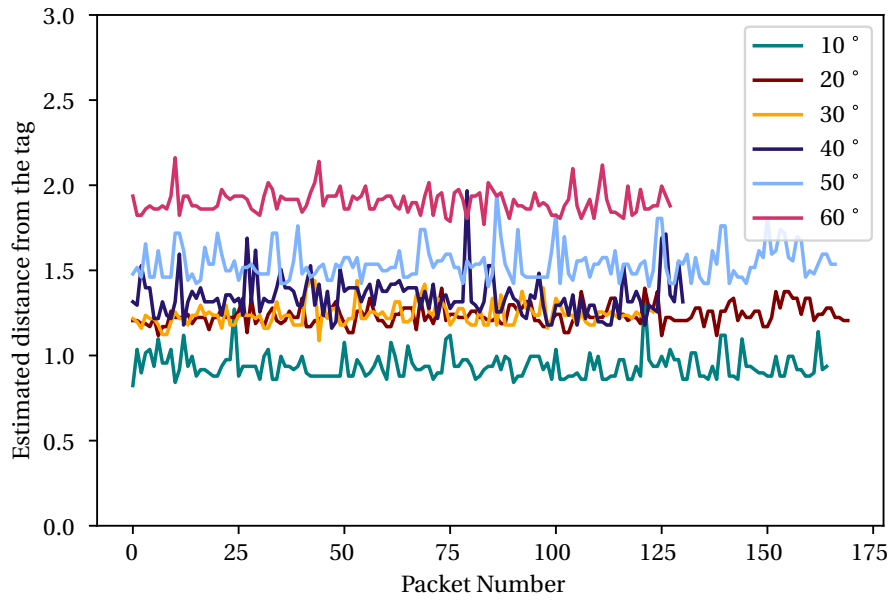
Figure 6.25: The estimated distance from the anchors at different angles and locations using the RSSI-distance formula. The unit of distance is meter (1 m)

have the following equation:

$$x_n = \frac{d_k \tan(\theta)}{\tan(\theta) - \tan(\phi)} \tag{6.8}$$

$$y_n = \frac{d_k \tan(\theta) \tan(\phi)}{\tan(\theta) - \tan(\phi)} \tag{6.9}$$

In this equation 6.9, the d_k is the distance between the two anchors. This equation can be used for cases when two or more anchors are used 6.24.

6.3.1 Geometric Positioning

We implemented the first positioning method to evaluate the system's performance as a positioning solution. It is trivial that this method's accuracy is based on its components' accuracy. The more accurate the angle estimation, the more accurate the final result. This is why we tried to improve the angle estimation for positioning. Figure 6.24 presents how having the angle and the RSSI can provide the location in 2D. We can use the same analogy for a 3D space having both the azimuth and the elevation angle. We can estimate an area where it is more probable for the tag to exist at that location.

This method has three different steps. First, we can estimate the tag's location from the RSSI (d_{RSSI}). It is the same equation mentioned in Chapter 3 for distance estimation (equation 3.3) with some modification. We can calculate the distance based on $10^{\frac{RSSI}{P_{TX}}}$ if the fraction of $\frac{RSSI}{P_{TX}} < 1$. This is essentially the range where the equation 3.3 is valid. We measured the average
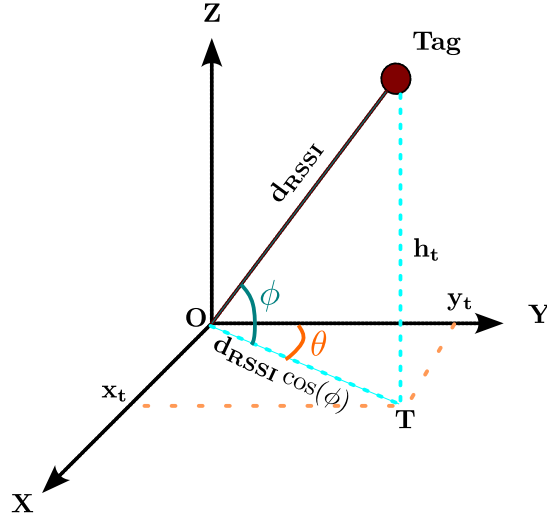
Figure 6.26: The geometrical relation between the estimated angles (θ, ϕ) and the estimated distance based on RSSI (d_{RSSI}). The origin (**O**) is the center of the antenna array.

transmitter power for all the antennas used, and we are using, and its value is $-23dBm$. Using this method, we can estimate the relative distance between the tag and the antenna array (it can be called d_{RSSI} as presented in figure 6.24a).

Figure 6.25 presents the estimated distance between the tag and the URA antenna array being tested at different distances and angles. The Euclidean distance between the tag and the antenna array is the calculated distance in this figure. We will later use this value, along with the estimated distance from the elevation and the azimuth angle, to calculate the exact position of the tags. Figure 6.26, presents the geometric relation between the estimated AoDs and the estimated distance from RSSI d_{RSSI}. Following trigonometry, the tag's location (x_t, y_t, h_t) can be calculated through the following equations:

$$h_t = d_{RSSI} \sin(\phi) \tag{6.10}$$
$$x_t = d_{RSSI} \cos(\phi) \sin(\theta) \tag{6.11}$$
$$y_t = d_{RSSI} \cos(\phi) \cos(\theta) \tag{6.12}$$

In equation 6.12, θ, ϕ are the azimuth and the elevation angles estimated by the 2D array at a given time. As it is trivial, these equations primarily depend on the estimated d_{RSSI}. For the case of only one anchor, this is the only method to reach a 3D estimation. However, this results in inferior precision (below 50%).

We designed an experiment where the Z and Y axis are not changing, and the value is known to be $h_t = 1\ m$ and d_{RSSI} is equal to $\sec(90 - \phi)$. Now in figure 6.26, we change the notation d_{RSSI}, to $d_{toAnchor}$, and $(90 - \phi)$ is the actual estimated elevation angle. Also, this means that the **OT** distance in XY plane that is noted in figure 6.26, is equal to $\tan(\phi)$.

Real Elevation (deg)	Estimated Elevation (deg)	Real **OT** (m)	Estimated **OT** (m)	|Error| (%)
10°	6.8°	0.17	0.31	45
20°	18.7°	0.36	0.34	5
30°	23.7°	0.57	0.86	33
40°	28.8°	0.83	0.55	33
50°	56.8°	1.19	1.52	21
60°	65.6°	1.73	2.21	21
70°	65.8°	2.74	2.23	18
80°	79.3°	5.67	5.32	6

Table 6.2: The array's estimation and actual relative distance from the tag in XY plane in the respective estimated elevation angle. At Y direction, the distance is 40 cm during all measurements. The tag is placed 1 m below the antenna array.
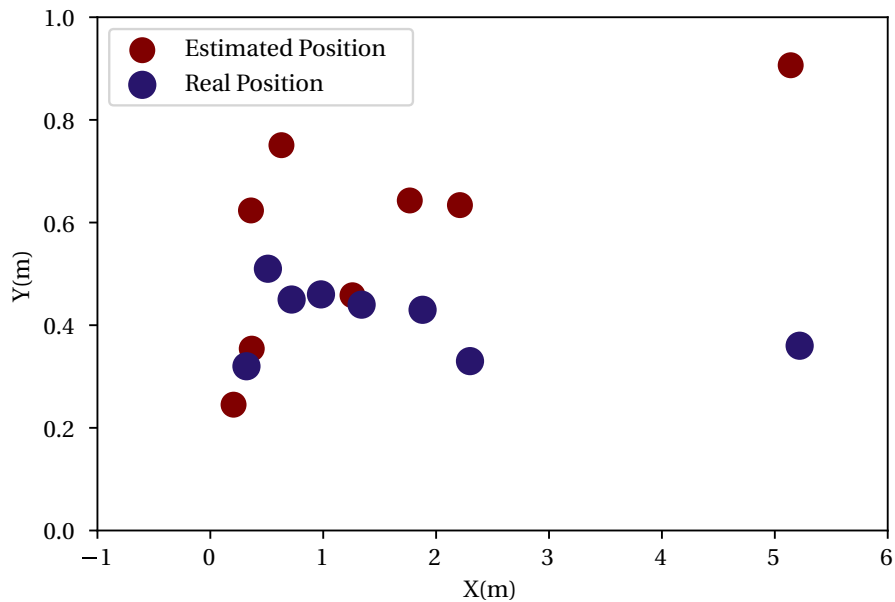
Figure 6.27: The estimated position of collected packets at each testing location in 2D

As explained before, we are changing the tag's location along a line in the room; therefore, the angle and the distance will change. This change starts at a short range of about 37 cm in the horizontal plane (XY) to up to approximately 6 m distance. The elevation angle changes within this range, and the relative vertical distance between the tag and the array remains approximately 1 m (the blue line presented in figure 6.21). The testing room is 10 $m \times$ 12 m. At 60°, the tag is approximately 2 m away from the center of the URA array ($d_{toAnchor}$), which results in a distance of approximately 1.7 m in XY plane.

Table 6.2 shows the tag's distance at the respective angle from the origin during our tests. $d_{toAnchor}$ is the value we can calculate by the elevation angle. This table calculated the expected value for $d_{toAnchor}$ in the second column at each angle. The fifth column shows the percentage of the absolute error at each position.

With the estimated azimuth angle, the (x, y) position is simply found by trigonometry. Also, the $d_{toAnchor}$ can be calculated based on the estimated azimuth angle. Which later can be used in a multilateration algorithm. Figure 6.27 presents the estimated vs. real location of the tag being tested in several locations. The calculations are based on the equations 6.12 and with the knowledge of both azimuth and elevation angle. Using this method, the average error in the Y direction is 22 cm, and at X direction is 16 cm.

6.3.2   Multilatration Algorithm

In this configuration, the estimated position can also be found by the $d_{toAnchor}$. After calculating the distance to the anchors from equation $d_{toAnchor} = \sec(90 - \phi)$, we are using a multilateration algorithm to estimate the location of the tags. Knowing the location of the anchors in the room, we use a function to minimize the error from the anchor location. Therefore, we can estimate the tag's location by having the distance from the RSSI and AoD measurements. Even if the distance does not converge, the algorithm finds the coordinates that minimize the function and returns the most optimal solution possible.

We implemented a multilateration algorithm that computes an initial guess of the tag's location using a weighted average of the anchor coordinates. Then we optimize this guess to minimize the error between the estimated position and the actual positions of the anchors, given the distances. This method can also perform multilateration for cases with multiple sources. We use the estimated distance from the RSSI and the AoD estimation to minimize the error. We use the Nedler-Mead [170] method to minimize the error. Also, the error is formulated as follows:

$$E(x, c, r) = \sum_{i=1}^{N} (||(x - c_i)|| - r_i^2) \tag{6.13}$$

Where $||(x - c_i)||$ represents the Euclidean distance between the estimated position of x and the ith anchor c_i. Which is, in fact, the estimated distances we already calculated. The goal is to minimize $E(x, c, r)$. We are using the Nelder-Mead [170] for the optimization algorithm since it is a gradient-free method, so it does not require computing the function's gradient. As a result, it is a fast computing method suitable for real-time applications. Instead, this method uses a set of points, called a simplex, to explore the function landscape and converge to a minimum iteratively. Using this method, we can estimate the tag's location in real time. Moreover, the whole algorithm is robust when having more than one anchor. Because in this case, the algorithm will use all the estimated distances from all the anchors and can calculate the position knowing the location of the anchors.

Figure 6.28 presents the estimated location of a tag tested at $\phi = 10°, \theta = 50°$, with $h_t = 1\ m$. Each dot in this figure presents the estimated location of a data packet. The dot size is the estimated distance calculated by the RSSI-distance formula. The star presents the average of the estimated location. This method has a very high accuracy of 10 cm for this angle. Using this method, at $\phi = 10°, \theta = 50°$, the average of the estimated location id ($X = 0.35, Y = 0.59, Z =$

0.94). This value is very close to the expected value of ($X = 0.32$, $Y = 0.4$, $Z = 1$). After averaging through all the packets and removing the outliers, this is the estimated value. As discussed, position estimation accuracy is strongly connected to angle estimation accuracy. Therefore, without collecting enough packets, achieving this accuracy is not possible.

In algorithm 8, The weight of each anchor is proportional to the ratio of the sum of all distances to the sum of the distances from the object to each anchor. The initial guess is calculated as the weighted average of the anchor coordinates, where the weights are given by the weight vector. All the weight and initial guess calculation details are presented in algorithm 8. We also defined the error function mentioned above; the final goal is minimizing this function. This algorithm is robust because it can change based on the number of anchors being used. The algorithm can adapt if more than one anchor is being used. For each anchor, we receive two values from two different sources that we call both $d_{toAnchor}$. To sum up the process of

---

Algorithm 8 Multilateration Algorithm

1: **function** MULTILATERATION($d_{toAnchor}, anchor\_coordinate$)
2:     Define error function $E(x, c, r)$ as:
3:         $E(x, c, r) \leftarrow \sum_{i=1}^{l} (|x - c_i| - r_i)^2$
4:            where l is the length of $anchor\_coordinate$
5:            and $|x - c_i|$ denotes the Euclidean distance between x and c_i
6:     $S \leftarrow \sum_{i=1}^{l} d_{toAnchor_i}$
7:     Compute weight vector W as:
8:         $W_i \leftarrow \frac{(l-1)S}{S - d_{toAnchor_i}}$ for $i = 1$ to l
9:     Compute initial guess x_0 as:
10:        $x_0 \leftarrow \sum_{i=1}^{l} W_i \cdot anchor\_coordinate_i$
11:     Optimize distance using the Nelder-Mead method
12:     **return** Estimated position x
13: **end function**

---

location estimation, the following algorithm is very helpful. Therefore, for each packet of

---

Algorithm 9 Localization Algorithm

1: **function** LOCALIZATION($Azimuth, Elevation, RSSI, anchor\_coordinate$)
2:     $d_{toAnchor} \leftarrow RSSI = -10nlog(d) + A$
3:     $d_{toAnchor} \leftarrow \sec(90 - \phi)$
4:     Estimate location $\leftarrow$ **MULTILATERATION**($d_{toAnchor}, anchor\_coordinat$)
5:     **return** Estimated position
6: **end function**

---

data, this algorithm 9 is used to estimate the tag's location. Figure 6.28 presented the result of the algorithm 9 implemented on a set of data we collected at $10°, 45°$ elevation and azimuth, respectively, in real-time. However, we only present the data where the absolute Z-score of the azimuth and the estimated elevation angle is below 1. The removed data packets from this data set are near 25% of the whole packets.
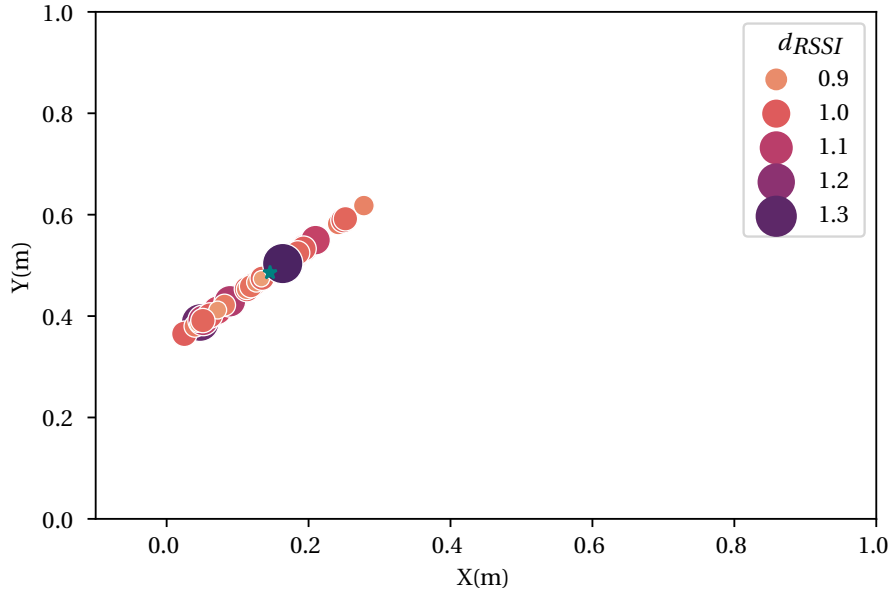
Figure 6.28: The estimated location of the tag at elevation and azimuth angles of $10°, 45°$ and vertical distance of $1\ m$ from the origin. The green star is the average of the samples. with the ground truth of $(X = 0.32, Y = 0.4)$

We performed the same test on the other collected data points from different angles at different locations. We used the estimated $d_{toAnchor}$ to establish the relative distance of the anchors and their locations. Since at the Y direction, the movement is small, the estimated location at this direction approximately stays the same during our calculation, and it is around $35\ cm$, which is very close to the real value. However, the important aspect is the estimated X value, which changes during our experiment. In our algorithm, the anchor's X coordinate changes according to the estimated $d_{toAnchor}$ because, in reality, the tag is the origin of movement. Table 6.3 presents the estimated X of the tag being moved during the experiment. The second column shows the actual location of the tag from the origin (presented in figure 6.21) in the X direction. In fact, these values are in the $-X$ direction, but for the sake of simplicity, we are

Estimated $X(m)$	Correct $X(m)$	|Error| (%)
0.40	0.32	25
0.53	0.51	3
1.03	0.72	43
0.77	0.98	21
1.52	1.34	13
2.35	1.88	25
2.41	2.29	4
5.86	5.22	10

Table 6.3: The estimation and actual location (X) of the tag, at Y direction, the distance is approximately $40\ cm$, and the height remains equal to $1\ m$ in Z direction.

only showing the distance. In some cases, the values in table 6.3 are very close to the correct value. However, as angles grow, these values tend to be less accurate. The absolute error of estimation is 30 cm, which is very close to the value we expect from the angle estimation precision.

6.4 Summary

This section summarizes all the recorded results in different sections of this chapter. In section 6.1.1, the performance of the three antenna array in an anechoic chamber is analyzed. The study shows that using the TI array, the average estimation error is $(7.8°, 8.4°)$ with ESPRIT and MUSIC algorithm with raw data. The e-lib antenna has an accuracy of $(5.9°, 3.9°)$, and the fast switch has $(0.9°, 1.4°)$ using ESPRIT and MUSIC algorithm with raw data in an anechoic chamber. The effect of channels also is studied in the same section, which confirms the expectation that the changes in the channels in an anechoic chamber should not affect the angle estimation precision.

In section 6.2.1, the performance of the TI array is studied in an indoor environment. As presented in table 6.1, estimation accuracy without any phase modification is below 50%, whereas by correcting the phase, the accuracy jumps to above 90%. This indicates that the phase modification process can increase the angle estimation precision up to 40%. In a range of 5 m by the proposed method a precision of up to 83% is reached.
Compared to the state of the art, [24], reached an accuracy of 25° which indicated an improvement of up to 86%. In another work, [8], reached an accuracy of 0.19, using a vector signal generator by performing a search procedure through all the possible angles. While very promising, this method is time-consuming and requires 360 ms to evaluate. [73], collected data from 4 anchors in an area of 5 $m \times 5$ m, and used a CNN algorithm to estimate the position. This work reached 87% accuracy in non-real-time conditions.

In section 6.2.2, the performance of the e-lib antenna array is studied in an indoor space. By this array, a precision of up to 5.3° is reached using phase modification and spatial smoothing method. Spatial smoothing is proposed to remove second peaks in the MUSIC spectrum, which proved to be up to 35% efficient as it removes the peaks caused by multipath 6.2.2.

In section 6.2.3, the performance of the fast switch and the antenna array is studied in the architecture of AoD. To the authors' knowledge, very few works have studied the BLE-AoD functionality in literature. The specially designed antenna switch allowed experimenting with a 1 μs sampling slot in AoD configuration. These experiments were all performed in real time. By averaging through the collected samples and using a ULA array, we could reach up to 2° of precision using the root-MUSIC algorithm. It is concluded that root-MUSIC is the fastest and most accurate among the three proposed algorithms 6.2.5. The effect of the antenna pattern by switching between the reference antenna and the rest of the antennas using a ULA array is studied in 6.2.3, which indicates that this method can improve the precision by up to 40%. This practice can be used when facing hardware limitations to improve precision.

Another aspect studied during this chapter is the antenna array's shape. A new dimension was introduced to the array to increase the estimation precision as well as another angle (elevation) to the mix. Such a system can estimate the location in 3D. Comparing the results of UCA and URA arrays suggested that the URA array can improve the estimation accuracy by about 70%, which will result in about 30 cm accuracy in location estimation 6.3. A GMM method is proposed to predict the most probable AoA for collected data. This method increased the precision by up to 85% and was studied in section 6.2.6. Practically, using the URA arrays have other advantages of being easier to produce and possibly using only one row at a time to increase calculation speed if required.

In section 6.3, a localization algorithm is proposed to calculate the position per packet. After extracting the data outliers every 20-30 packets, the algorithm reached the promising accuracy of 30 cm. This method is dependent on the abundance of measurement. Hence, it might be interesting to increase the number of anchors and perform a triangulation algorithm to decrease the number of required packets.

7 Conclusion

Positioning is a century-old question. Even though the question is old, advanced solutions have been proposed with the development of technology. Indoor positioning, however, has a shorter history and is becoming more relevant as the concept of smart cities is rising. Location estimation of an unknown target, whether a robot or a parcel, or even humans, is critical in many cases in industry and daily life. This thesis focuses on providing solutions for indoor positioning systems by presenting two different applications. First, we use access control as an example of indoor positioning to create a system. Second, in a broader sense, we use BLE direction finding for positioning at a room level. The evolution of the initial idea and the final prototype for each system is presented in this thesis.

This thesis focuses on indoor positioning and specifically examines the use of RF-based solutions to develop a system that can operate within 12 meters. The author reviews various indoor positioning technologies in Chapter 2 and aims to present a room-level positioning system with sub-meter accuracy. To achieve this goal, two methods were selected and tested in real-world conditions to assess their strengths and weaknesses.

7.1 The Thesis in a Nutshell

7.1.1 Smart Active Card and Hybrid System

This research proposed an RF-based system comprising three transmitters and a smart card, which falls under the category of active RFID with a frequency of $125kHz$. With the primary objective of tackling the issue of barrier-less access control in semi-enclosed environments. The proposed system offers several advantages, such as its ability to function effectively in challenging settings like concrete and snow or semi-enclosed areas where various structures may interfere with signals. Additionally, the proximity-based nature of our system ensures that it consumes minimal energy and only activates when in proximity to the transmitter, making it location-focused and ideal for access control solutions. The proposed Neural Network model improved the precision by 58% compared to traditional trilateration methods. This

Chapter 7. Conclusion

significantly improved compared to the expected range for active RFIDs, typically under 1 m.

The proposed hybrid system comprises a magnetic positioning system and two depth cameras. The magnetic system utilizes the same coils and frequency range as the smart card system and takes advantage of the electromagnetic field to provide more precise results and the ability to measure orientation. In addition, it includes an internal measurement unit (IMU) for enhanced precision and orientation measurements. Two depth cameras were developed by our collaborators at HE-Arc and e-liberty. The proposed real-time merging algorithm achieved high accuracy (> 94%) in detecting fraudulent attempts to gain access without impeding authorized users. However, the magnetic positioning system's reliance on the electromagnetic properties of the 3D coil made it highly susceptible to interference from bulk metallic bodies, rendering it unusable in their vicinity. To address this limitation, we opted for another technology, Bluetooth Direction Finding.

7.1.2 Bluetooth Direction Finding System

Bluetooth direction finding introduced in late 2019 is an evolution of the Bluetooth standard that uses IQ sampling to obtain phase information about the received signal. This technology is in its prime age and requires research and development in various aspects. This technology is mainly proposed for two reasons. First, it is widely used in electronic devices and can be easily integrated with other RF solutions, such as WiFi or cellular networks. Second, it is cost-effective and energy-efficient and provides both RSSI and AoA/AoD, enabling a positioning system with sub-meter accuracy in a room-level range. Additionally, this technology is scalable with BLE-mesh, which allows for broader range coverage and the creation of a network of connected anchors similar to WLAN with connected APIs.

The mission to complete the progress of this system is as follows:

The performance of BLE-DF in indoor spaces for real-time To address this question these are the steps were taken through chapters 4 to 6 respectively:

Step 1. Designing the specific hardware (antenna array) for BLE-DF protocol

Step 2. Processing of the samples to obtain AoA or AoD and distance estimates

Step 3. Localization from the results obtained by step 2

Two new antenna arrays and switches are investigated in Chapter 4. The e-lib antenna array introduced a 2D array of 2 × 4 and doubled the switching speed. The fast switch and antenna panel increased the number of antennas up to 74 (section 4.6.3). This antenna array also enabled 2D angle estimation with different UCA and URA configurations. This chapter delves into presenting the angle estimation algorithms.

One of the essential contributions of this thesis lies in the unique data extraction, magnitude correction, and phase compensation proposed specifically for BLE-DF, which is presented in Chapter 5. This method is based on the received signal's physical properties, which are used to correct the received data. Another contribution of the thesis is adapting the signal model

for the BLE-DF application. This model explains the process of converting the BLE signal as an input for the angle estimation algorithm and creating the auto-covariance matrix based on the received signal by the BLE modules.

Chapter 6 studies the performance of the angle estimation process and antenna arrays in different conditions. It highlights the importance of the phase compensation method in the estimation precision in practice. The experiment was conducted in an anechoic chamber and revealed that the fast array 4.12, 4.13 is up to 88%, 68% more accurate in comparison to TI 4.10 and e-lib 4.11 antenna array in an anechoic chamber.

The experiments in Chapter 6 revealed several interesting aspects of BLE-DF. The study has shown that the proposed phase compensation method increased the angle precision up to 40% compared to the raw data. In a range of 5 m by the proposed method, an accuracy of up to 93% in angle estimation is reached. This is an 86% improvement compared to the real-time state-of-the-art [24]. The e-lib antenna array and the spatial smoothing process increased the precision by up to 35% using the root-MUSIC algorithm with respect to the achieved precision by the TI array using the same algorithm.

The effect of fast switches and the AoD configuration is studied. Using a ULA array, excluding the outliers, and averaging through the channels, a precision of 2° is reached by the root-MUSIC algorithm in real-time application. This will result in 97% location precision in a radius of 5 m. This is one of the most important contributions of this thesis and is thanks to the angle estimation algorithm.

Moreover, the differences between UCA and URA arrays are thoroughly studied by these experiments. The study revealed that the URA array improves the angle estimation by up to 70% using the root-MUSIC algorithm compared to UCAs. The 2D arrays are superior for estimating both azimuth and elevation angles simultaneously. Using the URA array, a precision of up to 3.7° is reached in real-time, which is another essential aspect of this thesis. Performing the experiments, a conclusion is reached that no more than 8 antennas are required to achieve the discussed accuracy. Adding more antennas to the mix will mainly increase the calculation process. Therefore, there must be a trade-off between the number of antennas and the number of calculations required to achieve a reliable solution.

Existing of the multipath in an indoor environment makes the calculations less accurate. One of the methods to decrease this error is to sample at several channels and use an averaging method to estimate the angle precisely. Chapter 6 proposes another approach based on GMM to improve the estimation precision by 85%. This method can also be used on the server side after receiving several angle information from different anchors to estimate the angle or the position.

In Chapter 6, we also discussed estimating the position of the unknown tag, which is the ultimate goal of all the previous steps. A multilateration algorithm is employed based on the maximum likelihood of estimating the position with one or more anchors. This thesis

demonstrates that an accuracy of 30 *cm* with the AoD architecture is achieved for location estimation by BLE-AoD.

7.2 Contributions

The main scientific contributions, as they are described throughout this chapter, can be summarized as follow:

Characterize and comprehensive analysis of the proposed smart card system for access control: presented in section 3.2, 3.4

Propose a neural network model for localization by smart card: presented in section 3.4.5

Formulate a real-time merging algorithms for the hybrid system: explained in section 3.5.4, 3.5.6, and 3.5.8, 3.5.5 reaching to 94% precision in detecting unauthorized access

Introducing antenna arrays optimized for BLE-DF: studied in section 4.6.2 and 4.6.3

Formulate a real-time angle estimation algorithm with the precision of 97% by BLE-AoD at 1μs

Proposing a phase compensation method that improved angle estimation up 40%

Achieve simultaneous 2D angle estimation by the precision of 95%

Enhance 2D angle estimation in high SNR environments by up to 85% using a Gaussian Mixture Model: presented in section 6.2.6

7.3 Outlook

Nowadays, the design and development of non-blocking access control have many practical applications, such as in trains, in private resorts, or even in buildings and malls. These systems have room for improvement based on their specific application. For instance:

- *Using more transmitters for active card*: In our proposed structure, we utilized three transmitters to generate the electromagnetic field for the tags. As previously mentioned, positioning accuracy is higher in one direction due to the presence of more anchors. An interesting aspect to be explored is incorporating additional anchors at greater distances to assess their impact on performance. Furthermore, adding another dimension (Z) to the experiment to obtain 3D location information can be considered.

- *Range expansion of the system*: An area that requires improvement in the proposed hybrid system is its limited surveillance range. Expanding the range of the system to cover a larger area can be an interesting study. The AmfiTrack system has a wide range of up to 2.5 *m* without compromising accuracy. Incorporating additional cameras into the system may increase its range further.

Achieving very high angle estimation precision is the key to developing a high-precision IPS based on BLE-DF, which is thoroughly studied in this thesis. This work is mainly focused on

processing IQ data. Some aspects need to be studied in order to improve the system further. For example:

- *Using several anchors:* Using several AoD anchors simultaneously and synchronization between these anchors can be an interesting aspect to study and improve estimation accuracy with only one packet.

- *Compact antenna array design:* Designing the antenna array can be challenging, considering the concerns about phase change during switching times. Depending on the application, one might need a more compact antenna array.

- *Security considerations:* One of the concerns of any systems-based BLE is cybersecurity vulnerabilities. In 2023, a new vulnerability has been found in BLE periodic advertisement event which can be used in the AoD application [171]. Also, when using BLE for industrial IoT, certain vulnerabilities might occur that require attention and further research.

These are some of the aspects that require further study in order to achieve a fully functioning BLE-DF system.

Bibliography

[1] W. Sakpere, M. Adeyeye-Oshin, and N. B. Mlitwa, "A state-of-the-art survey of indoor positioning and navigation systems and technologies," *South African Computer Journal* **29**(3), pp. 145–197, 2017.

[2] D. Dardari, P. Closas, and P. M. Djurić, "Indoor tracking: Theory, methods, and technologies," *IEEE Transactions on Vehicular Technology* **64**(4), pp. 1263–1278, 2015.

[3] "statista." Available at: https://www.statista.com/topics/2637/internet-of-things/#topicOverview. Accessed: 28-05-2023.

[4] Z. Farid, R. Nordin, and M. Ismail, "Recent advances in wireless indoor localization techniques and system," *Journal of Computer Networks and Communications* **2013**, 2013.

[5] R. Mautz, "Indoor positioning technologies," 2012.

[6] Y. Li, Y. Zhuang, X. Hu, Z. Gao, J. Hu, L. Chen, Z. He, L. Pei, K. Chen, M. Wang, X. Niu, R. Chen, J. Thompson, F. M. Ghannouchi, and N. El-Sheimy, "Toward location-enabled iot (le-iot): Iot positioning techniques, error sources, and error mitigation," *IEEE Internet of Things Journal* **8**(6), pp. 4035–4062, 2021.

[7] F. Zafari, A. Gkelias, and K. K. Leung, "A survey of indoor localization systems and technologies," *IEEE Communications Surveys & Tutorials* **21**(3), pp. 2568–2599, 2019.

[8] C. Huang, Y. Zhuang, H. Liu, J. Li, and W. Wang, "A performance evaluation framework for direction finding using ble aoa/aod receivers," *IEEE Internet of Things Journal* **8**(5), pp. 3331–3345, 2021.

[9] N. B. Suryavanshi, K. Viswavardhan Reddy, and V. R. Chandrika, "Direction Finding Capability in Bluetooth 5.1 Standard," *Lecture Notes of the Institute for Computer Sciences, Social-Informatics and Telecommunications Engineering, LNICST* **276**, pp. 53–65, 2019.

[10] H. Ye, B. Yang, Z. Long, and C. Dai, "A method of indoor positioning by signal fitting and pdda algorithm using ble aoa device," *IEEE Sensors Journal* **22**(8), pp. 7877–7887, 2022.

[11] S.-H. Fang, C.-H. Wang, T.-Y. Huang, C.-H. Yang, and Y.-S. Chen, "An enhanced zigbee indoor positioning system with an ensemble approach," *IEEE Communications Letters* **16**(4), pp. 564–567, 2012.

[12] X. Du, K. Yang, and D. Zhou, "Mapsense: Mitigating inconsistent wifi signals using signal patterns and pathway map for indoor positioning," *IEEE Internet of Things Journal* **5**(6), pp. 4652–4662, 2018.

[13] C. Chen, Y. Chen, Y. Han, H.-Q. Lai, F. Zhang, and K. J. R. Liu, "Achieving centimeter-accuracy indoor localization on wifi platforms: A multi-antenna approach," *IEEE Internet of Things Journal* **4**(1), pp. 122–134, 2017.

[14] D. Feng, C. Wang, C. He, Y. Zhuang, and X.-G. Xia, "Kalman-filter-based integration of imu and uwb for high-accuracy indoor positioning and navigation," *IEEE Internet of Things Journal* **7**(4), pp. 3133–3146, 2020.

[15] P. Schwarzbach, R. Weber, and O. Michler, "Statistical evaluation and synthetic generation of ultra-wideband distance measurements for indoor positioning systems," *IEEE Sensors Journal* **22**(6), pp. 4836–4843, 2022.

[16] W. Storms, J. Shockley, and J. Raquet, "Magnetic field navigation in an indoor environment," in *2010 Ubiquitous Positioning Indoor Navigation and Location Based Service*, pp. 1–10, IEEE, 2010.

[17] N. Fallah, I. Apostolopoulos, K. Bekris, and E. Folmer, "Indoor human navigation systems: A survey," *Interacting with Computers* **25**(1), pp. 21–33, 2013.

[18] T. K. Tsang and M. N. El-Gamal, "Ultra-wideband (uwb) communications systems: an overview," in *The 3rd International IEEE-NEWCAS Conference, 2005.*, pp. 381–386, IEEE, 2005.

[19] J.-S. Lee, Y.-W. Su, and C.-C. Shen, "A comparative study of wireless protocols: Bluetooth, uwb, zigbee, and wi-fi," in *IECON 2007-33rd Annual Conference of the IEEE Industrial Electronics Society*, pp. 46–51, Ieee, 2007.

[20] V. Pasku, A. De Angelis, G. De Angelis, D. D. Arumugam, M. Dionigi, P. Carbone, A. Moschitta, and D. S. Ricketts, "Magnetic field-based positioning systems," *IEEE Communications Surveys & Tutorials* **19**(3), pp. 2003–2017, 2017.

[21] R. T. Pål Frenger, "A technical look at 5g energy consumption and performance." Available at : https://www.ericsson.com/en/blog/2019/9/energy-consumption-5g-nr.

[22] N. I. with UWB, "Nearby interaction with uwb." Available at : https://developer.apple.com/nearby-interaction/.

[23] Decawave, "Decawave." Available at : https://www.qorvo.com/products/p/DW1000.

[24] L. Botler, M. Spörk, K. Diwold, and K. Römer, "Direction finding with uwb and ble: A comparative study," in *2020 IEEE 17th International Conference on Mobile Ad Hoc and Sensor Systems (MASS)*, pp. 44–52, 2020.

[25] E. Gönültaş, E. Lei, J. Langerman, H. Huang, and C. Studer, "Csi-based multi-antenna and multi-point indoor positioning using probability fusion," *IEEE Transactions on Wireless Communications* **21**(4), pp. 2162–2176, 2022.

[26] M. Kotaru, K. Joshi, D. Bharadia, and S. Katti, "SpotFi," *ACM SIGCOMM Computer Communication Review* **45**(4), pp. 269–282, 2015.

[27] Q. H. Nguyen, P. Johnson, T. T. Nguyen, and M. Randles, "Optimized indoor positioning for static mode smart devices using BLE," *IEEE International Symposium on Personal, Indoor and Mobile Radio Communications, PIMRC* **2017-October**, pp. 1–6, 2018.

[28] R. Ayyalasomayajula, D. Vasisht, and D. Bharadia, "BLoc: CSI-based accurate localization for BLE tags," *CoNEXT 2018 - Proceedings of the 14th International Conference on Emerging Networking EXperiments and Technologies*, pp. 126–138, 2018.

[29] F. S. Parizi, E. Whitmire, and S. Patel, "Auraring: Precise electromagnetic finger tracking," *Proc. ACM Interact. Mob. Wearable Ubiquitous Technol.* **3**, Dec. 2019.

[30] Polhemus, "G4 ™wireless motion tracker and digitizing stylus." Available at : https://polhemus.com/motion-tracking/all-trackers/g4 (visited on 09.01.2023).

[31] B. Denis, J. Keignart, and N. Daniele, "Impact of nlos propagation upon ranging precision in uwb systems," in *IEEE conference on Ultra Wideband Systems and Technologies, 2003*, pp. 379–383, IEEE, 2003.

[32] S. Gezici, Z. Tian, G. B. Giannakis, H. Kobayashi, A. F. Molisch, H. V. Poor, and Z. Sahinoglu, "Localization via ultra-wideband radios: a look at positioning aspects for future sensor networks," *IEEE signal processing magazine* **22**(4), pp. 70–84, 2005.

[33] R. Mautz and S. Tilch, "Survey of optical indoor positioning systems," in *2011 international conference on indoor positioning and indoor navigation*, pp. 1–7, IEEE, 2011.

[34] S. Holm, "Hybrid ultrasound-rfid indoor positioning: Combining the best of both worlds," in *2009 IEEE International Conference on RFID*, pp. 155–162, IEEE, 2009.

[35] R. V. Kulkarni, A. Förster, and G. K. Venayagamoorthy, "Computational intelligence in wireless sensor networks: A survey," *IEEE communications surveys & tutorials* **13**(1), pp. 68–96, 2010.

[36] A. Lazaro, D. Girbau, and D. Salinas, "Radio link budgets for uhf rfid on multipath environments," *IEEE transactions on antennas and propagation* **57**(4), pp. 1241–1251, 2009.

[37] M. Cassel, T. Dépret, and H. Piégay, "Assessment of a new solution for tracking pebbles in rivers based on active rfid," *Earth Surface Processes and Landforms* **42**(13), pp. 1938–1951, 2017.

[38] A. D. Koutsou, F. Seco, A. R. Jiménez, J. O. Roa, J. L. Ealo, C. Prieto, and J. Guevara, "Preliminary localization results with an rfid based indoor guiding system," in *2007 IEEE International Symposium on Intelligent Signal Processing*, pp. 1–6, IEEE, 2007.

[39] F.-j. Zhu, Z.-h. Wei, B.-j. Hu, J.-g. Chen, and Z.-m. Guo, "Analysis of indoor positioning approaches based on active rfid," in *2009 5th International Conference on Wireless Communications, Networking and Mobile Computing*, pp. 1–4, IEEE, 2009.

[40] T. F. Bechteler and H. Yenigun, "2-d localization and identification based on saw id-tags at 2.5 ghz," *IEEE Transactions on Microwave Theory and Techniques* **51**(5), pp. 1584–1590, 2003.

[41] V. Chawla and D. S. Ha, "An overview of passive rfid," *IEEE Communications Magazine* **45**(9), pp. 11–17, 2007.

[42] H. Vogt, "Efficient object identification with passive rfid tags," in *Pervasive Computing: First International Conference, Pervasive 2002 Zurich, Switzerland, August 26–28, 2002 Proceedings 1*, pp. 98–113, Springer, 2002.

[43] M. Cassel, H. Piégay, and J. Lavé, "Effects of transport and insertion of radio frequency identification (rfid) transponders on resistance and shape of natural and synthetic pebbles: applications for riverine and coastal bedload tracking," *Earth Surface Processes and Landforms* **42**(3), pp. 399–413, 2017.

[44] J. Schweizer, M. Genswein, F. Jarry, and D. Létang, "Transceiver performance when searching for multiple burials," *The Avalanche Journal* **102**, pp. 72–77, 01 2012.

[45] G. yao Jin, X. yi Lu, and M.-S. Park, "An indoor localization mechanism using active rfid tag," in *IEEE International Conference on Sensor Networks, Ubiquitous, and Trustworthy Computing (SUTC'06)*, **1**, pp. 4 pp.–, 2006.

[46] F. H. Raab, E. B. Blood, T. O. Steiner, and H. R. Jones, "Magnetic position and orientation tracking system," *IEEE Transactions on Aerospace and Electronic systems* (5), pp. 709–718, 1979.

[47] E. Paperno, I. Sasada, and E. Leonovich, "A new method for magnetic position and orientation tracking," *IEEE Transactions on Magnetics* **37**(4), pp. 1938–1940, 2001.

[48] B. Gozick, K. P. Subbu, R. Dantu, and T. Maeshiro, "Magnetic maps for indoor navigation," *IEEE Transactions on Instrumentation and Measurement* **60**(12), pp. 3883–3891, 2011.

[49] O. Talcoth and T. Rylander, "Optimization of sensor positions in magnetic tracking," tech. rep., Chalmers University of Technology, 2011.

[50] J. Blankenbach, A. Norrdine, and H. Hellmers, "A robust and precise 3d indoor positioning system for harsh environments," in *2012 international conference on indoor positioning and indoor navigation (IPIN)*, pp. 1–8, IEEE, 2012.

[51] J. Huang, T. Mori, K. Takashima, S. Hashi, and Y. Kitamura, "Im6d: magnetic tracking system with 6-dof passive markers for dexterous 3d interaction and motion," *ACM Transactions on Graphics (TOG)* **34**(6), pp. 1–10, 2015.

[52] AmfiTrack, "Amfitrack ™." Available at : https://www.amfitrack.com/(visited on 09.01.2023).

[53] "The Difference Between Classic Bluetooth and Bluetooth Low Energy." Available at: https://www.bluetooth.com/bluetooth-resources/the-difference-between-classic-bluetooth-and-bluetooth-low-energy/. Accessed: 26-6-2023.

[54] "The Difference Between Classic Bluetooth and Bluetooth Low Energy." Available at: https://blog.nordicsemi.com/getconnected/the-difference-between-classic-bluetooth-and-bluetooth-low-energy. Accessed: 26-6-2023.

[55] R. Ayyalasomayajula, D. Vasisht, and D. Bharadia, "BLoc: CSI-based accurate localization for BLE tags," *CoNEXT 2018 - Proceedings of the 14th International Conference on Emerging Networking EXperiments and Technologies* , pp. 126–138, 2018.

[56] R. Faragher and R. K. Harle, "An analysis of the accuracy of bluetooth low energy for indoor positioning applications," 2014.

[57] "AirTag." Available at: https://www.apple.com/airtag/. Accessed: 12-04-2023.

[58] R. M. Faragher, C. Sarno, and M. Newman, "Opportunistic radio slam for indoor navigation using smartphone sensors," in *Proceedings of the 2012 IEEE/ION Position, Location and Navigation Symposium*, pp. 120–128, 2012.

[59] T. Instrument, "Application note." https://www.ti.com/lit/an/swra478d/swra478d.pdf, 2019.

[60] D. Ronald D, "The constrained music problem," *IEEE Trans on SP* **41(3)**, p. P1445 1449, 1993.

[61] M. L. Miller., "Maximum likelihood narrow-band direction finding and em algorithms," *IEEE Trans on ASSP* **36(10)**, p. P1560 1577, 1990.

[62] Z. I. M. M, "Maximum likelihood localization of multiple sources by alternating projection," *IEEE Trans on ASSP* **36(10)**, p. P1553 1560, 1988.

[63] F. Richard, "Analysis of min-norm and music with arbitrary array geometry," *IEEE Trans on AES* **26(6)**, p. P976 985, 1990.

Bibliography

[64] Z. Jianyong, L. Haiyong, C. Zili, and L. Zhaohui, "Rssi based bluetooth low energy indoor positioning," in *2014 International Conference on Indoor Positioning and Indoor Navigation (IPIN)*, pp. 526–533, IEEE, 2014.

[65] Q. H. Nguyen, P. Johnson, T. T. Nguyen, and M. Randles, "Optimized indoor positioning for static mode smart devices using ble," in *2017 IEEE 28th Annual International Symposium on Personal, Indoor, and Mobile Radio Communications (PIMRC)*, pp. 1–6, 2017.

[66] S. Yong, "Tests of bluetooth low energy 5.1 indoor navigation-direction finding application note." Available: http://www.rohde-schwarz.com/appnote/GFM327„ 2020.

[67] R. Giuliano, G. C. Cardarilli, C. Cesarini, L. Di Nunzio, F. Fallucchi, R. Fazzolari, F. Mazzenga, M. Re, and A. Vizzarri, "Indoor localization system based on bluetooth low energy for museum applications," *Electronics* **9**(6), 2020.

[68] M. Woolley, "Bluetooth Direction Finding," (March), 2021.

[69] bluetooth SIG, "Real time localization system (rtls) based on bluetooth low energy." https://dev.ti.com/tirex/explore/node?node=A__AIDWKpsVKd69FVe1wxeXgA__com.ti.SIMPLELINK_ACADEMY_CC13XX_CC26XX_SDK__AfkT0vQ__LATEST&r=pTTHBmu__5.10.00.48, 2023.

[70] bluetooth SIG, "Bluetooth-direction-finding." https://www.nordicsemi.com/Products/Bluetooth-Direction-Finding, 2023.

[71] T. Instrument, "Angle of arrival boosterpack." Available: https://www.ti.com/lit/pdf/swau110, 2018.

[72] T. Instrument, "Simplelink bluetooth 5.1 low energy wireless mcu." https://www.ti.com/lit/ds/symlink/cc2640r2f.pdf?ts=1687842742671, 2020.

[73] Z. HajiAkhondi-Meybodi, M. Salimibeni, A. Mohammadi, and K. N. Plataniotis, "Bluetooth low energy and cnn-based angle of arrival localization in presence of rayleigh fading," in *ICASSP 2021 - 2021 IEEE International Conference on Acoustics, Speech and Signal Processing (ICASSP)*, pp. 7913–7917, 2021.

[74] A. Koutris, T. Siozos, Y. Kopsinis, A. Pikrakis, T. Merk, M. Mahlig, S. Papaharalabos, and P. Karlsson, "Deep learning-based indoor localization using multi-view ble signal," *Sensors* **22**(7), 2022.

[75] A. Khan, S. Wang, and Z. Zhu, "Angle-of-Arrival Estimation Using an Adaptive Machine Learning Framework," *IEEE Communications Letters* **23**(2), pp. 294–297, 2019.

[76] F. A. Toasa, L. Tello-Oquendo, C. R. Peńafiel-Ojeda, and G. Cuzco, "Experimental demonstration for indoor localization based on aoa of bluetooth 5.1 using software defined radio," in *2021 IEEE 18th Annual Consumer Communications & Networking Conference (CCNC)*, pp. 1–4, 2021.

[77] SliliconLab, "Sliliconlab direction finding." https://www.silabs.com/wireless/bluetooth/direction-finding, 2023.

[78] BlueIot, "Blueiot." https://www.blueiot.com/, 2023.

[79] S. Yiu, M. Dashti, H. Claussen, and F. Perez-Cruz, "Wireless rssi fingerprinting localization," *Signal Processing* **131**, pp. 235–244, 2017.

[80] H. Sallouha, A. Chiumento, and S. Pollin, "Localization in long-range ultra narrow band iot networks using rssi," in *2017 IEEE International Conference on Communications (ICC)*, pp. 1–6, IEEE, 2017.

[81] F. Gustafsson and F. Gunnarsson, "Positioning using time-difference of arrival measurements," in *2003 IEEE International Conference on Acoustics, Speech, and Signal Processing, 2003. Proceedings.(ICASSP'03).*, **6**, pp. VI–553, IEEE, 2003.

[82] X. Li, Z. D. Deng, L. T. Rauchenstein, and T. J. Carlson, "Contributed review: Source-localization algorithms and applications using time of arrival and time difference of arrival measurements," *Review of Scientific Instruments* **87**(4), p. 041502, 2016.

[83] P. Rong and M. L. Sichitiu, "Angle of arrival localization for wireless sensor networks," in *2006 3rd annual IEEE communications society on sensor and ad hoc communications and networks*, **1**, pp. 374–382, Ieee, 2006.

[84] R. Peng and M. L. Sichitiu, "Angle of arrival localization for wireless sensor networks," in *2006 3rd annual IEEE communications society on sensor and ad hoc communications and networks*, **1**, pp. 374–382, Ieee, 2006.

[85] Z. Yang, Z. Zhou, and Y. Liu, "From rssi to csi: Indoor localization via channel response," *ACM Computing Surveys (CSUR)* **46**(2), pp. 1–32, 2013.

[86] M. Gholami, N. Cai, and R. Brennan, "An artificial neural network approach to the problem of wireless sensors network localization," *Robotics and Computer-Integrated Manufacturing* **29**(1), pp. 96–109, 2013.

[87] L. Gogolak, S. Pletl, and D. Kukolj, "Neural network-based indoor localization in wsn environments," *Acta Polytechnica Hungarica* **10**(6), pp. 221–235, 2013.

[88] H. Zhang and C. Ye, "An indoor wayfinding system based on geometric features aided graph slam for the visually impaired," *IEEE Transactions on Neural Systems and Rehabilitation Engineering* **25**(9), pp. 1592–1604, 2017.

[89] Y. Xie, Y. Wang, A. Nallanathan, and L. Wang, "An improved k-nearest-neighbor indoor localization method based on spearman distance," *IEEE signal processing letters* **23**(3), pp. 351–355, 2016.

[90] M. T. Hoang, Y. Zhu, B. Yuen, T. Reese, X. Dong, T. Lu, R. Westendorp, and M. Xie, "A soft range limited k-nearest neighbors algorithm for indoor localization enhancement," *IEEE Sensors Journal* **18**(24), pp. 10208–10216, 2018.

[91] I. A. Junglas and R. T. Watson, "Location-based services," *Communications of the ACM* **51**(3), pp. 65–69, 2008.

[92] M. F. Goodchild, "Location-based services," in *Encyclopedia of Social Network Analysis and Mining. 2nd Ed.*, 2018.

[93] D. Balakrishnan and A. Nayak, "An efficient approach for mobile asset tracking using contexts," *IEEE Transactions on Parallel and Distributed Systems* **23**(2), pp. 211–218, 2012.

[94] S. Yoo, S. Kim, E. Kim, E. Jung, K.-H. Lee, and H. Hwang, "Real-time location system-based asset tracking in the healthcare field: lessons learned from a feasibility study," *BMC medical informatics and decision making* **18**(1), pp. 1–10, 2018.

[95] R. N. Kandalan and K. Namuduri, "Techniques for constructing indoor navigation systems for the visually impaired: A review," *IEEE Transactions on Human-Machine Systems* **50**(6), pp. 492–506, 2020.

[96] A. F. G. Gonçalves Ferreira, D. M. A. Fernandes, A. P. Catarino, and J. L. Monteiro, "Localization and positioning systems for emergency responders: A survey," *IEEE Communications Surveys & Tutorials* **19**(4), pp. 2836–2870, 2017.

[97] N. Simon, J. Bordoy, F. Höflinger, J. Wendeberg, M. Schink, R. Tannhäuser, L. Reindl, and C. Schindelhauer, "Indoor localization system for emergency responders with ultra low-power radio landmarks," in *2015 IEEE International Instrumentation and Measurement Technology Conference (I2MTC) Proceedings*, pp. 309–314, 2015.

[98] Y. Zhuang, Y. Li, H. Lan, Z. Syed, and N. El-Sheimy, "Wireless access point localization using nonlinear least squares and multi-level quality control," *IEEE Wireless Communications Letters* **4**(6), pp. 693–696, 2015.

[99] J. Zhang, X. Wang, Z. Yu, Y. Lyu, S. Mao, S. C. Periaswamy, J. Patton, and X. Wang, "Robust rfid based 6-dof localization for unmanned aerial vehicles," *IEEE Access* **7**, pp. 77348–77361, 2019.

[100] J. Landt, "The history of rfid," *IEEE potentials* **24**(4), pp. 8–11, 2005.

[101] R. Want, "An introduction to rfid technology," *IEEE pervasive computing* **5**(1), pp. 25–33, 2006.

[102] D. Zhang, L. T. Yang, M. Chen, S. Zhao, M. Guo, and Y. Zhang, "Real-time locating systems using active rfid for internet of things," *IEEE Systems Journal* **10**(3), pp. 1226–1235, 2016.

[103] L. Ni, Y. Liu, Y. C. Lau, and A. Patil, "Landmarc: indoor location sensing using active rfid," in *Proceedings of the First IEEE International Conference on Pervasive Computing and Communications, 2003. (PerCom 2003).*, pp. 407–415, 2003.

[104] B. V. Gmbh, Applied Sensors Sciosense, "As3933, 3d low frequency wake-up receiver, data sheet." Available at : https://www.sciosense.com/wp-content/uploads/documents/AS3933_DS000353_1-00.pdf (visited on 10.01.2023).

[105] E. Systems, "Esp32 data sheet." Available at : https://www.espressif.com/sites/default/files/documentation/esp32_datasheet_en.pdf (visited on 10.01.2023).

[106] R. Weinstein, "Rfid: a technical overview and its application to the enterprise," *IT Professional* **7**(3), pp. 27–33, 2005.

[107] M. A. Khan, M. Sharma, and B. R. Prabhu, "A survey of rfid tags," *International Journal of Recent Trends in Engineering* **1**(4), p. 68, 2009.

[108] C. Technology, "Relay reed spst 500ma 5v data sheet." Available at : https://www.digikey.ch/en/products/detail/coto-technology/9007-05-40/710440 (visited on 10.01.2023).

[109] "Emitter antenna." Available at: https://www.grupopremo.com/en/kgea-bfcr-keyless-go-tx-antenna-housing-plastic-with-resin-outside-connector-0161mh-0426mh/1015-kgea-bfcr-b-0500j.html. visited on: 10.01.2023.

[110] AMS, "Ams: Demo kit manual." Available at : https://www.mouser.ch/datasheet/2/1081/AS3933_Demo_kit_User_Guide-2400548.pdf (visited on 10.01.2023).

[111] I. Technologies, "Irf7389trpbf, mosfet array n and p-channel 30v 2.5w surface mount 8-so, data sheet." Available at : https://www.infineon.com/dgdl/irf7389pbf.pdf?fileId=5546d462533600a4015355f9f3441b90 (visited on 10.01.2023).

[112] E. Richards, H. Schantz, J. Unden, K. Laven, D. Compston, and C. Weil, "Electrically small antenna design for low frequency systems," 09 2010.

[113] A. J. Compston, J. D. Fluhler, and H. G. Schantz, "A fundamental limit on antenna gain for electrically small antennas," in *2008 IEEE Sarnoff Symposium*, pp. 1–5, IEEE, 2008.

[114] D. Yates, A. Holmes, and A. Burdett, "Optimal transmission frequency for ultralow-power short-range radio links," *Circuits and Systems I: Regular Papers, IEEE Transactions on* **51**, pp. 1405 – 1413, 08 2004.

[115] Item, "Profile kh." https://www.item24.com/en-ch/mb-building-kit-system/components-made-of-special-materials/profile-kh/ (visited on 09.01.2023).

[116] E. Mosquitto, "Eclipse mosquitto ™, an open source mqtt broker." Available at : https://mosquitto.org/ (visited on 10.01.2023).

Bibliography

[117] M. Organization, "Mqtt: The standard for iot messaging." Available at : https://mqtt.org/ (visited on 10.01.2023).

[118] M. Abdelhadi, M. Anan, and M. Ayyash, "Efficient artificial intelligent-based localization algorithm for wireless sensor networks," *Cyber Journals: Multidisciplinary Journals in Science and Technology, Journal of Selected Areas in Telecommunications (JSAT)* **3**, pp. 10–18, 2013.

[119] P. K. Hansen, "Magnetic position and orientation measurement system," Nov. 11 1986. US Patent 4,622,644.

[120] I. RealSense, "Intel realsense™depth camera d435i." Available at : https://www. intelrealsense.com/depth-camera-d435i/ (visited on 09.01.2023).

[121] B. Li, T. Gallagher, A. G. Dempster, and C. Rizos, "How feasible is the use of magnetic field alone for indoor positioning?," in *2012 International Conference on Indoor Positioning and Indoor Navigation (IPIN)*, pp. 1–9, IEEE, 2012.

[122] J. Chung, M. Donahoe, C. Schmandt, I.-J. Kim, P. Razavai, and M. Wiseman, "Indoor location sensing using geo-magnetism," in *Proceedings of the 9th international conference on Mobile systems, applications, and services*, pp. 141–154, 2011.

[123] C. E. Galván-Tejada, J. P. García-Vázquez, and R. F. Brena, "Magnetic field feature extraction and selection for indoor location estimation," *Sensors* **14**(6), pp. 11001–11015, 2014.

[124] R. Montoliu, J. Torres-Sospedra, and O. Belmonte, "Magnetic field based indoor positioning using the bag of words paradigm," in *2016 International Conference on Indoor Positioning and Indoor Navigation (IPIN)*, pp. 1–7, IEEE, 2016.

[125] Inteltek, "Premo, 3d electromagnetic motion tracking technology." Available at: https://www.ineltek.com/en/premo-3d-electromagnetic-motion-tracking-technology/. last accessed 09.01.2023).

[126] "postgresql." Available at: https://www.postgresql.org/. Accessed: 30-04-2023.

[127] A. Sinha, Z. Ding, T. Kirubarajan, and M. Farooq, "Track quality based multitarget tracking approach for global nearest-neighbor association," *IEEE Transactions on Aerospace and Electronic Systems* **48**(2), pp. 1179–1191, 2012.

[128] T. Fortmann, Y. Bar-Shalom, and M. Scheffe, "Sonar tracking of multiple targets using joint probabilistic data association," *IEEE journal of Oceanic Engineering* **8**(3), pp. 173–184, 1983.

[129] D. Reid, "An algorithm for tracking multiple targets," *IEEE transactions on Automatic Control* **24**(6), pp. 843–854, 1979.

[130] D. Malioutov, M. Cetin, and A. Willsky, "A sparse signal reconstruction perspective for source localization with sensor arrays," *IEEE Transactions on Signal Processing* **53**(8), pp. 3010–3022, 2005.

[131] R. Schmidt, "Multiple emitter location and signal parameter estimation," *IEEE Transactions on Antennas and Propagation* **34**(3), pp. 276–280, 1986.

[132] Z.-Q. Wang, P. Wang, and D. Wang, "Complex spectral mapping for single- and multi-channel speech enhancement and robust asr," *IEEE/ACM Transactions on Audio, Speech, and Language Processing* **28**, pp. 1778–1787, 2020.

[133] P. Z. Sotenga, K. Djouani, A. M. Kurien, and M. Mwila, "Implementation of an indoor localisation algorithm for internet of things," *Future Generation Computer Systems* , 2018.

[134] J. Gubbi, R. Buyya, S. Marusic, and M. Palaniswami, "Internet of things (iot): A vision, architectural elements, and future directions," *Future generation computer systems* **29**(7), pp. 1645–1660, 2013.

[135] A. M. Elbir, "DeepMUSIC: Multiple Signal Classification via Deep Learning," *IEEE Sensors Letters* **4**(4), 2020.

[136] E. A. Ince, M. K. Allahdad, and R. Yu, "A tensor approach to model order selection of multiple sinusoids," *IEEE Signal Processing Letters* **25**(7), pp. 1104–1108, 2018.

[137] R. Roy and T. Kailath, "Esprit-estimation of signal parameters via rotational invariance techniques," *IEEE Transactions on Acoustics, Speech, and Signal Processing* **37**(7), pp. 984–995, 1989.

[138] I. Ziskind and M. Wax, "Maximum likelihood localization of multiple sources by alternating projection," *IEEE Transactions on Acoustics, Speech, and Signal Processing* **36**(10), pp. 1553–1560, 1988.

[139] K. W. K. Lui, H. C. So, and W.-K. Ma, "Maximum a posteriori approach to time-of-arrival-based localization in non-line-of-sight environment," *IEEE Transactions on Vehicular Technology* **59**(3), pp. 1517–1523, 2010.

[140] M. I. AlHajri, N. T. Ali, and R. M. Shubair, "Indoor localization for iot using adaptive feature selection: A cascaded machine learning approach," *IEEE Antennas and Wireless Propagation Letters* **18**(11), pp. 2306–2310, 2019.

[141] Anritsu, "Bluetooth low energy direction finding and measurement for quality assurance." https://dl.cdn-anritsu.com/en-en/about-anritsu/r-d/technical/e-29/29-02.pdf, 2021.

[142] P. Andersson and L. Persson, "Evaluation of Bluetooth 5.1 as an Indoor Positioning System," (2020:529), p. 112, 2020.

[143] M. Lemmens, "Indoor positioning," *GIM International* **27**(10), pp. 24–31, 2013.

[144] J. Xiong and K. Jamieson, "Arraytrack: A fine-grained indoor location system," in *Proceedings of the 10th USENIX Conference on Networked Systems Design and Implementation, nsdi'13*, p. 71–84, USENIX Association, (USA), 2013.

[145] M. Woolley, "Core specification 5.1." Available: https://www.bluetooth.com/specifications/specs/core-specification-5-1, 2019.

[146] T. Instrument, "Real time localization system (rtls) based on bluetooth low energy." https://dev.ti.com/tirex/explore/node?node=A__AIDWKpsVKd69FVe1wxeXgA__com.ti.SIMPLELINK_ACADEMY_CC13XX_CC26XX_SDK__AfkT0vQ__LATEST&r=pTTHBmu__5.10.00.48, 2023.

[147] T. Instrument, "Bluetooth angle of arrival (aoa) antenna design." https://www.ti.com/lit/an/tida029/tida029.pdf, 2019.

[148] "BTDirectionFinding." Available at: https://labinfo.ing.he-arc.ch/gitlab/explore/projects?archived=true&language=7&sort=name_asc. Accessed: 30-04-2023.

[149] P. Semiconductor, "Pe42452." https://www.psemi.com/pdf/datasheets/pe42452ds.pdf, 2013-2014.

[150] N. Semiconductor, "nrf52840 dk." https://www.nordicsemi.com/Products/Development-hardware/nRF5340-DK, 2023.

[151] T. Instrument, "Simplelink multi-standard cc26x2r wireless mcu launchpad development kit." Available: https://www.ti.com/tool/LAUNCHXL-CC26X2R1?keyMatch=LAUNCHXL-CC2652R1, 2019.

[152] Z. Project, "About the zephyr project." https://www.zephyrproject.org/learn-about/, 2023.

[153] P. Mohaghegh, A. Boegli, and Y. Perriard, "Bluetooth low energy direction finding principle," in *2021 24th International Conference on Electrical Machines and Systems (ICEMS)*, pp. 830–834, 2021.

[154] P. Mohaghegh, A. Boegli, and Y. Perriard, "New design of antenna array for bluetooth direction finding," in *2022 25th International Conference on Electrical Machines and Systems (ICEMS)*, pp. 1–6, 2022.

[155] N. Semiconductor, "Direction finding." https://infocenter.nordicsemi.com/pdf/nwp_036.pdf, 2023.

[156] E. Soltanaghaei, A. Kalyanaraman, and K. Whitehouse, "Multipath triangulation: Decimeter-level wifi localization and orientation with a single unaided receiver," in *Proceedings of the 16th Annual International Conference on Mobile Systems, Applications, and Services, MobiSys '18*, p. 376–388, Association for Computing Machinery, (New York, NY, USA), 2018.

[157] Z. Hajiakhondi-Meybodi, M. Salimibeni, K. N. Plataniotis, and A. Mohammadi, "Bluetooth low energy-based angle of arrival estimation via switch antenna array for indoor localization," *Proceedings of 2020 23rd International Conference on Information Fusion, FUSION 2020* (July), 2020.

[158] J.-N. Shim, H. Park, C.-B. Chae, D. K. Kim, and Y. C. Eldar, "Cramér–rao lower bound on aoa estimation using an rf lens-embedded antenna array," *IEEE Antennas and Wireless Propagation Letters* **17**(12), pp. 2359–2363, 2018.

[159] A. Badawy, T. Khattab, D. Trinchero, T. M. Elfouly, and A. Mohamed, "A simple aoa estimation scheme," *CoRR* **abs/1409.5744**, 2014.

[160] "Design and Analysis Using Antenna Array Designer." Available at: https://ch.mathworks.com/help/antenna/gs/design-and-analysis-using-antenna-array-designer-app.html. Accessed: 30-04-2023.

[161] "BOSCH GLM500 PROFESSIONAL." Available at: https://www.bosch-professional.com/ae/en/products/glm-500-0601072H00. Accessed: 30-04-2023.

[162] A. Badawy, T. Khattab, D. Trinchero, T. M. Elfouly, and A. Mohamed, "A simple aoa estimation scheme," *CoRR* **abs/1409.5744**, 2014.

[163] V.-S. Doan, T. Huynh-The, V.-P. Hoang, and J. Vesely, "Phase-difference measurement-based angle of arrival estimation using long-baseline interferometer," *IET Radar, Sonar & Navigation* **17**(3), pp. 449–465, 2023.

[164] L. Jin, L. li, and H. Wang, "Investigation of different types of array structures for smart antennas," in *2008 International Conference on Microwave and Millimeter Wave Technology*, **3**, pp. 1160–1163, 2008.

[165] T.-J. Shan, M. Wax, and T. Kailath, "On spatial smoothing for direction-of-arrival estimation of coherent signals," *IEEE Transactions on Acoustics, Speech, and Signal Processing* **33**(4), pp. 806–811, 1985.

[166] S. U. Pillai and B. H. Kwon, "Forward/backward spatial smoothing techniques for coherent signal identification," *IEEE Transactions on Acoustics, Speech, and Signal Processing* **37**(1), pp. 8–15, 1989.

[167] D. A. Reynolds *et al.*, "Gaussian mixture models.," *Encyclopedia of biometrics* **741**(659-663), 2009.

[168] S. O. Ba and J.-M. Odobez, "Recognizing visual focus of attention from head pose in natural meetings," *IEEE Transactions on Systems, Man, and Cybernetics, Part B (Cybernetics)* **39**(1), pp. 16–33, 2008.

Bibliography

[169] N. P. Waweru, D. B. O. Konditi, and P. K. Langat, "Performance analysis of music, root-music and esprit doa estimation algorithm," *International Journal of Electronics and Communication Engineering* **8**(1), pp. 209–216, 2014.

[170] S. Singer and J. Nelder, "Nelder-mead algorithm," *Scholarpedia* **4**(7), p. 2928, 2009.

[171] CVE, "Description." Available: https://cve.mitre.org/cgi-bin/cvekey.cgi?keyword=ble, 2023.

Pooneh Mohaghegh

Lausanne, Switzerland | +41-76 682 24 39 | pooneh.mohaghegh@epfl.ch

Education

DOCTOR OF PHILOSOPHY |2019-2023

· Integrated Actuators Laboratory (LAI), École Polytechnique Fédéral Lausanne, Switzerland

· "Indoor Real-time Localization System for Internet of Things Application"

· Thesis Director & co-director: Prof. Yves Perriard, Dr. Alexis Boegli

MASTER OF SCIENCE | 2016-2019

· University of Tehran, Tehran, Iran

· "Application of Electrochemical Biosensors for *Anti-Cancer Drugs*"

Bachelor OF SCIENCE | 2016-2019

· University of Shiraz, Shiraz, Iran

Publications

· **P. Mohaghegh**, A. Boegli and Y. Perriard, "New Design of Antenna Array for Bluetooth Direction Finding," *2022 25th International Conference on Electrical Machines and Systems (ICEMS)*, Chiang Mai, Thailand, 2022, pp. 1-6, doi: 10.1109/ICEMS56177.2022.9982869.

· **P. Mohaghegh**, A. Boegli and Y. Perriard, "Bluetooth Low Energy Direction Finding Principle," *2021 24th International Conference on Electrical Machines and Systems (ICEMS)*, Gyeongju, Korea, Republic of, 2021, pp. 830-834, doi: 10.23919/ICEMS52562.2021.9634353.

· **Pooneh Mohaghegh**, Rabia Saeed, Francois Tieche, Alexis Boegli, and Yves Perriard. 2021. Depth Camera and Electromagnetic Field Localization System For IoT Application: High level, lightweight data fusion. In 2021 2nd Asia Service Sciences and Software Engineering Conference (ASSE '21). Association for Computing Machinery, New York, NY, USA, 94–101. https://doi.org/10.1145/3456126.3456145

· **P. Mohaghegh**, D. Pravica, J. S. Botero-Valencia, A. Boegli and Y. Perriard, "Application of a Low Frequency, Low Power Radio Frequency Positioning System for Real Time Indoor Positioning," *2020 23rd International Conference on Electrical Machines and Systems (ICEMS)*, Hamamatsu, Japan, 2020, pp. 406-410, doi: 10.23919/ICEMS50442.2020.9291201.

· **P. Mohaghegh**, D. Pravica, A. Boegli and Y. Perriard, "Investigating Optimal Settings for Distance Calculation with a Low Frequency Low-Power RF system," *2020 23rd International Conference on Electrical Machines and Systems (ICEMS)*, Hamamatsu, Japan, 2020, pp. 401-405, doi: 10.23919/ICEMS50442.2020.9291156.

· T. Loayza, S. L. Ntella, **P. Mohaghegh**, C. Koechli and Y. Perriard, "Microfluidic device for analysis of magnetorheological fluids' properties," *2022 IEEE/ASME International Conference on Advanced Intelligent Mechatronics (AIM)*, Sapporo, Japan, 2022, pp. 563-568, doi: 10.1109/AIM52237.2022.9863248.

· Q. De Menech, S. Konstantinidi, A. Walter, **P. Mohaghegh**, T. Martinez and Y. Perriard, "Characterization of Dielectric Elastomer Actuators: A Design of Experiments Approach," *2022 25th International Conference on Electrical Machines and Systems (ICEMS)*, Chiang Mai, Thailand, 2022, pp. 1-6, doi: 10.1109/ICEMS56177.2022.9983027.

· S. L. Ntella, M. -T. Duong, P. Mohaghegh, Y. Civet, Z. Pataky and Y. Perriard, "Optimization of Radial Magnetorheological Valves with Constraints of Volume, Pressure Drop and Power Consumption," 2020 23rd International Conference on Electrical Machines and Systems (ICEMS), Hamamatsu, Japan, 2020, pp. 1578-1582, doi: 10.23919/ICEMS50442.2020.9290870.

Patents

PAdmin bo100295121, *Procédé et système de controle de visiteurs dans une zone d'accès à l'intérieur d'un parc de loisir*

US Patent, US 11179076B2 , *An electrochemical probe for in-vivo measurement of H2O2 oxidation within a living tissue*

Skills

Python, C++, Matlab, Qt QML, MQTT, Bluetooth, RTOS, Data Analytics, Altium Designer, Machine Learning for IoT, COMSOL Multiphysics